UNIVERSITY OF CAMBRIDGE

Chemically Modified Titanium-Oxo Clusters as Molecular Materials

Towards Functional Coatings and Host Scaffolds

Ning Li

Gonville and Caius College

August 2018

This dissertation is submitted for the degree of

Doctor of Philosophy

Declaration

The work in this thesis was done in the Department of Chemistry, University of Cambridge, U.K., and the Institute of Materials Research and Engineering (IMRE), Agency for Science, Technology and Research (A*STAR), Singapore, under the joint supervision of Prof. Dominic S. Wright and Dr. He-Kuan Luo from October 2014 to August 2018.

This thesis is the result of the author's own work and not the results of any type of collaboration unless otherwise stated. The work is original and has not been submitted, in full or in part, for a degree or diploma or other qualification at the University of Cambridge or any other university or similar institution.

The word count of this thesis is approximately 44700, which does not exceed the word limit set by the Degree Committee of Physics and Chemistry.

Ning Li

Gonville and Caius College

August 2018

Abstract

Inspired by the widespread applications of TiO_2, titanium-oxo clusters (TOCs) of the type $[Ti_xO_y(OR)_z]$ (OR = alkoxide) have attracted considerable attentions recently. In this thesis, new TOCs involving both heterogeneous metal doping and functional ligand modification, namely $[Ti_{18}Mn_4O_{30}(OEt)_{20}Phen_3]$ (Phen = 1,10-phenanthroline) and $[LnTi_6O_3(O^iPr)_9(salicylate)_6]$ (Ln = La, Ce, Pr, Nd, Sm, Eu, Gd, Tb, Dy, Ho and Er) have been synthesised and thoroughly characterised.

One particular feature of the $[Ti_{18}Mn_4O_{30}(OEt)_{20}Phen_3]$ cluster is its capability for *in situ* self-assembly into hollow microparticles. A novel coating technology involving such *in situ* self-assembly has been demonstrated to fabricate multifunctional cotton fabrics in a single-step operation, producing spherical microparticles of 0.8 μm average diameter. These microparticles are firmly mounted on the underlying cotton substrate, imparting the coated surface with robust hydrophobicity, antibacterial activity and UV-blocking performance.

For the $[LnTi_6O_3(O^iPr)_9(salicylate)_6]$ clusters, their isostructural features allow a systematic investigation of the influence of the paramagnetic Ln^{3+} ions on the NMR behaviour of the ^1H and ^{13}C nuclei in the peripheral ligands. Compared to conventional Ln^{3+}-complexes, the ligands in these clusters are separated from the Ln^{3+} ions by oxo-Ti^{4+} linkages, and therefore experience a weaker paramagnetic influence. As a result, all the ^1H and ^{13}C resonance signals can be observed and unambiguously assigned, which makes the in-depth data analysis possible.

The Ln-TOCs can also act as an excellent platform for investigating the photophysical interplay between the coordinated salicylate ligands, Ln^{3+} dopants and Ti^{4+} ions in TOCs. Both visible and near-infrared Ln^{3+}-centred photoluminescence can be sensitised in solution, and their excitation bands all extend into the visible region up to 475 nm. An energy transfer mechanism involving the salicylate-to-Ti^{4+} charge-transfer state is proposed to account for the largely red-shifted excitation wavelengths, which is supported by both steady-state and time-resolved photoluminescence spectroscopic data.

Acknowledgements

Writing of this thesis comes with a reflection on the past four years that I have spent in Cambridge, U.K., and Singapore, during which many individuals and groups have helped and supported me in one way or another. Without them, I would not be in the position that I am in today.

First and foremost, I would like to thank my supervisors, Prof. Dominic S. Wright (Cambridge) for his always insightful advices and encouragement throughout my postgraduate studies, as well as Dr. He-Kuan Luo (Singapore) for his constant support and guidance in my entire research career so far, stretching from my undergraduate final year project to the close of my Ph.D. Their enthusiasm and expertise have enormously helped my project move in an interesting and stimulating direction. It has been an honour and privilege to work with them both.

I also wish to thank the members of the Wright group in Cambridge and of the Luo Group in Singapore, who have made the duration of my Ph.D very enjoyable. In particular, I owe a huge debt of gratitude to Dr. Peter D. Matthews, who has been an incredible source of moral and scientific support, especially during the first two years. Special thanks also go to Dr. Raúl García-Rodríguez for his assistance in many NMR measurements and Ms. Schirin Hanf for numerous fruitful discussions.

This work would not have been possible without the expertise and assistance of many collaborators with whom I have had the pleasure of working, including Prof. Erwin Reisner, Dr. Paul T. Wood, Ms. Jane J. Leung, Dr. Timothy E. Rosser and Mr. James Xiao from Cambridge; Dr. Floriana Tuna and Prof. Richard Winpenny from Manchester; Dr. Vijila Chellappan, Ms. Gomathy Sandhya Subramanian, Prof. En-Tang Kang and Dr. Dicky Pranantyo from Singapore. I would also like to thank Dr. Andrew D. Bond (Cambridge) for taking the time to help me with single-crystal X-ray crystallography, which constitutes an important part in this thesis.

Finally, I would like to express my heartfelt gratitude to my family and friends during my entire education journey, especially my wife, Wenqi Zhang, for her constant and unconditional support and for putting up with my ridiculous working hours throughout the past four years.

Financial support from the A*STAR Graduate Scholarship (Overseas) is also greatly appreciated.

Abbreviations

COSY	Correlation Spectroscopy
CV	Cyclic Voltammetry
D	Debye
DEPT	Distortionless Enhancement by Polarisation Transfer
DI	De-Ionised
DoS	Density of States
DRS	Diffuse Reflectance Spectroscopy
DSSCs	Dye-Sensitised Solar Cells
EDX	Energy Dispersive X-ray Spectroscopy
ESI	Electrospray Ionisation
ESR	Electron Spin Resonance
FESEM	Field Emission Scanning Electron Microscopy
FTIR-ATR	Fourier Transform Infrared Spectroscopy-Attenuated Total Reflection
FTO	Fluorine-doped Tin Oxide
HMBC	Heteronuclear Multiple Bond Correlation
HMQC	Heteronuclear Multiple Quantum Correlation
HOMO	Highest Occupied Molecular Orbital
IR	Infra-Red Spectroscopy
K	Kelvin
L-TOCs	Ligand-modified Titanium-Oxo Clusters

LUMO	Lowest Unoccupied Molecular Orbital
M-TOCs	Metal-doped Titanium-Oxo Clusters
MOF	Metal-Organic Framework
mol	Moles
MPs	Microparticles
MS	Mass Spectrometry
NIR	Near-Infrared
NMR	Nuclear Magnetic Resonance
NOESY	Nuclear Overhauser Effect Spectroscopy
Oe	Oersted
RHE	Reversible Hydrogen Electrode
TGA	Thermogravimetric Analysis
TOCs	Titanium-Oxo Clusters
UV-Vis	Ultra-Violet and Visible light spectroscopy
V	Volts
XPS	X-ray Photoelectron Spectroscopy
XRD	X-Ray Diffraction

Contents

List of Figures

List of Tables

List of Schemes

Chapter 1.

Background

Since the *Industrial Revolution* in the 19th century, the economic development of our modern society has relied heavily on global energy consumption, which is directly reflected by the close correlation between total energy consumed and the Gross Domestic Product per capita, or the Human Development Index.[1] Over the past decades, despite the availability of renewable and clean energy alternatives (*e.g.*, hydroelectric, wind, nuclear, etc.), a dominant percentage of the global energy consumption is still supplied by fossil fuels, which are non-renewable and also incur serious environmental problems, such as water/air pollution and global warming. These problems pose a great threat not only to the continued growth in the standard of living on the planet but also to the very survival of human race.

To resolve this pressing energy and environmental crisis, the search for new materials that can generate clean energy and/or alleviate pressing environmental problems has been of tremendous research interests in recent decades, among which titanium dioxide (*i.e.*, TiO_2) stands out as one of the most promising candidates to support the desired green and sustainable future.

1.1. Titanium Dioxide (TiO_2) Materials

Following its large-scale production in the early 20th century, TiO_2 has been widely employed in many commercial products, such as white pigment,[2,3] sunscreens,[4,5] and toothpaste,[6] etc. It was later in 1972 that the capability of TiO_2 electrodes to photocatalytically split water under UV irradiation was revealed by Honda and Fujishima.[7] Ever since then, worldwide research communities have devoted great efforts to TiO_2 materials, and demonstrated many technologically important applications in areas ranging from photovoltaics to photocatalysis, and further to photo-/electrochromics and sensors.[8-11] As the most promising photocatalyst, there is a great deal of hope that TiO_2-based materials can ease the impending energy and environmental crisis through effective utilisation of abundant solar energy, based on photovoltaic devices as well as photocatalytic water splitting and organic pollutant degradation systems.

As a result, continued breakthroughs have been made in the preparation and modification of various TiO_2 materials in recent years.[12]

There are three common polymorphs of TiO_2, namely anatase, rutile and brookite, with their unit-cells being shown in Figure 1.1, and crystal parameters summarized in Table 1.1. Both anatase and rutile adopt a tetragonal structure, and the TiO_6 octahedra are slightly distorted, with two Ti-O bonds being longer than the other four and the O-Ti-O angles deviating from 90°. One difference is that the TiO_6 octahedra in anatase share four common edges with neighbouring octahedra, whereas the number of common edges is two in rutile.[13,14] The third polymorph of TiO_2, brookite, has a more complicated crystal structure (Figure 1.1c), compared to anatase or rutile. In contrast to the latter cases where only two types of Ti-O bond lengths and O-Ti-O angles exist, there are six different Ti-O bond lengths ranging from 1.87 Å to 2.04 Å, and therefore twelve different O-Ti-O angles in the range of 77° – 105° in brookite, and each TiO_6 octahedron shares three common edges with its surrounding units.[15] A complementary way of viewing the TiO_2 crystal structures is to focus on the three-fold coordinated oxygen ions in the planar Ti_3O building blocks. The Ti_3O units primarily adopt a Y-shaped conformation in rutile and a T-shape in anatase, whereas in brookite both Y- and T-shaped Ti_3O units are present.[16]

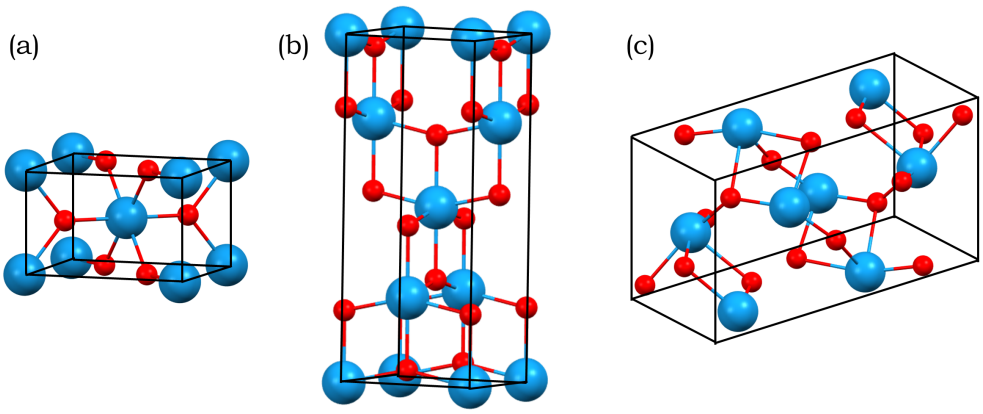

Figure 1.1. Crystal structures of common TiO_2 polymorphs, (a) rutile, (b) anatase, and (c) brookite. Colour code for atoms: Ti = cyan, O = red.

Table 1.1. Crystal structure data of common TiO_2 polymorphs. Data for anatase and rutile are adapted from Ref. 13, and that for brookite is from Ref. 15.

	Anatase	Rutile	Brookite
Crystal structure	tetragonal	tetragonal	orthorhombic
Lattice constant (Å)	a = 3.784	a = 4.5936	a = 9.184
	c = 9.515	c = 2.9587	b = 5.447
			c = 5.145
Space group	$I4_1/amd$	$P4_2/mnm$	Pbca
Molecule/cell	4	2	8
Volume/molecule ($Å^3$)	34.061	31.2160	32.172
Density (g/cm^3)	3.79	4.13	3.99
Ti-O bond length (Å)	1.937(4)	1.949(4)	1.87 – 2.04
	1.965(2)	1.980(2)	
O-Ti-O bond angle	77.7°	81.2°	77.0° – 105.0°
	92.6°	90.0°	

As foreseen by Richard Feynman *'There's Plenty of Room at the Bottom'*,[17] new physical and chemical properties will emerge when the size of a material goes down to the nanometre scale (*i.e.*, 10^{-9} metre). In particular, the transport of charge carriers in nano-scale TiO_2 materials ('nano-TiO_2') is primarily governed by the quantum confinement effect, and therefore largely affected by the material's dimension and geometric shape. The specific surface area also increases dramatically with decreased material dimension. This is undoubtedly beneficial for TiO_2-based devices, as the reactions and interactions that TiO_2 facilitates usually occur on the surface or at the interface between TiO_2 and the reaction substrates.[7-11]

Heterogeneous doping by metal/non-metal atoms and surface modification by functional ligands are the two main approaches to tune the physical, chemical and electronic properties of nano-TiO_2, which have proved particularly effective for lowering the optical band gap and facilitating the transportation of photo-generated charge carriers, both of which are of great importance to improve the photocatalytic and photovoltaic activities of TiO_2-based systems. However, details of how heterogeneous doping and surface ligand modification help improve the

performance are still unclear, mainly hindered by the difficulties in precisely determining the local atomic connectivity of the metal/non-metal dopants and the coordination environment of the surface ligands in solid-state materials. Critically, the insolubility of TiO_2 in organic solvents or water also prevents any studies using various solution-based analytical techniques such as NMR spectroscopy.

1.2. Titanium-Oxo Clusters (TOCs) as TiO_2 Models

Using recently developed synthetic approaches,[18-20] the successful synthesis of titanium-oxo clusters (TOCs) of the type $[Ti_xO_y(OR)_z]$ (OR = alkoxide) has allowed chemists and material scientists to gain new insights into molecular activation using TiO_2 nanomaterials.[21] Various alternative nomenclatures are used for this type of cluster compound in the literature, such as polyoxotitanate, or polyoxotitanium cages.[22,23] In the context of this thesis, the term 'titanium-oxo clusters' is used throughout, mainly in regard to the fact that '*cage*' usually implies to the capability of hosting guest molecules in the structure, which is not necessarily true for the clusters described here. With atomically well-defined structures, the TOCs with Ti_xO_y cores and organic ligand peripheries represent a unique family of titanium oxide species with versatile but synthetically controllable structural features.[24-26] Although the local connectivity in the Ti_xO_y core may differs from that in the common polymorphs of TiO_2, mainly in the aspects of Ti coordination numbers (exclusively six in TiO_2 *vs.* four to seven in TOCs), Ti-O bond lengths and O-Ti-O bond angles,[21-23] they are still widely considered to be excellent models for studying the structural chemistry and electronic properties of nanoparticles of TiO_2.[27]

Solvothermal synthetic approaches in organic solvents are the most commonly employed methods for TOCs preparation,[26] usually with titanium alkoxide $[Ti(OR)_4]$ being the precursor. Similar methods can also be applied in ionic liquids,[28] or even in aqueous media,[29-31] with cautiously controlled reaction conditions. While their excellent solubility in common organic solvents allows

TOCs to be studied using solution-based techniques (*e.g.*, NMR,[24] mass spectrometry,[32-34] etc.), single-crystal X-ray diffraction is perhaps still the most preeminent tool for their characterisation, allowing unambiguous determination of structural features and comparison to TiO_2 nanoparticles. Crystallisation of TOCs can usually be achieved either by direct crystallisation methods (*i.e.*, slow cooling from the reaction temperature), or by crystallisation of the reaction solution using various standard conditions (*e.g.*, evaporation, vapour-diffusion, refrigeration, etc.).

1.3. Literature Summary on TOCs

TOCs, as a family of inorganic compounds, have been under intensive investigation for decades, and the early literature mainly focused on their syntheses, sol-gel processing, and structural characterization.[35-38] Later the Wright group in Cambridge and the Coppens group in New York re-visited these clusters and studied them as molecular models for solid-state TiO_2, aiming to establish the structure-property relationships for technologically important titanium oxide systems.[21-23] Currently related research interests on TOCs have been mainly focused on three aspects: (i) increasing the size of TOCs to mimic the structural features of TiO_2 nanoparticles better, (ii) introducing metal and/or non-metal dopant(s) to fine-tune their electronic structures, and (iii) attaching functional ligands at the cluster periphery to promote more versatile functionalities, such as enhanced light harvesting (Figure 1.2).

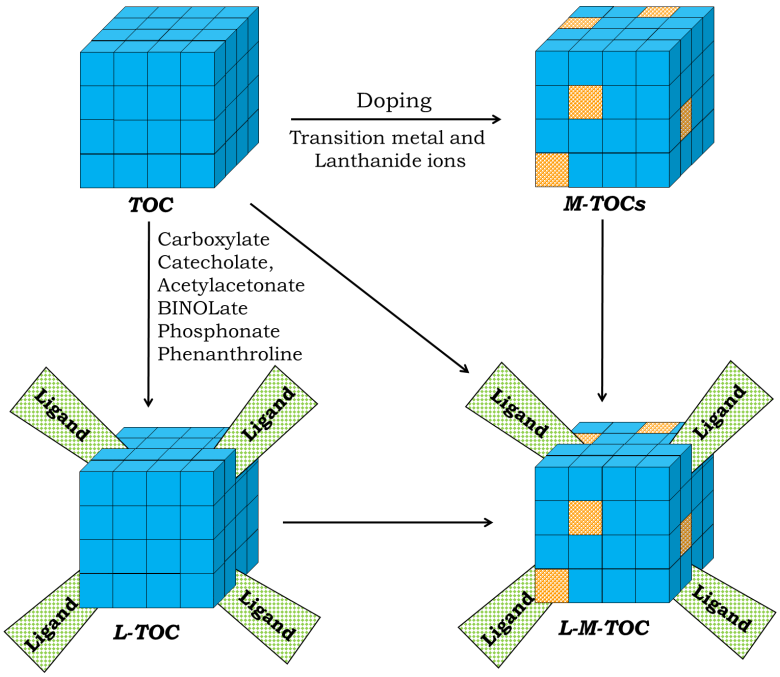

Figure 1.2. Illustration of the structural relationship between TOCs, metal-doped TOCs (M-TOCs) and ligand-modified TOCs (L-TOCs), as well as L-M-TOCs that possess both metal doping and ligand modification. The blue cubes represent the Ti_xO_y core, while the orange cubes are metal dopant ions.[23]

1.3.1.The size of TOCs

In comparison with TiO_2 nanoparticles, atomically well-defined TOCs are much smaller in size (usually in the sub-nm scale), especially when only considering the Ti_xO_y core. This difference in size incurs practical difficulties in relating their electronic structures that are heavily dependent on the number of Ti atoms in a single nanoparticle or cluster (Figure 1.3). As a result, there has been continuous research efforts to increase the dimensions of TOCs, mainly on the purpose of more accurately mimicking the structural features of TiO_2 nanoparticles that usually contain hundreds, or even thousands of Ti centres.

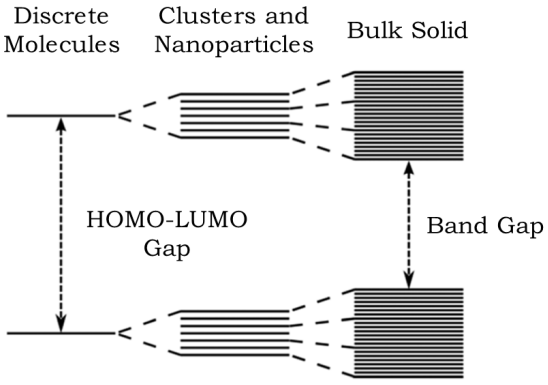

Figure 1.3. Illustration of the band and HOMO-LUMO structures of discrete molecules, clusters and nanoparticles, and the bulk solid. A gradual transition from localised molecular orbitals to band structures is demonstrated.[22]

The conventional synthetic methods for TOCs involve controlled hydrolysis of titanium alkoxide in inert atmospheres at room temperature, but these conditions merely produce small clusters containing only a few Ti centres. This is potentially because of the empirical observation that, with increasing cluster size, the hydrolytic and/or thermal stability decreases owing to increased thermodynamic instability with respect to TiO_2.[22] To overcome this drawback, more forcing solvothermal conditions (*i.e.*, higher temperature and pressure) and use of organic acids as stabilising ligands have been employed recently.[22] Using these approaches large TOCs with nuclearity (*i.e.*, number of Ti atoms in the cluster core) of 28 for a bridged dimer structure $[Ti_{28}O_{40}(O^tBu)_{20}(OAc)_{12}]$ (HOAc = acetic acid, O^tBu = tert-butoxide), of 42 for a spherical structure $[H_6Ti_{42}O_{60}(O^iPr)_{42}(OH)_{12}]$ (O^iPr = isopropoxide) and of 52 for a one-dimensional rod-like structure $[Ti_{52}O_{72}(O^iPr)_{28}(PA)_{34}(OH)_2]$ (HPA = propionic acid) have been achieved (Figure 1.4).[39-41] Despite these milestones, the synthesis of large TOCs still remains a significant challenge, and is still to be developed to the dimensions of polyoxometalates containing other metals, such as $[\{(Mo)Mo_5O_{21}(H_2O)_3(SO_4)\}_{12}(VO)_{30}(H_2O)_{20}]^{36-}$.[42]

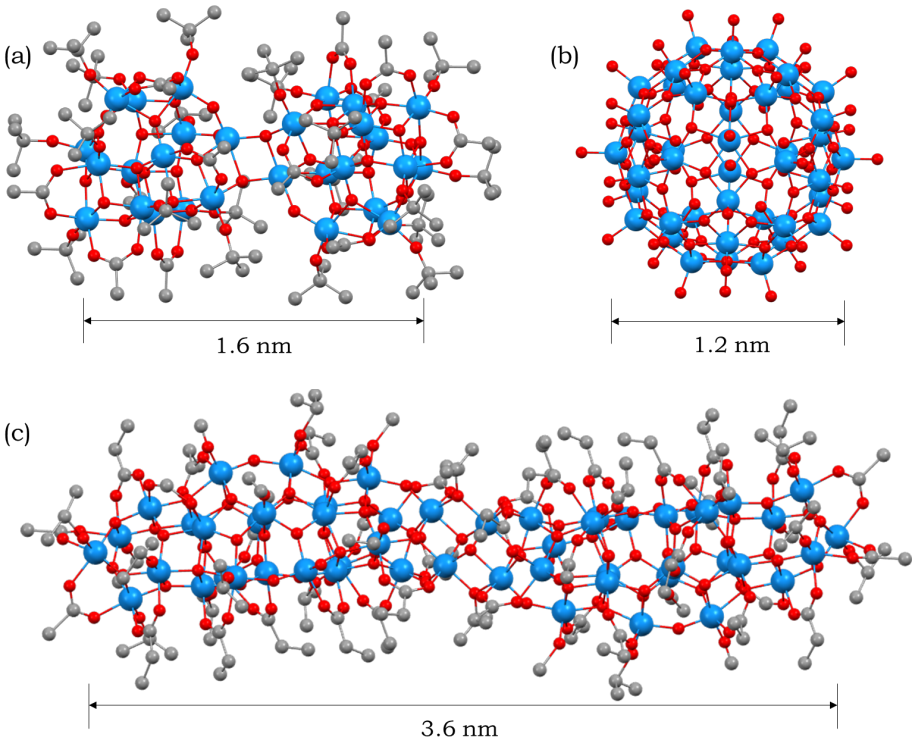

Figure 1.4. Ball-stick representations of the molecular structures of (a) $[Ti_{28}O_{40}(O^tBu)_{20}(OAc)_{12}]$ (HOAc = acetic acid, O^tBu = tert-butoxide), (b) $[H_6Ti_{42}O_{60}(O^iPr)_{42}(OH)_{12}]$ (O^iPr = isopropoxide) and (c) $[Ti_{52}O_{72}(O^iPr)_{28}(PA)_{34}(OH)_2]$ (HPA = propionic acid). Colour code for atoms: Ti = cyan, O = red, C = grey. Hydrogen atoms are omitted for clarity. Only the cluster core is depicted in (b), as the full structure is not available. The dimensions of the cluster cores are also shown.

1.3.2. Metal-Doping in TOCs

In a similar manner to TiO_2 nanoparticles or bulk TiO_2, metal-doping represents an effective approach to fine-tuning of the physical and electronic properties of TOCs.[22] Over the decades, a range of metal dopants has been successfully incorporated into different-sized TOCs, including the alkaline metals (Li, Na),[43] alkaline-earth metals (Mg, Ca),[44] transition metals (Mn,[45-49] Co,[44,47,49-53] Fe,[46,47,54] Cu,[47] Zn,[44,47] Mo,[55] Ni,[44,47,49] Cr,[55,56] In,[57] Cd,[44,52,58] Ga[46]) and lanthanides (La,[59,60] Ce,[20,59-61] Nd,[59,60,62] Sm,[59,63,64] Eu,[59,62-66] Gd,[59,63,64] Ho[59] and Er[67,68]). These metal dopants have been found either in an interstitial position or on the surface of the M-TOCs. The optical band gaps (or rather HOMO-LUMO gaps, due to their

discrete nature) of these M-TOCs are found to be dependent on (i) the nature of dopant metal ion(s), (ii) the size of the cluster, and (iii) the atomic arrangement in the cluster.

The influence of the nature of dopant metal ions is illustrated by a recent report on a group of $\{Ti_{14}M\}$ clusters, including $[Ti_{14}MnO_{14}(OEt)_{28}(OH)_2]$, $[Ti_{14}FeO_{14}(OEt)_{28}(OH)_2]$ and $[Ti_{14}GaO_{14}(OEt)_{28}(OH)]$ (OEt = ethoxide) (Figure 1.5).[46] Diffuse reflectance spectroscopy (DRS) data show that their band gaps follow the order $\{Ti_{14}Mn\}$ (3.36 eV) ≈ $\{Ti_{14}Fe\}$ (3.22 eV) < $\{Ti_{14}Ga\}$ (3.57 eV), with the value for $\{Ti_{14}Ga\}$ being comparable to that found for the undoped $[Ti_{16}O_{16}(OEt)_{32}]$ cluster of similar nuclearity (3.63 eV).[46] Density of States (DoS) calculations suggest the trend is due to the different 3*d* orbital positions of the interstitial dopant metal ions. Both Mn^{2+} (d^5) and Fe^{2+} (d^6) ions possess partially occupied 3*d* orbitals that can readily mix with the valence band of the Ti_xO_y core, which produces energy levels close to the valence band maximum and thus results in a decrease in the band gap. This feature resembles the band gap behaviour of transition metal doped bulk TiO_2 materials that can be described by the Anderson's impurity model in semiconductor physics.[69] Such band mixing is, however, not possible for $\{Ti_{14}Ga\}$, because the full-shell d^{10} configuration of the Ga^{3+} ion has a much lower energy that is incapable of affecting the Ti_xO_y band positions.

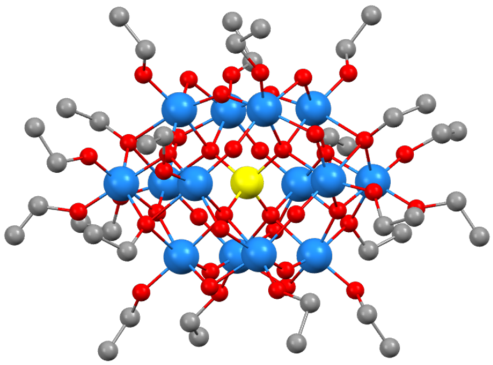

Figure 1.5. Ball-stick representation of the molecular structures of $[Ti_{14}MO_{14}(OEt)_{28}(OH)_x]$ (M = Mn or Fe, x = 2; M = Ga, x = 1; OEt = ethoxide). Colour code for atoms: Ti = cyan, M = yellow, O = red, C = grey. Hydrogen atoms are omitted for clarity.

The effect of M-TOCs size on the band gaps is reflected in a recent example involving the series of Co^{2+}-doped clusters $[Ti_4O(OEt)_{15}(CoBr)]$, $[Ti_7O_5(OEt)_{19}(CoBr)]$ and $[Ti_{24}O_{34}(OEt)_{30}(CoBr)_2]$ (Figure 1.6).[53] The onset in the experimentally determined absorption edge red-shifts from *ca.* 430 nm, to *ca.* 450 nm and further to *ca.* 475 nm with the cluster size increase along the series. The observed trend in the absorption edge is roughly inversely proportional to the Co^{2+} dopant concentration (*i.e.*, 5.8 wt.%, 4.2 wt.% and 3.5 wt.%), and is, therefore, not the result of the metal dopant concentration alone. In particular, DoS calculations show that the increase in the Ti_xO_y core size has the dominant effect on the decrease in the observed band gaps in this series of clusters, showing that as the cluster size increases from Ti_4 to Ti_{24}, the band gap states formed by *d* orbital and valence band mixing gradually merge together with a consequent increase in the valence band maximum, leading to a reduced optical band gap.[53]

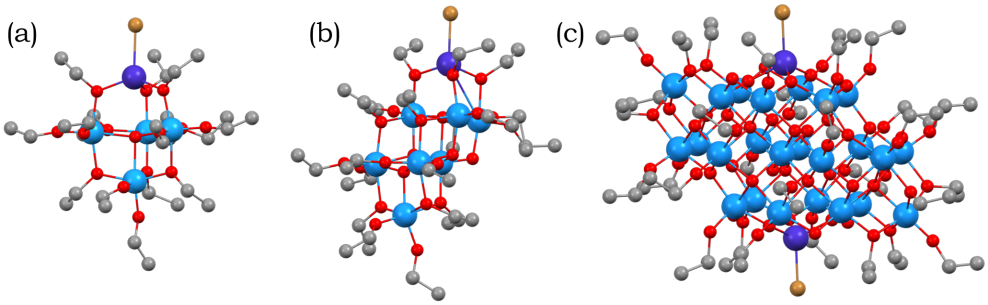

Figure 1.6. Ball-stick representations of the molecular structures of (a) $[Ti_4O(OEt)_{15}(CoBr)]$, (b) $[Ti_7O_5(OEt)_{19}(CoBr)]$ and (c) $[Ti_{24}O_{34}(OEt)_{30}(CoBr)_2]$. Colour code for atoms: Ti = cyan, Co = blue, Br = brown, O = red, C = grey. Hydrogen atoms are omitted for clarity.

A completely unexpected feature is seen for another Co^{2+}-doped $[Ti_{20}O_{28}(OEt)_{23}(Co_2I_3)(HPO_3)]$ cluster (Figure 1.7a), which, despite its lower nuclearity than $\{Ti_{24}Co_2\}$, exhibits a much greater reduction in the band gap (with absorption edge at *ca.* 530 nm).[53] DoS calculations reveal that the unexpected band gap reduction results from the significant molecular dipole moment present in the $\{Ti_{20}Co_2\}$ structure (Figure 1.7a). In contrast to the symmetric structure of

$\{Ti_{24}Co_2\}$ with no molecular dipole, the two Co^{2+} ions at one side of the $\{Ti_{20}Co_2\}$ structure result in a large molecular dipole of ~ 22 D. More importantly, the direction of this dipole is aligned with that of the HOMO-LUMO transition, leading to possible stabilisation of a photo-induced electron transfer along the dipole vector, and hence a consequent reduction in the band gap (Figure 1.7b). A recent theoretical study on the band diagrams of Li^+- and Na^+-doped TOCs further supports such dipole-induced mechanism, in which a band gap reduction occurs even without mixed states at the band edges.[43] This observation presumably also stems from the asymmetric structures of these clusters in the solid state, as a recent theoretical study has suggested that, dipolar solid-state photocatalysts with the valence and conduction bands being distributed on two opposite surfaces also results in a significant reduction in the band gaps.[70,71]

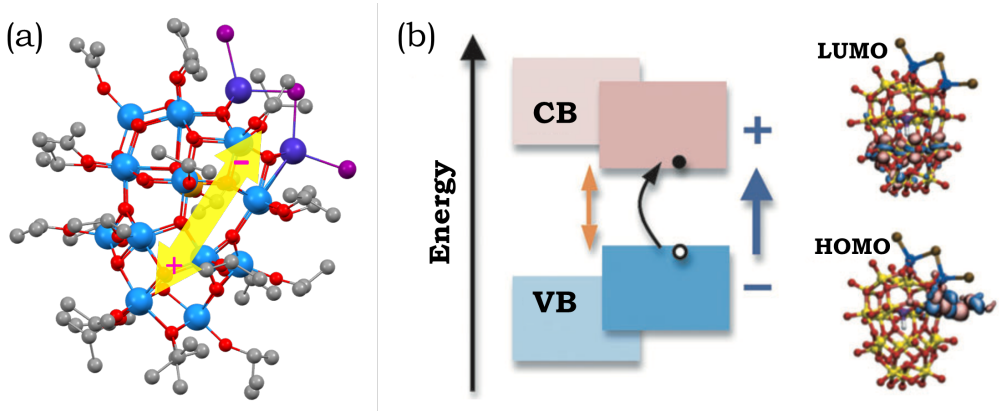

Figure 1.7. (a) Ball-stick representation of the molecular structure of $[Ti_{20}O_{28}(OEt)_{23}(Co_2I_3)(HPO_3)]$. Colour code for atoms: Ti = cyan, Co = blue, I = purple, O = red, C = grey, P = orange. Hydrogen atoms are omitted for clarity. (b) Schematic of the dipole-induced band gap decrease mechanism with the HOMO and LUMO of the cluster shown on the right.[53]

Departing from metal-doping, Hanf *et al.*[72] recently explored the influence that halide ions have on the optical band gaps and electronic properties of a series of halide-only, and cobalt-halide-doped TOCs. For the halide-doped TOCs $[Ti_3(O^iPr)_9X]$ (X = F, Cl, Br and I; Figure 1.8a), the band gap reduction is due to the alignment of built-in dipole moment and the HOMO-LUMO transition (Figure 1.8b), and also the effect of the energy increase in the valence orbitals of the

halide dopant (Figure 1.8c), whereas in the cobalt-halide-doped clusters, the additional effects of crystal-field splitting and electron repulsion need to be taken into account to explain the band gap behaviours. Considering the fact that a large amount of the literatures on doped TiO_2 has been directed towards the inclusion of non-metal dopants and their effect on the catalytic activities,[73-75] it is surprising that so little attention has been paid to the non-metal doping in TOCs, which definitely merits further investigations.

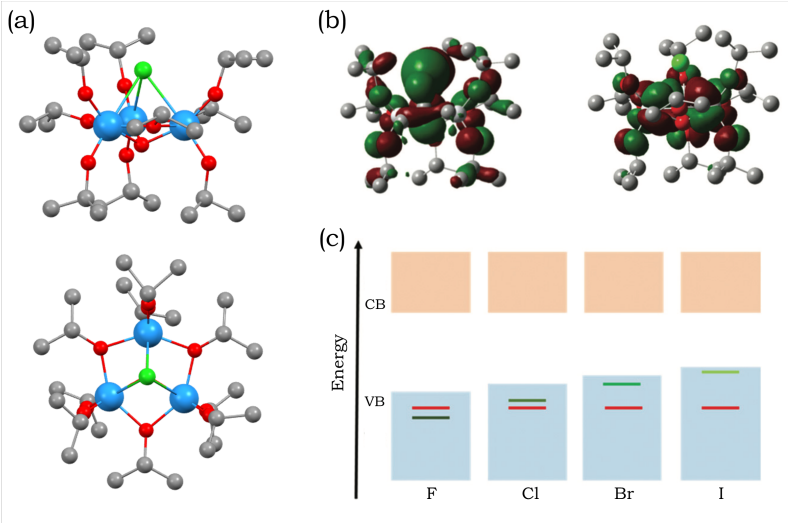

Figure 1.8. (a) Ball-stick representation of the molecular structure of $[Ti_3(O^iPr)_9Cl]$, viewed in the direct perpendicular to (top) and along (bottom) the C_3 axis. Colour code for atoms: Ti = cyan, Cl = green, O = red, C = grey. Hydrogen atoms are omitted for clarity. (b) Visualisation of the HOMO (left) and LUMO (right) of $[Ti_3(O^iPr)_9Cl]$. (c) Diagram showing the influence of the halide ions on the valence band in the halide-doped TOCs $[Ti_3(O^iPr)_9X]$ (X = F, Cl, Br and I). The red bar represents the oxygen *p* orbital contribution, while the green bar is for halide *p* orbital contribution.[72]

1.3.3. Ligand Functionalisation of TOCs

Another major area of interest has been the surface modification of TOCs with functional ligands, that impart additional structural diversity and chemical reactivity.[23,76,77] Functional ligand modified TOCs (L-TOCs) of the general type $[Ti_xO_y(OR)_z(L)_m]$ (OR = alkoxide, L = functional ligand) can be regarded as molecular fragments of surface-sensitised solid-state TiO_2 and are of value as

model compounds for studying the interfacial charge- and energy-transfer between the bound functional ligands and the underlying bulk semiconductor surface.[78-80]

In the majority of L-TOCs, the functional ligands are coupled to the Ti_xO_y core via bidentate carboxylate[81-83] or β-diketonate anchors,[80,84,85] with the coordination in either chelating or bridging modes. In terms of functionality, the relatively simple ligands (*e.g.*, acetate) mainly act as the stabilising moieties, replacing the highly hydrolysable alkoxide groups,[86] and/or serve to increase compatibility and transferability within organic matrices.[24] Those bearing more complex ligands (*e.g.*, ferrocene,[87-89] aromatics[90,91]) are usually capable of bringing about additional structural diversity and versatile functionalities, featuring various potential applications.

From the synthetic point of view, the functional ligands can either be introduced during '*one-pot*' synthesis of the clusters[81-83] or grafted onto pre-formed clusters via post-modification.[92-34] The former has been generally achieved by reacting the titanium precursors directly with desired functional ligands, but it is not easy to control the Ti_xO_y core structures, and the number and coordination modes of the surface functional ligands precisely. In contrast, the post-modification approach is less general and much more difficult to perform, mainly because it requires labile surface groups and simultaneously balancing the charge and coordination numbers during substitution. This type of substitution is therefore only possible when the number of the occupied coordination sites and the charges of the ligands are the same between the substituting and substituted ligands.

Apart from the popular carboxylate and β-diketonate moieties, others ligands including phosphonate,[85,94,95] azoles,[96-98] catecholate,[78,92,98,99] *p*-arsanilate,[100] 2,2'-biphenolate,[99] and 2,6-Bis(hydroxymethyl)-*p*-cresol[101] have also been used. In addition, more than one type of ligand can be present in a single L-TOC, producing some unique molecular structures and resulting in the synergy of the functionalities of each ligand.[94,96,102] For example, by simultaneously using the carboxylate and phosphonate ligands Fang *et al.*[94] reported a nano-sized cluster $H_2[Ti_{18}O_{20}(O_3P\text{-}Phen)_2(PA)_{16}(O^iPr)_{14}]$ (HPA = propionic acid, O_3P-Phen = phenyl

phosphonate) with a bridged dimeric structure. Similarly, Wu *et al.*[96] prepared two 5-sulfosalicylic acid (H_3ssal) and 1,10-phenanthroline (Phen) substituted TOCs with formulae $[Ti_6O_8(Hssal)_2(Phen)_6(H_2O)_4]$ and $[Ti_4O_4(Hssal)_4(Phen)_4]$, both showing efficient homogeneous catalytic activity in the oxidation of sulphides to sulfoxides with H_2O_2 as the oxidant.

Functional ligands are also capable of tuning the overall electronic properties of the resultant L-TOCs. A recent thorough study done by Liu *et al.*[103] revealed that, through the labile coordination sites on a robust phosphonate-stabilized TOC, fourteen different O-donor ligands could be successfully introduced without changing the cluster core (Figure 1.9a). They further showed that increasing the electron-withdrawing capability of the organic ligands allows the gradual reduction of the band gaps of the resultant L-TOCs (Figure 1.9b). Another interesting feature of L-TOCs is that, upon light irradiation, electrons can be excited from the ligand HOMO level directly into the Ti^{4+} *d* orbitals (ligand-to-metal charge-transfer, LMCT), which requires photons of much lower energy than that for the O^{2-}-to-Ti^{4+} charge-transfer process or the ligand HOMO-LUMO transition.[104,105] This is the reason why certain L-TOCs exhibit red to yellow colours, even when the Ti_xO_y cores and the organic ligands used are both colourless on their own.

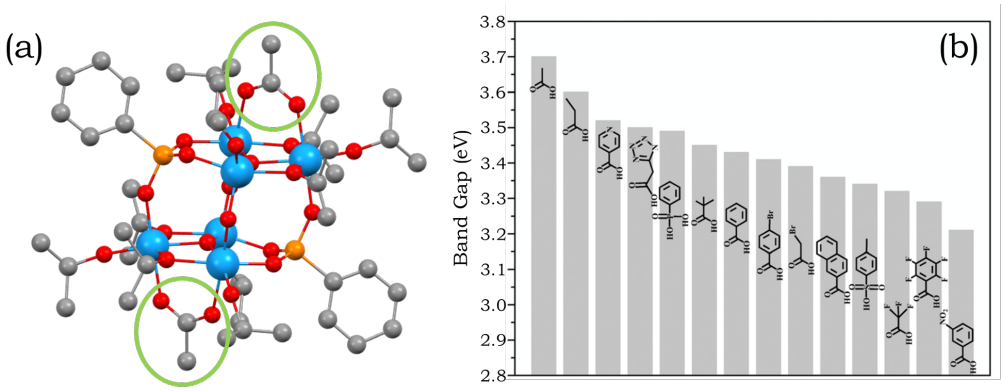

Figure 1.9. (a) Ball-stick representation of the molecular structure of $[Ti_6O_4(O^iPr)_{10}(O_3P\text{-}C_6H_5)_2(OOCR)_2]$. Colour code for atoms: Ti = cyan, P = orange, O = red, C = grey. Hydrogen atoms are omitted for clarity. (b) Band gaps of the $\{Ti_6\}$ clusters with different carboxylate ligands at the positions highlighted by the green circles in (a).[103]

1.3.4. Potential Applications of TOCs

Although the interest in TOCs originates from their role as atomically well-defined models for the solid-state semiconductor TiO_2, their unique molecular structures containing various functional groups and metal dopants gives them further properties and functionalities that are useful for various applications. In this section, the potential applications of TOCs are discussed and illustrated by selected examples, including (i) single-source precursors for TiO_2 materials, (ii) nano-building blocks for hybrid materials construction, (iii) photocatalysts, (iv) photochromism and photoluminescence, (v) dye-synthesised solar cells, (vi) asymmetric catalysts, and (vii) gas adsorption.

1.3.4.1. Single-Source Precursors for TiO_2 Materials

The presence of readily hydrolysable alkoxide groups surrounding the inorganic Ti_xO_y core introduces the prospect of using TOCs as single-source precursor for the deposition of TiO_2 materials by hydrolysis.[22,106,107] One of the principal advantages of using TOCs over other solid-state approaches is that their solubility in organic solvents facilitates the fabrication of thin films by relatively simple methods, like drop-casting and spin-coating. A further advantage is the low temperatures at which this deposition can occur, normally directly from solution at room temperature in the presence of ambient air (the source of H_2O), although a subsequent calcination step is usually required to achieve crystalline phase TiO_2 and also to remove organic impurities (Scheme 1.1). More interestingly, by sintering the classic $[Ti_{16}O_{16}(OEt)_{32}]$ cluster together with the 2-D graphene oxide, anatase TiO_2 nano-flakes made of nanoparticles of less than 10 nm in diameter can be produced,[108] which outperforms TiO_2 material prepared from only the $[Ti_{16}O_{16}(OEt)_{32}]$ cluster by a factor of forty in the rate of photocatalytic H_2 production from aqueous methanol suspensions, and by a factor of five compared to the benchmark P25 TiO_2.

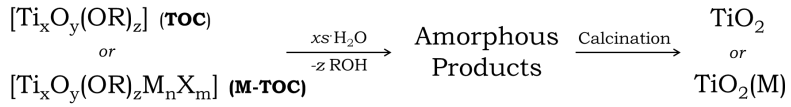

Scheme 1.1. Reaction of TOCs or M-TOCs upon hydrolysis and further calcination, forming TiO_2 or metal-doped TiO_2 [TiO_2(M)].[23]

The use of M-TOCs as precursors further allows atomic control over the metal dopant concentration present in the metal-doped TiO_2 materials obtained.[22] This feature is demonstrated in a recent study on the deposition of Ce-doped TiO_2 using a series of Ce-TOCs, including $[Ti_{28}O_{38}(OEt)_{38}(EtOH)_{1.4}CeCl]$, $[Ti_8O_7(OEt)_{21}(EtOH)Ce]$ and $[\{Ti_2O(OEt)_8\}(EtOH)CeCl]_2$.[61] Hydrolysis of the $\{Ti_{28}Ce\}$ or $\{Ti_8Ce\}$ clusters followed by calcination at 150 °C gives the corresponding Ce^{3+}-doped anatase TiO_2, which contains the same Ti : Ce ratio as that present in their respective precursors. However, phase separation was observed in the hydrolysed product of $\{Ti_4Ce_2\}$, with a much higher Ti : Ce (2 : 1) ratio after calcination. Raman spectroscopy in combination with EDX and XPS analysis indicates that the material produced consists of nanoparticles of $Ce_2Ti_2O_7$ coated with a layer of TiO_2 in a core-shell configuration.[61] The formation of $Ce_2Ti_2O_7$ at such a low temperature is particularly worthy of note, as this has only previously been made by solid-state techniques at much higher temperatures (*ca.* 1000 °C).[109]

Hydrolysis of the L-TOCs is, however, often hindered by the presence of the more robust 'L' ligand peripheries, which usually survive *intact* under aqueous conditions (in water or ambient air) without degradation and may require further special treatment such as heating, autoclaving and addition of specific nucleation tuners for degradation to TiO_2 to occur.[110-112] The titanium oxide produced directly from L-TOC hydrolysis is usually amorphous in nature, which upon calcination at 400 °C can be converted to crystalline anatase TiO_2 and further to rutile at 500 °C.[113] The presence of functional ligands under these circumstances may allow the conversion to TiO_2 to follow different reaction routes. For example, the tetra-nuclear cluster $[Ti_4(\mu_4\text{-}O)(\mu\text{-furfuryloxo})_{14}]$ can be converted to TiO_2 via cationic polymerisation using trifluoromethanesulfonic anhydride as the initiator

(Scheme 1.2). The phase purity of TiO_2 produced can be fine-tuned by altering the thermal treatment conditions. Pre-treatment with excess distilled water at 100 °C before calcination at 400 °C produces solely anatase, but direct calcination at 400 °C gives rise to mixtures of anatase and rutile.[114]

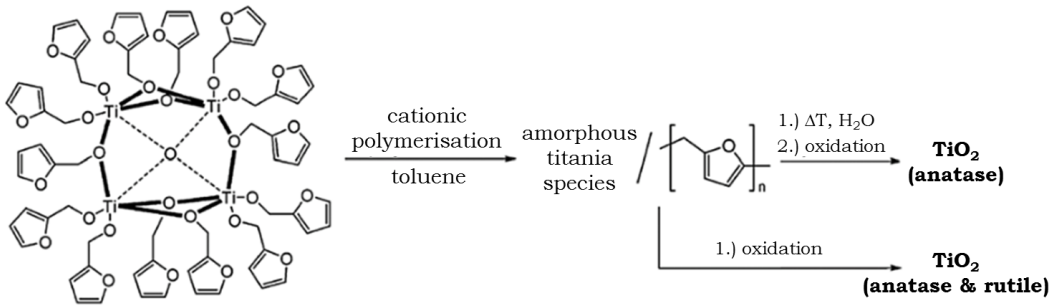

Scheme 1.2. The cationic polymerisation reaction involving the L-TOC $[Ti_4(\mu_4\text{-}O)(\mu\text{-furfuryloxo})_{14}]$ into TiO_2.[23]

The influence of the 'L' ligands on the obtained TiO_2 materials has been further investigated by Xu *et al.*[115] recently, and they have shown that the ligands on TOCs with the same wheel-like $\{Ti_8O_8\}$ cluster core not only affect the phase-transition during thermolysis, but more importantly tune the photocatalytic activities of the TiO_2 obtained. Through 500 °C calcination, the $\{Ti_8O_8\}$ cluster stabilized by benzoate gives rise to a TiO_2 material with a H_2 production rate of 611 μmol h^{-1} g^{-1}, whereas by changing the stabilizing ligands to inorganic SO_4^{2-}, a significant improvement in H_2 evolution activity was achieved, which is over seven times higher at 4527 μmol h^{-1} g^{-1}.

1.3.4.2. Nano-Building Blocks for Hybrid Materials Construction

The nano-building block (NBB) based method is particularly attractive in constructing inorganic-organic hybrid materials, which combine the inorganic and organic components on the molecular scale to achieve a synergic marriage of properties of each constituents.[116,117] As pre-formed monodispersed nano-objects that retain their molecular integrity and intrinsic properties during superstructure assembly, TOCs represent an excellent family of NBBs.[118,119] In

2011, Rozes and Sanchez[24] thoroughly reviewed the '*Lego-Like*' construction of nanostructured hybrid materials using TOCs, as well as their syntheses, structures and NBB applications. In general, the construction of TOC-based hybrid materials relies on the possibility of modifying the pre-formed clusters with polymerisable functional ligands, by which the TOCs can be inter-connected through ligand-induced aggregation, crosslinking and metal-organic framework (MOF) formation.[120-122] These functional ligands, especially multi-dentate ones, can readily stabilise the cluster against hydrolysis by substituting the more reactive alkoxide groups. Such substitution is regioselective and can be carried out in a controlled manner,[86,93,123] paving the way for the broad use of TOCs in constructing hybrid materials.

It is worthy of special note that, owing to their uses in various fields (*e.g.*, photocatalysis, optoelectronics, gas adsorption, etc.) Ti-based MOFs are one of the most promising classes reported to date.[124-127] Nonetheless, they are very scarce because of the challenging synthesis, which is associated with a poor degree of control over their chemistry and crystallisation.[121,128] Compared to mononuclear titanium alkoxides, the multinuclear TOCs usually demonstrate much better stability towards hydrolysis, especially for those with surface ligand modification. This provides a unique opportunity to use the pre-formed TOCs and organic linkers to construct Ti-MOFs.[129-132] For example, Wang *et al.*[131] reported that the 0-D $[(Ti_3O)(O^iPr)_8]^{2+}$ or $[(Ti_4O_2)(O^iPr)_6]^{6+}$ clusters can be assembled into 1-D tube-, ribbon-, or helical chain-shape architectures, 2-D layered structures, and a rare parallel 2D→3D polycatenation framework with copper iodide dopants. In another similar example, Fang *et al.*[132] produced TOC-based materials with structures spanning across the full dimension range from 0-D nanoclusters to 1-D chains, 2-D layers and 3-D diamond-like frameworks.

On a separate note, the concept of NBBs can be extended to the interaction of TOCs with macro-surfaces. As a proof of concept, Eslava *et al.*[34] successfully modified the classic $[Ti_{16}O_{16}(OEt)_{32}]$ cluster using a thiol-ether linker $[HO(CH_2)_4SCH_3]$. The resulting $[Ti_{16}O_{16}(OEt)_{24}\{O(CH_2)_4SCH_3\}_8]$ cluster was then covalently tethered onto an Au surface using five out of the eight thiol anchors in the modified structure (Figure 1.10). In contrast, the parent cluster

$[Ti_{16}O_{16}(OEt)_{32}]$ undergoes extensive decomposition on Au, revealing the importance of the soft thiol-modification for enhancing molecular stability and effective tethering onto the Au surface. Such tethering techniques could have broad-ranging applications in sensors, heterogeneous catalysis and other surface-based technologies.

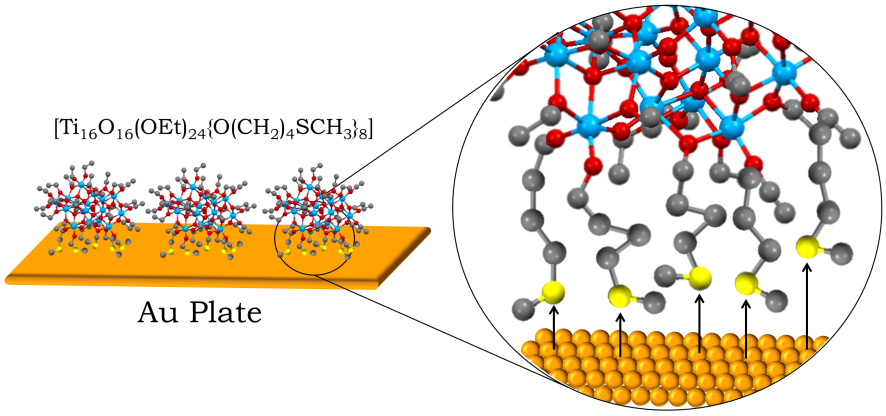

Figure 1.10. Schematic illustration of the possible tethering mode of the $[Ti_{16}O_{16}(OEt)_{24}\{O(CH_2)_4SCH_3\}_8]$ cluster onto Au surface. Colour code for atoms: Ti = cyan, O = red, C = grey, S = yellow, Au = orange. Hydrogen atoms are omitted for clarity. The Au-S interactions are indicated by black arrows.[23]

1.3.4.3. Photocatalysts

The general mechanism by which TOCs mediate photocatalysis involves the photo-induced electron excitation from the valence [predominantly O(2*p*)] to the conduction band [mainly Ti(3*d*)] of the Ti_xO_y cores. The electrons and holes generated then migrate to the cluster surface where redox reactions occur. However, band gaps of unmodified TOCs are usually in the range of 3.5 – 4.0 eV. This means that electronic excitation from the valence to conduction band requires photons of wavelength less than *ca.* 350 nm, ruling out over 95% of the incident solar flux. For TOCs and M-TOCs containing highly hydrolysable alkoxide groups, photocatalytic activity has only been investigated using their hydrolysed products.[22,133,134] For example, a nano-composite water-oxidation photocatalyst was prepared by a straightforward single-step spin-coating

procedure onto nanostructured WO_3 electrode using the Ni-TOC $[Ti_2(OEt)_9(NiCl)]_2$ as precursor.[135] The active catalyst is a mixture of TiO_2 and NiO_x with the same 2 : 1 stoichiometric ratio of Ti : Ni as that in the cluster. The photo-anode oxidizes water to O_2 with good activity and stability in alkaline solutions, and features a photoelectrochemical process involving efficient light absorption, charge separation and water oxidation catalysis.

With the protection of water-stable ligands, many of the L-TOCs with and without metal doping have been shown to remain *intact* upon exposure to air or aqueous environments, and act as efficient photocatalysts mainly in the areas of water splitting and organic pollutant degradation. The functional ligands themselves can also act as photo-sensitisers to boost the photocatalytic activity, mainly by enhancing light absorption efficiency,[103] with the photo-excited electrons then being transferred to the TOC core. It is worth mentioning that the surface functional ligands do not necessarily absorb at the same energy as the L-TOC. This is because, upon coordination with TOCs, the ligand HOMO and LUMO can be mixed with the energy bands of the TOC core, giving rise to a much narrower energy gap for the photo-excited electrons to overcome.[136,137]

One convenient way of investigating the photocatalytic activity of L-TOCs is to deposit them onto transparent conducting substrates [*e.g.*, fluorine-doped tin oxide (FTO), indium tin oxide (ITO)] and then measuring the generated photocurrent upon irradiation with or without applied voltages.[49,63,90] However, the magnitude of the photocurrent is usually limited and the shape of the photocurrent plot is not an ideal square wave with cycled irradiation, potentially due to the non-conducting nature of the organic components. In particular, it is worthy of note that the photocurrent response is not necessarily equivalent to photocatalytic activity, but merely an indication of it, as the photo-generation of electrons and holes has to be balanced against the rate of their recombination. Therefore, the optimum characteristics for a good photocatalytic system include a reasonably small HOMO-LUMO gap and a slow recombination rate, so that visible light absorption is combined with the potential of electrons and holes to migrate towards the cluster surface, where redox reactions can occur. This point has been verified by a recent study,[44] in which a Ti vacancy in $[Ti_{11}O_{13}(O^iPr)_{18}]$

does not reduce the band gap of the cluster (relative to $[Ti_{12}O_{16}(O^iPr)_{16}]$ of similar structure), but can potentially serve as a surface reaction site and promote the efficient separation of the photo-generated electrons and holes. As a result, significantly improved photo-activity responses have been observed under UV irradiation.

Moving from photocurrent response to the realms of photocatalytic activity itself, L-TOCs have been widely investigated in hydrogen evolution and organic pollutant photo-degradation.[82,83,138-140] Recently, Lin *et al.*[141] synthesised three carboxylate-modified TOCs containing isostructural $\{Ti_6O_4\}$ cores. Under UV, suspensions consisting of these L-TOCs, water and methanol (10%, as a sacrificial electron donor) produced gaseous hydrogen, with the highest rate of 326 μmol h^{-1} g^{-1} being observed from $[Ti_6O_4(OEt)_4(O^iPr)_4(OOCC_6H_5)_8]$ (Figure 1.11a and c). This rate is comparable to (or even higher than) that found for nanostructured TiO_2 counterparts. The identical XRD patterns before and after the photocatalytic reaction confirm the stability of the cluster structure in aqueous conditions, implying that the photocatalytic activity originates from the L-TOC itself rather than from any of the hydrolysed products (such as TiO_2). In particular, incorporation of metal dopants into these L-TOCs can further enhance the photocatalytic activity by lowering the optical band gaps.[56,58] As a proof of concept, Zhang *et al.*[56] reported a stable $[Ti_{12}Cr_6O_{18}(OOCC_6H_5)_{30}]$ cluster, which exhibits a pronounced photocatalytic hydrogen evolution rate and photocurrent density using the full solar spectrum, including the NIR regions.

Instead of attacking water molecules to produce gaseous H_2, the photo-generated electrons and holes can also be consumed for degrading organic pollutants under light irradiation. This photocatalytic degradation is exemplified by a recent study in which the indicator methyl orange (MO) was destroyed using white light irradiation in the presence of a UV filter (long pass with 420 nm cut-off) in an aqueous dispersion of microcrystals of $[Ti_6O_3(o\text{-}BDC)_2(O^iPr)_{14}]$ (BDC = benzene dicarboxylate, Figure 1.11b).[83] More than 90% of the MO was degraded after irradiation for 100 min (Figure 1.11d). This photocatalytic effect is believed to be due to the formation of photo-induced $O_2^{\bullet-}$ ions and the proposed mechanism is shown in Figure 1.11e.

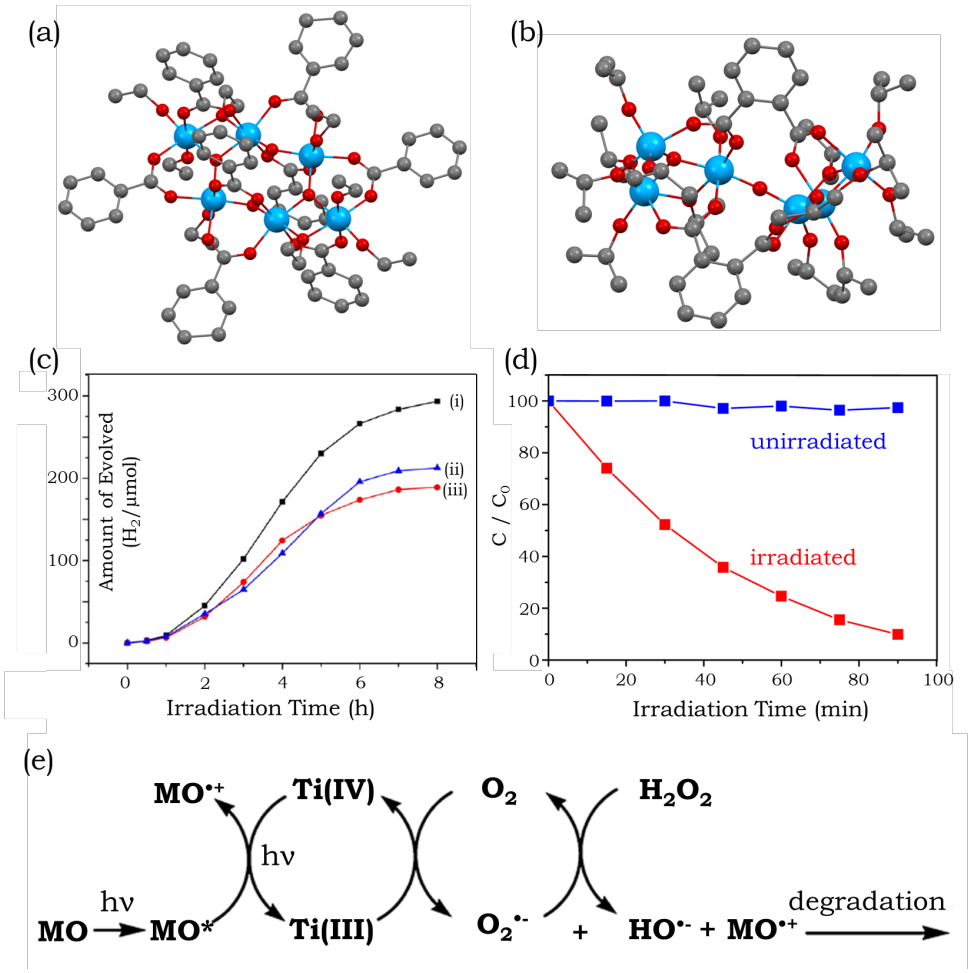

Figure 1.11. Ball-stick representation of the molecular structures of (a) $[Ti_6O_4(OEt)_4(O^iPr)_4(OOCC_6H_5)_8]$ and (b) $[Ti_6O_3(o\text{-}BDC)_2(O^iPr)_{14}]$ (BDC = benzene dicarboxylate). Colour code for atoms: Ti = cyan, O = red, C = grey. Hydrogen atoms are omitted for clarity. (c) Amount of H_2 evolved *vs.* UV irradiation time for the cluster $[Ti_6O_4(OEt)_4(O^iPr)_4(OOCC_6H_5)_8]$ (curve i), and the analogues $[Ti_6O_4(OEt)_8\{OOC(CH_3)_3\}_8]$ (curve ii) and $[Ti_6O_4(OMe)_8\{OOC(CH_3)_3\}_8]$ (curve iii) clusters. (d) Photo-degradation of methyl orange (MO) *vs.* irradiation time using $[Ti_6O_3(o\text{-}BDC)_2(O^iPr)_{14}]$ as the photocatalyst. (e) The proposed mechanism of MO photo-degradation.[23]

Very recently, Jiang *et al.*[142] introduced TOCs into a binary system comprising the MIL-101(Cr) metal-organic framework and CdS nanoparticles, giving rise to highly efficient visible light responsive H_2-evolution photocatalysts (Figure 1.12). The TOCs/CdS/MIL-101(Cr) composites obtained show excellent H_2 production

activity that can be attributed to a synergic effect between the individual components: CdS nanoparticles produce photo-generated electrons under visible-light irradiation, TOCs transfer the generated electrons to MIL-101(Cr), and finally the porous MIL-101(Cr) MOF structure provides catalytic sites to produce gaseous H_2. It has also been shown that increasing aromatic decoration (hence better electron conductivity) in TOCs can further enhance the H_2 evolution activity of the ternary composite photocatalysts.

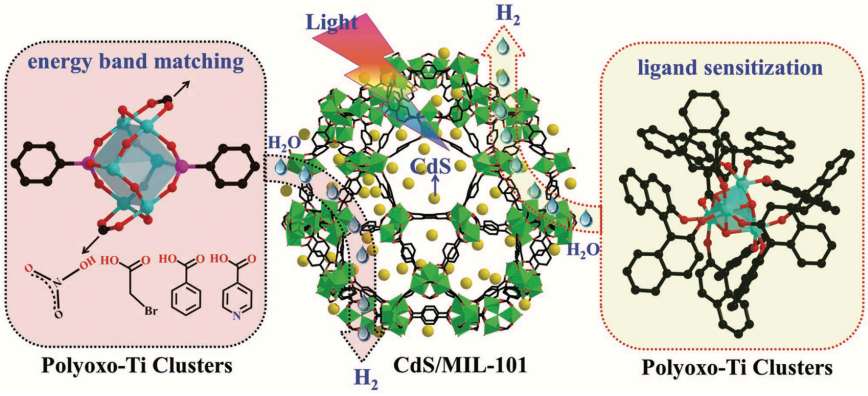

Figure 1.12. Strategy for the construction of ternary TOCs/CdS/MIL-101(Cr) photocatalysts.[142]

1.3.4.4. Photochromism and Photoluminescence

Photochromic behaviour (*i.e.*, colour change under light illumination) has been observed for $[Ti_6O_4(o\text{-BDC})_2(o\text{-BDC-}^{i}Pr)_2(O^{i}Pr)_{10}]$ (Figure 1.13a), for which the colourless crystalline blocks became purple-grey under UV-Vis irradiation (Figure 1.13b and c).[83] This colour change was attributed to the formation of photo-induced Ti^{3+} ions that have been detected using ESR spectroscopy. Although the UV-Vis spectrum of the cluster after irradiation is not available, that of an analogous photochromic cluster $[Ti_6O_3(o\text{-BDC})_2(O^{i}Pr)_{14}]$ shows the formation of a new broad peak at *ca.* 2.46 eV after irradiation (Figure 1.13d), which can be readily assigned to the overlapped Ti^{3+} *d-d* and inter-valence transitions. Back-oxidation of Ti^{3+} ions to Ti^{4+} could be achieved simply by exposing the coloured crystals to oxygen, which is associated with the reduction of the molecular

oxygen into superoxide ions $O_2^{\bullet-}$ (confirmed by ESR). The detailed reaction route behind such photochromic behaviour is still elusive, but it seems that the overall cluster structure (including a specific Ti_xO_y core and some special peripheral ligands) is crucial since no photochromism was observed for $Ti(O^iPr)_4$ under identical conditions, and it is also rare for other TOCs and L-TOCs.

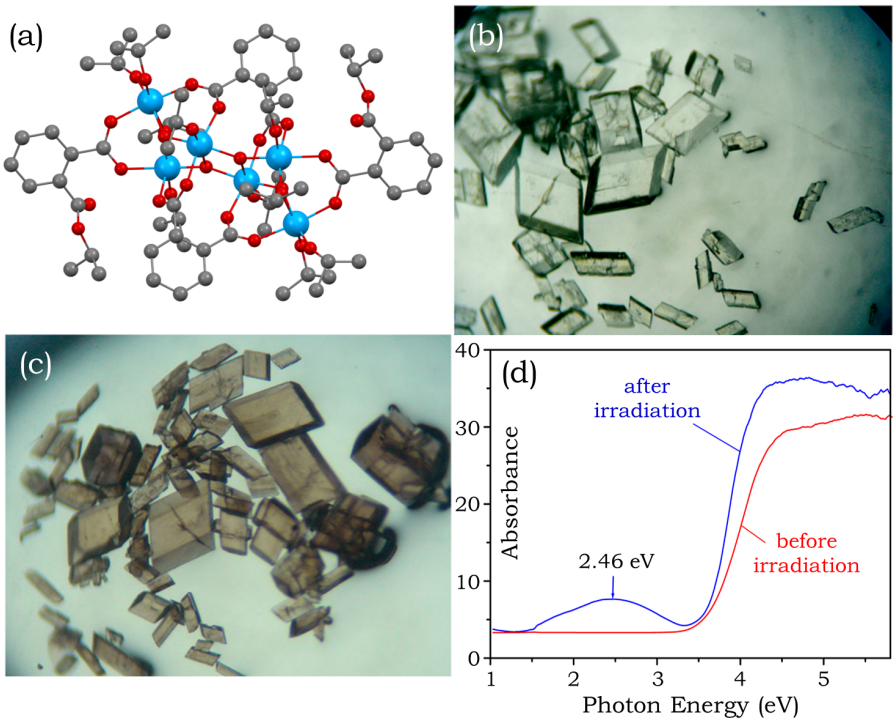

Figure 1.13. (a) Ball-stick representation of the molecular structure of $[Ti_6O_4(o\text{-BDC})_2(o\text{-BDC-}^iPr)_2(O^iPr)_{10}]$. Colour code for atoms: Ti = cyan, O = red, C = grey. Hydrogen atoms are omitted for clarity. Optical microscope images of the $[Ti_6O_4(o\text{-BDC})_2(o\text{-BDC-}^iPr)_2(O^iPr)_{10}]$ crystalline blocks before (b) and after (c) irradiation. (d) UV-Vis absorbance spectra of the analogous photochromic L-TOC $[Ti_6O_3(o\text{-BDC})_2(O^iPr)_{14}]$ before and after irradiation.[83]

Photoluminescence (PL) has been observed for the 9-AC modified TOC $[Ti_6O_6(O^iPr)_6(9\text{-AC})_6]$ (9-AC = 9-anthracenecarboxylate),[90] consisting of a '*stacked*' structure of two Ti_3O_3 ring units and six antenna 9-AC groups at its periphery (Figure 1.14a). As a result of solvent interactions with the frontier orbitals, the photoluminescence colour is closely related to the dipole moment of the utilized solvents, giving rise to green, blue and purple coloured emission in CH_2Cl_2,

CH_3CN and H_2O, respectively (Figure 1.14b and c). Upon continuous irradiation, the PL intensity decreases and becomes completely extinct after *ca.* 60 min (Figure 1.14d), but it can be partially recovered quickly by bubbling gaseous oxygen through the solution (Figure 1.14e). Similar photoluminescence was also observed for $[Ti_6O_4(O^iPr)_6(cat)_4(9\text{-AC})_2]$ (cat = catecholate), which possesses a totally different cluster core structure, but an identical coordination environment of the 9-AC ligands (bridging two adjacent Ti centres), compared to the $[Ti_6O_6(O^iPr)_6(9\text{-AC})_6]$ cluster shown in Figure 1.14a.[90]

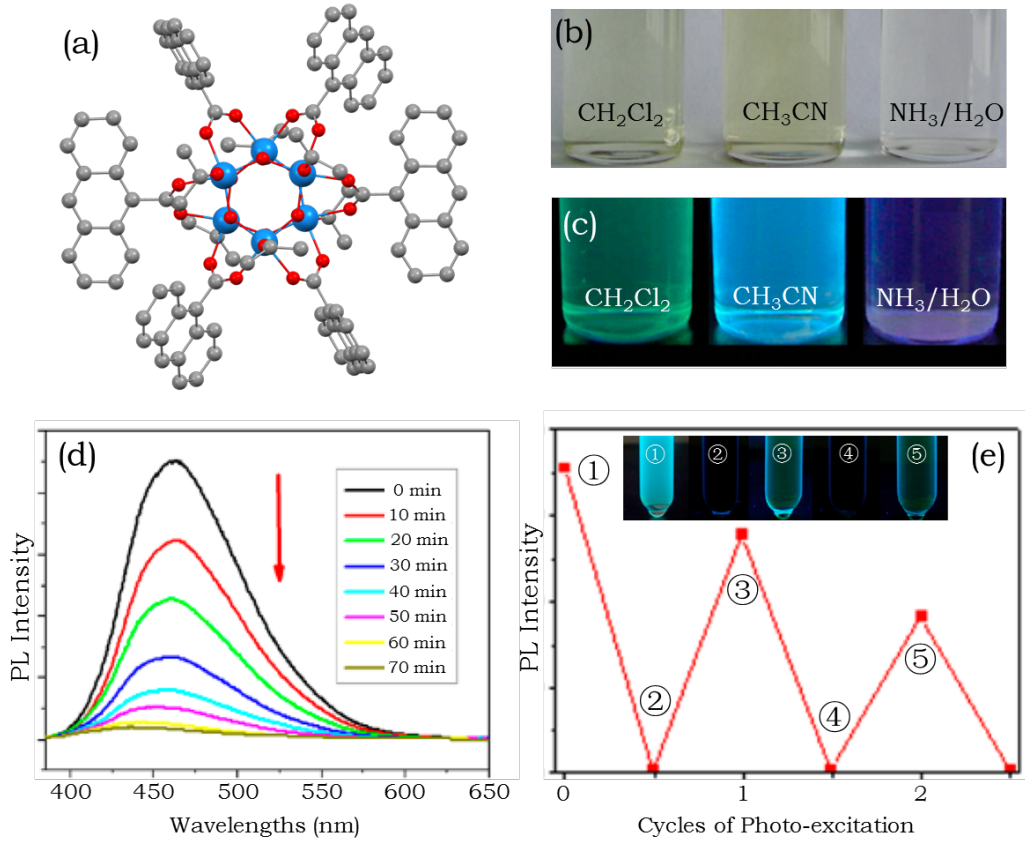

Figure 1.14. (a) Ball-stick representation of the molecular structure of the $[Ti_6O_6(O^iPr)_6(9\text{-AC})_6]$ (9-AC = 9-anthracenecarboxylate) cluster. Colour code for atoms: Ti = cyan, O = red, C = grey. Hydrogen atoms are omitted for clarity. Digital photographs of the cluster compound in different solvents under visible light (b) and UV (c) irradiation. (d) Photoluminescence intensity of the cluster compound in dichloromethane (100 μM) upon continuous UV irradiation. (e) Photoluminescence intensity and digital photographs (inset) of the solution of the cluster compound upon alternating irradiation and oxygen bubbling.[90]

In follow-up work, the 9-AC modified heterometallic TOCs $[Ti_{10}Ln_2O_{14}(ClO_4)_2(O^iPr)_{14}(9\text{-AC})_2(CH_3CN)_2]$ (Ln = Nd or Eu, Figure 1.15a) were isolated.[62] These isostructural clusters demonstrate similar PL spectra with band maxima at *ca.* 460 nm (Figure 1.15c), but the intensity of the $\{Ti_{10}Nd_2(9\text{-AC})_2\}$ cluster is about 0.6 times higher than that of the Eu-containing counterpart under identical conditions. Two other analogous clusters of general formula $[Ti_{10}Ln_2O_{14}(ClO_4)_2(O^iPr)_{14}(bza)_2(HO^iPr)_2]$ (Ln = Nd or Eu, bza = benzoate, Figure 1.15b) with the 9-AC ligands replaced by photoluminescence-inactive benzoate, were also prepared in order to explore the detailed energy transfer mechanism. Cluster $\{Ti_{10}Eu_2(bza)_2\}$ exhibits a typical Eu^{3+}-centred red emission (Figure 1.15d), but such emission is completely absent from $\{Ti_{10}Eu_2(9\text{-AC})_2\}$, as only a single band of ligand-centred emission at 460 nm was observed. Even coupled with a 540 nm long-pass filter to minimize the influences of the strong ligand-centred emission, the Eu^{3+}-centred emission was still absent (Figure 1.15e). This absence can be explained by the mismatch of energy levels, as the triplet energy level of 9-AC is lower than the Eu^{3+}-centred emissive states. A diagram of the proposed energy transfer process for $\{Ti_{10}Eu_2(9\text{-AC})_2\}$ is depicted in Figure 1.15f, which explains not only the absence of the Eu^{3+}-centred emission signals but also the enhanced ligand-centred emission intensities relative to $\{Ti_{10}Nd_2(9\text{-AC})_2\}$. When irradiated at 320 nm, the Eu^{3+}-doped TOC core of $\{Ti_{10}Eu_2(9\text{-AC})_2\}$ is excited. The energy is then transferred from the cluster conduction band to the S_1 state of 9-AC, which consequently enhances the ligand-centred emission. Moreover, the long lifetime of the ^5D excited state of Eu^{3+} also plays an important role in this energy transfer process. This provides a possible reason why such an energy transfer process does not occur in $\{Ti_{10}Nd_2(9\text{-AC})_2\}$, as the lifetime of Nd^{3+} excited state is only 0.2 – 0.5 ms, significantly shorter than that of Eu^{3+} (1 – 11 ms).[62]

Very recently, Lu *et al.*[143] prepared three heterometallic Eu^{3+}-containing TOCs with $\{Ti_4Eu_2\}$, $\{Ti_4Eu_5\}$ and $\{Ti_{10}Eu_8\}$ cores, coordinated with acetylacetonate and 4-tert-butylbenzoate ligands. The photoluminescence in these TOCs mainly originate from the Eu^{3+} centres with the energy transferred directly from the peripheral organic ligands. Furthermore, the solution photoluminescence investigation revealed a size-dependent quantum yield phenomenon, and the

solid-state study showed that these three TOCs exhibit temperature-dependent photoluminescent properties.

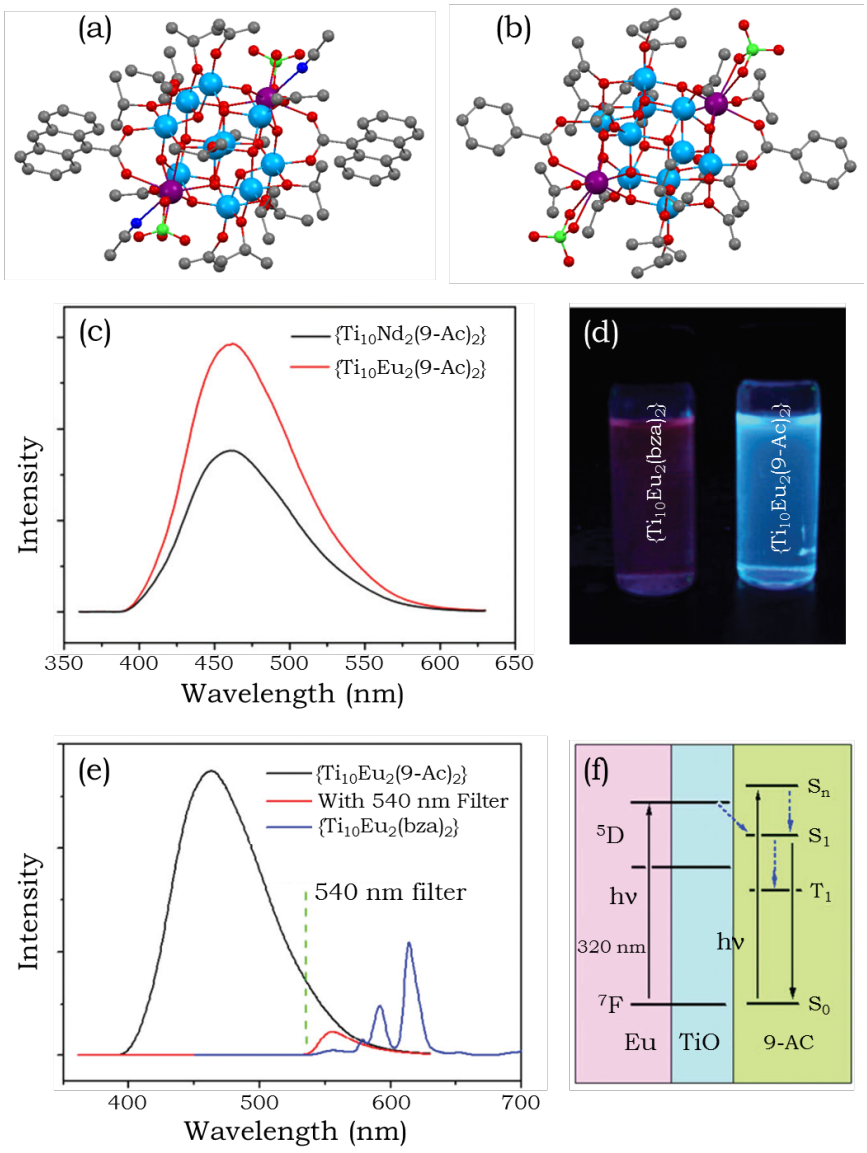

Figure 1.15. Ball-stick representation of the molecular structures of (a) $[Ti_{10}Ln_2O_{14}(ClO_4)_2(O^iPr)_{14}(9\text{-AC})_2(CH_3CN)_2]$ and (b) $[Ti_{10}Ln_2O_{14}(ClO_4)_2(O^iPr)_{14}(bza)_2(HO^iPr)_2]$ (bza = benzoate). Colour code for atoms: Ti = cyan, Ln = purple, O = red, C = grey, Cl = green, N = dark blue. Hydrogen atoms are omitted for clarity. (c) Photoluminescence spectra of the $\{Ti_{10}Ln_2(9\text{-AC})_2\}$ cluster in a mixed solvent of methanol and dichloromethane. (d) Digital photograph of photoluminescence colours of $\{Ti_{10}Eu_2(bza)_2\}$ and $\{Ti_{10}Eu_2(9\text{-AC})_2\}$ under irradiation. (e) Photoluminescence spectra of the $\{Ti_{10}Eu_2(9\text{-AC})_2\}$ and $\{Ti_{10}Eu_2(bza)_2\}$ cluster compounds with and without a 540 nm long-pass optical filter. (f) Proposed energy transfer mechanism in $\{Ti_{10}Eu_2(9\text{-AC})_2\}$.[62]

1.3.4.5. Dye-Sensitised Solar Cells

Dye-sensitised solar cells (DSSCs) have attracted enormous attention in the past decades, for their low cost and high efficiency in converting the abundant solar energy into electricity.[144] A general working mechanism of DSSCs is shown in Figure 1.16, in which photoexcitation of the sensitizer dyes leads to the injection of electrons into the conduction band of the semiconducting metal oxide (*e.g.*, TiO_2), generating the oxidized form of the dye. After electron injection, the ground state of the dye is subsequently restored by electron donation from the electrolyte redox couple (*e.g.*, I^-/I_3^-), which in turn is regenerated by the reduction of the electrolyte oxidant at the counter-electrode.

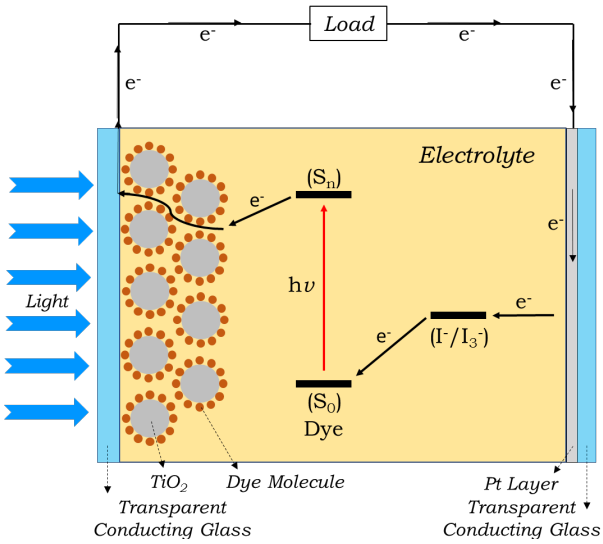

Figure 1.16. Illustration of the general structure and working principles of dye sensitised solar cells.

It has been widely reported that the energy conversion efficiency of DSSCs is not only related to the photo-sensitivity and electronic structure of the utilized dye molecules, but it is also closely related to an efficient charge migration in the system,[145] which is strongly dependent on the coordination environment of the dye molecule to the underlying semiconductor surface (*e.g.*, TiO_2). This is exactly where the L-TOCs can come into play, as the $Ti(OR)_x$ moieties can be used as

anchors to enhance the interaction between the dye molecules (*i.e.*, the functional ligand in L-TOCs) and the underlying TiO_2 surface. In other words, the structure of L-TOCs can be divided into two functional parts: an organic photoactive antenna to capture incident solar energy and a hydrolysable titanium alkoxide anchor to construct a highly efficient pathway for electron migration.[146]

As a proof of concept, Prof. Dai's group in Soochow University, China, have recently reported three new titanium-alkoxide-dyes (TADs): $[Ti_2(O^iPr)_5(Az)(X\text{-}BA)]$ (H_2Az = alizarin dye, HBA = benzoic acid, X = NO_2, F or Br), in which the titanium alkoxide clusters are coordinated with alizarin dye and an auxiliary ligand, namely a benzoic acid substituted with -NO_2, -F or -Br (Figure 1.17).[147] In comparison with the organic dye-treated TiO_2, considerable improvement in the photocurrent density was observed for the TAD-treated TiO_2 electrodes. The effect of differently substituted auxiliary ligands on the photocurrent conversion was also evaluated, with the photocurrent density achieved being in the order of NO_2 > F > Br, which is in accordance with their electron-withdrawing capabilities.

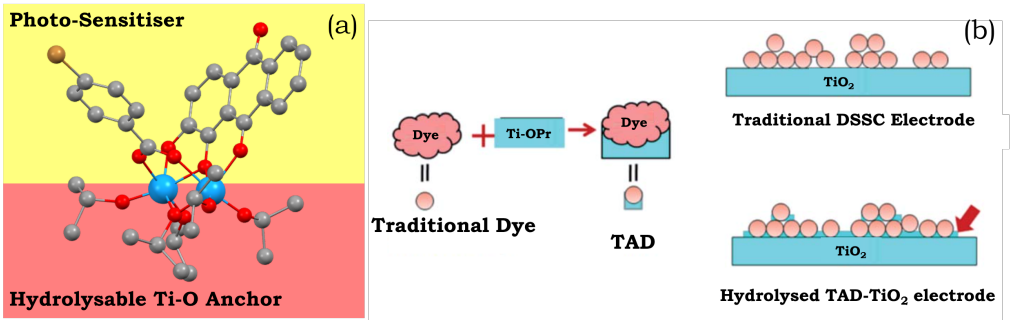

Figure 1.17. (a) Ball-stick representation of the molecular structure $[Ti_2(O^iPr)_5(Az)(X\text{-}BA)]$ (H_2Az = alizarin dye, HBA = benzoic acid, X = NO_2, F or Br). Colour code for atoms: Ti = cyan, O = red, C = grey, X = brown. Hydrogen atoms are omitted for clarity. (b) Illustration of the differences between a traditional DSSC electrode and a hydrolysed titanium-alkoxide-dyes (TADs)-TiO_2 electrode.[147]

1.3.4.6. Asymmetric Catalysts

Catalysts based on TOCs, especially those coordinated with 1,1'-bi-2-naphthol (BINOL) and their derivatives, have been applied to a number of organic/inorganic reactions, such as oxidation of thilanisole, cyanosilylation of aldehydes, Diels-Alder cycloaddition, carbonyl-ene reactions, nitro-aldol reactions, asymmetric allylation of aldehydes/ketones and asymmetric sulphide oxidation.[148,149] The Ti-BINOL catalysed reactions can undergo a ligand-accelerated catalytic process that involves *in situ* selection of the active species from many thermodynamically accessible complexes present, even though the catalytically-active species may be present only in a small amount.[150] This makes it difficult to identify and to isolate the actual catalytically-active species. As a result, so far structural information on the real catalysts in this area is largely lacking. For example, the mononuclear complex [Ti(BiNOLato)(O^iPr)$_2$] is a pre-catalyst for many reactions, but the complex itself is not an active species.[151]

The literature involving structurally-characterised Ti-BINOL catalysts is relative sparse, compared to the large amount of reports solely investigating their catalytic performance.[18,91,148,152-155] Among the catalysts with known structures, the tetra-nuclear clusters [$Ti_4(\mu_3\text{-}OH)_4(\mu\text{-}BINOLato)_6$] (*R*-BINOLato and *S*-BINOLato) are of particular interest (Figure 1.18a), as they are extremely stable, even in strongly acidic or basic conditions under reflux. All six BINOLato ligands within the *R*- and *S*-clusters have the same stereochemistry (either *R* or *S*), bonding with the distorted cubic cluster core via Ti-O bonds. Mahrwald *et al.*[91] have demonstrated that the *S*-cluster can act as an effective catalyst to promote aldol addition reactions with high regioselectivity at the more steric α-encumbered side of unsymmetrical ketones (Scheme 1.3). Catalyst loadings as low as 0.2 mol.% were enough to afford complete conversion very smoothly without the formation of a significant amount of by-products. Moreover, the tetra-nuclear clusters [$Ti_4(\mu_3\text{-}OH)_4$(7,7'-di-R-(*R*)-BINOLato)$_6$] (R = H, Br, BnO, Ph, or PhC≡C, Figure 1.18b) have been shown to catalyse [2+3] cycloaddition reactions (Scheme 1.4).[155] The introduction of the sterically-bulky 7,7'-Ph-substituent leads to an increase in enantioselectivity for the exo-product (Scheme 1.4). In the exo-transition state, tert-butyl vinyl ether approaches from the Re-

face of the nitrone preferentially affording the 3*R*,5*S* product because access to the Si-face (leading to the 3*S*,5*R* product) is sterically hindered by the bulky 7,7'-substituents (Figure 1.18c).[155]

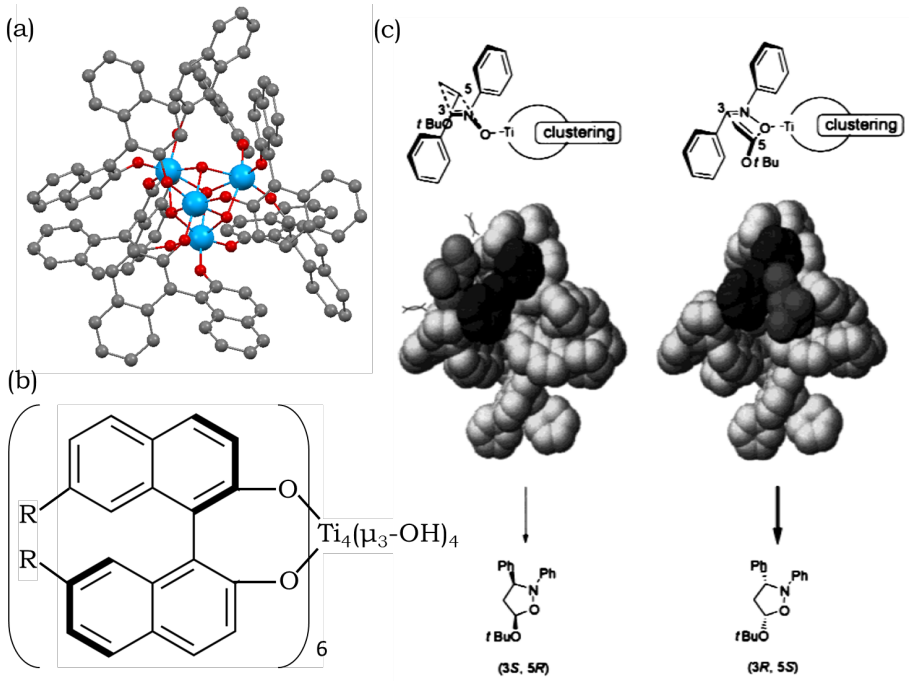

Figure 1.18. (a) Ball-stick representation of the molecular structure of the tetra-nuclear [$Ti_4(\mu_3\text{-}OH)_4$(*R*-BINOLato)$_6$] cluster. The *S*-BINOL enantiomer structure has a similar configuration (not shown). (b) Molecular representation of 7,7'-substituted [$Ti_4(\mu_3\text{-}OH)_4$(7,7'-di-R-(*R*)-BINOLato)$_6$] cluster. (c) Illustration of the steric reason for the favourable production of (3*R*,5*S*) over (3*S*,5*R*) products.[23]

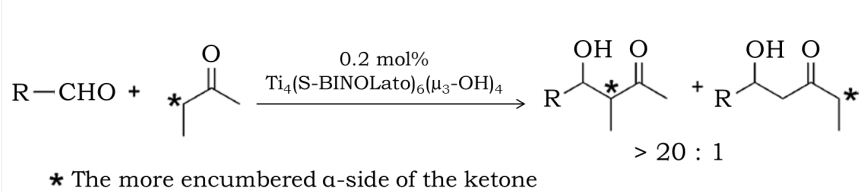

Scheme 1.3. Direct aldol addition catalysed by [$Ti_4(\mu_3\text{-}OH)_4$(*S*-BINOLato)$_6$] with high regioselectivity at the more sterically α-encumbered side of unsymmetrical ketones.[23]

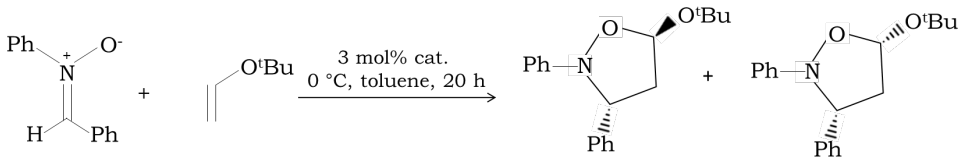

cat.:[$Ti_4(\mu_3\text{-}OH)_4$(7,7'-di-R-(*R*)-BINOLato)$_6$]

endo (3R,5R) *exo (3R,5S)*

R group	Yield (%)	***Endo*** **(% ee)**	***Exo*** **(% ee)**
H	73	70 (18)	30 (62)
Br	64	79 (35)	21 (74)
BnO	32	70 (25)	30 (64)
Ph	99	78 (18)	22 (78)
PhC≡C	98	77 (7)	23 (66)

Scheme 1.4. The [2+3] cycloaddition reaction catalysed by [$Ti_4(\mu_3\text{-}OH)_4$(7,7'-di-R-(*R*)-BINOLato)$_6$]. The table at the bottom shows the catalytic capability of different 7,7'-substituted compounds.[23]

1.3.4.7. Gas Adsorption

Crystalline blocks of TOCs can be described as molecular solids, owing to the absence of intermolecular covalent or coordination bonds between them that would form extended network structures, as is the case for metal-organic frameworks (MOFs).[156,157] Such molecular solids possess clear advantages as potential gas adsorbents over many other physisorption materials, as: (i) they do not lose adsorption properties upon amorphisation (unlike most MOFs) and therefore can be utilized under a wide range of conditions, (ii) being inherently discrete (molecular) in nature, they are soluble in common organic solvents and, therefore, can readily be modified or processed into other forms using solution-based techniques, and (iii) their facile synthesis and vast structural diversity is nearly comparable to that of MOFs.[158,159]

In general, crystallites of densely packed TOCs are stable against thermal treatment and desolvation, unlike less densely packed lattices which lose their crystallinity after similar treatment.[157] For example, solid [$Ti_6O_6(abz)_6(O^iPr)_6$] (abz = aminobenzoate) (Figure 1.19a), with only 10% of solvent-accessible void volume in the lattice, maintains its crystallinity after heating to 200 °C, whereas under identical conditions [$Ti_8O_8(abz)_{12}$] (Figure 1.19b) crystallites (with 33% solvent-

accessible lattice void) completely lose their crystallinity. Although neither $[Ti_6O_6(abz)_6(O^iPr)_6]$ nor $[Ti_8O_8(abz)_{12}]$ demonstrate any N_2 or CH_4 adsorption properties, a significant uptake of CO_2 at 195 K was observed for both compounds (Figure 1.19c and d), possibly due to the small kinetic diameter of CO_2 (*ca.* 3.3 Å) and the strong quadrupole moment interacting with the polar regions of the structure.[157,160] More interestingly, after complete amorphisation of the $[Ti_6O_6(abz)_6(O^iPr)_6]$ crystallites, its CO_2 adsorption capability is still maintained (inset to Figure 1.19c), which suggests that the selective and reversible adsorption of gaseous CO_2 by molecular carboxylate-TOCs even without intramolecular pores can occur exclusively through intermolecular voids, and that the adsorption seems to be related to the actual packing patterns of the clusters, regardless of whether the sample is in a crystalline state or not.

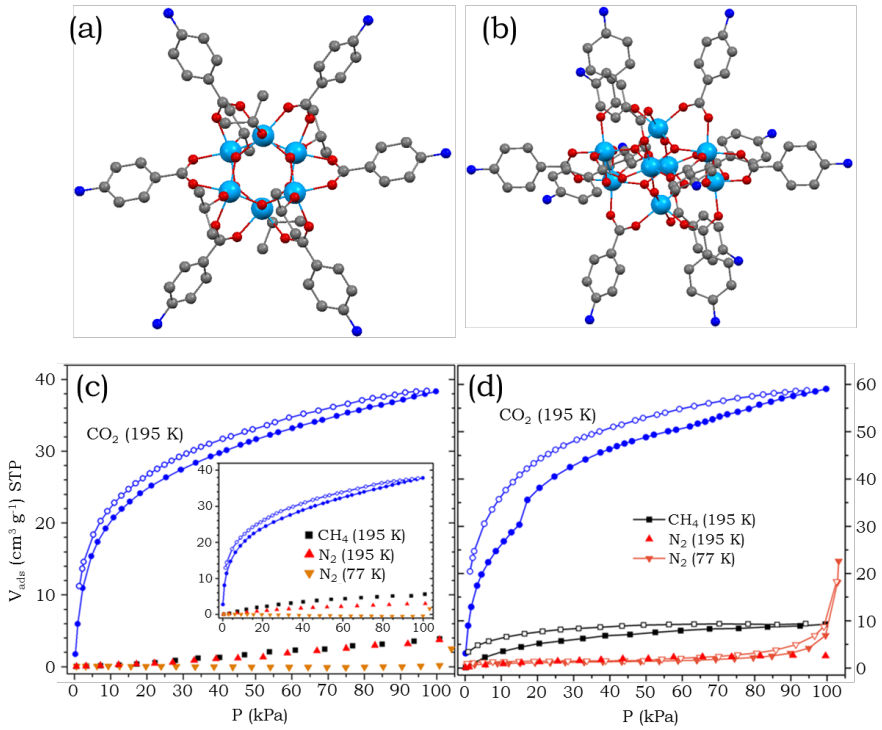

Figure 1.19. Ball-stick representations of the molecular structures of (a) $[Ti_6O_6(abz)_6(O^iPr)_6]$ and (b) $[Ti_8O_8(abz)_{12}]$ (abz = aminobenzoate). Colour code for atoms: Ti = cyan, O = red, N = blue, C = grey. Hydrogen atoms are omitted for clarity. Gas adsorption isotherms measured for (c) $[Ti_6O_6(abz)_6(O^iPr)_6]$ and (d) $[Ti_8O_8(abz)_{12}]$. Inset of (c) is the isotherms of $[Ti_6O_6(abz)_6(O^iPr)_6]$ with complete amorphisation. Filled and open symbols denote adsorption and desorption, respectively.[23]

The specific packing of the cluster molecules in the crystallites does have an apparent impact on CO_2 adsorption, though this has little effect in the case of the above-discussed $[Ti_6O_6(abz)_6(O^iPr)_6]$ and $[Ti_8O_8(abz)_{12}]$ clusters. In general, the adsorption in loosely-packed compounds, such as is seen in the lattice of $[Ti_6O_6(4\text{-tbbz})_6(O^iPr)_6]$ (4-tbbz = 4-tert-butyl-benzoate) (Figure 1.20a), can occur in the intermolecular voids without significantly disturbing the molecular arrangement. As a result, a typical absorption type I curve is observed without hysteresis between the adsorption and desorption branches (Figure 1.20e, blue trace for $\{Ti_6(4\text{-tbbz})_6\}$). On the other hand, in a densely-packed lattice, as is the case for $[Ti_6O_6(4\text{-tbbz})_{10}(O^iPr)_2]$ (Figure 1.20b), the adsorption of gas molecules can only occur with the expansion of the lattice parameters. This structural expansion is believed to be responsible for the distinct step in the adsorption branch for CO_2 for $[Ti_6O_6(4\text{-tbbz})_{10}(O^iPr)_2]$ (Figure 1.20e, blue trace for $\{Ti_6(4\text{-tbbz})_{10}\}$).[156] Further studies have revealed that the substituents on the carboxylate ligands also play an important role in the adsorption of gaseous CO_2.[156] By using relatively linear carboxylate ligands (*e.g.*, 4-tbbz, Figure 1.20c), the intermolecular voids between adjacent ligands can be preserved or even enlarged. Clusters bearing such ligands (*i.e.*, $[Ti_6O_6(4\text{-tbbz})_6(O^iPr)_6]$ and $[Ti_6O_6(4\text{-tbbz})_{10}(O^iPr)_2]$) can, therefore, adsorb almost the same number of CO_2 molecules (*ca.* 5.5 per cluster), despite the different molecular geometries and crystal packings present (Figure 1.20e, blue traces). For comparison, the clusters $[Ti_6O_6(2\text{-bpyc})_6(O^iPr)_6]$ and $[Ti_6O_6(2\text{-bpyc})_{10}(O^iPr)_2]$, in which the linear 4-tbbz ligands have been replaced by non-linear and bulky biphenyl-2-carboxylate (2-bpyc, Figure 1.20d), exhibit a far lower CO_2 adsorption capacity of approximately one CO_2 molecule per cluster molecule (Figure 1.20e, red traces). This can be ascribed to the fact that the phenyl group at the 2-position of the carboxylate ligand occupies the intermolecular space between the clusters in the lattice, resulting in the blocking of the voids where the adsorption of CO_2 occurs.

An interesting two-step adsorption profile of CO_2 adsorption has also been observed for TOCs that possess both intermolecular voids as well as intramolecular pores.[157] For example, with the CO_2 pressure below a critical value (P/P_0 ~ 0.6), perfectly reversible type I adsorption is observed for the

$[Ti_8O_{10}(bza)_{12}]$ cluster with a cyclic core structure, because of the presence of permanent intramolecular pores of *ca.* 4 Å in diameter (Figure 1.21a). The almost saturated adsorption then shows a sudden increase with large hysteresis at higher pressures (Figure 1.21b). This second step is due to adsorption into the lattice voids that interconnect adjacent cluster molecules. Also of note is the non-selective sorption of N_2 and CH_4 at 195 K for $[Ti_8O_{10}(bza)_{12}]$, again due to the presence of the permanent intramolecular pore in the molecule (Figure 1.21b). Relatively higher absorption of CH_4 compared to N_2 at the same temperature is a generally observed phenomenon that potentially originates from the greater polarizability of CH_4 (2.59 $Å^3$ for CH_4 *vs.* 1.74 $Å^3$ for N_2), which leads to stronger interactions with crystalline solids containing discrete molecules.[138]

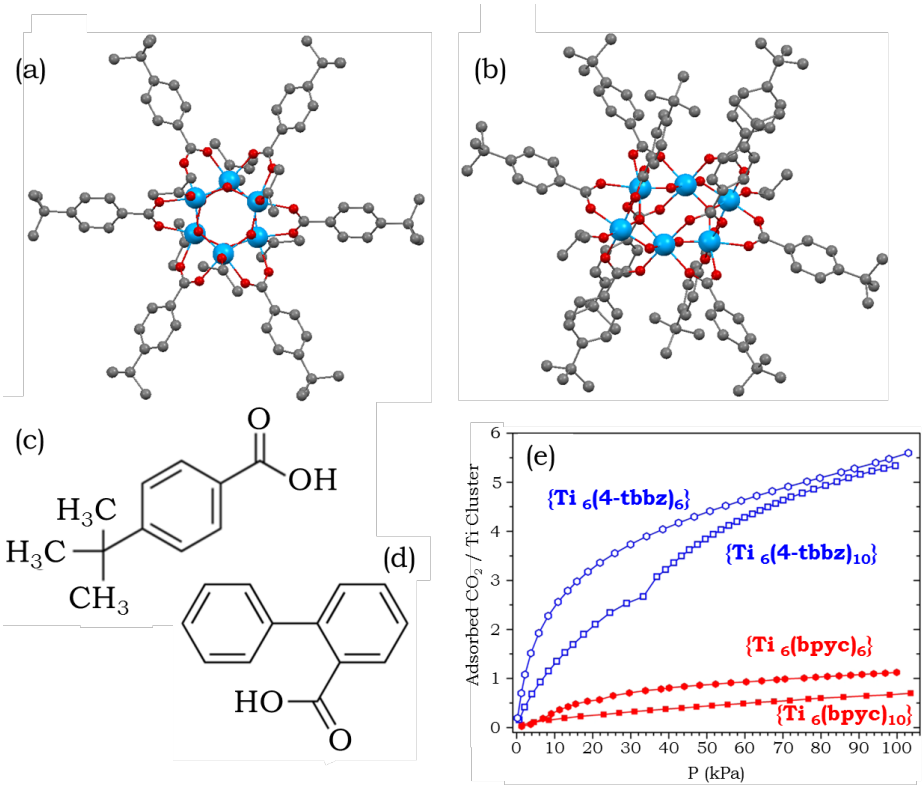

Figure 1.20. Ball-stick representations of the molecular structures of (a) $[Ti_6O_6(4\text{-tbbz})_6(O^iPr)_6]$ and (b) $[Ti_6O_6(4\text{-tbbz})_{10}(O^iPr)_2]$ (4-tbbz = 4-tert-butyl-benzoate). Colour code for atoms: Ti = cyan, O = red, C = grey. Hydrogen atoms are omitted for clarity. Molecular structure of the functional ligands (c) 4-tert-butyl-benzoic acid (4-tbbzH) and (d) biphenyl-2-carboxylic acid (2-bpycH). (e) CO_2 adsorption isotherms of the related cluster compounds.[23]

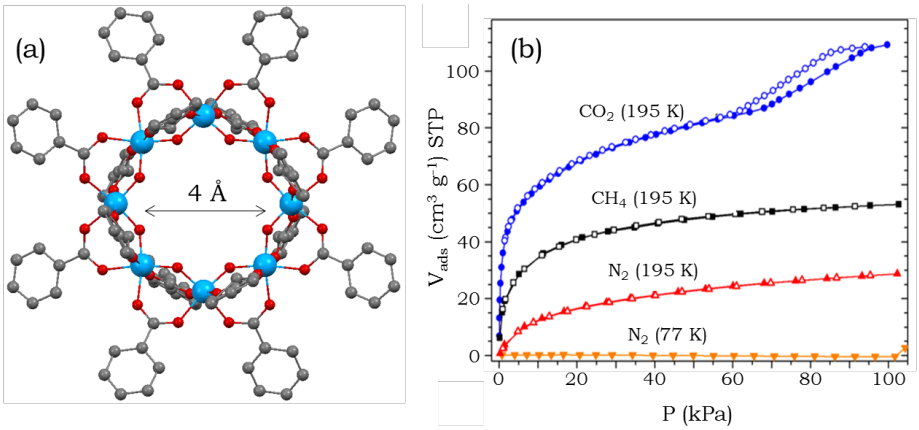

Figure 1.21. (a) Ball-stick representation of the molecular structure of $[Ti_8O_{10}(bza)_{12}]$ with permanent inner pore of *ca.* 4 Å in size. Colour code for atoms: Ti = cyan, O = red, C = grey. Hydrogen atoms are omitted for clarity. (b) Gas adsorption (filled symbols) and desorption (empty symbols) isotherms of the cluster.[23]

CHAPTER 2.

Project Objectives

Considering the aforementioned diverse applications, the synthesis of new TOCs with novel structural features constitutes the initial step of any new study in this area and probably is still the most crucial part of related research, as it is the structure that determines the properties and functionalities of TOCs in real-life applications. In this context, the project has been focused on the design and synthesis of novel TOCs involving both metal doping and surface ligand modification, followed by the exploration of their intriguing properties and potential applications that are highly desired but have not been demonstrated in the literature before.

2.1. TOCs as Coating Precursors on Cotton Fabrics

The first section of this thesis deals with TOCs that feature the ability of *in situ* self-assembly into microparticles on flexible surfaces. The major aim of this topic was to synthesise and fully characterise a TOC of appropriate molecular structure, and more importantly, to assess its performance as precursors towards multifunctional coating on cotton fabrics.

2.2. TOCs as Host Scaffolds for Lanthanide Ions

The second part of this project is to explore the possibility of using TOCs as host scaffolds for lanthanide ions. To this end, a series of lanthanide-containing TOCs of general formula $[LnTi_6O_3(O^iPr)_9(salicylate)_6]$ (Ln = La - Er, except for Pm) have been synthesised and fully characterised, which provides an excellent platform for studying the influence of Ln^{3+} ions on the paramagnetic NMR behaviour of the peripheral ligands, as well as the photophysical interplay between the Ln^{3+} ions, Ti^{4+} centres and the coordinated ligands.

CHAPTER 3.

TOCs as Coating Precursors on Cotton Fabrics

3.1. Introduction

Despite the structural diversity of TOCs, the majority of their applications are still limited to that of solid-state bulk-/nano-TiO_2 materials.[22,23] The TOCs size ranges from a few angstroms to nanometres, and this should give them unique properties that are not seen for their smaller mononuclear Ti^{4+}-complex or larger TiO_2 nanoparticle counterparts. In the literature, the use of TOCs as single-source precursors for producing titanium oxide materials merely takes advantage of their chemical composition,[133,135] whereas another more important facet of these clusters is their unique structural and physical properties, which combine excellent processability and precise control of the local atomic connectivity. These features give TOCs great potential for functional materials fabrication that are not possible using other precursors (such as less well-defined nanoparticles).

In this chapter, the synthesis and characterisation of a novel TOC $[Ti_{18}Mn_4O_{30}(OEt)_{20}Phen_3]$ (**1**, Phen = 1,10-phenanthroline) are elaborated. Its unique atomic arrangement allows the cluster molecules to self-assemble into hollow microparticles upon solvent evaporation, on either solid surfaces or highly flexible fabrics. The micro-particulate morphology on solid surfaces (such as glass) can be retained after high temperature calcination, which provides a template-free approach for fabricating hollow nanostructures of metal oxide materials. More importantly, a novel coating technology involving *in situ* self-assembly is also demonstrated to fabricate multifunctional cotton fabrics with robust hydrophobicity, antibacterial activity and enhanced UV-blocking capabilities.

3.2. Materials Characterisation Results

The cluster **1** was obtained by the solvothermal reaction of titanium tetra-ethoxide $[Ti(OEt)_4]$ with manganese(III) acetate dihydrate $[Mn(OAc)_3{\cdot}2H_2O]$ and 1,10-phenanthroline (19 : 1 : 1 equivalents) in anhydrous ethanol at 150 ºC for 72 hours. Slow cooling of the reaction to room temperature gave orange block-

shaped crystals of **1** in *ca.* 20% isolated yield with respect to $Mn(OAc)_3{\cdot}2H_2O$ supplied. As shown in Figure 3.1, the cluster structure consists of a C_3-symmetric $\{Ti_{18}Mn_4O_{30}\}$ core in which all the Ti atoms are exclusively six-coordinate, resembling that in the common polymorphs of TiO_2. Nonetheless, the Ti-O bond lengths in **1** are in the range of 1.729(8) Å to 2.326(7) Å, differing from that of solid-state TiO_2 (Table 1.1). Though the O-Ti-O angles of **1** [*i.e.*, 74.7(3)° – 105.8(4)°] fall into the similar range to that in brookite, the coordination numbers of non-surface oxygen ions span the range 3 to 5, in contrast to the exclusive three-fold coordination in TiO_2. The three-fold coordinated Ti_3O units in **1** are not planar either, indicating the substantial structural differences between TOC **1** and the solid-state TiO_2.

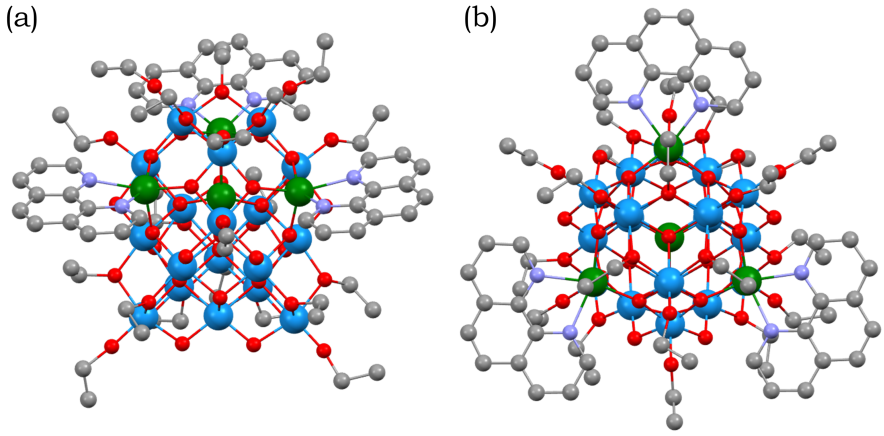

Figure 3.1. Ball-stick representation of the molecular structure of TOC $[Ti_{18}Mn_4O_{30}(OEt)_{20}Phen_3]$ (**1**, Phen = 1,10-phenanthroline) viewed in the direction (a) perpendicular to and (b) along the C_3 axis. Colour code for atoms: Ti = cyan, Mn = green, O = red, N = light blue, C = grey. Hydrogen atoms are omitted for clarity.

One of the four Mn^{2+} centres is located in an interstitial tetrahedral coordination site, being bonded to four oxygen atoms in the core. The remaining three symmetry-related Mn^{2+} ions are complexed at the periphery of the cluster molecule and have approximate trigonal bipyramidal geometries, being bonded to three μ_3-O atoms of the core and the two N atoms of the 1,10-phenanthroline ligands. This cluster represents a special example among M-TOC structures,

containing a single type of metal dopant (*i.e.*, Mn^{2+}) in two distinct coordination environments. Strong support for the exclusive presence of Mn^{2+} within **1** comes from the X-ray photoelectron spectroscopy (XPS) data (Figure 3.2), in which the observed splitting of the doublet Mn*3s* peaks (6.06 eV, Figure 3.2b) corresponds to an Mn valence of 1.97 based on the following equation:[161-163]

$$\upsilon_{Mn} = 9.67 - 1.27\Delta E_{3s}/\text{eV} \qquad \text{[Eqn. 3.1]}$$

where ΔE_{3s} is the measured Mn*3s* doublet splitting, and υ_{Mn} is the Mn valence. This Mn*3s* splitting value of 6.06 eV is also in line with other literature reports for Mn^{2+}.[164,165] In addition, the satellite feature in the Mn*2p* high-resolution spectrum (Figure 3.2c) is also an indication of the presence of Mn^{2+} in fresh crystalline blocks of **1**. As expected, the Ti*2p* high-resolution spectrum shows the two characteristic peaks of Ti^{4+} at 458.4 and 464.1 eV in the fresh crystalline blocks of **1** (Figure 3.2d).

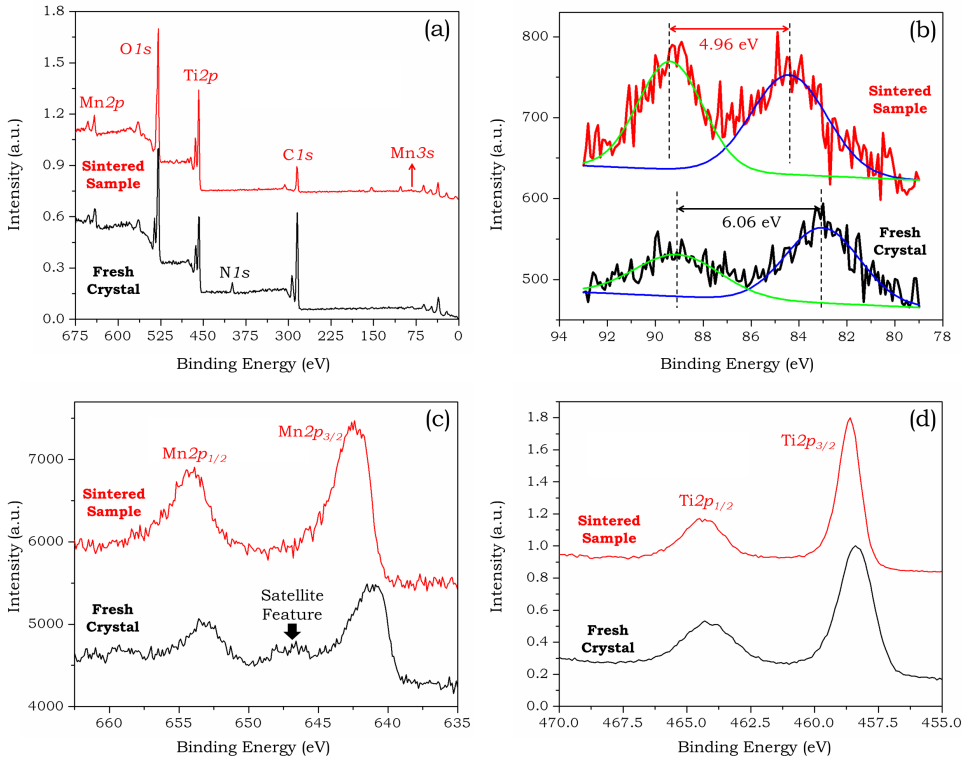

Figure 3.2. XPS spectra of fresh crystalline blocks of **1** (black trace) and that after 600 °C sintering in air (red trace): (a) the survey scan, and high-resolution scan for (b) Mn*3s*, (c) Mn*2p* and (d) Ti*2p* signals.

The presence of the 1,10-phenanthroline and ethoxide ligands in **1** is confirmed by the peaks in the 3100 – 3000 cm^{-1} and 3000 – 2850 cm^{-1} ranges in the FTIR-ATR spectrum (Figure 3.3, black trace). The broad feature at 3350 cm^{-1} is probably due to the small amount of adsorbed moisture on the crystallites of **1**. The peak at the same wavelength range in the 1,10-phenanthroline spectrum is much more intense (Figure 3.3, red trace), indicating the relatively larger amount of water molecules present. Due to the complex molecular structure, it is impractical to unambiguously assign the peaks in the fingerprint regions, although they can be conveniently used as reliable indicators to probe the quality of the samples synthesised in different batches.

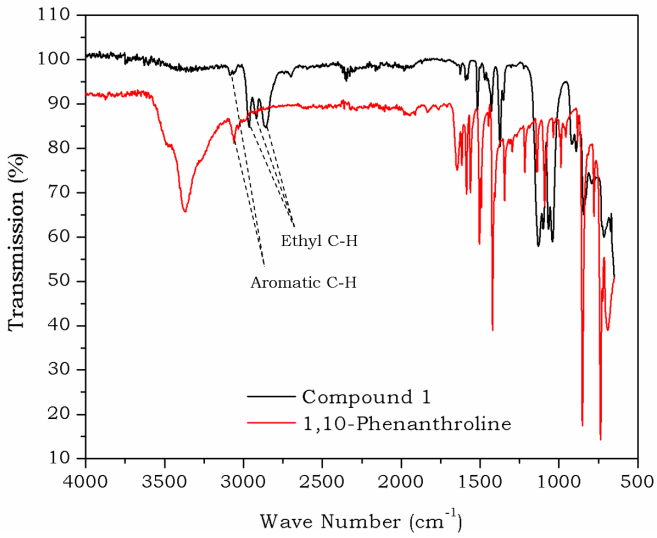

Figure 3.3. FTIR-ATR spectra of **1** (black trace) and 1,10-phenanthroline powder (red trace). Peaks for some functional groups are indicated.[166]

Direct support for the crystallographic formulation of cluster **1** comes from the high-resolution +ve ESI mass spectrometry (Figure 3.4a). The higher mass region of the spectrum is shown in Figure 3.4b, with the simulated isotopic pattern for the molecular ion being compared with the experimental envelope in Figure 3.4c and d, respectively. The experimental isotope pattern agrees well with the simulated data for the molecular ion, calculated from the crystal structure ($[M + H]^+$ m/z = 3004.5588, *cald.* 3004.5575). Some of the peaks found above the

molecular ion also appear, potentially originating from the molecular ion picking up extraneous solvent molecules, such as $[M + H + toluene]^+$ (*found* 3096.6517, *cald.* 3096.6201) and $[M + H + 2MeOH]^+$ (*found* 3068.5906, *cald.* 3068.6099). Furthermore, the peaks below the molecular ion all have peak positions that are *ca.* 14 mass units distant from their neighbours, ascribed to OEt-to-OMe ligand exchange arising from the mixture solvent used (*i.e.*, toluene and methanol). This mixture solvent of toluene and methanol is chosen because it was the only identified solvent system in which **1** can be dissolved well.

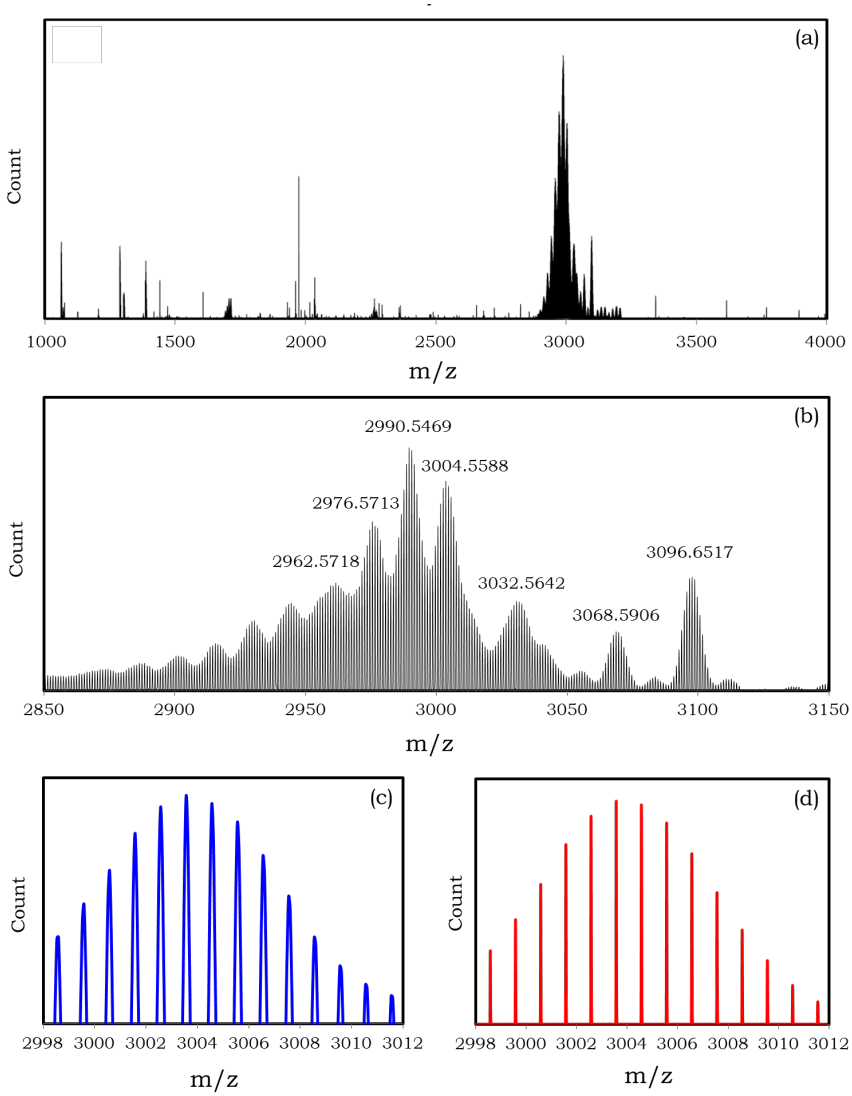

Figure 3.4. +ve ESI-MS spectra of **1** with cone voltage of 42 V: (a) the full MS spectrum from 1000 to 4000 m/z; (b) magnified MS spectrum from 2850 to 3150 m/z; (c) simulated and (d) experimental isotope distribution pattern at the molecular ion region.[166]

One striking feature of the crystalline samples of **1** is their stability in air, even in contact with water under moderately acidic conditions (pH ≥ ~3). As can be seen in Figure 3.5, which compares the powder XRD pattern of a crystalline sample of **1** ground in air with the theoretical pattern calculated from its single-crystal diffraction data, the bulk material contains few (if any) impurities or hydrolysed products. The purity of **1** is also supported by elemental analysis, in which the experimentally-measured weight percentages of C, H and N all satisfactorily match with the calculated values from the solid-state structure (see later Experimental Section). Crystallites of **1** also remain *intact* for several days in ambient air without any visible degradation and there is no change in the powder XRD pattern after *ca.* 30 h exposure to air. It is common to obtain mixtures of products in solvothermal synthesis of TOCs and for these clusters to be moderately or even extremely moisture-sensitive, degrading into low band gap metal-doped TiO_2.[22] The isolation of a single cluster component and its long-term stability in air are important in regard to its practical applications.

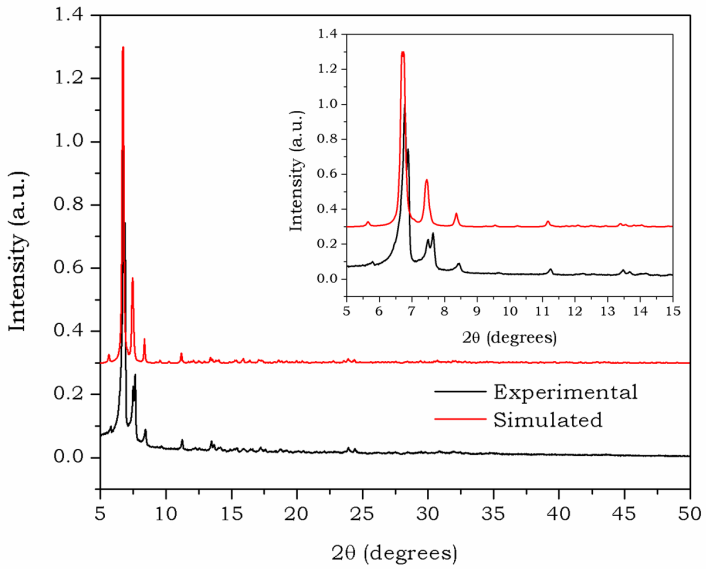

Figure 3.5. Comparison of the simulated (red trace) and experimental (black trace) powder XRD patterns of compound **1**; the inset is the magnification of the region 5 – 15°, in which most of the peaks are located.[166]

The optical properties of **1** were explored using UV-Vis diffuse reflectance spectroscopy. Although previous analysis had shown that the compound is air- and moisture-stable for prolonged periods at room temperature, high-purity crystalline blocks of **1** were ground into powders in a N_2-filled glove box and sealed in between quartz windows before transferring to the spectrometer. This was done in order to ensure that there was no possibility of surface aerial hydrolysis of the sample, which would give Mn-doped TiO_2 with low band gaps of *ca.* 2.7 eV.[46] Figure 3.6 shows the UV-Vis diffuse reflectance data of **1** in the form of a plot of the Kubelka-Munk function F(R) against the incident photon energy (black trace), which provides a method of estimating the band gap (or HOMO-LUMO gap) by extrapolation of the plot linear section to zero on the x-axis. In this case, a band gap of *ca.* 2.90 eV is determined.

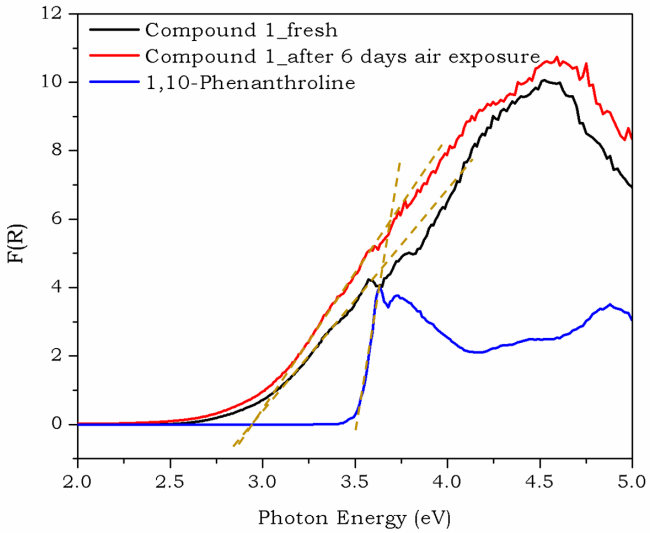

Figure 3.6. Kubelka-Munk function F(R) for the solid-state compound **1** (fresh crystallites and that after 6 days of air exposure) obtained by UV-Vis diffuse reflectance spectroscopy, as well as that for the 1,10-phenanthroline ligand.

Previous studies have suggested that the band gaps for M-TOCs in solid state are higher than those found for bulk metal-doped TiO_2, but overlap with metal-doped TiO_2 nanoparticles.[22] The value found here (*ca.* 2.90 eV) is in the expected range. The blue trace is the corresponding UV-Vis diffuse reflectance data for the 1,10-

phenanthroline powder itself, illustrating that the band gap cut-offs do not result from the ligand alone. Moreover, the reflectance spectroscopic data for compound **1** after 6 days air exposure was also recorded (red trace), confirming that the cluster is air-stable, as no hydrolysed products of narrower band gaps were detected at all.

A sample of 51.6 mg of freshly prepared crystalline blocks of **1** was used for magnetic analysis. Under a magnetic field of 5000 Oe, the magnetic susceptibility, χ_{mol}, increases when the sample is cooled until a maximum (3.49 $cm^3\ mol^{-1}$) is reached at 2 K (Figure 3.7a). The measured χ_{mol}·T value of 17.2 $cm^3\ mol^{-1}$ K at 300 K is comparable with the expected spin-only value for four Mn^{2+} ions (*i.e.*, 17.5 $cm^3\ mol^{-1}$ K, high spin, S = 2.5, g = 2.0). This is consistent with the expected d^5 A-ground state, and can be seen as further evidence of the exclusive presence of Mn^{2+} ions in **1**. Upon cooling from room temperature, χ_{mol}·T slowly decreases until about 50 K and then rapidly decreases upon further cooling before reaching a minimum value of 6.98 $cm^3\ mol^{-1}$ K at 2 K (Figure 3.7a). This indicates weak antiferromagnetic interactions between the Mn^{2+} centres. A plot of $1/\chi_{mol}$ *vs.* T in the temperature range of 2 – 300 K fits the Curie-Weiss Law [$\chi_{mol} = C/(T-\theta)$] with Weiss constant θ = -4.11 K and Curie Constant C = 17.83 $cm^3\ mol^{-1}$ K (inset to Figure 3.7a). The negative Weiss constant further confirms the antiferromagnetic interactions between the Mn^{2+} centres. Measurements under stronger (*i.e.*, 10000 Oe) or weaker (*i.e.*, 1000, 500, 200, 100 and 50 Oe) magnetic fields were also carried out, with all giving similar conclusions. The field-dependent magnetisation at 1.8 K is depicted in Figure 3.7b, in which the saturation of magnetisation is not reached even at the magnetic field as high as 70000 Oe, and no significant hysteresis behaviour is observed either.

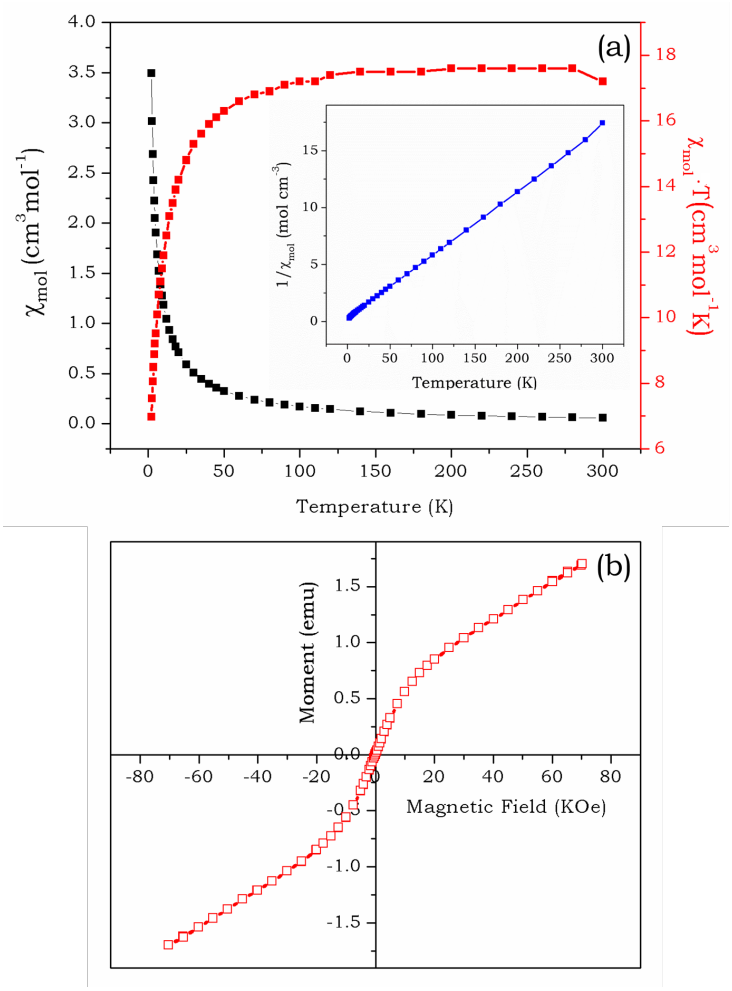

Figure 3.7. (a) Temperature dependence of molecular susceptibility of compound **1** (χ_{mol} *vs.* T and χ_{mol}·T *vs.* T) at 5000 Oe. Inset is the plot of $1/\chi_{mol}$ *vs.* T. (b) Field dependence of the magnetization of compound **1** at 1.8 K.

The thermal stability of **1** was investigated using TGA in air. As shown in Figure 3.8, weight loss from **1** takes place in several stages. Below 230 °C, compound **1** decomposes at a relatively slow rate, corresponding to a *ca.* 5 % weight loss in this temperature range. **1** further loses *ca.* 10 % of its weight in the temperature range from 230 °C to 285 °C, *ca.* 7.5 % in the range 285 – 450 °C and *ca.* 18.5 % in the range 450 – 540 °C, before the weight percentage stabilises at around 59.2 %. The product after thermal treatment in air is black in appearance (inset to Figure 3.8). This could be due to the formation of manganese dioxide MnO_2, supported by the fact that the weight percentage at 540 °C (*i.e.*, 59.2%) agrees

well with the calculated value (*i.e.*, 59.5%), assuming **1** completely converts into TiO_2 and MnO_2.

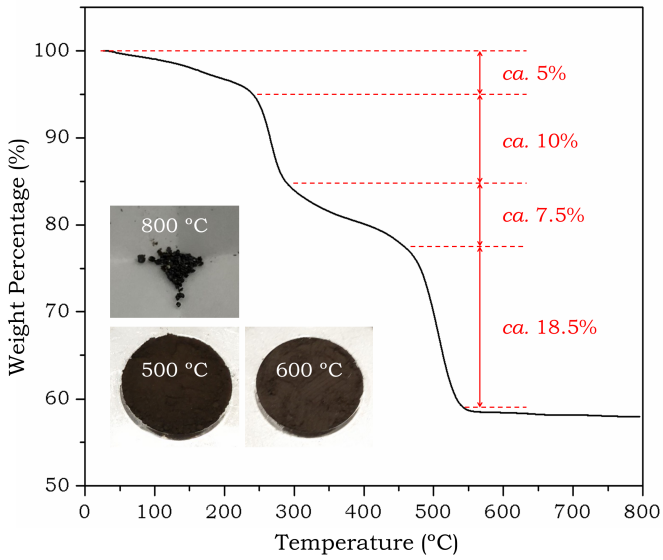

Figure 3.8. TGA profile of compound **1** in an air flow (60 mL min^{-1}) with temperature ramping rate of 10 °C min^{-1}. Inset is the digital photograph of the product after thermal treatment in air.

The state of the compound after thermal treatment was monitored using powder X-ray diffraction (pXRD). As shown in Figure 3.9, the ground powder of **1** remains crystalline until 200 °C, and crystallises into a mixed phase TiO_2 (*i.e.*, rutile and anatase) at 500 °C. The resulting pXRD peaks can be unambiguously assigned to the rutile [(110) at 27.4°, (101) at 36.1°, (200) at 39.0°, (111) at 41.3°, (210) at 44.0°, (211) at 54.3°, (220) at 56.5°, (002) at 62.7°, (310) at 63.9°, (301) at 69.0°, (112) at 69.6°, JCPDS No. 21-1276] and the anatase [(101) at 25.2°, [200] at 48.0°, JCPDS No. 89-4921] structure, with the rutile being the major phase. Generally, a temperature of 500 °C is not high enough for the formation of the thermally stable rutile TiO_2 (in contrast to the metastable anatase), whereas the emergence of rutile in the present case is potentially due to the presence of Mn dopants that is known to be beneficial for rutile phase formation.[167] Furthermore, sintering **1** at 600 °C for 12 hours leads to nearly 100% conversion to rutile TiO_2, except for some extraneous peaks that could be unambiguously

assigned to α-Mn_2O_3 [(211) at 23.0°, (222) at 32.8°, (400) at 38.0°, (332) at 45.0°, (431) at 49.1°, (440) at 54.9°, (622) at 65.5°, JCPDS No. 41-1442, Figure 3.9].[168] The α-Mn_2O_3 is believed to derive from MnO_2, as the MnO_2-to-Mn_2O_3 conversion has been reported in the literature to be in the range 500 – 600 °C.[169] This assignment is also supported by the further decrease in the sample weight beyond 500 °C and the slight colour change from black to dark brown of the material (inset to Figure 3.8). The high-resolution Mn*3s* XPS spectrum of the 600 °C sintered sample exhibits a doublet splitting of 4.96 eV (Figure 3.2b), corresponding to a Mn valence of 3.37 (by [Eqn. 3.1]). This data suggests that the MnO_2-to-Mn_2O_3 conversion is not complete, and hence both Mn^{3+} and Mn^{4+} are present in the material. It is also worth mentioning that no obvious pXRD peak shift is observed for the 600 °C sintered sample, in comparison with pure rutile TiO_2, suggesting that the manganese dopants are not substituting the Ti^{4+} ions in the TiO_2 crystal lattice. Instead, they may be present in an interstitial manner in the lattice or simply dispersed in an amorphous state on the material surface.

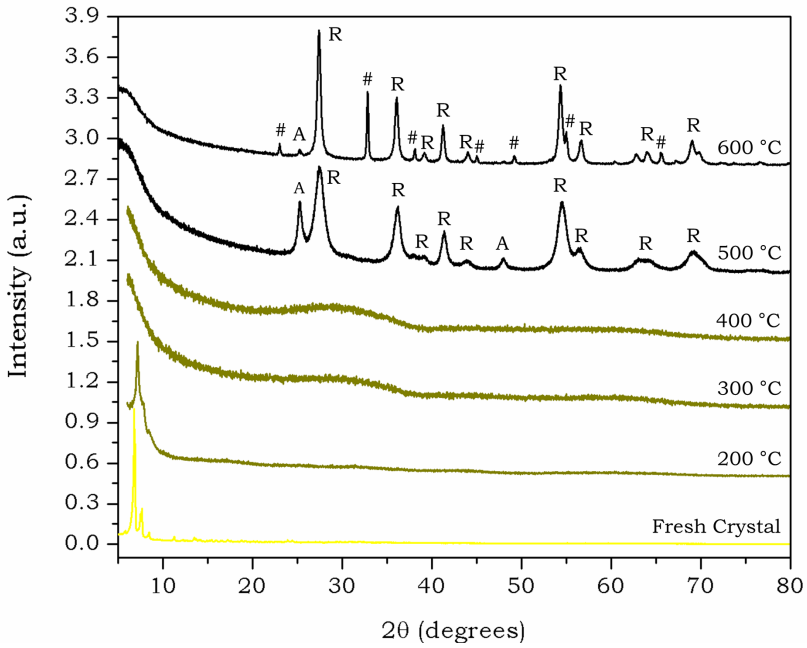

Figure 3.9. Powder XRD patterns of compound **1** and sintered samples at different temperatures in air. The material coverts to mixed phase TiO_2 at 500 °C, with 'A' denoting the anatase and 'R' the rutile phase. The line colours reflect the actual physical appearance of the respective samples. Some extraneous peaks are also present in the '600 °C' spectrum, denoted by '#', which can be assigned to α-Mn_2O_3.[166]

The UV-Vis reflectance spectra of **1** were taken after sintering at different temperatures (Figure 3.10). However, the presence of low band gap manganese oxides masks the optical properties of TiO_2. Assuming a direct band gap for α-Mn_2O_3, the modified Kubelka-Munk function $[F(R)\cdot hv]^2$ *vs.* incident photon energy was plotted and the band gap was estimated to be *ca.* 1.8 eV after 600 °C sintering (Figure 3.10b). This value for the band gap agrees well with the literature value for α-Mn_2O_3 (1.2 – 2.1 eV).[170,171] The micro-scale morphology of the resultant TiO_2/α-Mn_2O_3 material is depicted in Figure 3.11, in which nano-/microparticles of irregular shape of a few hundred nanometres to several micrometres in size are observed.

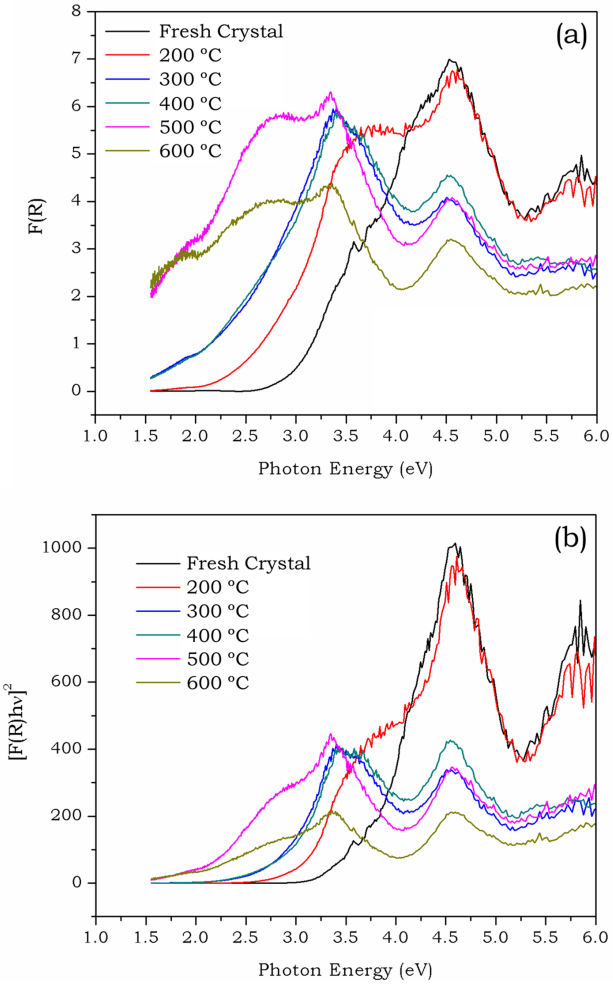

Figure 3.10. UV-Vis diffuse reflectance data for compound **1** after sintering at different temperatures in air: (a) Kubelka-Munk function F(R); and (b) modified Kubelka-Munk function $[F(R)\cdot hv]^2$ assuming a direct band gap model.[166]

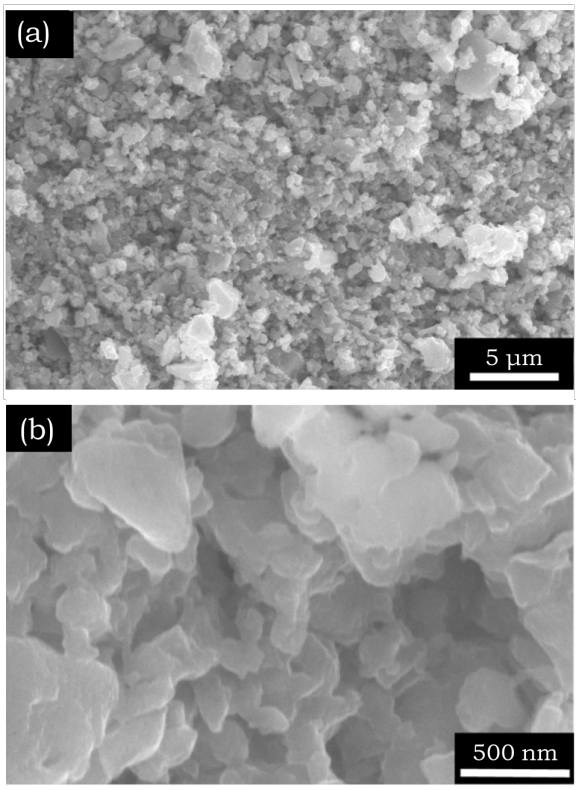

Figure 3.11. FESEM images of the black powdered sample of **1** sintered at 600 °C in air (mixture of TiO_2 and α-Mn_2O_3): (a) low and (b) high magnification.[166]

Cluster **1** retains its molecular structure after drop-casting in air, shown by the FTIR-ATR spectrum of **1** drop-cast on FTO (**1**|FTO), which is almost identical to that of solid **1** (Figure 3.12). Moreover, **1** also appears to survive further electrochemical measurements in aqueous solution (Figure 3.12). Cyclic voltammetry (CV) of **1**|FTO at a scan rate of 50 mV s^{-1} in aqueous solution of Na_2SO_4 (0.1 M, pH 6.54) exhibits oxidation and reduction waves at 1.44 V and 1.22 V *vs.* RHE, respectively (Figure 3.13a), which are ascribed to the Mn^{2+}/Mn^{3+} couple. Confirming this assignment, a similar redox wave is also observed for FTO coated with $[Ti_{27}MnKO_{35}(OH)_2(OEt)_{39}]_{0.33}[Ti_{28}MnKO_{37}(OH)(OEt)_{40}]_{0.67}$ (denoted as $Ti_{28}Mn$|FTO),[46] while there is no such wave for FTO coated with the undoped TOC $[Ti_7O_4(OEt)_{20}]$ (denoted as Ti_7|FTO)[172] or for a bare FTO electrode (Figure 3.13a). In addition, following the Mn^{2+}/Mn^{3+} oxidation, a further large anodic response emerges and exhibits an onset potential of 1.73 V *vs.* RHE for **1**|FTO,

with the unmodified FTO, Ti_7|FTO and $Ti_{28}Mn$|FTO electrodes all showing more positive onset potentials of *ca.* 1.88 V *vs.* RHE. This cathodic shift for **1** is unlikely to result from water oxidation catalysis because the electrode stability test shows exponential decay of the current density over time. The detailed mechanism is subject to further investigation. In addition, a second minor redox wave emerges with an increase of the CV scan rate, which resides next to the major waves (at 1.44 and 1.22 V *vs.* RHE) that are discussed above (Figure 3.13b).

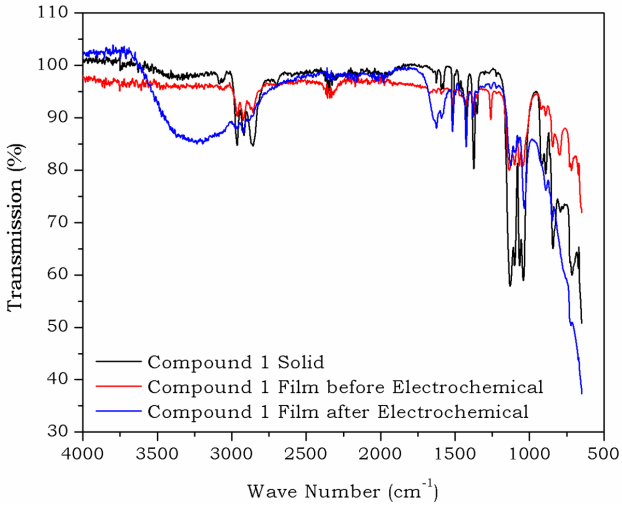

Figure 3.12. The FTIR-ATR spectra of compound **1** in the form of a solid powder (black trace) and drop-cast film before (red trace) and after (blue trace) electrochemical analysis in aqueous environment.[166]

The combination of major and minor redox waves is also seen in the solution phase electrochemical analysis using glassy carbon as working electrode, Pt mesh as counter and Ag/AgCl toluene/methanol as reference electrode in a saturated solution of compound **1** (Figure 3.13c). The saturated solution was prepared by adding *ca.* 90 mg crystalline blocks of **1** in 3.0 mL of a toluene and methanol mixture (3 : 2 volume ratio). After 30 min stirring at room temperature, the yellow cloudy suspension was centrifuged to obtain a clear bright yellow solution of **1**. 0.1 M NBu_4BF_4 was used as electrolyte and the solution was purged with N_2 for 15 min before measurements. The observation of two Mn^{2+}/Mn^{3+} redox couples for **1** is consistent with the presence of two Mn^{2+}

coordination environments in the cluster molecule. In the solution phase CV scans, the magnitude of each oxidation peak is found to be linearly proportional to the square root of the applied scan rate (inset to Figure 3.13d), however, it is not possible to identify which Mn^{2+} environment in the cluster structure (interstitial or peripheral) corresponds to each wave from the electrode or solution data at this stage.

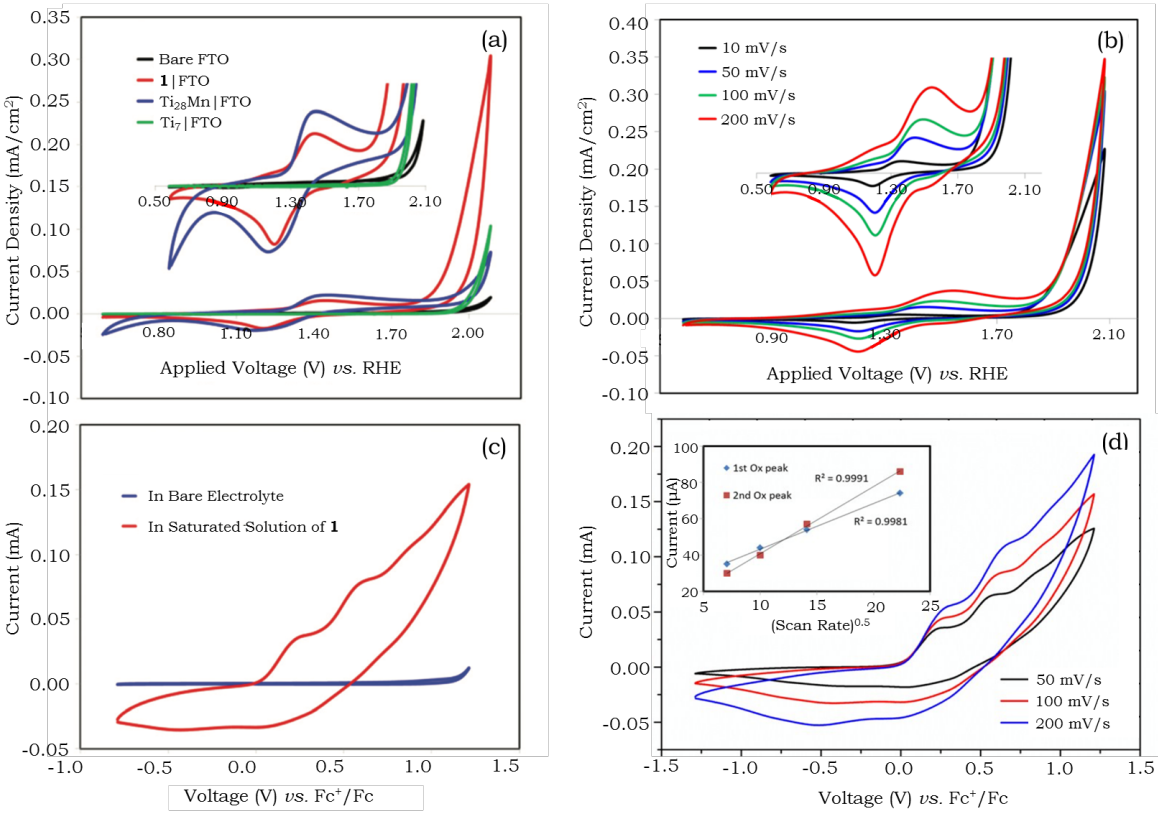

Figure 3.13. (a) Electrode-based CV of bare FTO (black), **1**|FTO (red), $Ti_{28}Mn$|FTO (blue) and Ti_7|FTO (green) electrodes with 50 mV s^{-1} scan rate. (b) Electrode-based CV of **1**|FTO with different scan rates; inset is the magnification of the redox waves. (c) Solution phase CV of **1** using a saturated solution in toluene and methanol mixture with 100 mV s^{-1} scan rate; the electrolyte is 0.1 M NBu_4BF_4. (d) Solution phase CV with different scan rates; inset shows the linear relation between the oxidation peak heights and the square root of scan rate.[166]

The freshly prepared **1**|FTO electrode exhibits a uniform distribution of **1**, as observed by field emission scanning electron microscopy (FESEM) (Figure 3.14a). The magnified image (Figure 3.14b) shows that the electrode surface is covered by self-assembled microparticles of **1** of various sizes, spanning from 0.3 to 2.1 μm in diameter. After the electrochemical test, the active film on the FTO remains *intact* by the naked eye. However, FESEM shows aggregation of the particles into clusters and less uniform distribution of the material, compared to the pre-test morphology (Figure 3.14c and d). No significant change in the size distribution of the particles was observed between the pre- and post-test electrodes. For comparison, another electrode was prepared by a similar drop-casting procedure but done at room temperature, on which inhomogeneous films can be seen (Figure 3.14e). Although FESEM shows that spherical microparticles are still produced, they only cover a limited portion of the FTO substrate (Figure 3.14e). Magnification shows that the microparticles are much larger (range 0.7 to 4.3 μm, Figure 3.14f) compared with those drop-cast at 80 °C. Some interesting doughnut-like structures are also observed, indicating the observed microparticles could be hollow in nature. At room temperature, the solvent evaporation rate is much slower than that at higher temperatures. As a result, a slow rate of microparticle growth can be expected, leading to larger particles. However, if the particles become too large, presumably they can no longer hold their spherical shape, and the hollow structures tend to collapse and form the doughnut-like morphology observed (Figure 3.14f).

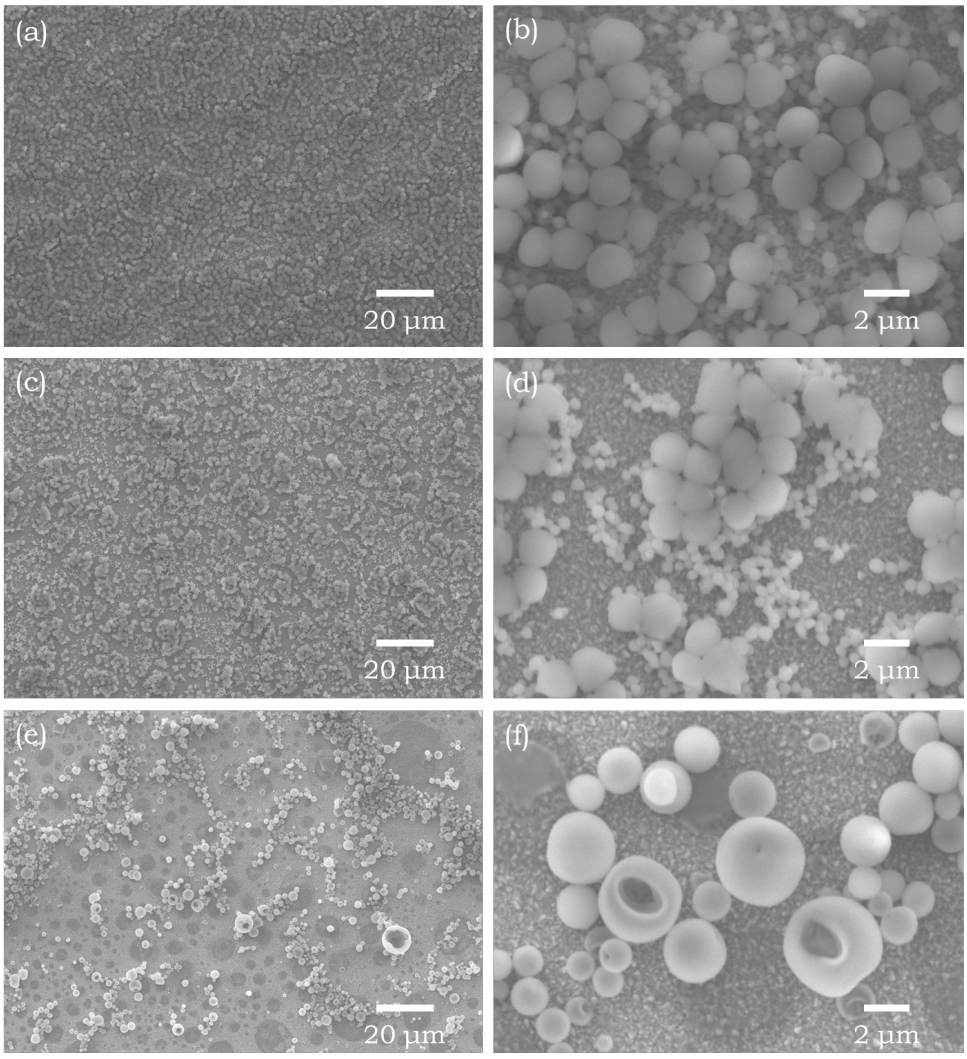

Figure 3.14. FESEM images of the prepared electrode: (a) & (b) **1**|FTO (drop-cast at 80 °C) before the electrochemical test; (c) & (d) **1**|FTO after electrochemical test; (e) & (f) **1**|FTO drop-cast at room temperature.[166]

These self-assembled hollow microparticles on solid-state surfaces were retained after sintering at 500 °C for 2 hours, despite the reduction in the particle size (Figure 3.15), possibly due to the loss of the organic components. The atomic ratio between Ti and Mn in TOC **1** is also maintained in the sintered hollow microparticles as indicated by EDX spectroscopy. In this context, the self-assembly of TOC **1** represents a special example of template-free fabrication of hollow metal oxide micro-/nanoparticles, and **1** is the first single-source

precursor to this type of material. More interestingly, the hollow microparticles have nano-sized pores on their surfaces (Figure 3.15b), which not only enlarges the specific surface area but also provide extraneous passages for mass transport in and out of the hollow microparticles, which could give many interesting potential applications.[173,174]

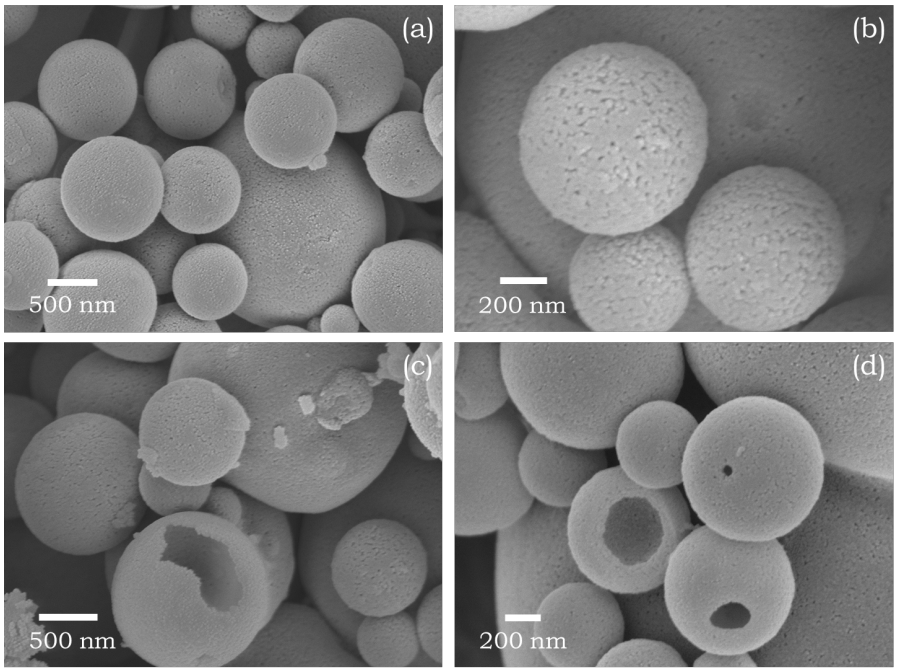

Figure 3.15. FESEM images of (a) & (b) the self-assembled microparticles of **1** on a glass substrate after sintering at 500 °C in air for 2 hours, and (c) & (d) the incomplete/broken microparticles showing the hollow nature and the wall thickness (*ca.* 50 – 100 nm).

Unfortunately, it has been experimentally confirmed that the sintered hollow microparticles are inactive for the photocatalytic degradation of rhodamine B in aqueous solution, despite the prominent visible light absorption of **1** after sintering. This inactivity could arise from the band-bending properties of the sintered hollow microparticles comprising TiO_2 and α-Mn_2O_3, which may require an external voltage to trigger photocatalytic activity.[175] Also of note is that the manganese species present may also result in electron-hole recombination and blocking of TiO_2 reaction sites, which are both detrimental to the photocatalytic performance.[176,177] Other potential applications, such as the use as an electrode

in lithium ion batteries or supercapacitors, and gas adsorption/separation, are currently under investigation.

3.3. Use as Multifunctional Coating Precursors

In addition to solid-state FTO substrates, TOC **1** can also self-assemble into hollow microparticles on the cellulosic microfibres of cotton textile. This feature can be employed for developing a novel room temperature coating technology for the fabrication of multifunctional flexible materials and devices.

Over recent years, multifunctional flexible materials have shown great promise for numerous applications,[178-180] as they have the potential to make large contributions to alleviate the current energy and environmental crisis,[181,182] and also to advance the development of healthcare technology.[183-186] Among other strategies, surface coating is widely considered to be a powerful approach to fabricate multifunctional flexible materials, because it is able to introduce new functionalities from the coating precursor while, at the same time, retain the inherent advantages of the flexible substrate.[187] TiO_2 has received intensive attention for its extensive applications in photovoltaics,[188] photocatalysis,[189] antibacterial,[190] self-cleaning,[191] and UV-blocking uses.[192] Consequently, coating of TiO_2 onto flexible substrates has also attracted considerable interest for transferring these beneficial functionalities onto flexible surfaces.[193-195] By virtue of the small size '*enhanced*' or '*enabled*' properties, micro-/nanoparticles are the most widely employed forms of TiO_2 for coating.[12] However, achieving a micro-/nanoparticle coating effectively and efficiently on highly flexible substrates remains a significant challenge.

The current state-of-the-art coating of TiO_2 micro-/nanoparticles onto flexible substrates is usually achieved by using pre-formed particles,[196-200] with their immobilisation being either by physical adsorption (Figure 3.16a, left panel),[196] which exhibits poor durability due to fraying or shedding of the coating layer, or by using a polymeric binder to bind the particles to the substrate (Figure 3.16a, right panel),[197] which requires a multi-step procedure and thus leads to high

overall cost. The polymeric binder also passivates the particle surface and consequently sacrifices the surface-related functionalities. Therefore, a powerful yet economic coating technology to fabricate titanium oxide materials on flexible substrate is highly desirable. In general, introducing multifunctionality, while maintaining the functional integrity of the cotton textile substrate, requires integration of the functional components at the fibre level.[201] Various materials have been introduced onto textile fibres,[202] but related coating methods usually require multi-step procedures and sophisticated instrumentation. For real-life applications, a strategy involving only a single-step procedure yet is still capable of achieving fibre-scale integration of the functional component, such as *in situ* self-assembly, is highly desired.

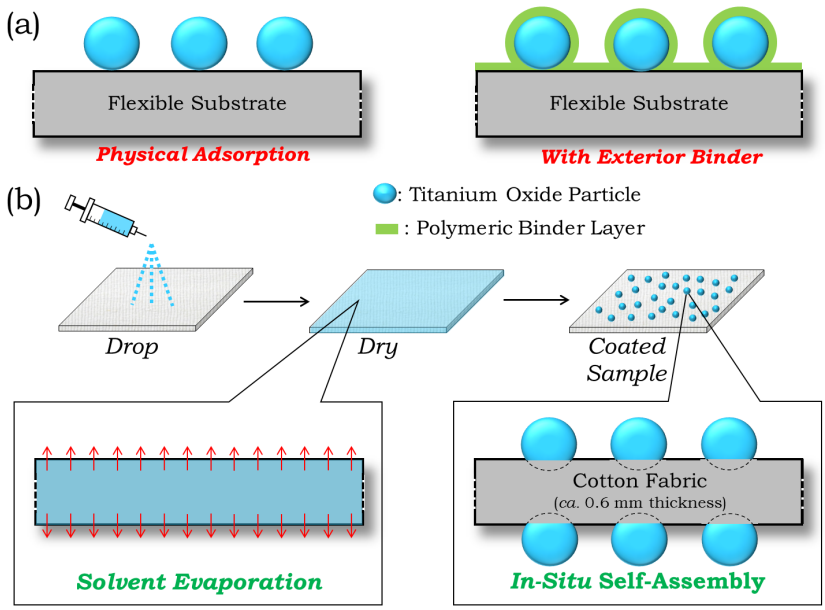

Figure 3.16. Illustration of (a) conventional approaches to flexible surface coating by pre-formed TiO_2 particles; (b) use of *in situ* self-assembly of TOCs to generate microparticles on cotton fabrics, the method developed in this thesis.[203]

In this section, a novel room-temperature coating method using *in situ* self-assembly of the TOC **1** $[Ti_{18}Mn_4O_{30}(OEt)_{20}Phen_3]$ on flexible cotton fabric is demonstrated (Figure 3.16b). The cluster molecules readily self-assemble into hollow microparticles (MPs) on the fibres of the cotton substrate, and this MP-

decorated cotton fabric (denoted as **1|Cotton**) displays an array of multifunctional characteristics, in which the physical properties of the fabrics are maintained and the MPs are firmly mounted on both sides of the fabric without the need for any exterior binder. The key features of **1|Cotton** include (i) robust hydrophobicity that is maintained even after hash test conditions, including washing, mechanical abrasion and UV irradiation, (ii) antibacterial activity against both Gram-positive and Gram-negative bacteria strains under ambient laboratory conditions, and (iii) enhanced UV-blocking capability of the cotton fabric. These features lead to a number of important applications, such as stain-resistant clothing and medical bandages and sustainable materials for the separation of organic pollutant from water. In the literature, similar multifunctional coating on fabrics was only achieved by multiple steps involving growing/depositing metal oxide nanostructures and silane compounds (*e.g.*, ZnO@SiO_2 nanorods with octadecyltrimethoxysilane,[204] SiO_2 nanoparticles with spirooxazine and triethoxyoctylsilane,[205] Ag nanoparticles with octyltriethoxysilane,[206] etc.).

Cotton was chosen as the substrate because of its low-cost, and sustainability. It is also chemically modifiable and physically tunable, and any straightforward modification should be easily integrated into existing industrial infrastructures.[201] The cotton substrates were prepared by cutting 100 % cotton fabrics (*ca.* 0.6 mm in thickness, area density of 168.9 ± 1.2 g m^{-2}) into swatches of 2 cm by 2 cm in size, washed with dichloromethane and ethanol before being dried in a pre-heated oven at 80 °C. In a typical '*drop-and-dry*' coating process, a 2.5 mg mL^{-1} solution of **1** was prepared in a binary solvent system of toluene and methanol (3 : 2 volume ratio). Initial attempts were done in a N_2-filled glove box, but later experiments showed that operation in air gives similar results. 0.1 mL of this solution was dropped onto a cotton swatch using a syringe attached with a needle. After complete solvent evaporation under ambient conditions, the process was repeated twice further to give **1|Cotton**. This method was found to result in the maximum water contact angle observed using a range of differently prepared samples (*e.g.*, varying solvent evaporation temperatures and atmospheric conditions, different amounts of solution used, etc.).

Figure 3.17a shows the FESEM image of **1|Cotton**. A micro-particulate morphology, which provides roughness at the microscale, is clearly observed at the fibre level. The microparticles (MPs) are all spherical with an average diameter of *ca.* 0.8 μm (Figure 3.17b). The average atomic ratio between Ti and Mn within the MPs on **1|Cotton** was determined by EDX to be 4.3 : 1, satisfactorily matching the ratio (4.5 : 1) present in precursor **1** (Figure 3.17c), and confirming that the MPs originate from **1**. As the coated material (after self-assembly in air) exhibits an almost identical FTIR-ATR spectrum to that of freshly prepared **1** (Figure 3.12), there appears to be minimal (if any) hydrolysis or decomposition of the cluster molecules. This result is in-line with the previous observation that **1** is indefinitely stable in ambient air, and further suggests that the observed MPs are made of *intact* molecules of **1** (but possibly with some OEt-to-OMe ligand exchange). The powder XRD pattern of the coated material after self-assembly exhibits a relatively broad peak at around 6.8°, indicating its semi-crystalline nature (Figure 3.18). Magnified FESEM images show that the spherical MPs are firmly embedded within the substrate fibres (Figure 3.17d-f). Some bowl-shaped structures that appear to arise from broken or incomplete spherical particles are also observed, strongly supporting the hypothesis that the MPs are hollow in nature, with a wall thickness of around 100 nm (Figure 3.17g).

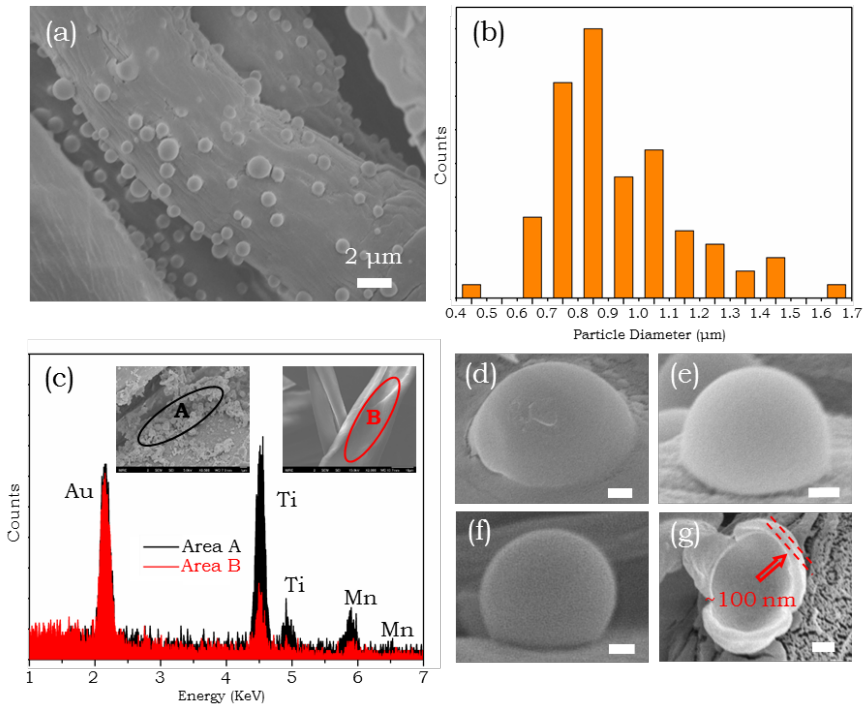

Figure 3.17. (a) FESEM images of **1|Cotton**. (b) Size distribution of the microparticles observed in (a). (c) EDX spectra of **1|Cotton** in areas with and without MPs; inset are the FESEM images of the areas studied. Magnified FESEM images (d-f) of individual embedded microparticles with different morphologies and (g) a broken microparticle, showing the hollow structure and wall thickness; the bars shown are all 200 nm in length.[203]

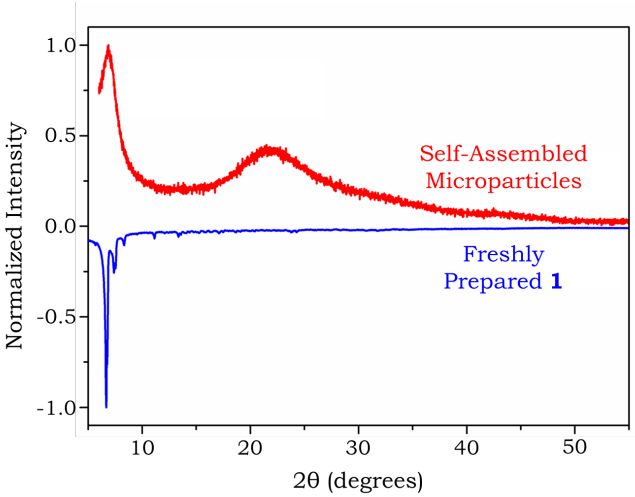

Figure 3.18. Powder XRD patterns of freshly prepared crystalline TOC **1** (blue trace) and after self-assembly in air (red trace); the broad peak at around 23° is from the sample holder.[203]

It is believed that the self-assembly of **1** occurs on the cotton surface during the process of solvent evaporation, by the mechanism shown in Figure 3.19. Upon dropping the solution of **1** onto substrate, the dissolved precursor molecules are evenly distributed within the bulk of the cotton substrate. Solvent evaporation then brings the precursor molecules towards the surface, where they self-assemble into MPs. As solvent evaporation occurs, the growing MPs initially form '*bubbles*' due to the presence of trapped solvent in the void. A similar process is also thought to occur in the formation of spherical arrangements of **1** on non-porous solid substrates (see previous section).

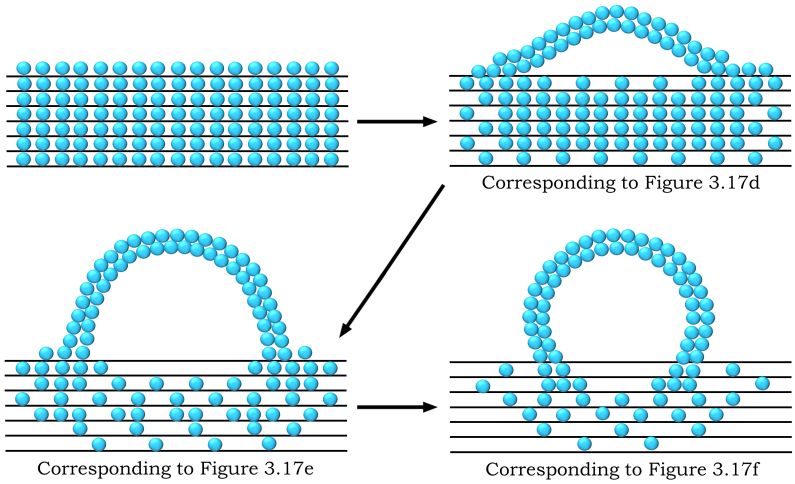

Figure 3.19. Proposed formation mechanism of microparticles via *in situ* self-assembly of the TOC **1** on cotton fabrics. Each cyan sphere represents a molecule of **1**. The black horizontal lines represent the cellulose microfibers of the cotton substrate.[203]

Crucially, however, in the present case the MPs are intimately embedded within the substrate fibre via anchoring to subcutaneous molecules of **1**. The presence of **1** within the bulk cotton fabric itself is confirmed by the significant amount of Ti and Mn detected at the bare regions of the cotton (Figure 3.17c). These residues are very likely to be located in the amorphous regions of the cellulose microfibres or within the inter-fibre spaces. This method differs fundamentally from the use of pre-formed TiO_2 micro-/nanoparticles since (i) the *in situ* self-assembly of TOCs generates spherical MPs that are firmly mounted to the

substrate without the assistance of exterior binders and (ii) it produces MPs on both sides of the cotton fabric simultaneously. Moreover, the self-assembly appears to be associated with the presence of Phen ligands, because other reported TOCs with Phen ligands also exhibit similar behaviour,[52] but not for those without Phen regardless of cluster size (*e.g.*, see Figure 3.20 where two such clusters were investigated).

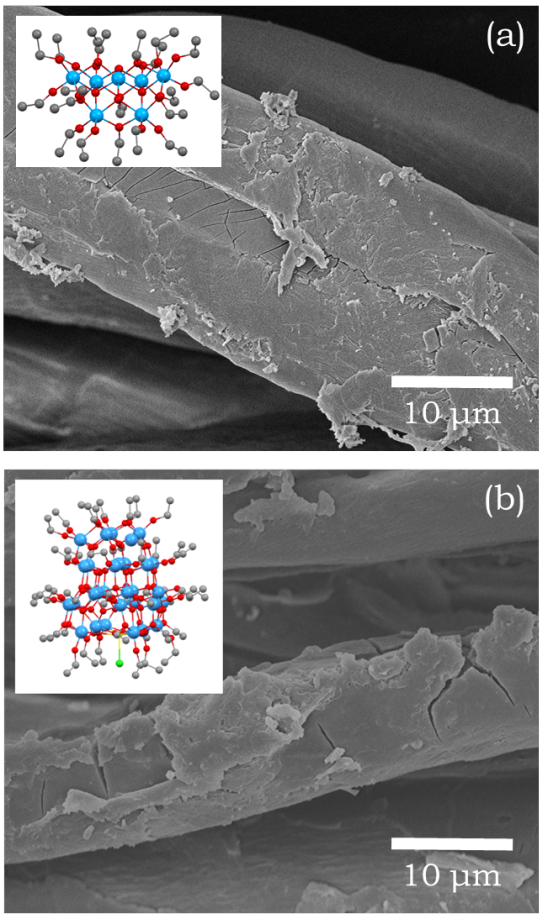

Figure 3.20. FESEM images of (a) Ti_7|Cotton and (b) Ti_{28}|Cotton. Ti_7 is the TOC $[Ti_7O_4(OEt)_{20}]$ with molecular structure shown in inset to (a), and Ti_{28} is the TOC $[Ti_{28}O_{36}(OEt)_{40}(OH)_2LaCl]_{0.7}[Ti_{28}O_{38}(OEt)_{38}LaCl]_{0.3}$ (inset to (b)). Colour code for atoms: Ti = cyan, O = red, C = grey, La = yellow, Cl = green. H atoms are omitted for clarity.[203]

The **1|Cotton** samples do not show any visually detectable change in their physical appearance compared to pristine cotton, except for a slight yellowish colour inherited from **1**. The FTIR-ATR spectrum of **1|Cotton** resembles that of

the pristine cotton fabric, except for a few new peaks that can all be assigned to the coating precursor **1** (Figure 3.21). Thermal gravimetric analysis (TGA) revealed that **1|Cotton** is stable up to 300 °C in air, similar to that of pristine cotton fabrics (Figure 3.22). A mass loss (*ca.* 5%) at around 70 °C was observed for both pristine and **1|Cotton** samples, corresponding to release of water molecules adsorbed or bound to the cellulosic cotton substrate. The mechanical strength of **1|Cotton** was also tested, demonstrating a similar performance to pristine cotton (74% strain at 15 MPa tensile stress, Figure 3.23). All of these observations verify that surface coating using **1** does not compromise the inherent thermal properties and mechanical strength of the cotton fabrics used.

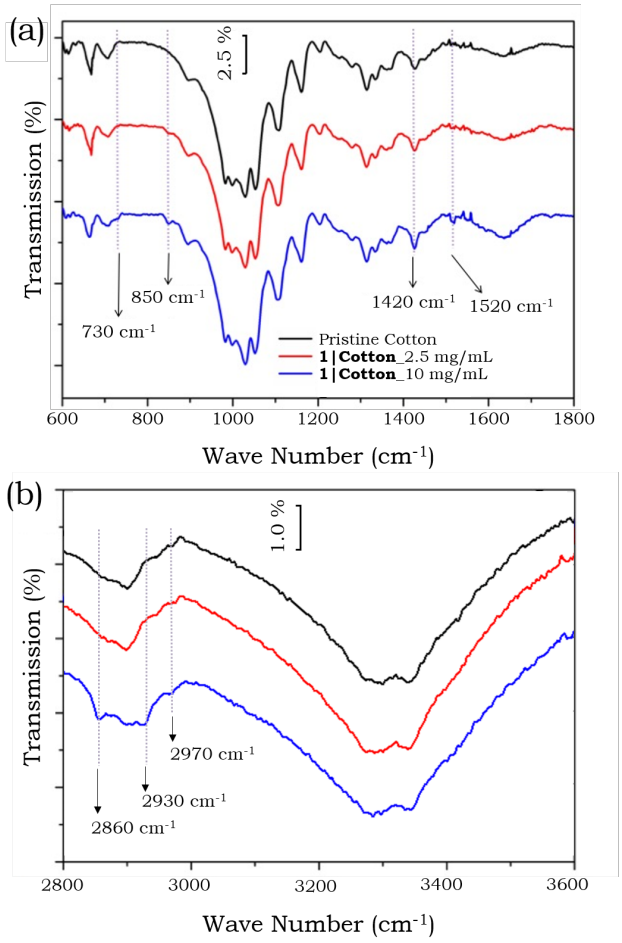

Figure 3.21. FTIR-ATR spectra of **1|Cotton** and pristine cotton fabrics: (a) the fingerprint region and (b) the higher-wavenumber functional group region.[203] '**1|Cotton**_x mg/mL' denotes the coated cotton sample using 0.3 mL solution of **1** of x mg mL^{-1} concentration.

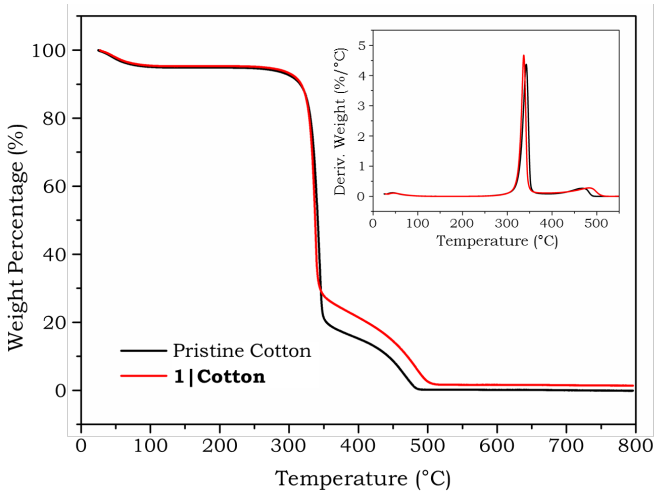

Figure 3.22. TGA profile of **1|Cotton** and pristine cotton fabrics in air flow (60 mL min^{-1}) with temperature ramping rate of 10 °C min^{-1}; inset is the plot of weight derivative (%) against temperature.[203]

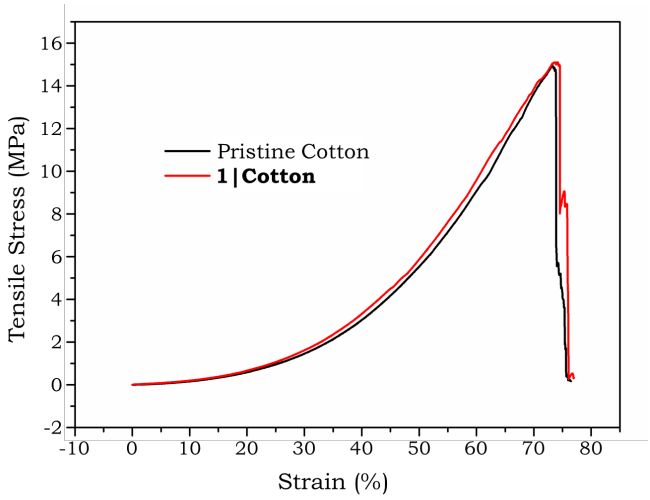

Figure 3.23. Tensile measurements of pristine cotton and **1|Cotton**.[203]

It is well known that natural cotton is hydrophilic, resulting from the available hydroxyl groups on its surface that have a high affinity towards water. This hydrophilicity makes cotton well suited for aqueous liquid absorption, but at the same time, it can also be easily stained by aqueous contaminants. Fabrication of hydrophobic cotton fabrics via surface coating has long been a popular approach to produce self-cleaning and water-repellent cotton-based devices. The micro-

structure of the lotus leaf is one of the most popularly referred to examples for the bio-inspired design of hydrophobic surfaces (Figure 3.24).[207] The combination of surface roughness and low surface free energy found in the lotus leaf can be mimicked well by surface coating of micro-/nanoparticles, especially on flexible substrates.[208-211] In this case, the self-assembled MPs and the presence of aromatic 1,10-phenanthroline ligands at the periphery of molecules of **1** make **1|Cotton** an excellent flexible hydrophobic material.

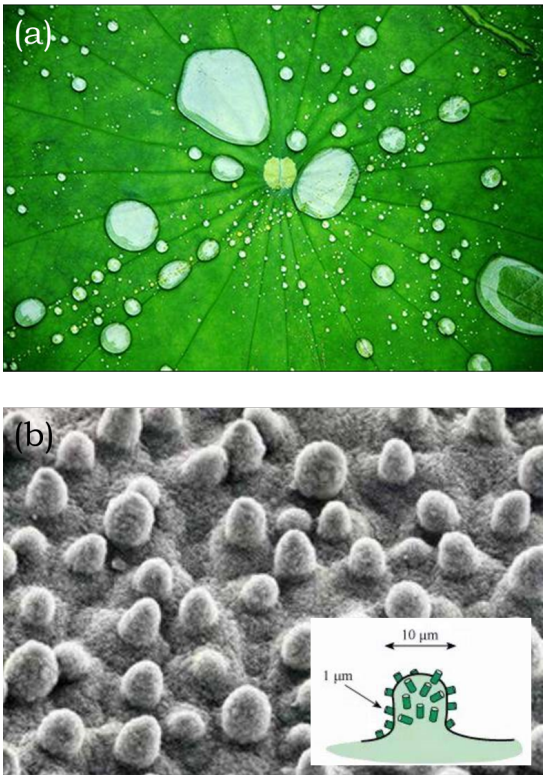

Figure 3.24. (a) Digital photograph of the hydrophobic lotus leaf. (b) The SEM image of lotus leaf, on which microparticles are observed; inset is the schematic illustration of the secondary structures of the microparticles shown.[212]

The hydrophobicity of **1|Cotton** was quantified by measuring the water contact angle (WCA) under ambient conditions. A de-ionized water droplet (5 μL) was almost spherical on **1|Cotton**, showing a WCA of 148.1 ± 5.4°, whereas it was absorbed into the pristine cotton fabric immediately upon contact (Figure 3.25a). The water droplet remains stable for at least 30 min, despite a decrease in size

due to evaporation (Figure 3.25b). The hydrophobicity of **1|Cotton** towards common beverages was also observed, in which both green tea and latte coffee form spherical droplets on the surface, with no stain being left upon removing the droplets after 5 min (Figure 3.25c). Such stain-resistant character is significant in regard to household textile materials and clothing. To determine the respective contribution of surface chemistry and micro-structural roughness to the hydrophobicity observed, Au sputtering was applied to **1|Cotton** to make a thin layer of Au on the surface (*ca.* 15 nm in thickness). This treatment completely alters the surface chemistry of **1|Cotton**, while retaining its micro-particulate morphology (Figure 3.25e). The WCA of **1|Cotton** after Au sputtering decreases to 76.8 ± 10.2°, suggesting that around half of the hydrophobicity is due to the surface roughness. In comparison, an Au layer on pristine cotton fabric did not exhibit any hydrophobicity, as the water droplet was absorbed immediately upon contact.

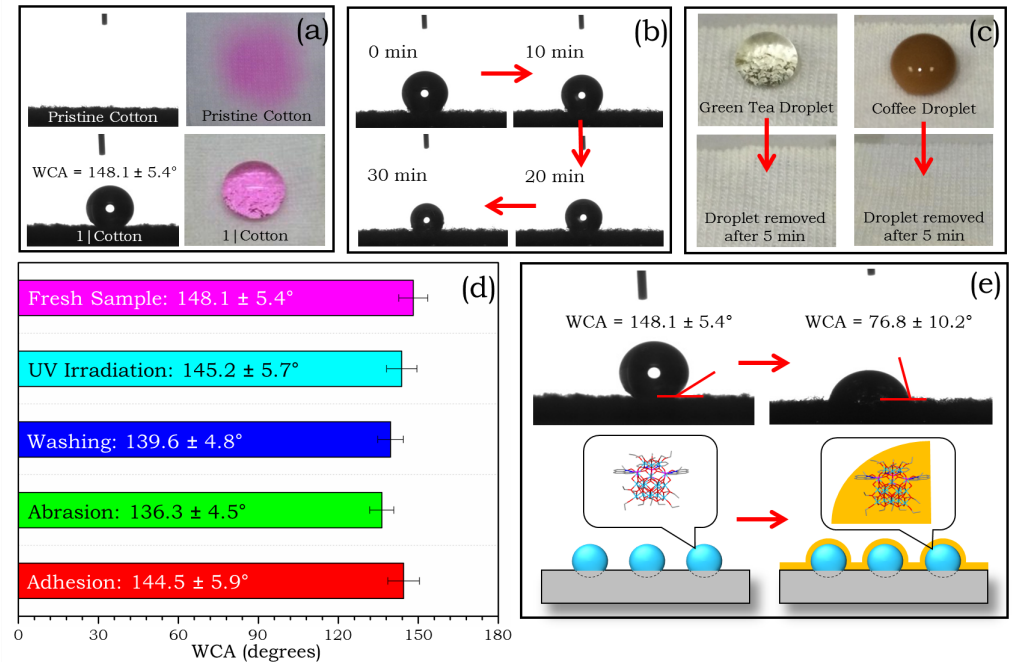

Figure 3.25. (a) WCA on **1|Cotton** and absorption of water on pristine cotton fabric; the water droplet in the digital photograph was coloured by rhodamine B for better visual contrast. (b) Water droplet on **1|Cotton** for 30 min under ambient conditions. (c) Green tea and coffee droplets on **1|Cotton**. (d) Comparison of WCA for **1|Cotton** and after various test conditions. (e) Water droplet on **1|Cotton** before (left) and after (right) Au sputtering.[203]

The washing durability of **1|Cotton** was evaluated in a simulated laundry process,[213] after which the WCA decreased only slightly to 139.6 ± 4.8° (Figure 3.25d and 3.26) and the MPs were also retained on the surface (Figure 3.27). More strict washing conditions (*e.g.*, using detergent, higher water temperature, longer washing duration, repeated washing cycles and additional mechanical wear) were also tested, and the WCA values either remain identical or only decrease slightly compared to that of the freshly prepared **1|Cotton** (Figure 3.26). The hydrophobicity was also retained after 365 nm UV irradiation for 40 min, mechanical abrasion and tape adhesion-and-peeling treatments, all showing similar WCAs compared to that of fresh **1|Cotton** sample (Figure 3.25d).

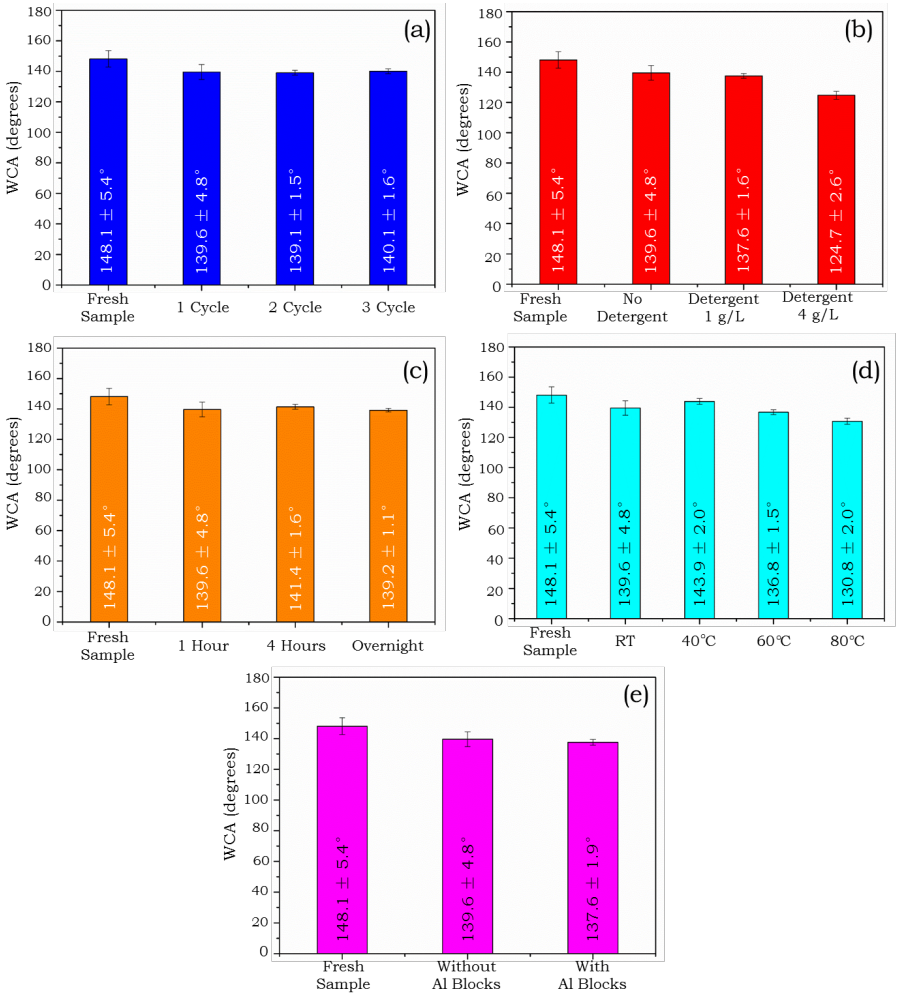

Figure 3.26. WCA values of **1|Cotton** after various washing conditions: (a) increased washing cycles, (b) use of detergent, (c) prolonged washing duration, (d) higher water temperatures, and (e) with additional mechanical wear.[203]

Moreover, **1|Cotton** maintains its hydrophobicity after being soaked in *n*-hexane, giving it the capacity for oil/water separation.[214] As a proof of concept, a simple filtration setup was constructed using **1|Cotton** (Figure 3.28), which was found to be capable of efficiently separating a mixture of *n*-hexane (30 mL) and water (30 mL) in just a few seconds. Dichloromethane/water and toluene/water separation can also be achieved using the same setup.

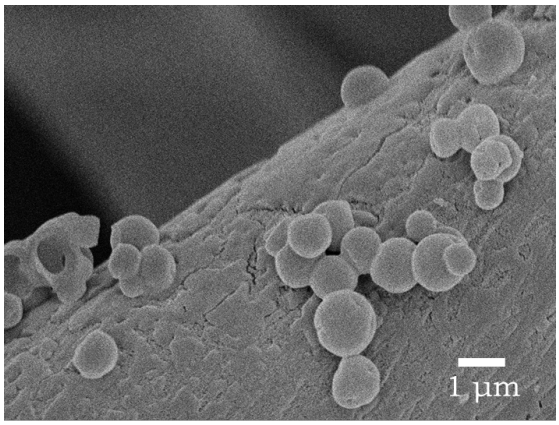

Figure 3.27. FESEM image of **1|Cotton** after the simulated washing process

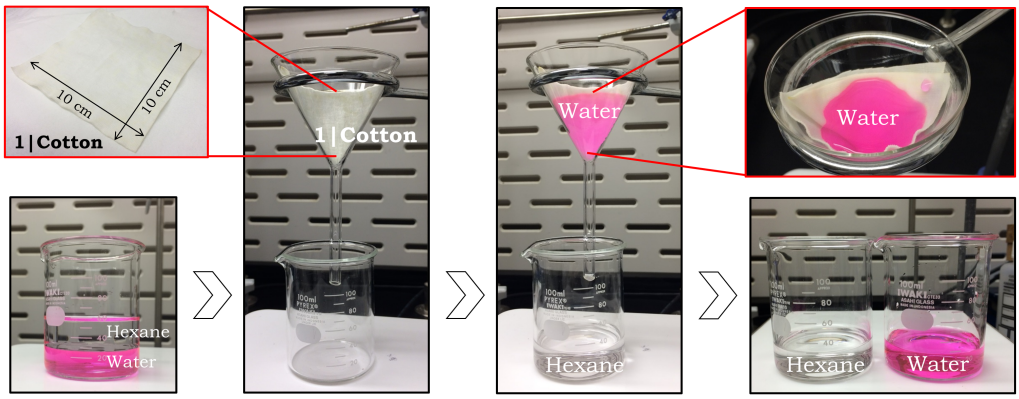

Figure 3.28. Demonstration of rapid water/*n*-hexane separation by a simple filtration setup constructed using **1|Cotton**. Water was coloured by rhodamine B for better visual contrast.[203]

Apart from robust hydrophobicity, **1|Cotton** also demonstrates antibacterial activity at 37 °C under ambient conditions. As shown in Figure 3.29a, c and e,

inhibition zones of 18 mm, 15 mm and 16 mm in diameter were clearly observed around **1|Cotton** on the agar plates of Gram-negative *E. coli*, and Gram-positive *S. epidermidis* and *S. aureus*, respectively, and as expected, not around the uncoated samples. For comparison, another parallel antibacterial test was conducted in the dark, in which **1|Cotton** shows a weaker inhibitory effect against *E. coli* (13 mm inhibition zone, Figure 3.29b) and none for the other two bacterial strains (Figure 3.29d and f). Therefore, the observed antibacterial activity against *E. coli* is a combined effect of the photo-activation of the TOC **1** and its unique molecular structure, while that against *S. epidermidis* and *S. aureus* is solely due to photo-activation of **1**. Importantly, the photo-induced antibacterial activity is responsive to ambient light, which significantly enhances its practical viability. This could be due to the narrowed band gap of **1** (*i.e.*, 2.90 eV) with Mn-doping and Phen-functionalisation, in contrast to unmodified TOCs or TiO_2 nanomaterials that usually possess much wider band gaps. The detailed antibacterial mechanism is likely to be complicated and will be subjected to further investigations.[215,216] Such antibacterial activity in an ambient light environment is potentially useful for in-built deodorant capacity in clothing or for would-dressing bandages to reduce bacterial infection.

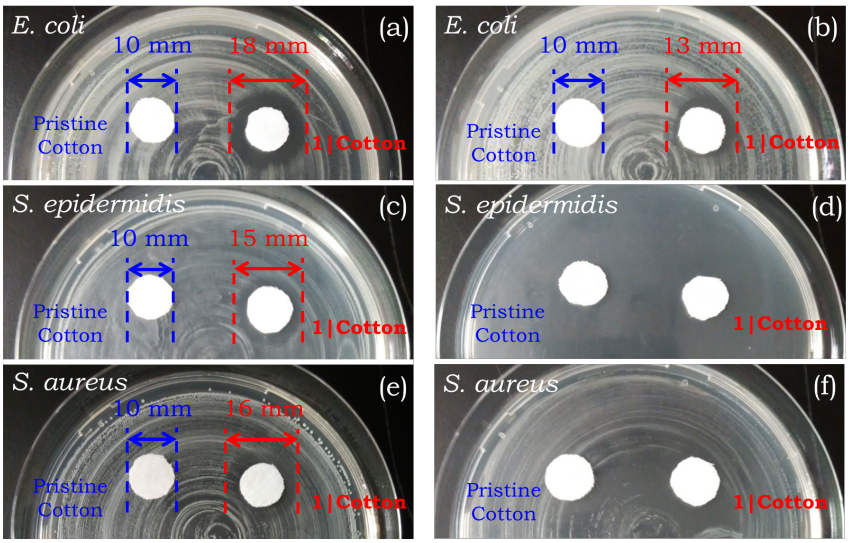

Figure 3.29. Digital photographs showing the antibacterial activity of **1|Cotton** against (a) *E. coli*, (c) *S. epidermidis* and (e) *S. aureus* in the presence of ambient light. (b), (d) and (f) show the results of a parallel test in the dark. The diameter of the **1|Cotton** samples used and the inhibition zones are indicated for comparison.[203]

UV blocking is another key consideration for textile materials like cotton. As shown in Figure 3.30, the UV transmission for **1|Cotton** is around 10.9 % at 350 nm and 4.8 % at 300 nm, which is about 50 % and 80 % lower than that of the pristine cotton fabric at the same wavelengths. The observed transmission edge at 300 – 350 nm is the result of charge-transfer from O*2p* to Ti*3d* in the precursor cluster core of **1**, and is commonly observed in other TOCs reported in the literatures. The diffuse reflectance spectrum of **1|Cotton** was also recorded, showing a much lower reflection than pristine cotton in the UV region (inset to Figure 3.30). This observation further suggests the UV-blocking capability of **1|Cotton** is due to the absorption by the TOC **1**.

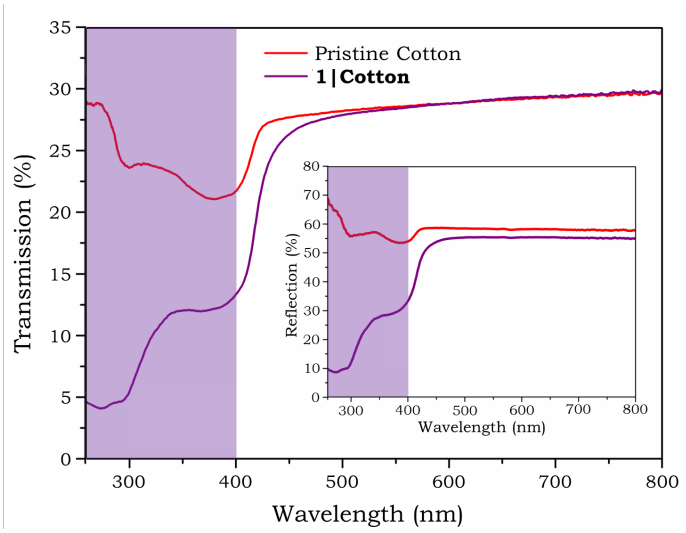

Figure 3.30. UV-Vis transmission and (inset) diffuse reflectance spectra of **1|Cotton** and pristine cotton fabric.[203]

The coating technology using *in situ* self-assembly can be readily extended to other flexible substrates, such as filter paper (Whatman™, area density of 87.3 ± 1.3 g m^{-2}, cut into swatches of 2 cm by 2 cm in size, dried in an oven at 80 °C before use). The experimental conditions were optimized in order to obtain the highest WCA values. It was found that 0.1 mL of 1.25 mg mL^{-1} solution of **1** with evaporation in air at room temperature gave the best performance for this filter paper substrate, which is denoted as **1|Paper**. In this case, the TOC **1** self-assembled into MPs of 0.5 μm average diameter (4.2 : 1 atomic ratio of Ti : Mn)

using a similar '*drop-and-dry*' procedure and 0.1 mL aliquots of 1.25 mg mL^{-1} solution of **1** (Figure 3.31a). As expected, the MP-coating transforms the filter paper surface from hydrophilic to hydrophobic, which exhibits a WCA of 134.3 ± 3.5° (Figure 3.31b). The water droplet on **1|Paper** remains stable for at least 30 min (Figure 3.31c), and the observed hydrophobicity is retained after UV irradiation (365 nm, 40 min, Figure 3.31d). Upon Au sputtering, the WCA of **1|Paper** only dropped slightly (Figure 3.31e), implying a higher contribution from the micro-structural roughness on the overall hydrophobicity compared to **1|Cotton**.

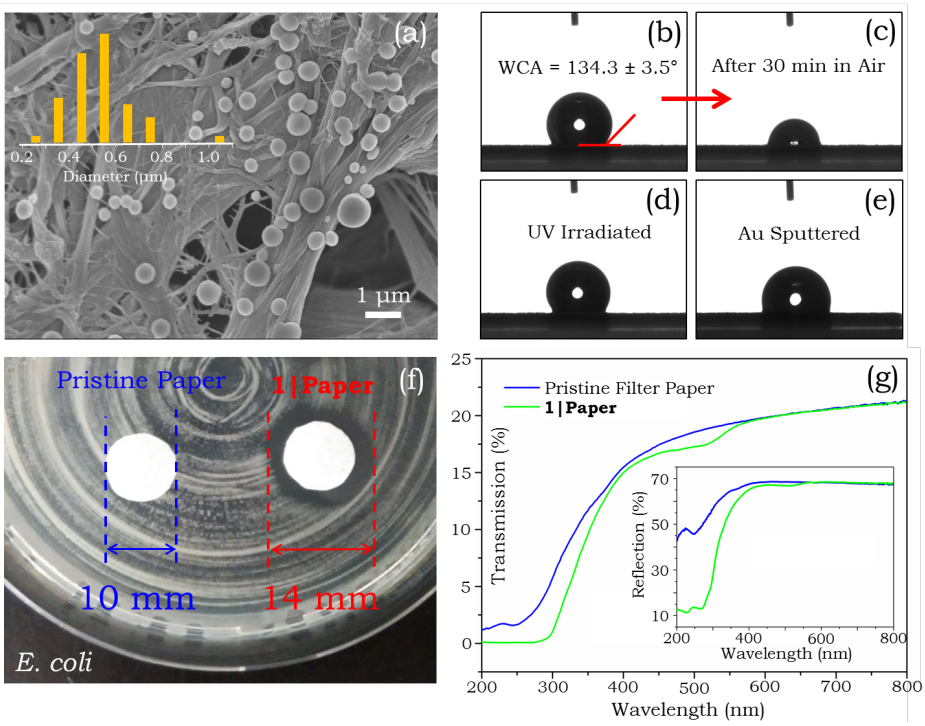

Figure 3.31. (a) FESEM image of **1|Paper**; the inset shows the size distribution of microparticles observed. A 5 μL de-ionised water droplet on **1|Paper**: (b) freshly prepared, (c) after 30 min in air, (d) pre-irradiated by 365 nm UV light, and (e) after Au sputtering. (f) The antibacterial activity of **1|Paper** against *E. coli*. (g) UV-Vis transmission and diffuse reflectance (inset) spectra of pristine filter paper and **1|Paper**.[203]

1|Paper also demonstrates antibacterial activity, but weaker than that of **1|Cotton** (Figure 3.31f and Figure 3.32), potentially because of the fact that the filter paper substrate has a much lower area density and is thinner than the

cotton fabrics. As a result, the amount of **1** present in **1|Paper** is lower than that in **1|Cotton**. Coating of filter paper with **1** also provides some enhancement in the UV-blocking capability (Figure 3.31g). The TGA profile (Figure 3.33) and FTIR-ATR spectra (Figure 3.34) of **1|Paper** were also recorded, both showing similar behaviour to that the pristine filter paper counterpart, implying the integrity of the filter paper substrate.

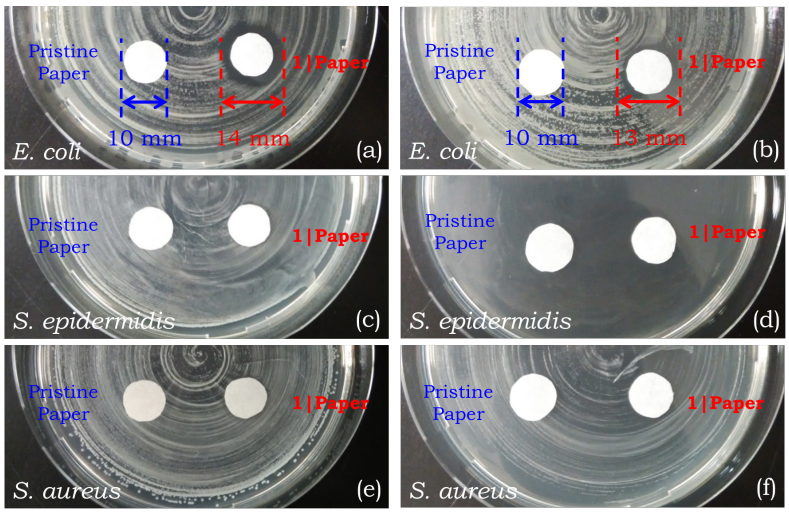

Figure 3.32. Digital photographs showing the antibacterial activity of **1|Paper** against (a) *E. coli* (already shown in Figure 3.31f), (c) *S. epidermidis* and (e) *S. aureus* at ambient light conditions (left column) and in dark [right column, (b) for *E. coli*, (d) for *S. epidermidis* and (f) for *S. aureus*].[203]

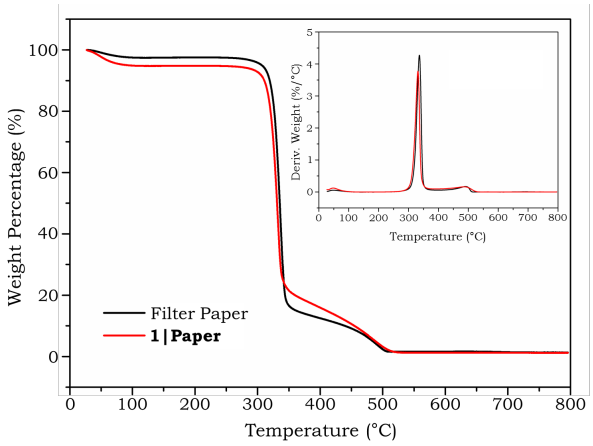

Figure 3.33. TGA profile of **1|Paper** and pristine filter paper in air flow (60 mL min^{-1}) with temperature ramping rate of 10 °C min^{-1}; inset is the plot of weight derivative (%) against temperature.[203]

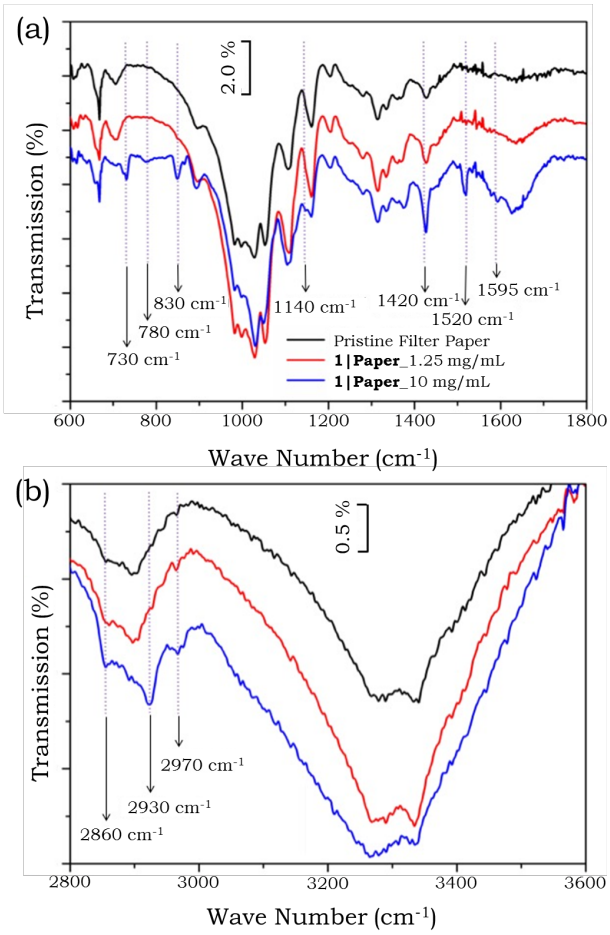

Figure 3.34. FTIR-ATR spectra of **1|Paper** and the pristine filter paper substrate: (a) the fingerprint and (b) the higher-wavenumber functional group regions.[203] '**1|Paper**_x mg/mL' denotes the coated filter paper sample using 0.1 mL solution of **1** of x mg mL^{-1} concentration.

3.4. Summary and Future Perspectives

In this chapter, the synthesis and characterisation of the novel TOC $[Ti_{18}Mn_4O_{30}(OEt)_{20}Phen_3]$ (**1**) which possesses a C_3 symmetric core structure, is discussed. Cluster **1** is the first example of a TOC with the same kind of metal dopant ions (*i.e.*, Mn^{2+}) in two distinct coordination environments. The cluster is air and water stable, and even survives aqueous electrochemical measurements. Optical spectroscopy suggests an optical band gap of *ca.* 2.90 eV for **1**. Electrochemical analysis shows two redox couples that probably arise from the

two distinct Mn^{2+} coordination environments in the cluster molecule. Sintering of **1** at 600 °C produces a black material consisting of rutile TiO_2 and α-Mn_2O_3, which exhibits a direct band gap of *ca.* 1.80 eV.

More importantly, the *in situ* self-assembly of **1** generates hollow microparticles that are firmly mounted on the underlying cotton fabrics, producing a multifunctionality in a single-step '*drop-and-dry*' operation. Without compromising the inherent properties of the cotton substrate, the reported method is able to introduce robust hydrophobicity, antibacterial activity and UV-blocking capabilities simultaneously, making it potentially useful for diverse applications, such as functional clothing, medical bandages and oil/water separation. This technology is also readily extendable, for example, to laboratory filter paper and potentially many more natural fibre materials. It is worth noting that the biosafety of **1** should be considered in the context of real life uses, as 1,10-phenanthroline is toxic, especially for aquatic life. For this reason, the described multifunctional coating technology here is a proof of concept for the potential applications of TOCs. Nonetheless, it is anticipated that such *in situ* self-assembly is not a unique feature for **1**, but instead, common for many TOCs with the proper molecular structure and peripheral groups. Morphologically, other micro- or nano-sized architectures, such as rods, tubes, cubes and flowers, could also be expected by controlling the surface chemistry. Moreover, by introducing specific functional ligands, such as the fluorescent, photo-thermal, electron-conductive ones, more functionalities might be achieved using TOCs, and consequently also on their coated textile substrates. To this end, a collection of rationally designed non-toxic TOCs (potentially also other related polyoxometalate structures) would provide a toolkit for a wide range of real-life applications beyond the ones described in this chapter.

3.5. Experimental Section

3.5.1. Synthesis of TOC 1

All chemicals were purchased from commercial sources and used as received, unless otherwise stated. Strict inert-atmospheric conditions (dry and O_2-free) were employed throughout all the synthesis and handling procedures [*i.e.*, vacuum-line and using of a N_2-filled glove box (Saffron type α)].

In a typical synthesis, titanium ethoxide [$Ti(OEt)_4$, 2.0 mL, 9.5 mmol], manganese(III) acetate dihydrate [$Mn(OAc)_3{\cdot}2H_2O$, 140 mg, 0.5 mmol], 1,10-phenanthroline (90 mg, 0.5 mmol) and anhydrous ethanol (10 mL, 170 mmol) were loaded into a Teflon-lined autoclave and heated at 150 °C for 72 hours. Gradually cooling the reaction to room temperature produced block-shaped orange-colour crystallites of compound **1**. The crystallites were filtered off at room temperature and washed with anhydrous ethanol before being dried *in vacuo* [80 mg product, 20 % isolated yield with respect to $Mn(OAc)_3{\cdot}2H_2O$ supplied]. It is worthy of note that, replacing $Mn(OAc)_3{\cdot}2H_2O$ by $Mn(OAc)_2{\cdot}4H_2O$ produced the same cluster, but in a lower yield.

Elemental analysis (%): *cald.* C 30.4, H 4.2, N 2.8; *found* (average of four measurements) C 31.1, H 4.3, N 2.7. Elemental analysis results were obtained using a Perkin-Elmer 240 Elemental Analyser.

3.5.2. X-Ray Diffraction

Single-crystal X-ray diffraction is the primary tool used in the initial characterisation of this type of cluster compound. The crystallographic data were collected on a Nonius Kappa CCD diffractometer using Mo(Kα) radiation (λ = 0.71 Å). The structure was solved and refined by full matrix least-squares on F^2 using SHELX programme.[217] All non-hydrogen atoms were refined anisotropically. The hydrogen atoms were introduced into calculated positions and refined with fixed geometry with respect to their C atoms. Details of the crystallographic data refinements of TOC **1** are provided in Table A1 in the Appendix. Powder X-ray diffraction (XRD) patterns were collected in the 2θ range of 5 – 80° using a PANalytical EMPYREAN Series 2 diffractometer with Cu Kα (1.54 Å) radiation.

3.5.3. Scanning Electron Microscopy

Field emission scanning electron microscopy (FESEM) images and energy-dispersive X-ray (EDX) spectra were recorded using a JEOL JSM-5510LV scanning electron microscope, and a JEOL JSM 6700F with an Oxford ISIS X-ray EDX microanalysis system, with 5 kV and 15 kV applied voltages for imaging and EDX studies, respectively. Au sputtering was applied on the samples to improve electrical conductivity. The same Au sputtering was also applied to change the sample surface chemistry, but retain the surface roughness of **1|Cotton** and **1|Paper**, in order to determine the sole contribution of roughness to the observed hydrophobicity.

3.5.4. Spectroscopic Analysis

FTIR spectra were obtained using a PerkinElmer Universal ATR spectrometer. UV-Vis absorbance spectra were obtained using VARIAN-50 Bio UV-Vis spectrophotometer. UV-Vis transmission and diffuse reflectance spectra were recorded using a Shimadzu UV 3600 UV-Vis-NIR spectrophotometer, with air and $BaSO_4$ powder being used as references for transmission and diffuse reflectance measurements, respectively. The XPS data was obtained using a Kratos AXIS Ultra DLD spectrometer, equipped with a monochromatized Al Kα X-ray source of 1486.71 eV photons with a constant dwell time of 100 ms, a pass energy of 40 eV, and a photoelectron take-off angle (α) of 90° with respect to the sample surface.

3.5.5. Electrochemical Analysis

The electrodes for electrochemical measurement were made by drop-casting fresh solutions of **1** onto clean FTO-coated glass with an exposed area of 1.0 cm^2 (denoted as **1**|FTO). The solution was prepared by dissolving 10 mg of **1** in 4.0 mL of a toluene and methanol mixture (3 : 2 in volume). 90 μL of this solution was drop-cast onto a plate FTO at 80 °C using a pipette in air and dried under the same condition. The as-prepared electrode was then immersed into an electrochemical cell containing an aqueous solution of sodium sulphate as the electrolyte ($NaSO_4$, 0.1 M, pH 6.54, purged with N_2 for 1 hour before use). The electrochemical experiments were performed using a conventional three-electrode

system with the as-prepared working electrode, a Pt foil counter electrode and an Ag/AgCl/saturated KCl reference electrode at room temperature.

3.5.6. Miscellaneous Tests and Measurements

Thermal decomposition behaviour was characterised in air using TGA Q500, TA Instruments. Magnetic data was collected by Dr. Floriana Tuna from the University of Manchester. Pascal's constants were taken into account to estimate the diamagnetic corrections, which were subtracted from the experimental susceptibility to give the molar susceptibility (χ_{mol}).[218] Water contact angles were measured using a contact angle goniometer (Ramé-Hart Instruments Co.) under ambient conditions. A water droplet of 5 μL was used for each measurement. For each sample, measurements were taken at eight different locations and the average WCA values are reported. The tensile strength was measured using an Instron 5569 Table Universal testing machine using samples of 2 cm by 10 cm in size. UV irradiation on **1|Cotton** was carried out using a hand-held UV lamp for 40 min at 365 nm. To test the stability of the coated samples further, a stronger light source (Hamamatsu, Lightningcure™, 150 W type LC8-03 with a xenon Lamp L8253) with a known wavelength spectrum spanning 300 nm to 700 nm was employed. The **1|Cotton** sample was placed 15 cm away from the light outlet and irradiated for 40 min. WCA of 145.3 ± 1.8° was achieved for the irradiated **1|Cotton** sample, showing the excellent UV-Vis light stability of the coating. A simulated laundry test was applied by tying a **1|Cotton** sample to a magnetic stirrer and immersing it in 100 mL DI water before starting the stirring at 200 revolutions-per-minute for 1 hour at room temperature. Various washing environments, such as using detergent (DYNAMO® Power Gel), higher water temperature (40 °C, 60 °C and 80 °C), prolonged washing duration (4 hours, overnight), repeated washing cycles, and additional mechanical wear (by adding six aluminium blocks with 96.5 mg average weight into the water) were also undertaken. The mechanical abrasion test was carried out by fixing the **1|Cotton** sample onto a glass slide and loaded with 75 g weight before pulling it over sand paper for 100 cm. The tape adhesion-and-peeling treatment was applied by pressing normal laboratory tape on the sample before peeling it off with care.

The oil/water separation experiments were conducted in a fume-hood under ambient conditions. In a typical test, DI water was coloured by rhodamine B (10 μM) for better visual contrast. A square sample of **1|Cotton** (10 cm × 10 cm) was prepared and folded into a cone. A water/*n*-hexane mixture (30 mL + 30 mL) was poured into the cone housed in a funnel. A similar filtration set-up and procedure were also used for water/toluene and water/dichloromethane separation.

The antibacterial tests were performed by Dr. Dicky Pranantyo from the National University of Singapore. *Escherichia coli* (*E. coli*, ATCC 25922), *Staphylococcus aureus* (*S. aureus*, ATCC 25923) and *Staphylococcus epidermidis* (*S. epidermidis*, ATCC 12228) were purchased from American Type Culture Collection (Manassas, VA). Tryptic soy broth, nutrient broth, and agar were purchased from Sigma-Aldrich (St. Louis, MO). The cotton samples (*i.e.*, **1|Cotton** and pristine cotton) were cut into round shapes (diameter 10 mm). *E. coli* and *S. aureus* were cultured in tryptic soy broth, while *S. epidermidis* was cultured in nutrient broth at 37 °C to a mid-log phase. The bacteria were washed and diluted to 10^7 colony forming unit (CFU) mL^{-1} in phosphate-buffered saline (PBS). In a petri dish (94 mm in diameter), 100 μL of *E. coli* or *S. aureus* suspension was spread onto tryptic soy agar, while *S. epidermidis* suspension was spread onto nutrient agar using a Digralasky spreader. **1|Cotton** and pristine cotton samples were placed onto the bacterial-inoculated agar plates and pressed gently. The plates were incubated in the presence of indoor ambient light or dark conditions at 37 °C. The growing bacterial colony was observed, and inhibition zones around the samples were measured. Antibacterial test on **1|Paper** and pristine filter paper samples was also carried out using similar procedures.

CHAPTER 4.

TOCs as Host Scaffolds for Lanthanide Ions

4.1. Introduction

TOCs benefit from their atomically well-defined structural features and can therefore act as host scaffolds for the systematic study of physical and chemical properties of the Ti_xO_y fragments. For example, Zhang *et al.*[219] reported a novel family of water-soluble TOCs with an isostructural hexagonal prismatic $\{Ti_{12}O_{18}\}$ core structure. The structure has the ability to host univalent cationic guests like K^+, Rb^+, Cs^+, and H_3O^+. Guest exchange of Cs^+ has been investigated using ^{133}Cs NMR, showing that the flexible pore of the host permits passage of a comparatively large cation, giving an equilibrium consistent of *ca.* 13 for displacement of Rb^+ by Cs^+ (Figure 4.1). Very recently, He *et al.*[220] have constructed a tetrahedral $\{Ti_4L_6\}$ cage with calixarene-like coordination-active vertices, which exhibits high solubility and stability in H_2O and DMF/H_2O solutions, affording interesting stepwise assembly with other metal ions. Through trapping of different amounts of Co^{2+} or Ln^{3+} ions, the $\{Ti_4L_6\}$ tetrahedra can be organized into architectures of various dimensions, including a $\{Ti_4L_6Co_3\}$ cage, a $\{Ti_4L_6Ln_2\}$ cage, a $\{Ti_4L_6Ln_2\}$ chain, and a 3-D $\{Ti_4L_6Ln\}$ framework. More remarkably, the calixarene-like oxygen vertices of the $\{Ti_4L_6\}$ cage can also be used for the recognition of C_3-symmetric dye molecules through N-H···O hydrogen bonding.

Figure 4.1. Schematic illustration of guest exchange in the $\{Ti_{12}O_{18}\}$ host.[219]

In this chapter, a group of isostructural lanthanide-containing TOCs of general formula $[LnTi_6O_3(O^iPr)_9(salicylate)_6]$ (**2-Ln**, Ln = La, Ce, Pr, Nd, Sm, Eu, Gd, Tb, Dy, Ho and Er) has been synthesized and characterised. These cages provide an almost ideal platform for the systematic investigation of the influence of the

central paramagnetic Ln^{3+} ions on the NMR spectroscopic behaviour of the ^{1}H and ^{13}C nuclei in the periphery ligands. Compared to conventional Ln^{3+}-complexes in which the ligands are directly bonded to the ions, the peripheral ligands in **2-Ln** are separated from the paramagnetic lanthanide centres by oxo-Ti^{4+} linkages, and therefore experience a weaker paramagnetic influence. As a result, all the ^{1}H and ^{13}C NMR signals can be observed and unambiguously assigned. Further analysis of the fully assigned resonance signals suggests that the *pseudo-contact* contribution dominates the ^{1}H NMR shifts, whereas both *pseudo-contact* and *Fermi-contact* contributions affect the ^{13}C shifts, although the majority of the resonance environments are at least four bonds distant from the central Ln^{3+} ion.

On a separate note, the **2-Ln** series can also act as an excellent model for studying the photophysical interplay between the coordinated ligands, Ln^{3+} dopants and Ti^{4+} ions in Ln-TOCs, as all the cluster compounds are isostructural and the series runs extensively from La^{3+} all the way to Er^{3+} (except for Pm^{3+}). Both visible (for **2-Pr**, **2-Sm**, **2-Eu**, **2-Ho** and **2-Er**) and NIR (for **2-Nd** and **2-Er**) Ln^{3+}-centred photoluminescence can be sensitised in solution, and most importantly, their excitation bands all extend well into the visible region up to 475 nm. With the assistance of steady-state and time-resolved photoluminescence spectroscopy, an energy transfer mechanism involving the salicylate-to-Ti^{4+} charge-transfer state is proposed to account for the largely red-shifted excitation wavelengths of the **2-Ln** clusters.

4.2. Materials Characterisation Results

The *d-f* heterometallic clusters **2-Ln** were prepared by a solvothermal reaction of $Ti(O^{i}Pr)_4$, $LnCl_3{\cdot}xH_2O$ (anhydrous or hydrate forms) and salicylic acid in a 33.6 : 1 : 5 molar ratio. The reaction mixture was heated at 150 ºC for 72 hours, followed by 40 ºC for 48 hours in a Teflon-lined autoclave. The yellow crystalline blocks produced were filtered off at room temperature, washed with anhydrous

isopropanol and dried *in vacuo*, before being stored in a N_2-filled glove box for further analysis.

The common molecular structure of the **2-Ln** clusters is shown in Figure 4.2. These isostructural clusters consist of a C_3-symmetric $LnTi_6O_3$ core with six tridentate salicylate ligands at the periphery (Figure 4.2a and b). All the Ti^{4+} ions are six-coordinated by one salicylate hydroxyl oxygen, two salicylate carboxylate oxygens (from different salicylate ligands), one μ_3-oxo bridge, one μ_2-O^{i}Pr and another terminal O^{i}Pr group, while the Ln^{3+} ion is nine-coordinate, being bonded to three μ_3-oxo bridges and six carboxylate oxygens (one from each salicylate ligand). The Ln-O bond lengths decrease only slightly across the series, following the general trend of lanthanide contraction (Figure 4.3), *i.e.*, there is a reduction in the bond lengths by 0.16 Å [2.41(1) Å for La-O *vs.* 2.25(4) Å for Er-O], almost identical to the reduction in the ionic size of the respective Ln^{3+} ions (1.17 Å for La^{3+} *vs.* 1.03 Å for Er^{3+}). The diamagnetic Ti^{4+} ions form a rigid shell encapsulating the central Ln^{3+} ion, in which TiO_6 octahedra and the LnO_9 distorted tricapped trigonal prism assemble into an edge-sharing polyhedral arrangement (Figure 4.2c).

The isolated yields for these **2-Ln** compounds are shown in Figure 4.4. The yield for **2-Nd**, **2-Sm** and **2-Eu** are significantly higher than the others. This feature can be explained by the unique structure of **2-Ln**. Due to the rigidity of the Ti-O bond, the shell constructed by the Ti^{4+}-oxo moieties only possess a void space with limited flexibility. Such a void space might be just right for the moderate-sized Nd^{3+}, Sm^{3+} and Eu^{3+} ions, but not for the larger (La^{3+} and Ce^{3+}) and smaller (Gd^{3+}, Tb^{3+}, Dy^{3+}, Ho^{3+} and Er^{3+}) ones. This may also explain the failure to synthesise other analogous **2-Ln** clusters beyond Er, due to the smaller size of the related Ln^{3+} ions.

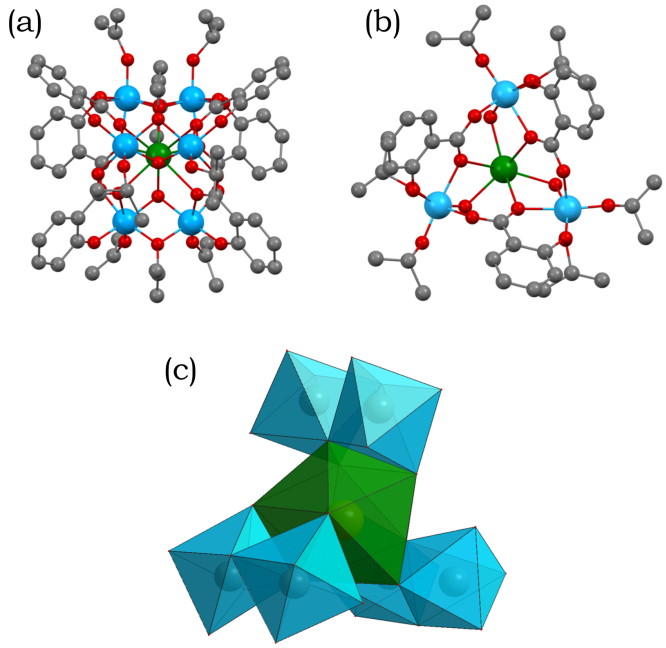

Figure 4.2. Ball-stick representation of the molecular structure of the **2-Ln** clusters, viewed in the direction (a) perpendicular to and (b) along the C_3 symmetry axis; (c) the polyhedral representation of the cluster core containing six Ti-octahedra and one Ln-tricapped trigonal prism. Colour code for atoms: Ti = cyan, Ln = green, O = red, C = grey. Hydrogen atoms are omitted for clarity.[221]

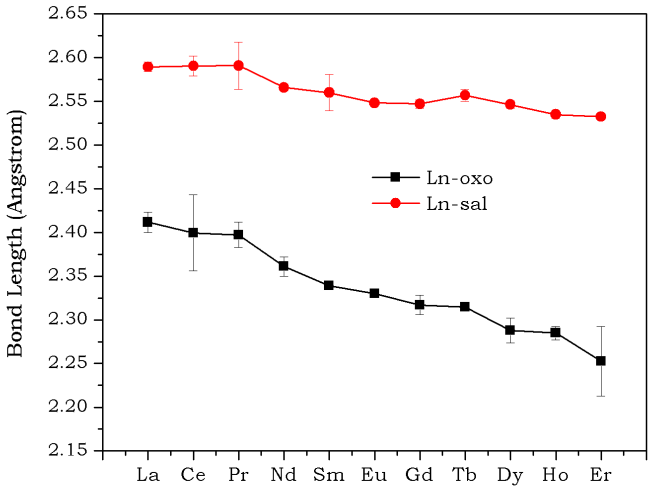

Figure 4.3. Average Ln-O bond lengths in the **2-Ln** cluster. The Ln-oxo bond lengths are shorter than that of the Ln-sal, although both follow the trend of lanthanide contraction.

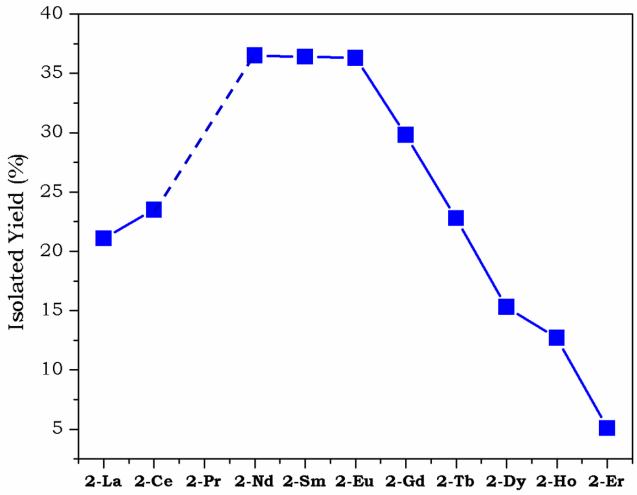

Figure 4.4. The isolated synthetic yield of **2-Ln**, with respect to the Ln^{3+} salt supplied. The data shown are the average of three repeated attempts. The data for **2-Pr** (dashed line) is not available because the Pr^{3+} precursor used is $PrCl_3 \cdot xH_2O$ with unknown molecular weight.

FTIR-ATR spectroscopic measurements on **2-Ln** and pure salicylic acid were performed on powder samples. For salicylic acid, the bending in-plane CH modes δ (C-H) vibrations are at 1031(s), 1090(m) and 1155(s) cm^{-1}. The bands in the 1160 – 1400 cm^{-1} region, namely at 1188(s), 1208(s), 1235(s), 1246(s), 1292(s), 1324(m) and 1384(m) cm^{-1}, could be assigned to the bending and/or stretching vibrations of the phenolic OH groups, with the stretching vibration of the carboxylic group being at 1235 and 1246 cm^{-1}, as well as the stretching vibration at 1324 cm^{-1} (Figure 4.5). The stretching vibrations of the benzene ring correspond to the bands at 1442(s), 1464(s), 1482(s), 1579(m) and 1610(s) cm^{-1}. The strong stretching vibration of the carbonyl group at 1654(s) cm^{-1} exists only in the protonated form of salicylic acid. All the **2-Ln** compounds have very similar FTIR-ATR spectra. The disappearance of the bands at 1188(s), 1208(s), 1292(s) and 1654(s) cm^{-1} (all corresponding to the carboxylic and phenolic groups of salicylic acid) results from the coordination of both groups to the metal centres in **2-Ln**. Ring frequencies are also affected by the new environment, indicating that the formation of the cluster structure of **2-Ln** changes the electronic distribution and symmetry of the aromatic ring. In the higher-wavenumber functional group

region, the broad bands in the 2450 – 3350 cm^{-1} range for salicylic acid are assigned to the O-H vibration of the carboxylic group and they disappear in the spectra of **2-Ln** as a result of deprotonation. A few new peaks (2850 – 3000 cm^{-1}) emerge for **2-Ln**, which can all be assigned to the C-H bonds in the isopropyl groups.

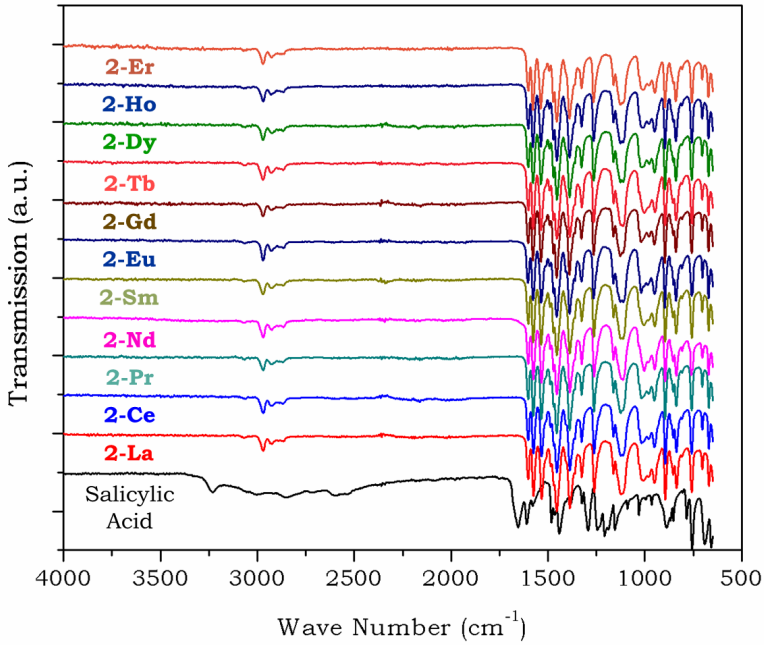

Figure 4.5. Solid-state FTIR-ATR spectra of pristine salicylic acid and the **2-Ln** compounds.

The phase purity of all the **2-Ln** compounds was initially confirmed by the satisfactory agreement between their experimental and simulated (derived from the single-crystal X-ray diffraction data) powder XRD patterns (Figure 4.6). It is worthy of note that **2-Eu** exhibits a different space group from the other **2-Ln** members. This is potentially because of presence of graphitic π-π interactions between salicylate groups in this case. The chemical purity of **2-Ln** was further verified by the elemental (C and H) analysis, which showed excellent matching between the calculated and experimentally determined C and H element content (Table 4.1).

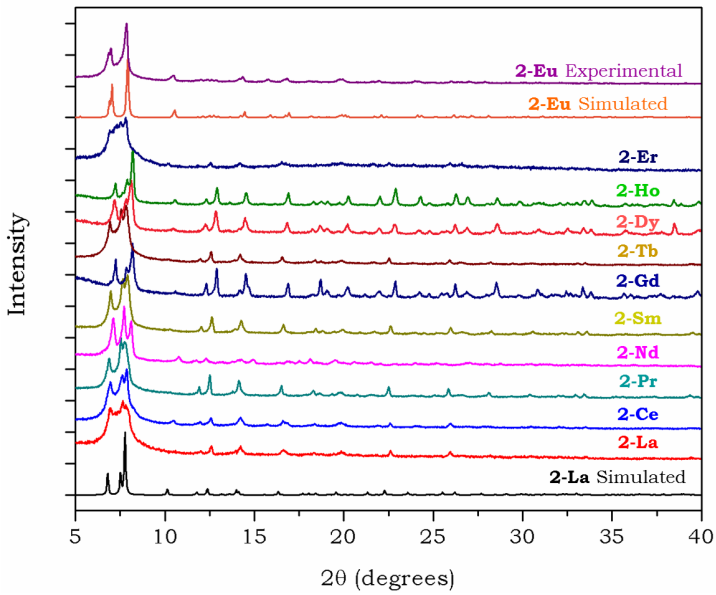

Figure 4.6. Comparison of simulated and experimental pXRD patterns of the **2-Ln** compounds. The simulated spectrum of **2-La** is shown, but that of other **2-Ln** clusters are all similar since they are isostructural. The simulated and experimental pXRD data for **2-Eu** are shown separately, as this has a different space group from the other **2-Ln** members.

Table 4.1. Comparison of the calculated and experimentally-determined C and H content of the **2-Ln** compounds

	Cald.		Found	
	C	H	C	H
2-La	45.4	4.8	45.0	4.8
2-Ce	45.4	4.8	44.9	4.7
2-Pr	45.4	4.8	45.2	4.8
2-Nd	45.3	4.8	44.5	4.8
2-Sm	45.2	4.8	44.8	4.7
2-Eu	45.2	4.8	44.9	4.7
2-Gd	45.0	4.8	44.7	4.7
2-Tb	45.0	4.8	44.4	4.7
2-Dy	44.9	4.8	44.6	4.8
2-Ho	44.8	4.7	44.7	4.8
2-Er	44.8	4.7	44.6	4.7

Figure 4.7 depicts the UV-Vis diffuse reflectance spectra of the **2-Ln** family. The samples were prepared by grinding high-purity crystalline blocks of **2-Ln** into fine powders in a N_2-filled glove box and sealing them between quartz windows before transferring to the spectrometer. This was done in order to ensure that there was no possibility of surface aerial hydrolysis on the crystallites, which would give Ln-doped TiO_2 materials. All of the **2-Ln** compounds have an absorption edge in the 400 – 475 nm region, corresponding to a band gap of *ca.* 2.70 eV using the direct extrapolation method. These values agree with the bright yellow colour of **2-Ln**. The sharp peaks observed at higher energy in the solid-state samples could be spin-orbit coupling transitions of the Ln^{3+} ions.

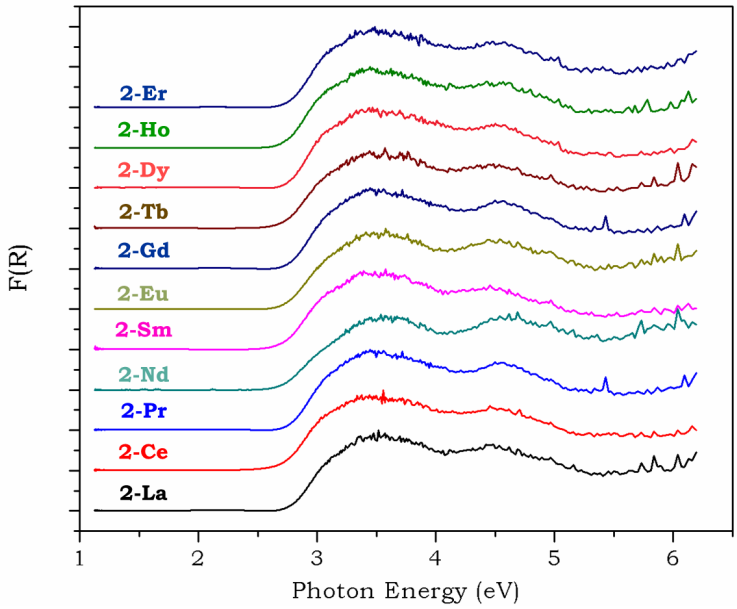

Figure 4.7. Kubelka-Munk function F(R) for the fresh crystallites of **2-Ln**, obtained by UV-Vis diffuse reflectance spectroscopy.

The solution phase absorbance spectra of **2-Ln** were also recorded and the combined results are shown in Figure 4.8. All the spectra are very similar, with a broad absorption band centred at *ca.* 350 nm and an absorption edge in the 250 – 300 nm range. It is worthy to note that the extinction coefficients of the 350 nm band for the **2-Ln** compounds differ from each other (Figure 4.8), in the range of

11565 – 81932 M^{-1} cm^{-1}, consistent with charge-transfer transitions (*e.g.*, ligand-to-metal). However, there is no observed correlation between Z_{eff} of the Ln^{3+} ions and the molar extinction coefficients.

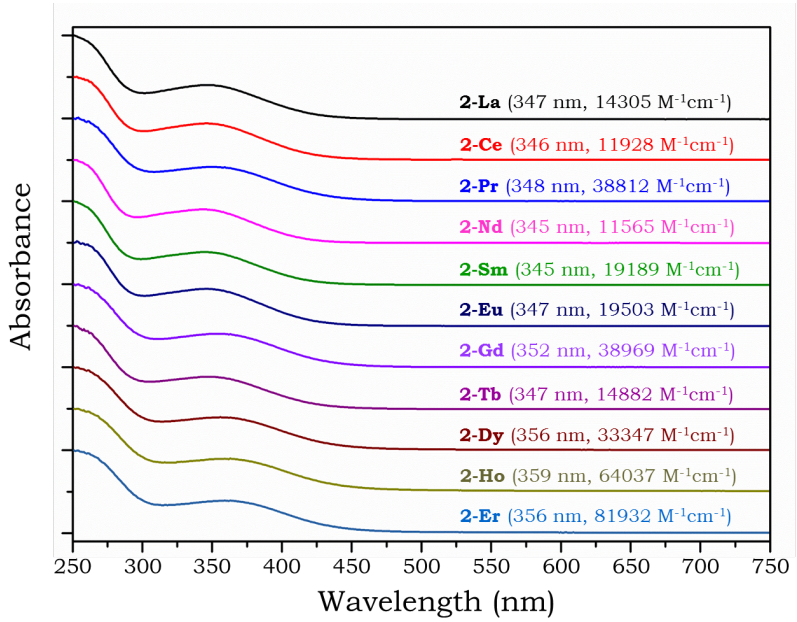

Figure 4.8. UV-Vis absorbance spectra of **2-Ln** in anhydrous chloroform. The peak positions and extinction coefficients (shown in bracket in the figure) for the *ca.* 350 nm band differ, depending on the Ln^{3+} ion.[221]

The thermal stabilities of **2-Ln** were investigated using TGA analysis in air, and they all demonstrate similar thermal decomposition behaviours. As an example, Figure 4.9a shows the TGA profile of **2-La**. It can be clearly seen that the decomposition takes place in different stages. The first occurs in the temperature range below 215 °C, corresponding to a weight loss of *ca.* 4 %. This could be ascribed to the adsorbed moisture on the crystalline blocks of **2-La**. Further weight losses occur in the temperature range of 215 – 275 °C, 275 – 405 °C and 405 – 480 °C, corresponding to weight loss of *ca.* 18 %, 20 % and 18 %, respectively. At around 710 °C, there is another minor weight loss of *ca.* 3 %, which is expected to be due to the evacuation of trapped carbonaceous residual species.[222] The final weight percentage of 36.6 % agrees reasonably well with the expected value of 35.2 %, assuming that a hybrid material of TiO_2 and La_2O_3 is

obtained. However, the hybrid material obtained is amorphous in nature (confirmed by pXRD), potentially because of the presence of a large amount of La^{3+} ions that could prevent the TiO_2 nucleation process during sintering. Similar TGA profiles have also been obtained for the other **2-Ln** members (Figure 4.9b), and the physical appearance of the final products after thermal treatment is dependent on the Ln^{3+} ions (Figure 4.9c).

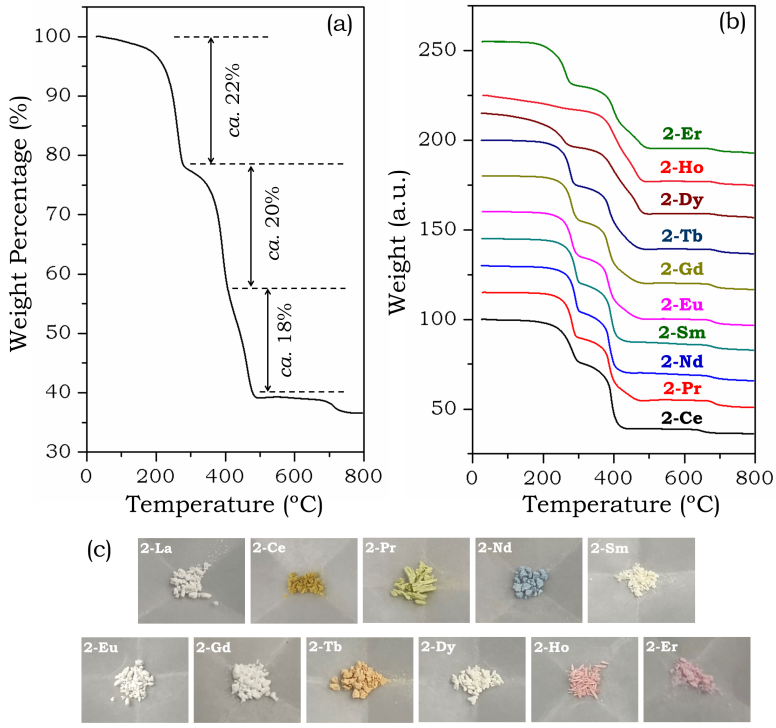

Figure 4.9. TGA profile of **2-Ln** in air flow (60 mL min^{-1}) with temperature ramping rate of 10 °C min^{-1}: (a) is for **2-La** and (b) shows the combined result for the rest of the **2-Ln** compounds. Panel (c) depicts the physical appearance of the **2-Ln** crystalline blocks after the TGA measurement.

4.3. Paramagnetic NMR Analysis of 2-Ln

4.3.1. Motivation

Nuclear magnetic resonance (NMR) spectroscopy has been a well-established technique for structural characterisation in chemistry and related disciplines for decades.[223] In a typical measurement, the NMR sample is placed in a strong

magnetic field. The signal is then produced by exciting nuclei with radio waves into resonance, and detected by sensitive radio receivers. The local magnetic field that each atom '*feels*' is highly dependent on the electron distribution in the compound. As a result, the resulting NMR signal is diagnostic of the electron density and (overall) distinctive to individual compounds. NMR has been generally seen as a reliable method to identify and investigate the structural features of various chemical species.

Given that it is closely related to the local magnetic field around each atom, the NMR behaviour can be affected greatly by the paramagnetic centres (if any) in the compound of interest, and such paramagnetic NMR studies in both solution and solid-state have drawn extensive research interest worldwide.[224-237] In this context, the paramagnetic centres refer to atoms/ions that possess at least one unpaired electron and impose a hyperfine interaction with the NMR nucleus. This interaction can reveal important information about the paramagnetic compound, such as bonding and their spatial arrangement, delocalisation of unpaired electron(s), etc.[238-241,263] Unfortunately, the paramagnetism also leads to difficulties in the acquisition and interpretation of the NMR data, mainly because of (i) the inefficient excitation of the nuclei, due to the large resonance frequency shift, and (ii) the rapid coherences decays after excitation. Therefore, understanding paramagnetic NMR data is not an easy task, which usually requires special experimental techniques and established theoretical models.[242]

Among others, lanthanides represent a unique family of elements with similar chemical properties, as well as interesting paramagnetic and photophysical characteristics.[243] They are usually (but not always) trivalent, with their unpaired electrons being in the contracted 4*f* orbital. Apart from La^{3+} ($4f^0$) and Lu^{3+} ($4f^{14}$), all other trivalent lanthanide ions (*i.e.*, Ce^{3+}, Pr^{3+}, Nd^{3+}, Pm^{3+}, Sm^{3+}, Eu^{3+}, Gd^{3+}, Tb^{3+}, Dy^{3+}, Ho^{3+}, Er^{3+}, Tm^{3+}, Yb^{3+}) are paramagnetic ($4f^1$ – $4f^{13}$) at room temperature. Therefore, they are mostly investigated as a group, except for Pm^{3+} that is radioactive and also extremely rare in Earth's crust. Addition of lanthanide complexes to organic analytes could induce a large change of chemical shift in their NMR spectra without causing significant signal broadening. For this reason, paramagnetic lanthanide-containing complexes were firstly

employed as NMR shift reagents to reduce the spectral complexity of organic compounds that have a large number of resonances in a similar spectral range.[244] Later, as high-field NMR spectrometers became routinely available, these features of lanthanide-containing shift reagents led to new roles in the analysis of enantiomers and in the assignment of absolute configurations,[245,246] as well as in the determination of the conformational properties of large flexible molecules.[247-251] Other applications have also emerged in the past decades, including probing the component distribution in mixed-monolayer-protected nanoparticles,[252] determining the dynamics of lanthanide-containing complexes in solution,[253,254] and also acting as contrast agents for magnetic resonance imaging (MRI).[255,256]

The most popular theoretical basis of lanthanide-induced NMR shift, developed by Bleaney, can be dated back to the 1970s.[257] According to the theory, the magnetic susceptibility anisotropy of Ln^{3+} ions accounts for the *pseudo-contact* shift (δ_{PC}, sometimes termed *dipolar* shift) in the NMR spectra of lanthanide complexes. Despite the reports in which Bleaney's theory agrees with experimental observation, the theory contains several assumptions that can limit its general applicability.[242] These assumptions state that (i) the ligand field splitting is much lower than kT (k is Boltzmann constant, and T is temperature in Kelvin) at room temperature, (ii) only part of the ligand field parameters is included, (iii) magnetic effects of the unpaired lanthanide electrons are approximated to a point dipole on the lanthanide ion itself, and (iv) the spin-orbit coupling can be adequately described by the Russell-Saunders coupling scheme.[242] Although these assumptions might be reasonable in the specific system that Bleaney investigated,[257] they have been questioned in several other reports and new theories/principles have been proposed.[258-262] For example, calculations from Suturina *et al.*[262] showed the assumption that ligand field splitting is much lower than the thermal energy did not hold for their lanthanide complexes. Mironov *et al.*[260] demonstrated the limitation of Bleaney's theory in dealing with the temperature-dependent terms of magnetic susceptibility. Charnock *et al.*[261] challenged the validity of the point dipole approximation, and proposed a new approach based on the unpaired electron probability density model. Funk *et al.*[258] also demonstrated the key limitations of Bleaney theory that

related to (i) comparability of ligand field splitting with spin-orbit coupling, (ii) variation in the position of the principal magnetic axis between lanthanide complexes, and (iii) the importance of multipolar terms in describing lanthanide ligand field interactions. Evaluating how well Bleaney's theory works for real systems is, however, not straightforward, because many of the parameters involved are difficult to determine by experiments and the number of systems with fully assigned paramagnetic NMR signals is limited.[239,242,263,264]

There is another effect that contributes to the overall paramagnetic NMR shift, namely *Fermi-contact* shift (δ_{FC}, or often simply known as *contact* shift). Differing from the *pseudo-contact* shift, the *Fermi-contact* shift results from the delocalisation of the unpaired electrons of the Ln^{3+} ions onto the NMR nucleus of interest and is transmitted through chemical bonds. It therefore occurs in a very similar way to J-coupling in normal diamagnetic NMR studies. As a result, the *Fermi-contact* shift decays rapidly with the number of intervening bonds, and is normally assumed to be negligible beyond four bonds (particularly for ^{1}H signals). One classic way of dealing with the *Fermi-contact* shift was proposed by Golding *et al.*,[265] which treated the electronic configuration of the lanthanide as a free ion, but added in a modification to account for the influence(s) of ligand bonding. Nonetheless, the observed paramagnetic NMR shifts in lanthanide coordination compounds (especially in which the ligands are in close contact with the Ln^{3+} ions) usually consist of both the *pseudo-contact* and the *Fermi-contact* contributions, which makes their separation the prerequisite for data analysis.

In this section, the paramagnetic NMR behaviour of the isostructural Ln-TOCs $[LnTi_6O_3(O^iPr)_9(salicylate)_6]$ (**2-Ln**, Ln = La, Ce, Pr, Nd, Sm, Eu, Gd, Tb, Dy, Ho and Er) is presented. Synthesising analogous structures containing other lanthanide centres was also attempted, but with little success. As shown previously, the structure of **2-Ln** represents a rare example in which Ln^{3+} ions are present in an '*interstitial*' arrangement.[22,23] The diamagnetic Ti^{4+} (d^0) ions in this case form a rigid shell encapsulating the central Ln^{3+} ion. Topology of this kind leads to a large separation between the paramagnetic Ln^{3+} ions and the NMR nuclei (*i.e.*, ^{1}H and ^{13}C) in the peripheral ^{i}Pr and salicylate ligands. This large separation is favourable for the point-dipole approximation of the unpaired

electron density in the 4*f* orbitals of lanthanide ions, which is one of the key assumptions of the Bleaney theory. This can be justified by the fact that the *f* electrons are confined to a relatively small space due to contraction. In **2-Ln**, the nearest nucleus to the Ln^{3+} centre is about 3.5 Å away. This should be a '*safe*' distance, as the cut-off separation for first-row transition-metal ions below which the point-dipole model collapses is around 4.0 Å, and for lanthanide should be smaller due to the more contacted 4*f* orbitals.[242] In the structure of **2-Ln**, the six salicylate ligands are in equivalent positions, whereas the nine $^{i}PrO^{-}$ ligands in the clusters are in two different environments, six being terminally bonded to and three μ_2-bridging Ti^{4+} ions. Scheme 4.1 shows the numbering scheme for the salicylate ligands and the terminal- and μ_2-O^{i}Pr groups used throughout the following discussion of the NMR characteristics of these lanthanide-containing compounds.

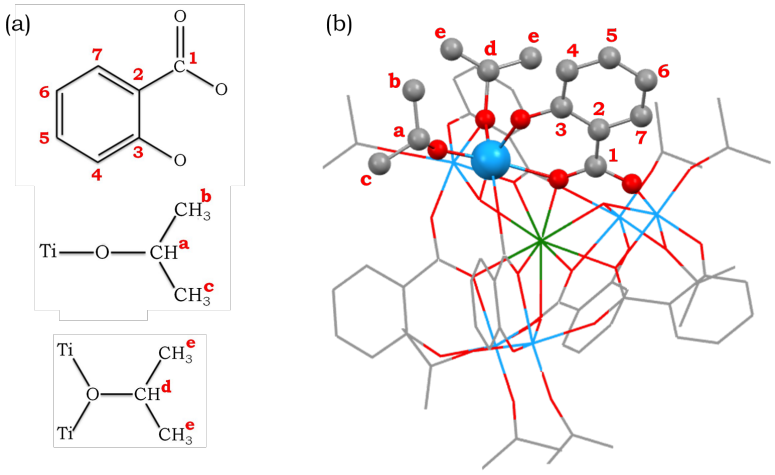

Scheme 4.1. (a) Numbering scheme of the NMR nuclei in the peripheral ligands of **2-Ln** and (b) position of the nuclei of interest in the **2-Ln** cluster structure. Colour code for atoms: Ti = cyan, Ln = green, O = red, C = grey. Hydrogen atoms are omitted for clarity.

4.3.2. Sample Preparation and Measurements

About 30 mg of **2-Ln** crystalline blocks were dissolved in 0.7 mL deuterated chloroform (*i.e.*, $CDCl_3$, Sigma Aldrich) in a N_2-filled glove box (Saffron type α).

The clear yellow solutions generated were transferred to J. Young NMR tubes, and sealed before being taken them out of the glove box for measurements.

4.3.3. ^{1}H and ^{13}C NMR of the Diamagnetic 2-La Cluster

The La^{3+} ion has no *f* electrons and is therefore diamagnetic. This makes **2-La** a good reference compound for the NMR signal assignment of the other paramagnetic **2-Ln** clusters. In total, there are nine resonances in the ^{1}H NMR spectrum (Figure 4.10) and twelve in the ^{13}C NMR spectrum (Figure 4.11) of **2-La** at room temperature, consistent with the C_3 symmetry of the solid-state structure and strongly supporting the maintenance of this structure in solution. The assignment of these NMR signals was achieved with the assistance of 2-D NMR (*i.e.*, ^{1}H-^{1}H COSY, ^{1}H-^{13}C HMQC and ^{1}H-^{13}C HMBC) and the DEPT-135 ^{13}C NMR spectral data (Figure A2 – A5 in the Appendix). An unexpected feature is the diastereotopicity of the Me-group of the terminal O^{i}Pr-ligands in the ^{1}H NMR spectrum, showing two distinct signals at δ 1.40 and 1.31 ppm for H^{b} and H^{c}, respectively (Figure 4.10). This could be due to the close proximity of the two O^{i}Pr-ligands at the periphery of the cluster structure, which inhibits their free rotation on the NMR time scale. Similar diastereotopicity was also observed for their corresponding C atoms in the terminal O^{i}Pr-ligands (*i.e.*, C^{b} and C^{c}), showing ^{13}C signals at δ 24.90 and 24.82 ppm (Figure 4.11). Of note, it was difficult to differentiate C^{4} and C^{6} (of the salicylate ligands for **2-La**) experimentally using the 2-D NMR cross-peaks, because of the closeness of their resonance frequencies. The assignments were made on the basis of the relative positions of the corresponding ^{1}H signals (H^{4} and H^{6}), which can be distinguished by their signal multiplicity (*i.e.*, H^{4} is a doublet and H^{6} is a triplet).

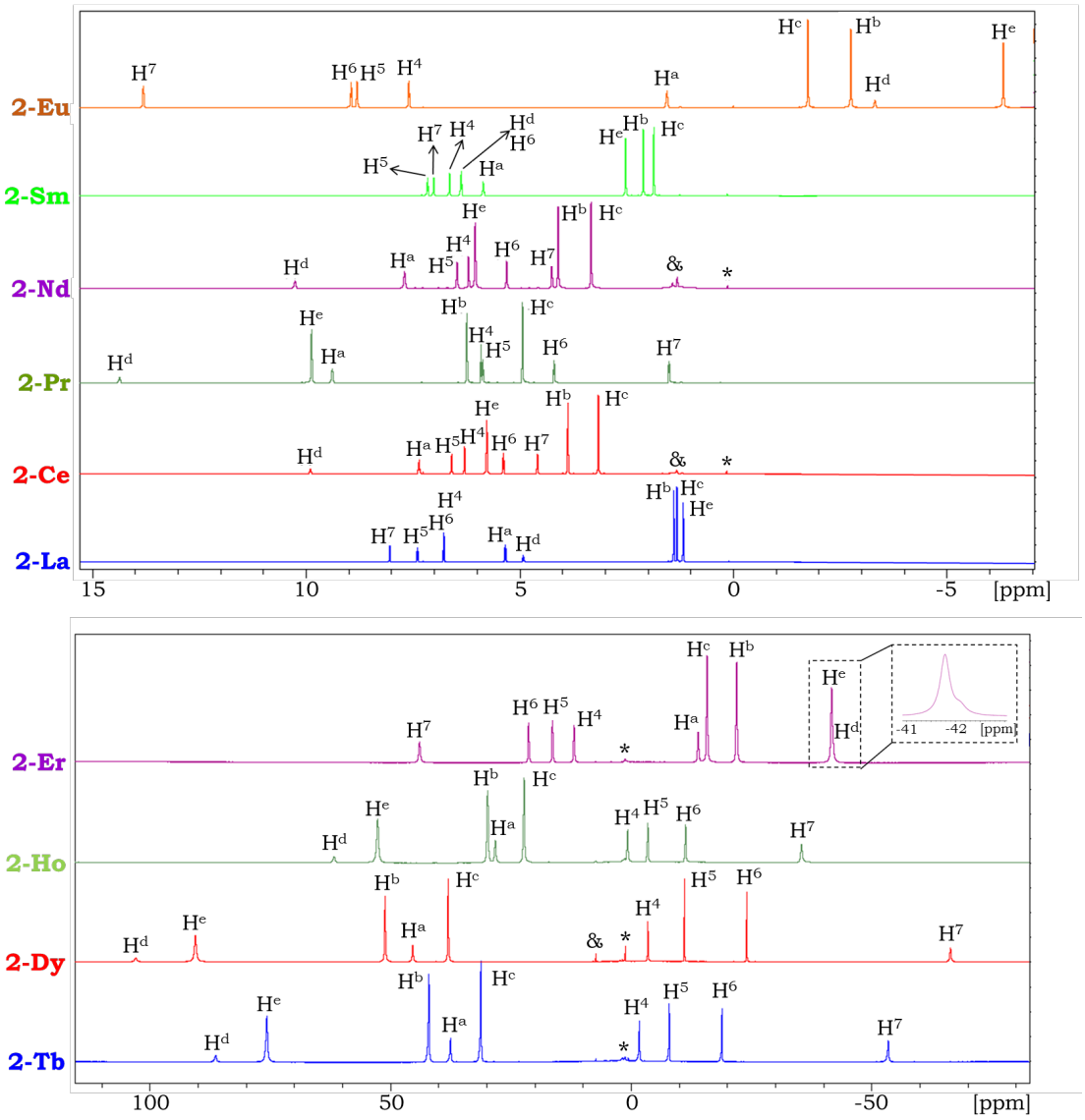

Figure 4.10. ^{1}H NMR spectra of **2-Ln** clusters in deuterated chloroform at 298 K. The top panel is for the **2-Ln** clusters containing the diamagnetic La^{3+} and the lighter Ln^{3+} ions, and the bottom panel is for that containing heavier Ln^{3+} ions. '*' denotes the signal from silicon grease and '&' denotes some unknown impurities. Inset in the bottom panel shows that the H^{e} and H^{d} signals of **2-Er** overlap with each other, resulting in a broad peak at δ -41.70 ppm and a shoulder at about δ -42.10 ppm.[266]

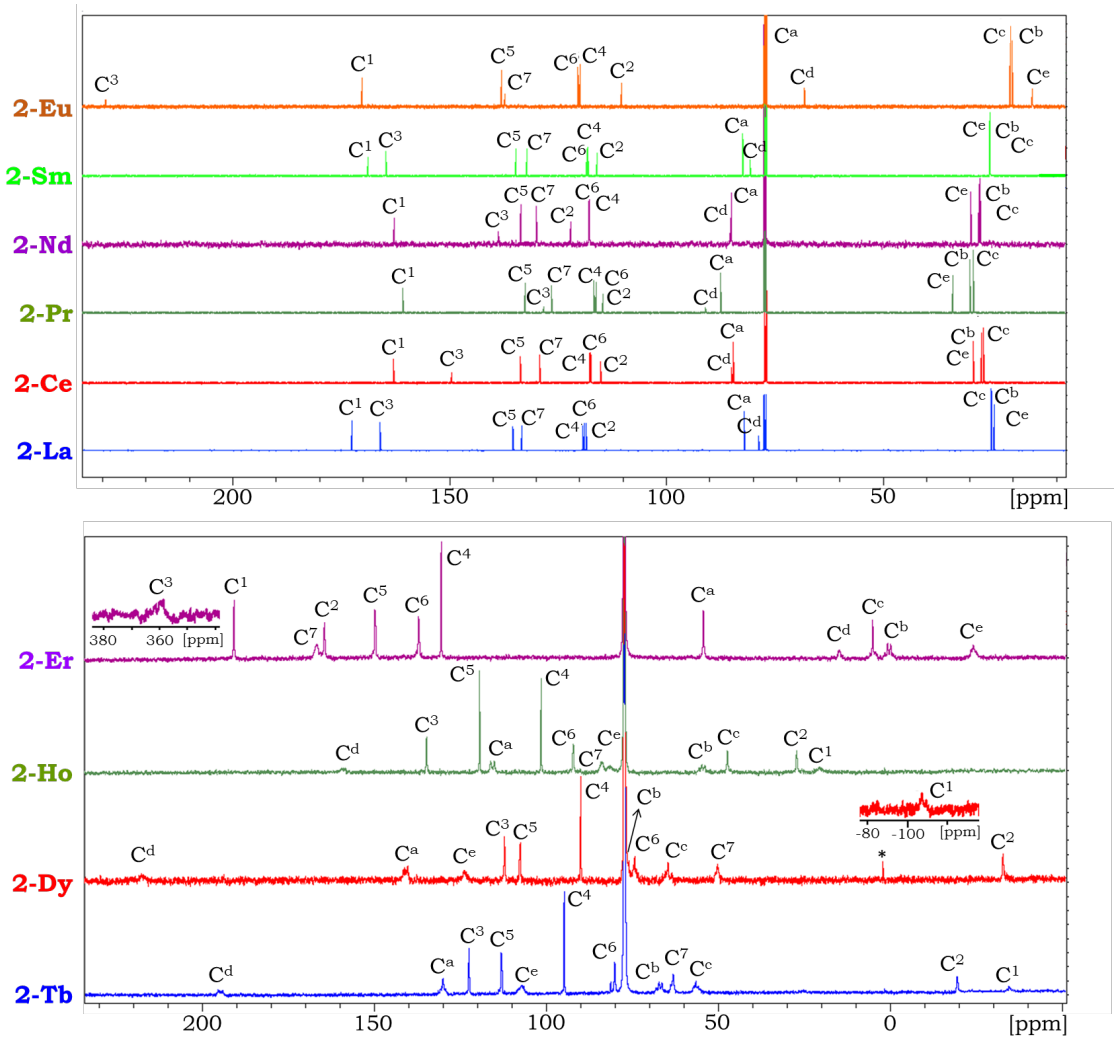

Figure 4.11. ^{13}C NMR spectra of **2-Ln** clusters containing the diamagnetic La^{3+} and lighter Ln^{3+} ions (top panel), and the heavier Ln^{3+} ions (bottom panel). The C^1 signal of **2-Dy** and the C^3 signal from **2-Er** are outside the range shown (see inset). '*' denotes the impurities from grease. The C^a signal for **2-Eu** at 76.91 ppm overlaps with the residual signals of the solvent. The diastereotopicity of C^b and C^c is present for all of the clusters.[266]

4.3.4. ^{1}H NMR of the Paramagnetic 2-Ln Clusters

In the other **2-Ln** clusters (Ln ≠ La), the paramagnetic Ln^{3+} ions induce fast NMR relaxation and shifted resonance frequencies, but without significant signal

broadening. However, Gd^{3+} is an exception, as only very broad signals were observed in the ^{1}H NMR spectrum of **2-Gd** (Figure 4.12), making it impractical for any further investigations. This observation can be ascribed to the half-full $^{4}f_{7}$ configuration of Gd^{3+}, defined by its $^{8}S_{7/2}$ ground state with a spherical electronic distribution.[267]

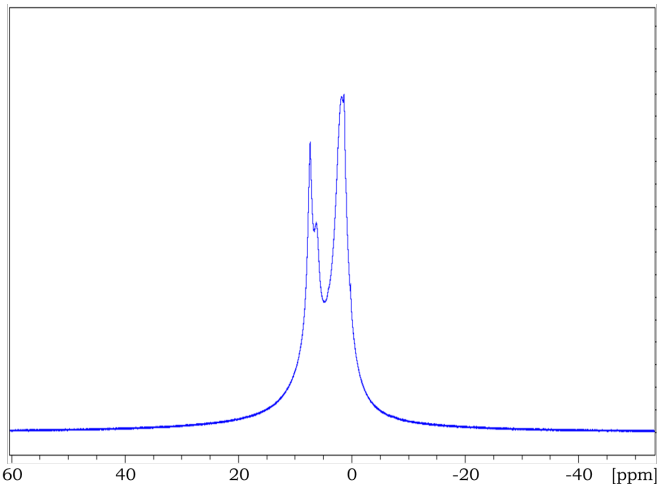

Figure 4.12. ^{1}H NMR spectrum of **2-Gd** in deuterated chloroform at 298 K.[266]

For the remaining paramagnetic Ln^{3+} ions, the signals are all sharp enough to allow for the unambiguous assignment of the ^{1}H NMR spectroscopic environments. The ^{1}H NMR resonances of the **2-Ln** clusters containing lighter paramagnetic Ln^{3+} ions (*i.e.*, Ce^{3+}, Pr^{3+}, Nd^{3+}, Sm^{3+} and Eu^{3+}) can be directly assigned with the assistance of the 2-D NMR data (Figure 4.10, Figure A6 – A25 in the Appendix, and Table 4.2). These paramagnetic spectra all show ^{1}H signals that spread out over a large spectral range, with many signals appearing outside their normal spectral range for the aryl and ^{i}Pr resonances. In addition, H^{4} and H^{6} of the aryl group of the salicylate ligands, which overlap in the case of diamagnetic **2-La**, are well separated for these paramagnetic **2-Ln** clusters (Figure 4.10).

Table 4.2. ^{1}H NMR signals (δ ppm) of **2-La** and **2-Ln** clusters containing lighter paramagnetic Ln^{3+} ions (*i.e.*, Ce^{3+}, Pr^{3+}, Nd^{3+}, Sm^{3+} and Eu^{3+}).

	2-La	**2-Ce**	**2-Pr**	**2-Nd**	**2-Sm**	**2-Eu**
H^{a}	5.33	7.35	9.34	7.68	5.82	1.54
H^{b}	1.40	3.86	6.20	4.10	2.08	-2.76
H^{c}	1.31	3.15	4.90	3.39	1.83	-1.76
H^{d}	4.91	9.88	14.32	10.24	6.35	-3.32
H^{e}	1.17	5.76	9.82	6.03	2.49	-6.33
H^{4}	6.76	6.29	5.87	6.18	6.60	7.58
H^{5}	7.39	6.59	5.84	6.45	7.12	8.80
H^{6}	6.77	5.37	4.16	5.29	6.33	8.94
H^{7}	8.03	4.58	1.47	4.24	6.97	13.80

Regarding the **2-Ln** clusters containing heavier Ln^{3+} ions (*i.e.*, Tb^{3+}, Dy^{3+}, Ho^{3+} and Er^{3+}), and therefore larger magnetic anisotropies, direct assignment of the ^{1}H resonances is difficult because of the absence of signal multiplicity in the 1-D spectra and of several important cross peaks in the 2-D spectra. The only ^{1}H signal that can be identified is H^{d} from the $O^{i}Pr$ ligand, as it gives a distinct integration value from all the other environments. Nevertheless, the three-nuclei-plot method developed by Reuben *et al.*[268] allows the assignment of the remaining ^{1}H signals. A full description of the three-nuclei-plot method can be found in the Appendix. This method works well for the ^{1}H signals of the **2-Ln** clusters containing heavier Ln^{3+} ions (*i.e.*, Tb^{3+}, Dy^{3+}, Ho^{3+} and Er^{3+}), giving predicted chemical shifts that match the experimental results closely (Table 4.3). As shown in Figure 4.10, the ^{1}H NMR spectra of the **2-Ln** clusters containing heavier Ln^{3+} ions span across an extraordinarily wide range from δ -66.37 to 102.96 ppm, with all the signals being broad and completely losing their signal multiplicity.

Table 4.3. Comparison of the calculated (using the three-nuclei-plot method) and experimentally-obtained ^{1}H NMR signals (δ ppm) for **2-Ln** clusters containing heavier Ln^{3+} ions (*i.e.*, Tb^{3+}, Dy^{3+}, Ho^{3+} and Er^{3+}).

		2-Tb	**2-Dy**	**2-Ho**	**2-Er**
H^a	Cald.	30.74	37.21	22.86	-14.28
	Expt.	37.68	45.38	28.16	-13.94
H^b	Cald.	39.17	47.18	27.56	-22.70
	Expt.	42.31	51.10	29.74	-21.96
H^c	Cald.	30.36	36.39	21.44	-16.74
	Expt.	31.38	38.00	22.20	-15.18
H^d	Expt.	86.73	102.96	61.64	-42.10
H^e	Cald.	76.20	91.12	53.19	-42.09
	Expt.	76.05	90.55	52.60	-41.70
H^4	Cald.	-2.60	-4.22	0.25	11.30
	Expt.	-1.74	-3.49	0.66	11.18
H^5	Cald.	-8.40	-11.15	-3.58	15.13
	Expt.	-7.96	-11.11	-3.51	16.29
H^6	Cald.	-19.01	-23.65	-11.13	19.90
	Expt.	-18.96	-24.04	-11.36	21.27
H^7	Cald.	-48.66	-60.13	-31.26	41.40
	Expt.	-53.67	-66.37	-35.48	43.97

With the fully assigned ^{1}H NMR signals in hand, it becomes possible to study the overall paramagnetic shifts in detail and to separate the *pseudo-contact* and *Fermi-contact* contributions using the so-called Reilley method.[269] It is worthy of note that the Reilley method is based on the assumptions including (i) the complexes are isostructural, (ii) the hyperfine coupling constant does not vary, and (iii) the crystal field parameter is the same across the whole series. The paramagnetic NMR shift $\delta_{para}^{Ln,i}$ of nucleus i in the **2-Ln** cluster can be calculated by subtraction of the observed chemical shifts of the diamagnetic **2-La** cluster from the observed values in the **2-Ln** spectrum [Eqn. 4.1]. Such a paramagnetic shift ($\delta_{para}^{Ln,i}$) should be the sum of the *Fermi-contact* shift ($\delta_{FC}^{Ln,i}$) and the *pseudo-contact* shift ($\delta_{PC}^{Ln,i}$) contributions [Eqn. 4.2].

$$\delta_{\mathrm{para}}^{\mathrm{Ln,i}} = \delta_{\mathrm{obs}}^{\mathrm{Ln,i}} - \delta_{\mathrm{dia}}^{\mathrm{La,i}} \qquad \text{[Eqn. 4.1]}$$

$$\delta_{\text{para}}^{\text{Ln,i}} = \delta_{\text{FC}}^{\text{Ln,i}} + \delta_{\text{PC}}^{\text{Ln,i}} \qquad \text{[Eqn. 4.2]}$$

As mentioned before, the *Fermi-contact* shift $\delta_{FC}^{Ln,i}$ is a consequence of delocalisation of the unpaired lanthanide electrons and can be described by [Eqn. 4.3],[270] in which μ_B is the Bohr magneton, k is the Boltzmann constant, $A_i/\hbar$ represents the hyperfine-coupling constant, γ_I is the gyromagnetic ratio of the nucleus and $\langle S_z \rangle_{Ln}$ is the time averaged value of the spin polarisation for the corresponding Ln^{3+} ion.[271] Furthermore, to a first approximation $\langle S_z \rangle_{Ln}$ only depends on the choice of the Ln^{3+} ion and remains unchanged for different nuclei in the same complex (Table 4.4),[271] whereas the hyperfine-coupling constant $A_i/\hbar$ is dependent on the nature of the NMR nucleus (*e.g.*, atomic identity, geometric position, local connectivity) and remains unaffected across the lanthanide series.[265,268,272-274]

$$\delta_{FC}^{Ln,i} = \langle S_z \rangle_{Ln} \cdot \frac{\mu_B}{3kT\gamma_I} \cdot \frac{A_i}{\hbar} 10^6 = \langle S_z \rangle_{Ln} \cdot F(i) \qquad \text{[Eqn. 4.3]}$$

$$\delta_{PC}^{Ln,i} = C_{Ln} \cdot B \cdot \frac{3cos^2\theta_i - 1}{{r_i}^3} = C_{Ln} \cdot B \cdot G(i) \qquad \text{[Eqn. 4.4]}$$

$$\delta_{para}^{Ln,i} = \langle S_z \rangle_{Ln} \cdot F(i) + C_{Ln} \cdot B \cdot G(i) \qquad \text{[Eqn. 4.5]}$$

$$\frac{\delta_{para}^{Ln,i}}{\langle S_z \rangle_{Ln}} = F(i) + \frac{C_{Ln}}{\langle S_z \rangle_{Ln}} \cdot B \cdot G(i) \qquad \text{[Eqn. 4.6]}$$

In contrast, the *pseudo-contact* shift $\delta_{PC}^{Ln,i}$ is linked to the axial and rhombic anisotropies of the magnetic susceptibility.[264] Since all the **2-Ln** cluster structures are axially symmetric, the rhombic term vanishes. The *pseudo-contact* contribution can therefore be simply described by [Eqn. 4.4], in which C_{Ln} is the Bleaney factor, that is assumed to be only dependent on the choice of the Ln^{3+} ion, B is the sum of crystal field parameters (of various orders), the geometric factor *G(i)* is a function of r_i (the length of the vector adjoining the nucleus i and the Ln^{3+} ion) and θ_i (the angle between this vector and the C_3 axis).[257,260]

Therefore, [Eqn. 4.2] can be expressed as [Eqn. 4.5], by substituting the $\delta_{FC}^{Ln,i}$ and $\delta_{PC}^{Ln,i}$ terms.

Table 4.4. The C_{Ln} and $\langle S_z \rangle_{Ln}$ values used in this thesis. The C_{Ln} values are adapted from Ref. 257. The $\langle S_z \rangle_{Ln}$ values are taken from Ref. 265, in which the right column values are calculated by considering the excited states at 300 K. They are very close to the values calculated by only considering the ground state (the column in the middle) except for Sm^{3+} and Eu^{3+}. The values shown for Eu^{3+} correspond to J = 0, 1 and 2, respectively.

	C_{Ln}	$\langle S_z \rangle_{Ln}$	
Ce^{3+}	-11.8	-0.98	-0.98
Pr^{3+}	-20.7	-2.9	-3.0
Nd^{3+}	-8.08	-4.4	-4.5
Sm^{3+}	0.94 (-1.16)	0.3	0.063
Eu^{3+}	–	–	10.7
	-4.5	1.0	
	-9.9	4.0	
Tb^{3+}	-157.5	31.9	31.8
Dy^{3+}	-181	28.6	28.5
Ho^{3+}	-71.2	22.6	22.6
Er^{3+}	58.8	15.4	15.4

These numerical values of C_{Ln} and $\langle S_z \rangle_{Ln}$ depend solely on the lanthanide ions in question, and therefore can be conveniently employed to compare the expected *pseudo-contact* or *Fermi-contact* shifts for a series of lanthanide complexes, if the coordination geometry and the crystal-field splitting factors remain unchanged. Nonetheless, it is worth noting that they cannot be used for direct comparison of the *Fermi-contact versus pseudo-contact* contributions. Moreover, these numbers have been tabulated in several studies and they all give similar values except for Sm^{3+} and Eu^{3+}, which varies significantly in different reports.[269,275,276] Such a variation could be due to the fact that, both the ground and the excited state(s) of these two ions are thermally occupied at room temperature.[242] In general, the lowest-lying excited states in free lanthanide ions are over 2000 cm^{-1} above the ground state, and hence they do not need to be taken into account. However, the lowest-lying excited state of Sm^{3+} is *ca.* 1000 cm^{-1} above the ground state, and for

Eu^{3+} the lowest-lying and the second lowest excited states are *ca.* 400 cm^{-1} and 1200 cm^{-1} above the ground state, respectively. These states can be easily populated at room temperature, and therefore have to be considered for their paramagnetic NMR analysis.

As both $\langle S_z \rangle_{Ln}$ and C_{Ln} are known (Table 4.4), a plot of $\delta_{para}^{Ln,i}/\langle S_z \rangle_{Ln}$ *vs.* $C_{Ln}/\langle S_z \rangle_{Ln}$ should yield a straight line with the slope and intercept being $B \cdot G(i)$ and $F(i)$, respectively [Eqn. 4.6]. The *Fermi-contact* and *pseudo-contact* contributions of the overall paramagnetic NMR shift can therefore be separated and calculated as $\langle S_z \rangle_{Ln} \cdot F(i)$ and $C_{Ln} \cdot B \cdot G(i)$. Due to the complication for Sm^{3+} and Eu^{3+} ions mentioned above, **2-Sm** and **2-Eu** are not included in this attempt to separate these terms. To this end, good linearity of the $\delta_{para}^{Ln,i}/\langle S_z \rangle_{Ln}$ *vs.* $C_{Ln}/\langle S_z \rangle_{Ln}$ plot was obtained when including all the other paramagnetic **2-Ln** clusters (Ln ≠ Gd, Sm or Eu), with the correlation coefficient R^2 larger than 0.92 for all the ^1H environments (Table 4.5). The calculated *Fermi-contact* (δ_{FC}) and *pseudo-contact* (δ_{PC}) contributions were also extracted (Table 4.6). As expected, the absolute value of δ_{FC} is generally much smaller than that of δ_{PC}. This is in agreement with the proposition that the *pseudo-contact* contribution dominates the overall paramagnetic ^1H NMR shifts, as all the ^1H environments are at least five bonds removed from the Ln^{3+} ions in **2-Ln**. However, it is observed that the sum of the calculated *pseudo-contact* and *Fermi-contact* terms is not perfectly equal to the observed experimental shift because $F(i)$ and $B \cdot G(i)$ were established via a linear fitting. Reilley *et al.*[269] further suggested that, the difference between calculated and experimental results can be distributed between the contact and dipolar values according to their relative absolute contributions, in order for the sum of the δ_{PC} and δ_{FC} values to add up to the experimental data.

Table 4.5. The calculated $B \cdot G(i)$ and $F(i)$ values for each proton environment using data from all the paramagnetic **2-Ln** clusters except for **2-Gd**, **2-Sm** and **2-Eu**.

	B·G(i)	F(i)	R^2	AF*
H^a	-0.2007	0.0414	0.9532	0.192
H^b	-0.2461	0.0789	0.9544	0.186
H^c	-0.1825	0.0564	0.9595	0.177
H^d	-0.4920	0.1503	0.9544	0.189
H^e	-0.4513	0.1284	0.9566	0.185
H^4	0.0486	-0.0281	0.9468	0.190
H^5	0.0858	-0.0519	0.9266	0.219
H^6	0.1458	-0.0855	0.9389	0.205
H^7	0.3566	-0.1715	0.9390	0.207

*The agreement factor (AF) is defined below, in which Ln is the lanthanide, and $\boldsymbol{\delta_{Ln}^{obs}}$ and $\boldsymbol{\delta_{Ln}^{cald}}$ are the observed and calculated chemical shifts, respectively.[269] Therefore, AF refers to one specific nucleus for all the paramagnetic **2-Ln** clusters except for **2-Sm, 2-Eu** and **2-Gd**.

$$AF = \sqrt{\frac{\sum_i (\delta_{Ln}^{obs} - \delta_{Ln}^{cald})^2}{\sum_i (\delta_{Ln}^{obs})^2}}$$

In addition, it should be noted that despite the general agreement between the calculated and experimentally obtained paramagnetic NMR shift in many cases (with the error, defined as $|(\delta_{para}^{cald} - \delta_{para}^{expt})/\delta_{para}^{expt}|$, being smaller than 0.20, 0.06, 0.02 and 0.08 for **2-Ce**, **2-Pr**, **2-Tb** and **2-Dy**), there are significant deviations for **2-Nd**, **2-Ho** and **2-Er**, with the errors being larger than 0.37, 0.32 and 0.40, respectively (Table 4.6). These large errors could be due to the collapse of the assumption(s) upon which the Reilley method is built (*i.e.*, isostructural complexes, constant hyperfine coupling constant and crystal-field parameters). To this end, further theoretical investigations on these **2-Ln** clusters would be highly desirable, and their experimentally observed ^{1}H shift data could be an excellent test bed for the new theories. Moreover, if the assumptions in the Reilley method, as well as in the Bleaney theory, are too important to be neglected, perhaps a more general electronic paramagnetic resonance formalism could be adopted.[242] Nevertheless, it should be emphasised that the Bleaney theory has

been remarkably successful and crucial for over four decades in describing the lanthanide-induced *pseudo-contact* NMR shift, and has made significant contributions in pushing the field of lanthanide-induced paramagnetic NMR forward.

Table 4.6. Summary of experimental and calculated overall paramagnetic shifts of ^{1}H resonance (in ppm, using the Reilley method), as well as the *Fermi-contact* and *pseudo-contact* contributions.

		2-Ce	**2-Pr**	**2-Nd**	**2-Tb**	**2-Dy**	**2-Ho**	**2-Er**
H^a	δ_{FC}(cald.)	-0.04	-0.12	-0.18	1.32	1.18	0.94	0.64
	δ_{PC}(cald.)	2.37	4.15	1.62	31.61	36.33	14.29	-11.80
	δ_{para}(cald.)	2.33	4.03	1.44	32.93	37.51	15.23	-11.16
	δ_{para}(expt.)	2.02	4.01	2.35	32.35	40.05	22.83	-19.27
	$\lvert\frac{\delta_{para}(cald.)-\delta_{para}(expt.)}{\delta_{para}(expt.)}$	15.3%	0.5%	38.9%	1.8%	6.3%	33.3%	42.1%
H^b	δ_{FC}(cald.)	-0.08	-0.23	-0.35	2.51	2.25	1.79	1.21
	δ_{PC}(cald.)	2.90	5.09	1.99	38.76	44.54	17.52	-14.47
	δ_{para}(cald.)	2.82	4.86	1.65	41.27	46.80	19.31	-13.26
	δ_{para}(expt.)	2.46	4.80	2.70	40.91	49.7	28.34	-23.26
	$\lvert\frac{\delta_{para}(cald.)-\delta_{para}(expt.)}{\delta_{para}(expt.)}$	14.9%	1.3%	39.4%	0.9%	5.8%	31.9%	43.0%
H^c	δ_{FC}(cald.)	-0.05	-0.17	-0.25	1.80	1.61	1.28	0.87
	δ_{PC}(cald.)	2.15	3.78	1.47	28.74	33.03	12.99	-10.73
	δ_{para}(cald.)	2.10	3.61	1.22	30.54	34.64	14.27	-9.86
	δ_{para}(expt.)	1.84	3.59	2.08	30.07	36.69	20.89	-16.49
	$\lvert\frac{\delta_{para}(cald.)-\delta_{para}(expt.)}{\delta_{para}(expt.)}$	14.1%	0.6%	41.2%	1.6%	5.6%	31.7%	40.2%
H^d	δ_{FC}(cald.)	-0.15	-0.44	-0.67	4.79	4.29	3.40	2.31
	δ_{PC}(cald.)	5.81	10.18	3.98	77.49	89.05	35.03	-28.93
	δ_{para}(cald.)	5.66	9.74	3.31	82.28	93.34	38.43	-26.62
	δ_{para}(expt.)	4.97	9.41	5.33	81.82	98.05	56.73	-47.01
	$\lvert\frac{\delta_{para}(cald.)-\delta_{para}(expt.)}{\delta_{para}(expt.)}$	18.9%	3.5%	38.0%	0.6%	4.8%	32.3%	43.4%
H^e	δ_{FC}(cald.)	-0.12	-0.38	-0.57	4.09	3.67	2.91	1.97

	δ_{PC}(cald.)	5.33	9.34	3.65	71.08	81.69	32.13	-26.54
	δ_{para}(cald.)	5.21	8.96	3.07	75.17	85.36	35.04	-24.57
	δ_{para}(expt.)	4.59	8.65	4.86	74.88	89.38	51.43	-42.87
	$\lvert\frac{\delta_{para}(\text{cald.}) - \delta_{para}(\text{expt.})}{\delta_{para}(\text{expt.})}$	13.3%	3.6%	36.8%	0.4%	4.5%	31.9%	42.7%
H^4	δ_{FC}(cald.)	0.03	0.08	0.13	-0.89	-0.80	-0.64	-0.43
	δ_{PC}(cald.)	-0.57	-1.01	-0.39	-7.65	-8.80	-3.46	2.86
	δ_{para}(cald.)	-0.54	-0.92	-0.26	-8.54	-9.60	-4.10	2.43
	δ_{para}(expt.)	-0.47	-0.89	-0.58	-8.50	-10.25	-6.10	4.42
	$\lvert\frac{\delta_{para}(cald.) - \delta_{para}(expt.}{\delta_{para}(expt.)}$	16.2%	3.7%	53.9%	0.6%	6.3%	32.8%	45.1%
H^5	δ_{FC}(cald.)	0.05	0.15	0.23	-1.65	-1.48	-1.17	-0.80
	δ_{PC}(cald.)	-1.01	-1.78	-0.69	-13.51	-15.53	-6.11	5.05
	δ_{para}(cald.)	-0.96	-1.63	-0.46	-15.16	-17.01	-7.28	4.25
	δ_{para}(expt.)	-0.80	-1.55	-0.94	-15.35	-18.50	-10.90	8.90
	$\lvert\frac{\delta_{para}(cald.) - \delta_{para}(expt.}{\delta_{para}(expt.)}$	20.3%	4.7%	50.9%	1.2%	8.0%	33.2%	52.3%
H^6	δ_{FC}(cald.)	0.08	0.25	0.38	-2.72	-2.44	-1.93	-1.31
	δ_{PC}(cald.)	-1.72	-3.02	-1.18	-22.96	-26.39	-10.38	8.57
	δ_{para}(cald.)	-1.64	-2.77	-0.80	-25.68	-28.83	-12.31	7.26
	δ_{para}(expt.)	-1.40	-2.61	-1.48	-25.73	-30.81	-18.13	14.50
	$\lvert\frac{\delta_{para}(cald.) - \delta_{para}(expt.}{\delta_{para}(expt.)}$	17.0%	5.9%	46.2%	0.2%	6.4%	32.1%	49.9%
H^7	δ_{FC}(cald.)	0.17	0.51	0.76	-5.46	-4.90	-3.88	-2.64
	δ_{PC}(cald.)	-4.21	-7.38	-2.88	-56.16	-64.54	-25.39	20.97
	δ_{para}(cald.)	-4.04	-6.87	-2.12	-61.63	-69.44	-29.27	18.33
	δ_{para}(expt.)	-3.45	-6.56	-3.79	-61.70	-74.40	-43.51	35.94
	$\lvert\frac{\delta_{para}(cald.) - \delta_{para}(expt.}{\delta_{para}(expt.)}$	17.1%	4.8%	44.2%	0.1%	6.7%	32.7%	49.0%

The dominance of the *pseudo-contact* component in the overall paramagnetic ^{1}H shift can be verified by the linear correlation between the paramagnetic NMR shifts $\delta_{para}^{Ln,i}$ and the corresponding geometric factors $G(i)$. The geometric factor

$G(i)$ was calculated using the molecular structures determined by single-crystal X-ray diffraction, and the values for a particular nucleus are almost invariant across the **2-Ln** series (Table 4.7). As shown in Figure 4.13, the paramagnetic NMR shift $\delta_{para}^{Ln,i}$ of the aromatic ^{1}H signals are all linearly proportional to their calculated geometric factors $G(i)$, with R^2 all greater than 0.98. This confirms not only the dominance of the *pseudo-contact* contribution in the overall paramagnetic ^{1}H NMR shift but also the invariant $C_{Ln} \cdot B$ for different NMR nuclei in the same **2-Ln** cluster.[269] Furthermore, the plot of $\delta_{para}^{Ln,i}$ *vs.* C_{Ln} is also linear, as a result of the dominance of the *pseudo-contact* shift (Figure 4.14). The correlation coefficients R^2 are all around 0.96 for all the ^{1}H resonance environments.

Table 4.7. Calculated geometric factors (Å^3) of salicylate carbon and proton nuclei using the solid-state molecular structures obtained by single-crystal X-ray diffraction.

	2-Ce	**2-Pr**	**2-Nd**	**2-Sm**	**2-Eu**	**2-Tb**	**2-Dy**	**2-Ho**	**2-Er**
C^1	0.01368	0.01475	0.01490	0.01485	0.01560	0.01526	0.01585	0.01560	0.01571
C^2	0.00508	0.00508	0.00504	0.00522	0.00548	0.00529	0.00526	0.00531	0.00526
C^3	0.00224	0.00231	0.00231	0.00235	0.00248	0.00232	0.00234	0.00232	0.00242
C^4	0.00116	0.00114	0.00112	0.00118	0.00127	0.00116	0.00113	0.00113	0.00121
C^5	0.00118	0.00099	0.00120	0.00121	0.00134	0.00121	0.00123	0.00119	0.00129
C^6	0.00170	0.00165	0.00163	0.00172	0.00186	0.00172	0.00165	0.00171	0.00176
C^7	0.00305	0.00297	0.00301	0.00311	0.00336	0.00311	0.00318	0.00314	0.00323
H^4	0.00058	0.00054	0.00051	0.00056	0.00061	0.00054	0.00048	0.00050	0.00058
H^5	0.00076	0.00080	0.00082	0.00081	0.00092	0.00081	0.00085	0.00080	0.00088
H^6	0.00136	0.00128	0.00124	0.00135	0.00143	0.00133	0.00129	0.00132	0.00133
H^7	0.00285	0.00275	0.00291	0.00292	0.00326	0.00288	0.00309	0.00301	0.00314

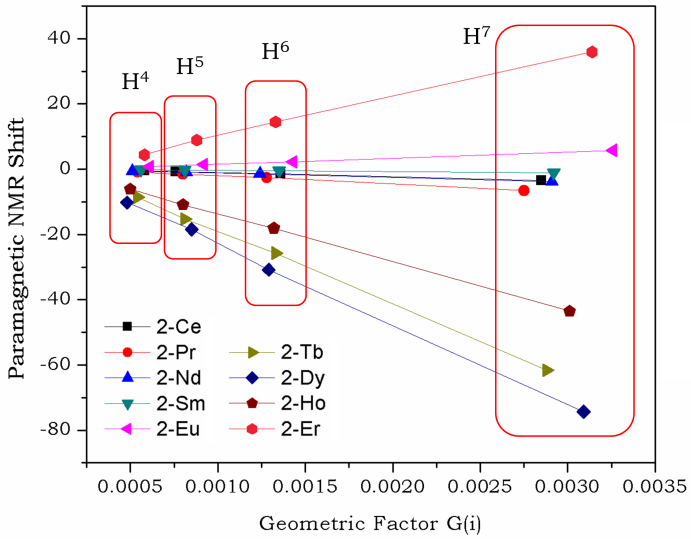

Figure 4.13. Linear fitting of the overall paramagnetic shift $\delta_{para}^{Ln,i}$ *vs.* the corresponding geometric factor $G(i)$ for the aromatic ^{1}H signals (*i.e.*, H^4, H^5, H^6 and H^7). The correlation coefficients R^2 are all greater than 0.98, with the intercept restricted to be zero. Only the salicylate ^{1}H environments are taken into account as the ligands are chelating the metal ions and thus should retain their positions in solution.[266]

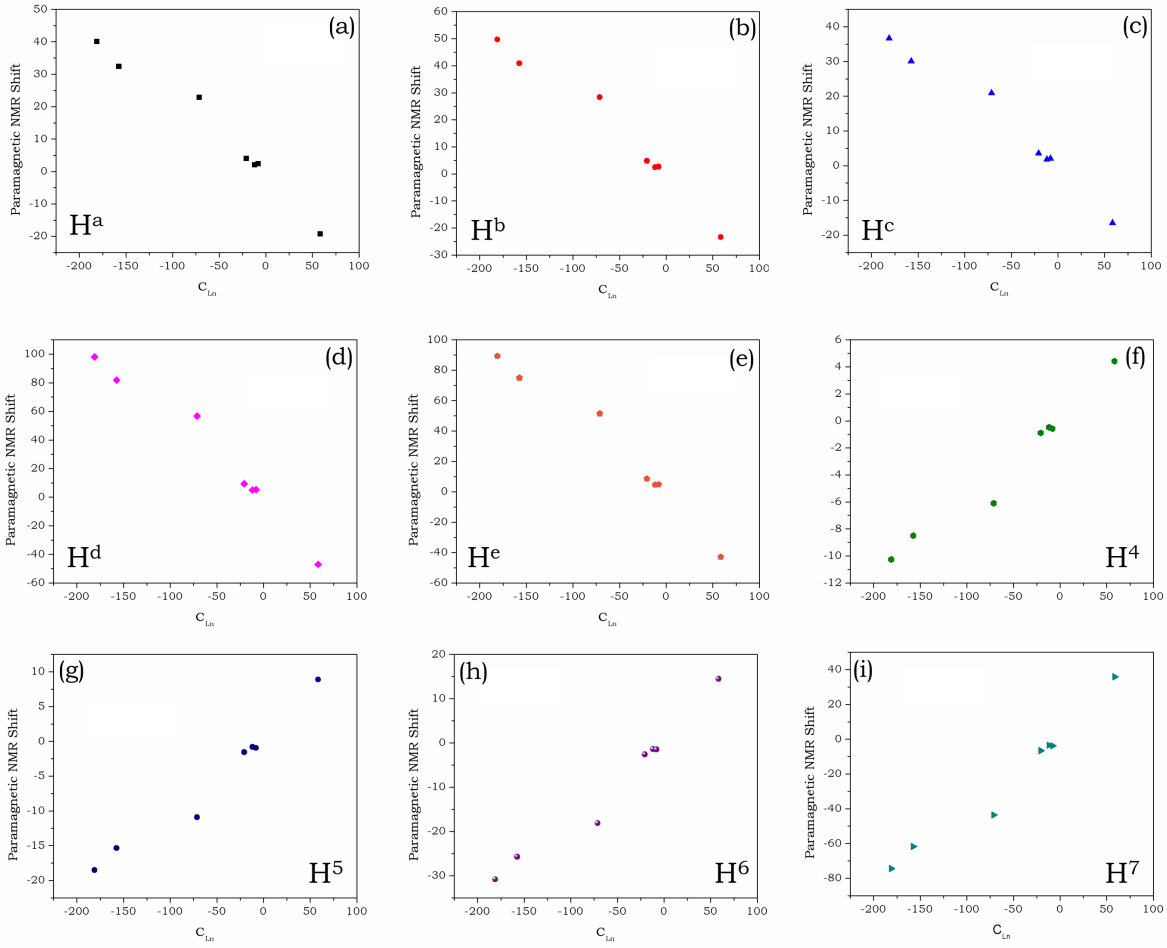

Figure 4.14. Linear fitting of the overall paramagnetic shift $\delta_{para}^{Ln,i}$ *vs.* the corresponding C_{Ln} for the ^{1}H signals in **2-Ln** clusters (excluding **2-La**, **2-Sm**, **2-Eu** and **2-Gd)**. The correlation coefficients R^2 are all greater than 0.96, with the intercept being restricted to zero.[266]

4.3.5. ^{13}C NMR of the Paramagnetic 2-Ln Clusters

The ^{13}C NMR signals are also significantly affected by the paramagnetism of the Ln^{3+} ions. Similar to the ^{1}H NMR resonances, the ^{13}C signals for **2-Ln** clusters containing lighter Ln^{3+} ions (*i.e.*, Ce^{3+}, Pr^{3+}, Nd^{3+}, Sm^{3+} and Eu^{3+}) can be assigned from experiment, with the aid of the 2-D NMR spectra (Figure 4.11 and Table 4.8). All of the ^{13}C signals are in their typical regions except for C^3 (of the salicylate ligand) which varies in a large range of δ 128.21 – 229.32 ppm, depending on the

Ln^{3+} ion. This is probably because C^3 is located near to that of the lanthanide-induced dipolar surfaces, making the chemical shift extremely sensitive to the atomic position of C^3. As a result, a slight distortion in its geometric position in solution will lead significant changes in its chemical shift.[269]

Table 4.8. The experimentally assigned ^{13}C NMR signals (δ ppm) of **2-Ln** clusters containing diamagnetic La^{3+} and lighter paramagnetic Ln^{3+} ions (*i.e.*, Ce^{3+}, Pr^{3+}, Nd^{3+}, Sm^{3+} and Eu^{3+}).

	2-La	**2-Ce**	**2-Pr**	**2-Nd**	**2-Sm**	**2-Eu**
C^1	172.38	163.02	160.68	162.61	168.85	170.18
C^2	118.29	115.24	114.57	121.94	116.12	110.36
C^3	165.83	149.64	128.21	138.61	164.74	229.32
C^4	119.11	117.74	116.59	117.58	118.19	119.88
C^5	135.22	133.74	132.51	133.46	134.97	138.05
C^6	118.80	117.52	116.10	117.79	118.44	120.37
C^7	133.21	129.34	126.35	129.83	132.25	137.24
C^a	81.86	84.66	87.38	84.87	82.46	76.91
C^b	24.82	27.41	29.92	27.75	25.55	20.27
C^c	24.90	26.99	29.11	27.48	25.43	20.69
C^d	78.51	85.02	90.88	85.09	80.76	68.12
C^e	24.22	29.30	33.85	29.64	25.59	15.59

As for the **2-Ln** members containing heavier Ln^{3+} ions (*i.e.*, Tb^{3+}, Dy^{3+}, Ho^{3+} and Er^{3+}), only some of the ^{13}C signals can be unambiguously assigned by experiments using the 2-D NMR spectra (Table 4.9, and Figure A26 – A29 in the Appendix). The three-nuclei-plot method utilized to calculate ^1H NMR shifts is not applicable for most of the ^{13}C signals (except for C^5, C^b and C^c). This is because a large *Fermi-contact* component is usually present for ^{13}C paramagnetic shifts whereas the three-nuclei-plot method only evaluates the *pseudo-contact* component. The success of the three-nuclei-plot method for C^5, C^b and C^c suggests the dominance of *pseudo-contact* contribution to their overall paramagnetic NMR shifts. This observation can be explained by the fact that C^5, C^b and C^c are the most distant ^{13}C environments from the central Ln^{3+} ion (Scheme 4.1). Therefore, they should experience the least paramagnetic influence.

Assignment of the remaining non-quaternary ^{13}C environments was accomplished by selective proton decoupling.[277] For example, **2-Tb** has two unassigned non-quaternary ^{13}C environments (*i.e.*, C^d and C^7). In the proton-coupled ^{13}C NMR spectrum of **2-Tb** (Figure 4.15, blue trace), many of the signals are split into multiplets due to the coupling between ^1H and ^{13}C nuclei. By setting the proton decoupling frequency at -53.67 ppm (corresponding to H^7), the ^{13}C doublet signal at 63.00 ppm was converted into a sharp singlet, implying that the ^1H signal at -53.67 ppm is coupled to the ^{13}C signal at 63.00 ppm. Since the ^1H signal at -53.67 ppm has been assigned to H^7, the ^{13}C signal at 63.00 ppm, therefore, must be corresponding to C^7. Using this selective proton decoupling method, all other non-quaternary ^{13}C signals (C^d for **2-Tb**; C^7, C^a, C^d and C^e for **2-Dy**; C^7, C^d and C^e for **2-Ho**; C^7 for **2-Er**) can be unambiguously assigned (Figure 4.16, Figure 4.17 and Figure 4.18).

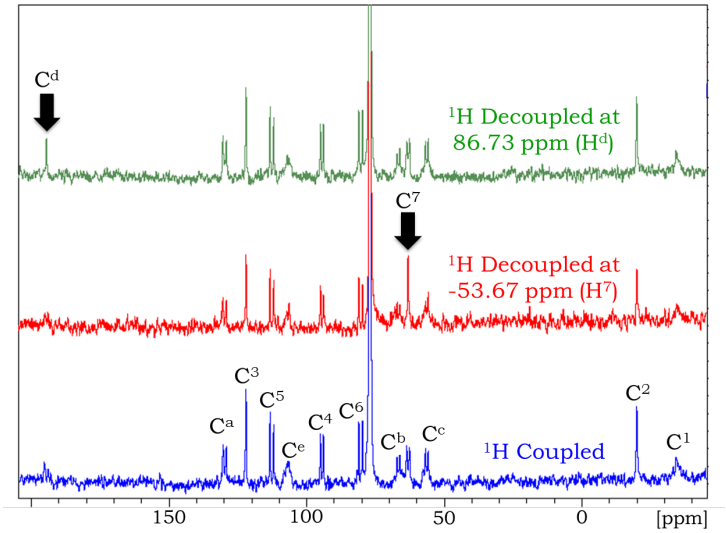

Figure 4.15. ^{13}C NMR spectra of **2-Tb**: ^1H-coupled (blue trace), ^1H-decoupled at -53.67 ppm (red trace) and 86.73 ppm (green trace). The black arrows mark the assigned signals by selective proton decoupling.[266]

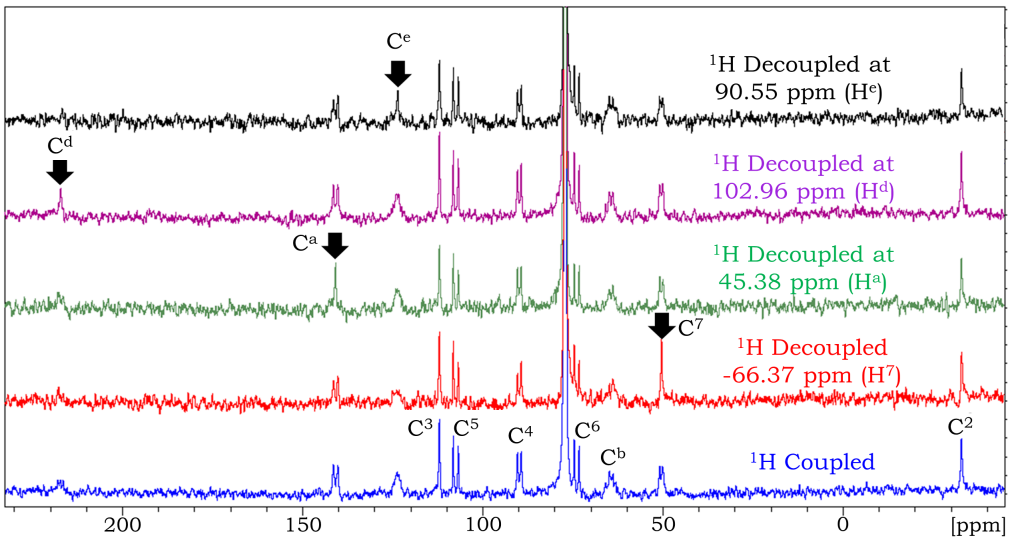

Figure 4.16. ^{13}C NMR spectra of **2-Dy**: ^{1}H-coupled (blue trace), ^{1}H-decoupled at -66.37 ppm (red trace), 45.38 ppm (green trace), 102.96 ppm (purple trace) and 90.55 ppm (black trace). The black arrows mark the assigned signals by selective proton decoupling.[266]

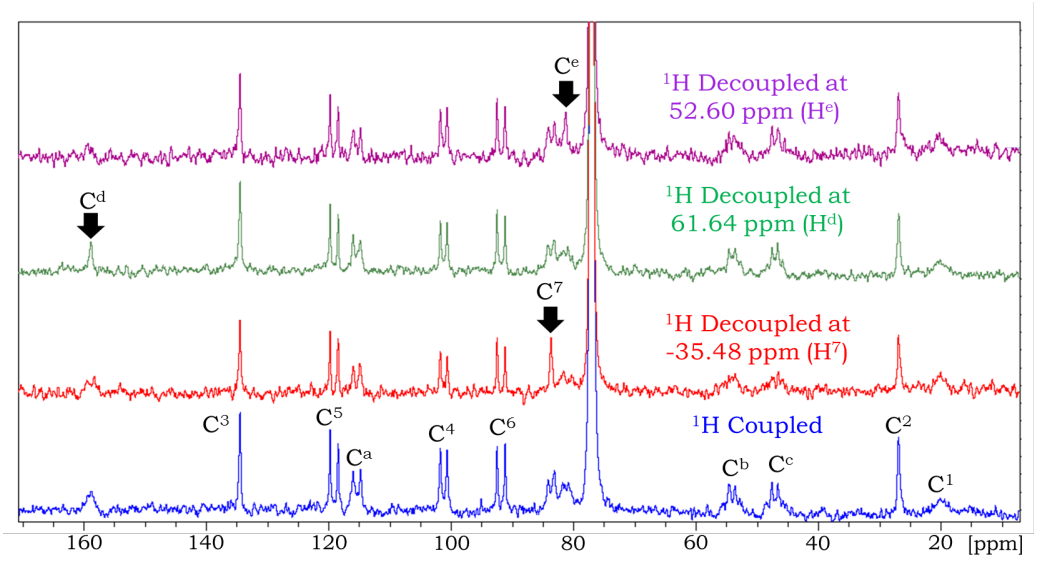

Figure 4.17. ^{13}C NMR spectra of **2-Ho:** ^{1}H-coupled (blue trace), ^{1}H-decoupled at -35.48 ppm (red trace), 61.64 ppm (green trace) and 52.60 ppm (purple trace). The black arrows mark the assigned signals by selective proton decoupling.[266]

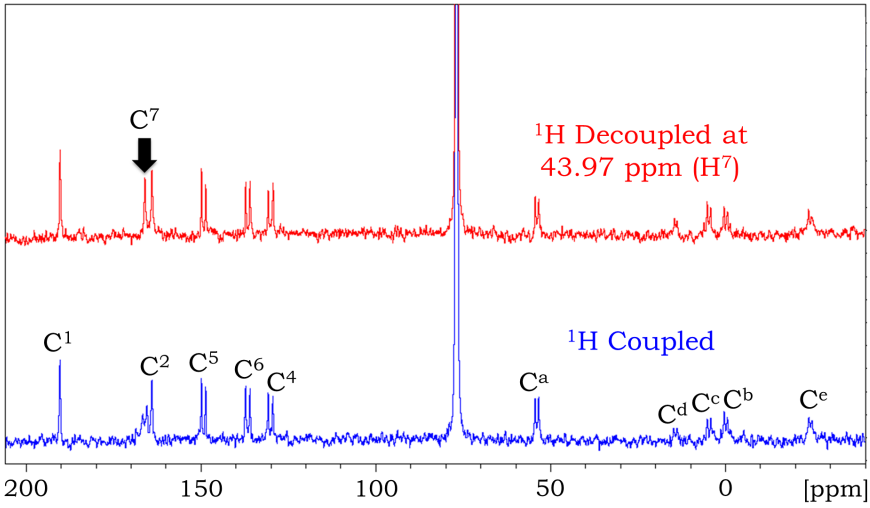

Figure 4.18. ^{13}C NMR spectra of **2-Er**: ^{1}H-coupled (blue trace) and ^{1}H-decoupled at 43.97 ppm (red trace). The black arrow marks the assigned signal by selective proton decoupling.[266]

Evaluation of the non-quaternary ^{13}C signal assignment, as well as further assigning the quaternary ^{13}C signals, can be done by the aforementioned Reilley method, because the linear correlation between $\delta_{para}{}^{Ln,i}/\langle S_z\rangle_{Ln}$ *vs.* $C_{Ln}/\langle S_z\rangle_{Ln}$ can only be established when the correct signal assignment is made. A summary of all the assigned ^{13}C signals for the heavier **Ln-1** clusters is shown in Table 4.9. Good linear correlation of $\delta^{Ln,i}_{para}/\langle S_z\rangle_{Ln}$ *vs.* $C_{Ln}/\langle S_z\rangle_{Ln}$ can be established for all the carbon environments (Table 4.10). The agreement between the experimentally obtained and calculated paramagnetic ^{13}C NMR shifts is generally acceptable. The *pseudo-contact* and *Fermi-contact* contributions were also extracted by the Reilley method (Table 4.11). As expected, the *Fermi-contact* shift for C^5, C^b and C^c is negligibly small compared to their *pseudo-contact* component because they are further away from the central Ln^{3+} ion, but not for the others.

Table 4.9. ^{13}C NMR signals (δ ppm) of **2-Ln** clusters containing heavier paramagnetic Ln^{3+} ions (*i.e.*, Tb^{3+}, Dy^{3+}, Ho^{3+} and Er^{3+}). The signals in bracket are assigned using the 2-D spectra. Assignment of the remaining non-quaternary signals is achieved by selective proton decoupling, and the quaternary signals are assigned using the Reilley method linear fitting.

	2-Tb	**2-Dy**	**2-Ho**	**2-Er**
C^1	-34.30	-107.66	20.45	190.20
C^2	-19.43	-33.00	27.09	163.92
C^3	122.28	111.99	134.60	359.60
C^4	(94.65)	(89.80)	(101.33)	(130.01)
C^5	(112.83)	(107.47)	(119.23)	(149.30)
C^6	(80.20)	(74.27)	(91.97)	(136.64)
C^7	63.00	50.22	83.65	166.35
C^a	(129.76)	141.00	(115.42)	(53.85)
C^b	(67.06)	(76.60)	(54.30)	(-0.10)
C^c	(56.41)	(65.07)	(47.21)	(4.66)
C^d	194.00	217.15	158.60	(14.35)
C^e	(106.97)	123.31	81.36	(-24.62)

Table 4.10. The calculated $B \cdot G(i)$ and $F(i)$ values using the Reilley method for the ^{13}C environments of all the paramagnetic **2-Ln** clusters except for **2-Gd**, **2-Sm** and **2-Eu**. The agreement factor, AF, is defined earlier in Table 4.5.

	B·G(i)	F(i)	R^2	AF
C^1	1.0138	-2.3665	0.9612	0.132
C^2	0.4930	-1.7443	0.8675	0.211
C^3	1.1511	4.5800	0.9439	0.378
C^4	0.1393	-0.1011	0.9620	0.165
C^5	0.1424	-0.0150	0.9527	0.199
C^6	0.1730	-0.3044	0.8850	0.228
C^7	0.3932	-0.3079	0.9608	0.170
C^a	-0.2859	0.1104	0.9470	0.197
C^b	-0.2583	0.0640	0.9525	0.191
C^c	-0.2046	0.0044	0.9527	0.197
C^d	-0.6667	0.3415	0.9481	0.193
C^e	-0.5009	0.1289	0.9533	0.192

Table 4.11. Summary of experimental and calculated paramagnetic shifts of ^{13}C resonances (in ppm, using the Reilley method), as well as *Fermi-contact* and *pseudo-contact* contributions.

		2-Ce	**2-Pr**	**2-Nd**	**2-Tb**	**2-Dy**	**2-Ho**	**2-Er**
C1	$\delta_{FC}(cald.)$	2.30	7.00	10.55	-75.37	-67.59	-53.55	-36.37
	$\delta_{PC}(cald.)$	-11.96	-20.99	-8.19	-159.67	-183.50	-72.18	59.61
	$\delta_{para}(cald.)$	-9.66	-13.99	2.36	-235.04	-251.09	-125.74	23.24
	$\delta_{para}(expt.)$	-9.36	-11.70	-9.77	-206.68	-280.04	-151.93	17.82
	$\lvert\frac{\delta_{para}(cald.)-\delta_{para}(expt.)}{\delta_{para}(expt.)}\rvert$	3.3%	19.5%	124.2%	13.7%	10.3%	17.2%	30.4%
C2	$\delta_{FC}(cald.)$	1.69	5.16	7.78	-55.56	-49.82	-39.47	-26.81
	$\delta_{PC}(cald.)$	-5.82	-10.21	-3.98	-77.65	-89.23	-35.10	28.99
	$\delta_{para}(cald.)$	-4.13	-5.05	3.80	-133.21	-139.05	-74.57	2.18
	$\delta_{para}(expt.)$	-3.05	-3.72	3.65	-137.72	-151.29	-91.20	45.63
	$\lvert\frac{\delta_{para}(cald.)-\delta_{para}(expt.)}{\delta_{para}(expt.)}\rvert$	35.3%	35.5%	4.0%	3.3%	8.1%	18.2%	95.2%
C3	$\delta_{FC}(cald.)$	-4.44	-13.56	-20.43	145.87	130.80	103.65	70.39
	$\delta_{PC}(cald.)$	-13.58	-23.83	-9.30	-181.30	-208.35	-81.96	67.68
	$\delta_{para}(cald.)$	-18.02	-37.39	-29.73	-35.43	-77.55	21.69	138.07
	$\delta_{para}(expt.)$	-16.69	-37.62	-27.22	-43.55	-53.84	-31.23	193.77
	$\lvert\frac{\delta_{para}(cald.)-\delta_{para}(expt.)}{\delta_{para}(expt.)}\rvert$	8.0%	0.6%	9.2%	18.7%	44.0%	169.4%	28.7%
C4	$\delta_{FC}(cald.)$	0.10	0.30	0.45	-3.22	-2.89	-2.29	-1.55
	$\delta_{PC}(cald.)$	-1.64	-2.88	-1.13	-21.94	-25.21	-9.92	8.19
	$\delta_{para}(cald.)$	-1.54	-2.58	-0.68	-25.16	-28.10	-12.21	6.64
	$\delta_{para}(expt.)$	-1.37	-2.52	-1.53	-24.46	-29.31	-17.78	10.9
	$\lvert\frac{\delta_{para}(cald.)-\delta_{para}(expt.)}{\delta_{para}(expt.)}\rvert$	12.8%	2.5%	55.9%	2.9%	4.1%	31.3%	39.1%
C5	$\delta_{FC}(cald.)$	0.01	0.04	0.07	-0.48	-0.43	-0.34	-0.23
	$\delta_{PC}(cald.)$	-1.68	-2.95	-1.15	-22.43	-25.77	-10.14	8.37
	$\delta_{para}(cald.)$	-1.67	-2.91	-1.08	-22.91	-26.20	-10.48	8.14
	$\delta_{para}(expt.)$	-1.48	-2.71	-1.76	-22.39	-27.75	-15.99	14.08
	$\lvert\frac{\delta_{para}(cald.)-\delta_{para}(expt.)}{\delta_{para}(expt.)}\rvert$	12.6%	7.1%	38.4%	2.3%	5.6%	34.5%	42.2%
C6	$\delta_{FC}(cald.)$	0.30	0.90	1.36	-9.70	-8.69	-6.89	-4.68
	$\delta_{PC}(cald.)$	-2.04	-3.58	-1.40	-27.25	-31.31	-12.32	10.17

	$\delta_{para}(cald.)$	-1.74	-2.68	-0.04	-36.95	-40.00	-19.21	5.49
	$\delta_{para}(expt.)$	-1.28	-2.70	-1.01	-38.60	-44.53	-26.83	17.84
	$\lvert\frac{\delta_{para}(cald.)-\delta_{para}(expt.)}{\delta_{para}(expt.)}\rvert$	36.4%	0.7%	96.0%	4.3%	10.2%	28.4%	69.2%
	$\delta_{FC}(cald.)$	0.30	0.91	1.37	-9.81	-8.79	-6.97	-4.73
	$\delta_{PC}(cald.)$	-4.64	-8.14	-3.18	-61.93	-71.17	-28.00	23.12
C^7	$\delta_{para}(cald.)$	-4.34	-7.23	-1.81	-71.74	-79.96	-34.97	18.39
	$\delta_{para}(expt.)$	-3.87	-6.86	-3.38	-70.21	-82.99	-49.56	33.14
	$\lvert\frac{\delta_{para}(cald.)-\delta_{para}(expt.)}{\delta_{para}(expt.)}\rvert$	12.2%	5.4%	46.6%	2.2%	3.6%	29.5%	44.5%
	$\delta_{FC}(cald.)$	-0.11	-0.33	-0.49	3.52	3.15	2.50	1.70
	$\delta_{PC}(cald.)$	3.37	5.92	2.31	45.03	51.75	20.36	-16.81
C^a	$\delta_{para}(cald.)$	3.26	5.59	1.82	48.55	54.90	22.86	-15.11
	$\delta_{para}(expt.)$	2.80	5.52	3.01	47.90	59.14	33.56	-28.01
	$\lvert\frac{\delta_{para}(cald.)-\delta_{para}(expt.)}{\delta_{para}(expt.)}\rvert$	16.7%	1.3%	39.6%	1.3%	7.2%	31.9%	46.0%
	$\delta_{FC}(cald.)$	-0.06	-0.19	-0.29	2.04	1.83	1.45	0.98
	$\delta_{PC}(cald.)$	3.05	5.35	2.09	40.68	46.75	18.39	-15.19
C^b	$\delta_{para}(cald.)$	2.99	5.16	1.80	42.72	48.58	19.84	-14.21
	$\delta_{para}(expt.)$	2.59	5.10	2.93	42.24	51.78	29.48	-24.92
	$\lvert\frac{\delta_{para}(cald.)-\delta_{para}(expt.)}{\delta_{para}(expt.)}\rvert$	15.3%	1.1%	38.5%	1.1%	6.2%	32.7%	43.0%
	$\delta_{FC}(cald.)$	0.00	-0.01	-0.02	0.14	0.13	0.10	0.07
	$\delta_{PC}(cald.)$	2.41	4.24	1.65	32.22	37.03	14.57	-12.03
C^c	$\delta_{para}(cald.)$	2.41	4.23	1.63	32.36	37.16	14.67	-11.96
	$\delta_{para}(expt.)$	2.09	4.21	2.58	31.51	40.17	22.31	-20.24
	$\lvert\frac{\delta_{para}(cald.)-\delta_{para}(expt.)}{\delta_{para}(expt.)}\rvert$	15.3%	0.3%	36.7%	2.7%	7.5%	34.3%	40.9%
	$\delta_{FC}(cald.)$	-0.33	-1.01	-1.52	10.88	9.75	7.73	5.25
	$\delta_{PC}(cald.)$	7.87	13.80	5.39	105.01	120.67	47.47	-39.20
C^d	$\delta_{para}(cald.)$	7.54	12.79	3.87	115.89	130.42	55.20	-33.95
	$\delta_{para}(expt.)$	6.51	12.37	6.58	115.49	138.64	80.09	-64.16
	$\lvert\frac{\delta_{para}(cald.)-\delta_{para}(expt.)}{\delta_{para}(expt.)}\rvert$	15.8%	3.4%	41.3%	0.3%	5.9%	47.1%	47.1%
C^e	$\delta_{FC}(cald.)$	-0.13	-0.38	-0.57	4.11	3.68	2.92	1.98
	$\delta_{PC}(cald.)$	5.91	10.37	4.05	78.89	90.66	35.66	-29.45

$\delta_{para}(cald.)$	5.78	9.99	3.48	83.00	94.34	38.58	-27.47
$\delta_{para}(expt.)$	5.08	9.63	5.42	83.75	99.09	57.14	-48.84
$\lvert\frac{\delta_{para}(cald.)-\delta_{para}(expt.)}{\delta_{para}(expt.)}\rvert$	13.9%	3.7%	35.9%	0.3%	4.8%	32.5%	43.8%

4.3.6. Summary and Future Perspectives

The isostructural L-M-TOCs $[LnTi_6O_3(O^iPr)_9(salicylate)_6]$ (**2-Ln**, Ln = La – Er excluding Pm) provide an excellent model system for the investigation of the influence of paramagnetic Ln^{3+} ions on the NMR behaviour of the periphery ligands, with all the ^1H and ^{13}C signals being observed and unambiguously assigned (apart that of **2-Gd**). For these **2-Ln** clusters, the *pseudo-contact* shift is found to dominate the overall paramagnetic ^1H shifts, whereas for ^{13}C both the *pseudo-contact* and *Fermi-contact* contributions are present in most signals, although the majority of the carbon atoms are at least four bonds distant from the central Ln^{3+} ion.

The most important contribution that the present study makes is perhaps that it provides a complete dataset of paramagnetic NMR signals from an extensive series of lanthanide-containing complexes. It paves the way for further investigating related theoretical principles and also the detailed reasons for the discrepancies between the experimental and predicted results according to the Bleaney's theory. This constitutes the next step for this piece of work.

On a separate note, the observed paramagnetic NMR shifts, particularly for the heavier lanthanides (*i.e.*, Tb^{3+}, Dy^{3+}, Ho^{3+} and Er^{3+}), suggest the potential of these **2-Ln** clusters as single molecule magnets (SMMs), which deserves further investigation. In general, SMMs are molecular materials displaying stable magnetisation below a critical temperature. Such magnetic behaviour originates from a combination of a large spin ground state and non-axial magnetic anisotropy. In contrast to multinuclear species, a preeminent feature of mononuclear lanthanide magnets is their tunability, which allows for increased control over structure, and therefore magnetic properties. To this end, encapsulation of Ln^{3+} ions in TOCs, as has been found for the **2-Ln** clusters, may

represent a new strategy for the design and construction of mononuclear Ln^{3+}-based SMMs.

4.4. Photoluminescence Properties of 2-Ln

4.4.1. Motivation

In the context of TOCs, lanthanide-containing clusters (Ln-TOCs) possess intriguing structural features and appealing properties,[20,59-68,278,279] mainly due to the diverse coordination environments of the Ln^{3+} ions.[280] The main reason for general interest in lanthanide complexes is their advantageous luminescence properties, such as long excited state lifetimes, narrow emission bandwidths and excellent resistance to photo-bleaching.[280] Ln^{3+} luminescence mainly originates from electronic transitions within their 4*f* orbitals, but most of these intra-*f* transitions are forbidden according to the Laporte rule. As a result, direct excitation of Ln^{3+} ions is usually inefficient, with extremely low molar extinction coefficients (*i.e.*, 1 - 10 M^{-1} cm^{-1}).[281] This limitation can be overcome with the assistance of highly absorbing '*antenna*' ligands located in close proximity to the Ln^{3+} ions via the classic $S_0 \rightarrow S_1 \rightarrow T_1 \rightarrow Ln^{3+}$ energy transfer route.[282] The majority of the previous reports on Ln-TOCs, however, have primarily focused on their syntheses and structural characterisation, leaving the photoluminescence properties less explored. In 2015, Wang *et al.*[62] studied the photoluminescence behaviour of anthracenecarboxylate-modified Ln-TOCs (with $\{Ln_2Ti_{10}\}$ cores, Ln = Eu and Nd) and investigated the energy transfer process between the ligands and the Ln^{3+} centres. In 2016, Zhang *et al.*[64] reported a group of Ln-TOCs (with $\{LnTi_{11}\}$ core arrangements, Ln = Sm, Eu and Gd) which could be used as potential molecule-based fluorescent labelling agents. Very recently, Lu *et al.*[66] synthesised three Eu^{3+}-containing TOCs (with $\{Eu_2Ti_4\}$, $\{Eu_5Ti_4\}$ and $\{Eu_8Ti_{10}\}$ cores) coordinated with 4-tert-butylbenzoate, and revealed a size-dependent quantum yield phenomenon in solution. The physical interplay between the coordinated ligands, Ln^{3+} centres and Ti^{4+} ions was, unfortunately, not clearly demonstrated in these studies, as the excitation of the Ln^{3+} photoluminescence arose either from direct intra-*f* transitions or from the coordinated ligands alone.

In this section, the energy transfer mechanism and photoluminescence properties of the **2-Ln** clusters are investigated. The salicylate-Ti^{4+} moiety is found to be an effective visible light responsive '*antenna*' for Ln^{3+} sensitisation, although salicylate itself is usually considered inefficient in this role.[283-285] Both visible (for **2-Pr**, **2-Sm**, **2-Eu**, **2-Ho**, **2-Er**) and NIR (for **2-Nd** and **2-Er**) photoluminescence can be sensitised by visible light excitation up to 475 nm, representing a special example in which one visible-responsive ligand system is suitable for Ln^{3+} ion sensitisation across the visible-NIR ranges.[286-290] A charge-transfer process from the salicylate HOMO to Ti^{4+} *d* orbitals is proposed to account for the largely red-shifted excitation wavelengths, supported by both steady-state and time-resolved photoluminescence spectroscopic data.

4.4.2. Photophysical Properties of 2-Ln

In the context of photophysical properties, the topology of **2-Ln** also has several advantages over other lanthanide complexes in which direct coordination of aromatic ligands to the Ln^{3+} ion occurs, including (i) the encapsulation of Ln^{3+} by diamagnetic Ti^{4+} ions significantly enlarges the distance between the Ln^{3+} ions and the X-H (X = C or O) oscillators located on solvent molecules or peripheral ligands, thus giving high intrinsic quantum yields;[291] (ii) the encapsulation of the Ln^{3+} ions within **2-Ln** is also potentially beneficial for *in vivo* biological applications where the cytotoxicity of heavy metal ions is usually critical;[292,293] and (iii) the isopropoxide ligands can be easily replaced by other ligands, which could promote more versatile functionalities.[24]

As shown in Figure 4.19a, **2-Gd**, being a representative of the **2-Ln** family, exhibits intense absorption in a wavelength range up to 475 nm, within which an absorption edge at 250 – 300 nm and a broad band centred at *ca.* 350 nm are observed. The 350 nm absorption band is due to the charge-transfer process from the salicylate HOMO level to Ti^{4+} *d* orbitals. This was confirmed by a control experiment in which a shoulder at similar wavelength emerges upon mixing salicylic acid with $Ti(O^iPr)_4$ in *n*-pentane (Figure 4.19a, blue trace), and is further supported by the similar charge-transfer behaviour observed for a number of other ligand-modified TOCs and TiO_2 nanoparticles.[294] The absorption edge at

250 – 300 nm can be attributed to the $O^{2-} \rightarrow Ti^{4+}$ transition in the Ti_xO_y core, which is also a commonly observed feature for many TOCs. Salicylic acid alone has an absorption band centred at *ca.* 310 nm arising from the transition from ground to singlet excited state ($S_0 \rightarrow S_1$). Upon excitation at 300 nm in solution, salicylic acid exhibits a broad emission band located at *ca.* 440 nm (Figure 4.19b), which can be assigned to the fluorescence from the S_1 excited state.

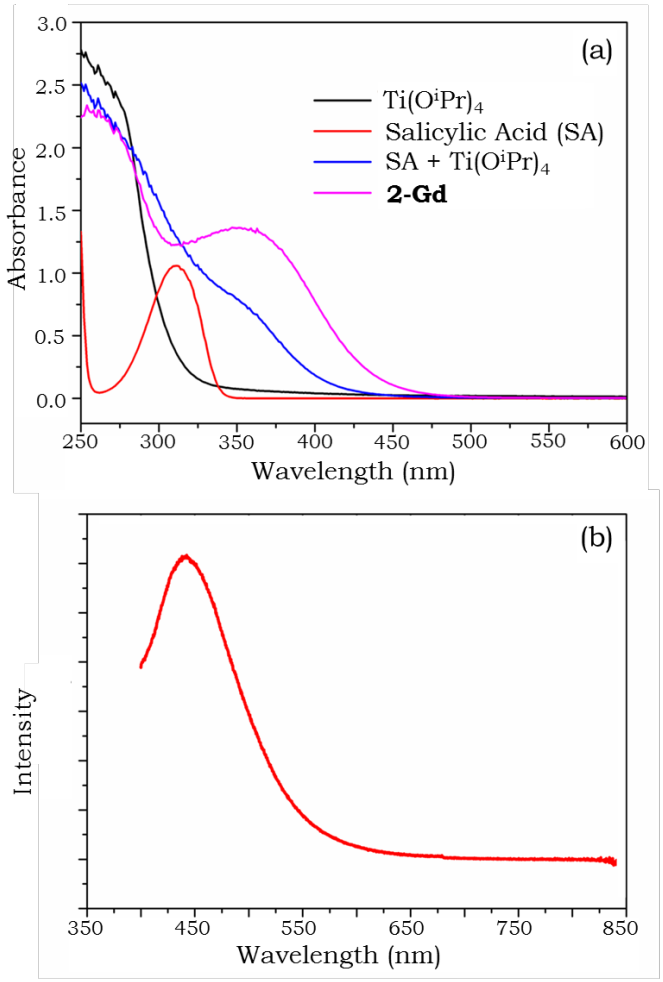

Figure 4.19. (a) The absorbance spectra of $Ti(O^iPr)_4$ (black trace), salicylic acid (red trace), mixture of salicylic acid and $Ti(O^iPr)_4$ (blue trace), and **2-Gd** (*ca.* 40 μM, pink trace) in anhydrous *n*-pentane. (b) The steady-state photoluminescence spectrum of salicylic acid in anhydrous *n*-pentane with 300 nm excitation.[221]

Among the eleven **2-Ln** clusters, only six (**2-Pr**, **2-Nd**, **2-Sm**, **2-Eu**, **2-Ho** and **2-Er**) show detectable Ln^{3+}-centred intra-*f* transition photoluminescence peaks in the visible-NIR range (Figure 4.20a). Upon monitoring the most intense Ln^{3+}-centred emission signals, similar excitation spectra were recorded for all these **2-Ln** clusters, consisting of a minor band centred at *ca.* 300 nm and a major one at *ca.* 400 nm, as well as some intra-*f* transition peaks (Figure 4.20a). The relatively lower intensity of the intra-*f* peaks suggests more efficient sensitisation via the '*antenna*' ligands, compared to direct intra-*f* transitions. Upon excitation at 405 nm, bright red/pink coloured luminescence can be clearly seen from **2-Pr**, **2-Sm** and **2-Eu** solutions by the naked eye (Figure 4.21).

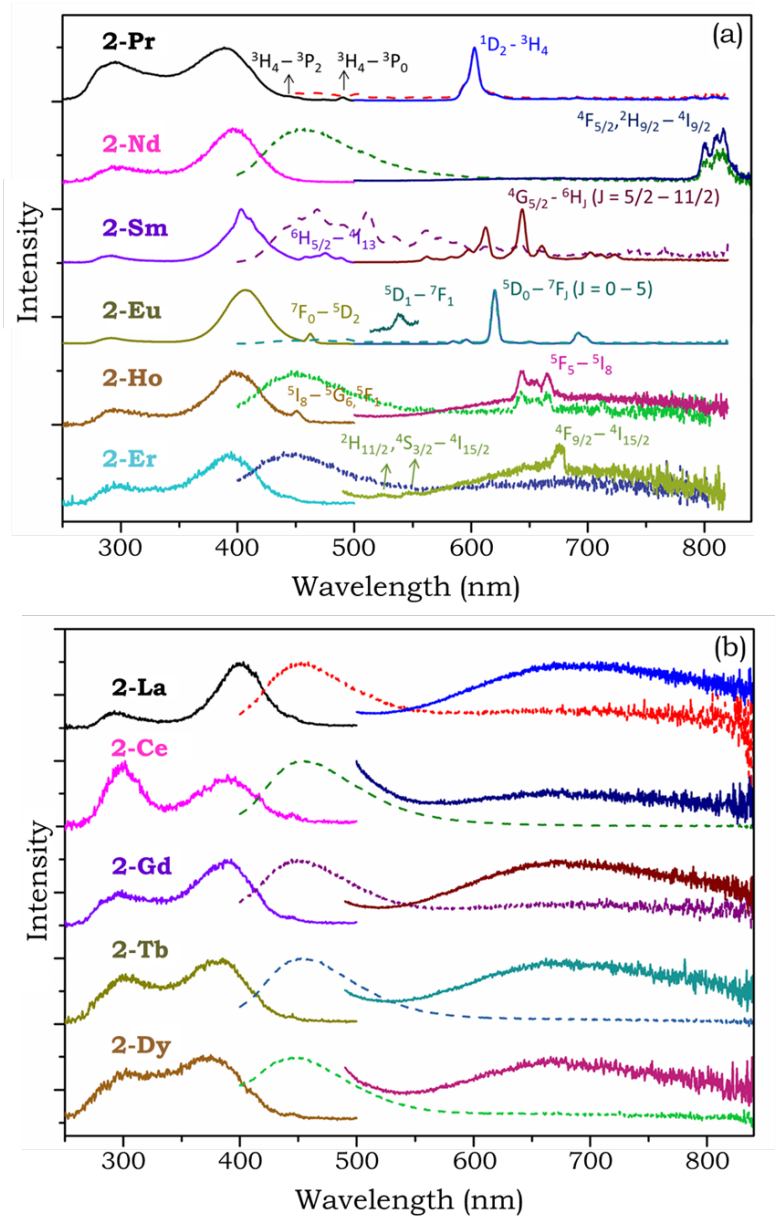

Figure 4.20. Normalized excitation and steady-state emission spectra of **2-Ln** compounds: (a) those showing Ln^{3+}-centred signals, and (b) those only showing ligand-centred signals. Excitation spectra were recorded by monitoring the most intense Ln^{3+}-centred emission peaks [for (a)] or emission at 650 nm [for (b)]. Two emission spectra are shown for each compound, which were excited at *ca.* 300 nm (dashed line) and *ca.* 400 nm excitation band (solid line), respectively. The peaks in the 450 - 500 nm range in the emission spectrum of **2-Sm** in (a) are residual signals from the xenon light source, which are also present in the emission spectra of **2-Pr** and **2-Eu** at similar wavelengths (only visible upon zooming in), but obscured by the broad ligand-centred emission band at *ca.* 450 nm for other **2-Ln** members.[221]

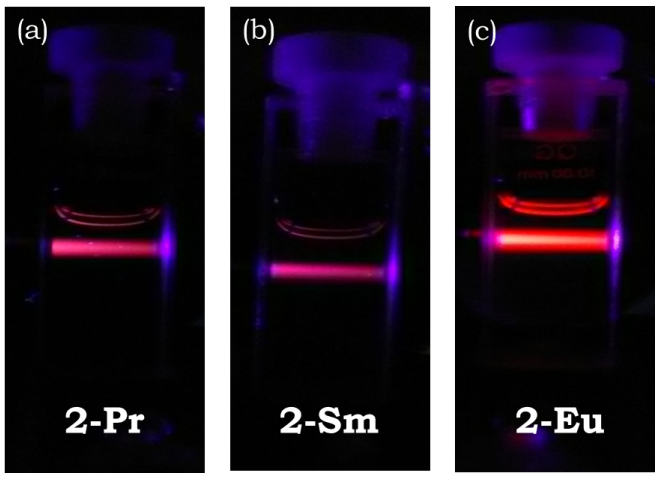

Figure 4.21. Digital photographs of the photoluminescence of (a) **2-Pr**, (b) **2-Sm** and (c) **2-Eu** in anhydrous *n*-pentane solution upon excitation by a 405 nm laser.[221]

The minor excitation band centred at *ca.* 300 nm matches the absorbance spectrum of deprotonated salicylic acid, which is slightly blue-shifted compared with the protonated molecule.[295] Therefore, this band can be attributed to the excitation of the salicylate ligand, undergoing a $S_0 \rightarrow S_1$ transition at this excitation wavelength.[283-285] Apart from the Ln^{3+}-centred emission, excitation at 300 nm also leads to a broad emission band at *ca.* 450 nm for **2-Nd**, **2-Sm**, **2-Ho** and **2-Er**, corresponding to the fluorescence of salicylate S_1 state.[296] This result suggests incomplete energy transfer from salicylate to Ln^{3+} emissive states. In addition, it is worth mentioning that the $O^{2-} \rightarrow Ti^{4+}$ transition might also play a role in the minor excitation band at *ca.* 300 nm, since a similar excitation mechanism has been revealed in solid-state Ln-doped TiO_2 materials.[297]

What makes these **2-Ln** compounds unique is the presence of the major excitation band in the region of 350 – 475 nm with the peak position at around 400 nm (Figure 4.20a). In general, UV excitation to visible/NIR emission or visible excitation to NIR emission are common for Ln^{3+}-containing complexes, but the visible excitation to visible emission process observed here is relatively rare and usually needs sophisticated ligand design.[298] Moreover, the salicylate ligand itself

is usually considered inefficient for the sensitisation of Ln^{3+} ions, because the energy levels of its excited states are too high and the excitation window is limited only to the UV range. In this case, upon coordinating with Ti^{4+} ions, the salicylate has been readily converted into an effective and visible light responsive ligand for Ln^{3+} photoluminescence sensitisation.

The remaining five clusters (**2-La**, **2-Ce**, **2-Gd**, **2-Tb** and **2-Dy**) merely show ligand-centred emission bands at *ca.* 450 nm with 300 nm excitation, as well as an extremely broad feature in the 550 – 800 nm region with either 300 or 400 nm excitation (Figure 4.20b). Solely ligand-centred emission is expected for **2-La**, **2-Ce** and **2-Gd** because they do not have any intra-*f* transitions within the visible-NIR range. However, it is surprising that neither Tb^{3+} nor Dy^{3+} photoluminescence signals were detected, despite the fact that they are very well-known green and yellow light emitters.[299] The excitation spectra of these five clusters were recorded at different emission wavelengths from 700 nm to 550 nm (in 50 nm steps) (Figure 4.22 and 4.23). The intensity of the major excitation band (*ca.* 400 nm) decreases, with the monitored emission wavelength shifting towards the blue direction for each of the compounds, clearly suggesting that the broad feature in the 550 – 800 nm range corresponds to the excitation band at *ca.* 400 nm. Of note, the difference between the excitation spectra of **2-Ce** and those shown in Figure 4.22 could be due to the relatively lower energy required for the *d-f* transitions of Ce^{3+} ions, although further investigations are required to reveal the detailed mechanisms behind. In contrast, the unique shape of **2-Eu** excitation spectra is due to the fact that emission signals from Eu^{3+} ion can be clearly observed. Therefore, the excitation spectra are dominated by the Eu^{3+}-centred emission signals, instead of the shifting of the monitored emission wavelengths.

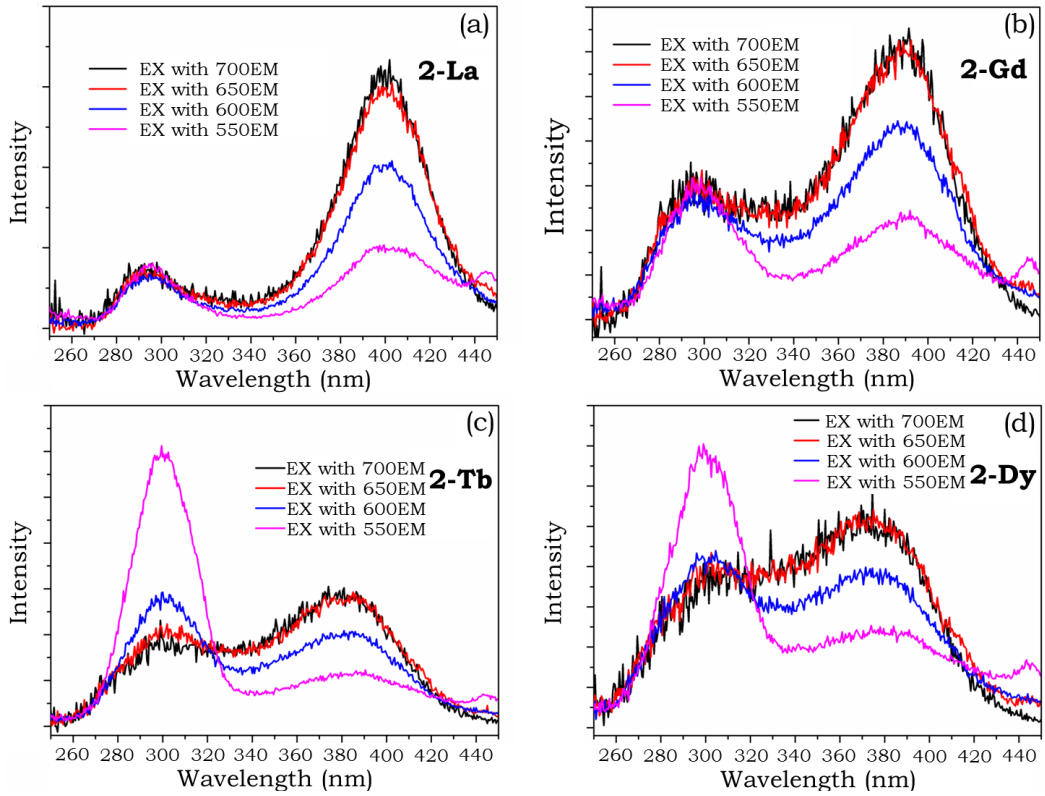

Figure 4.22. The excitation spectra upon monitoring emission signals across the 700 – 550 nm range in 50 nm steps for (a) **2-La**, (b) **2-Gd**, (c) **2-Tb** and (d) **2-Dy** in anhydrous *n*-pentane solution. 'EX with 700EM' means the excitation spectrum is recorded by monitoring the emission at 700 nm wavelength.[221]

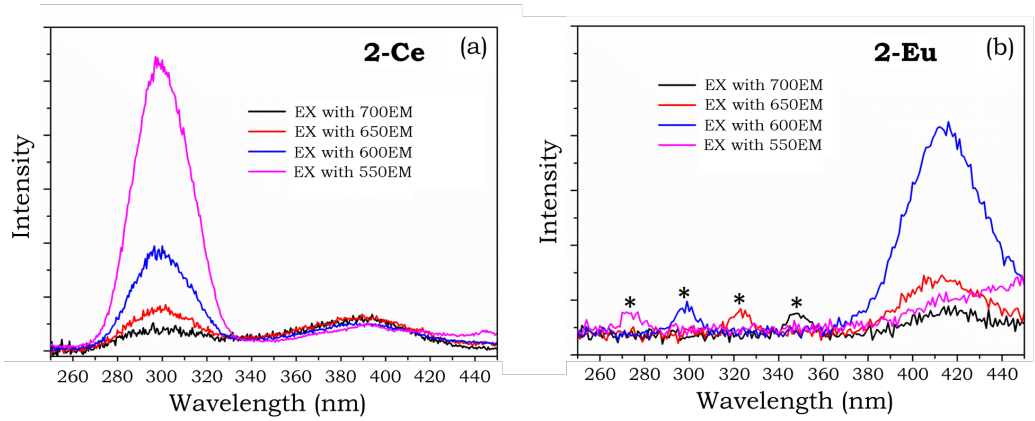

Figure 4.23. The excitation spectra upon monitoring emission signals across the 700 – 550 nm range in 50 nm steps for (a) **2-Ce** and (b) **2-Eu** in anhydrous *n*-pentane. The peaks labelled with '*' in (b) is not from **2-Eu**, as their positions are exactly half of the monitored emission wavelengths.[221]

The steady-state NIR (1000 – 1800 nm) emission spectra of **2-Ln** were also recorded, with only **2-Nd** and **2-Er** showing detectable Ln^{3+}-centred emission peaks upon 405 nm laser excitation (Figure 4.24). Because neither Nd^{3+} nor Er^{3+} have intra-*f* transitions with energy gaps corresponding to the 405 nm wavelength, the excitation must be via the '*antenna*' ligands.[300] The photoluminescence quantum yields for **2-Ln** in *n*-pentane solution were measured using the integration sphere method,[301] giving 0.037 ± 0.003% for **2-Eu** (using 405 nm excitation and $^5D_0 \rightarrow {}^7F_2$ emission) and 0.30 ± 0.01% for **2-Nd** (using 405 nm excitation, $^4F_{3/2} \rightarrow {}^4I_{9/2}$ and $^4F_{3/2} \rightarrow {}^4I_{11/2}$ emissions). The quantum yields for other **2-Ln** members are all below the sensitivity of the equipment employed. It is worth noting that the quantum yield of **2-Nd** (0.30 ± 0.01%) represents one of the highest values for Nd^{3+}-complexes reported in the literature,[302] suggesting an efficient energy transfer process.

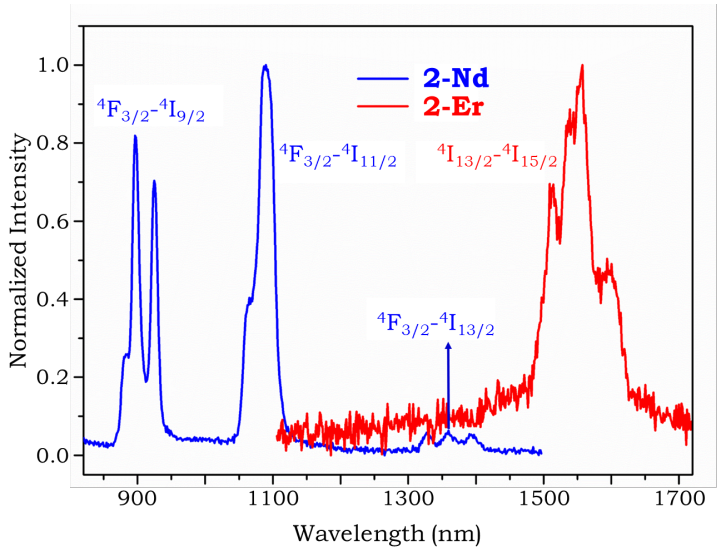

Figure 4.24. Normalized steady-state NIR emission spectra of **2-Nd** and **2-Er** in anhydrous *n*-pentane upon 405 nm laser excitation. Intra-*f* transition peaks are indicated.[221]

To establish the energy transfer mechanism within these species, time-resolved emission spectra of **2-Pr**, **2-Nd**, **2-Sm** and **2-Eu** were recorded at different time intervals (*i.e.*, 10 ns – 60 ns, 50 ns – 550 ns, 0.5 μs – 10.5 μs and 10 μs – 110 μs)

after the excitation laser pulse at 430 nm (Figure 4.25). In addition to the different increasing/decaying kinetics of the Ln^{3+} emission signals, perhaps the most striking feature is the appearance of a new broad band at *ca.* 500 nm observed for **2-Pr**, **2-Nd**, **2-Sm** and **2-Eu** in the interval of 10 ns – 60 ns.

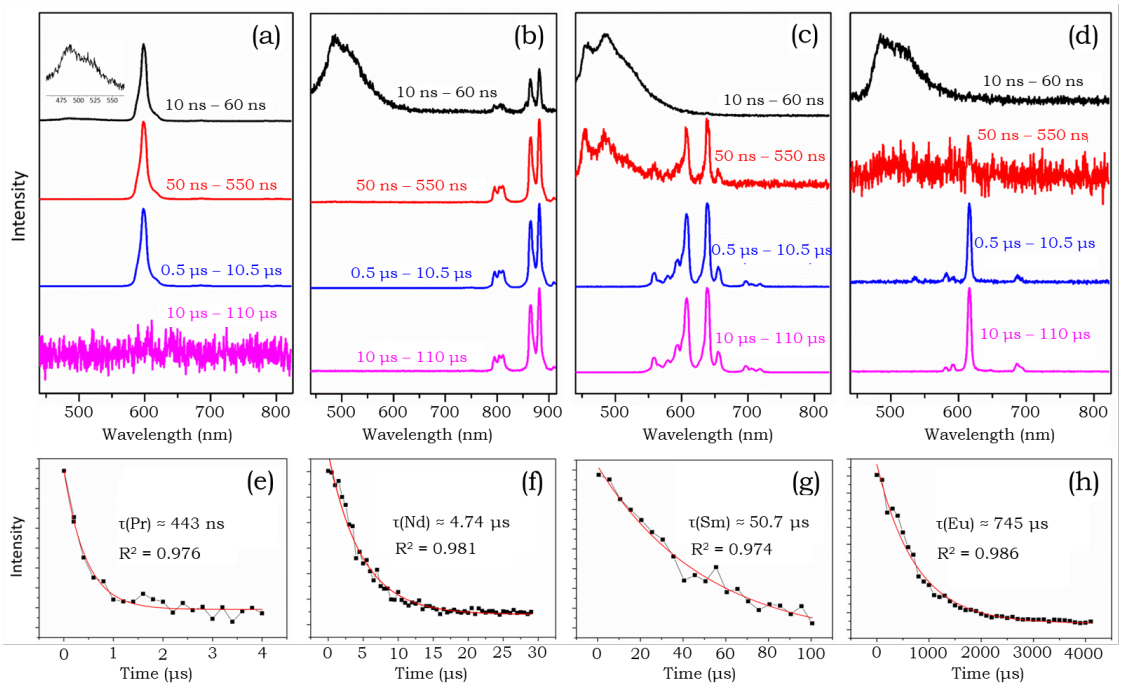

Figure 4.25. The time-resolved emission spectra of (a) **2-Pr**, (b) **2-Nd**, (c) **2-Sm** and (d) **2-Eu** at different intervals after the laser pulse excitation at 430 nm. The Ln^{3+}-centred emission decay profile of (e) **2-Pr**, (f) **2-Nd**, (g) **2-Sm** and (h) **2-Eu**. The estimated lifetimes are also shown.[221]

A similar emission band is also present for the other seven **2-Ln** members in the same time interval after the laser pulse (Figure 4.26), suggesting its origin from the salicylate-Ti^{4+} moieties in the **2-Ln** structure. To prevent potential interference from the residual light source, a long-pass optical filter with 515 nm cut-off was placed between the sample and the CCD detector, and the red edge of the emission band can still be observed, confirming the close correlation between the *ca.* 400 nm excitation and the *ca.* 500 nm emission bands. Lifetimes of the emission at 525 nm were measured with the optical filter in place. The lifetimes

shown in Figure 4.27 might not be accurate, because they are all close to the response time of the equipment employed.

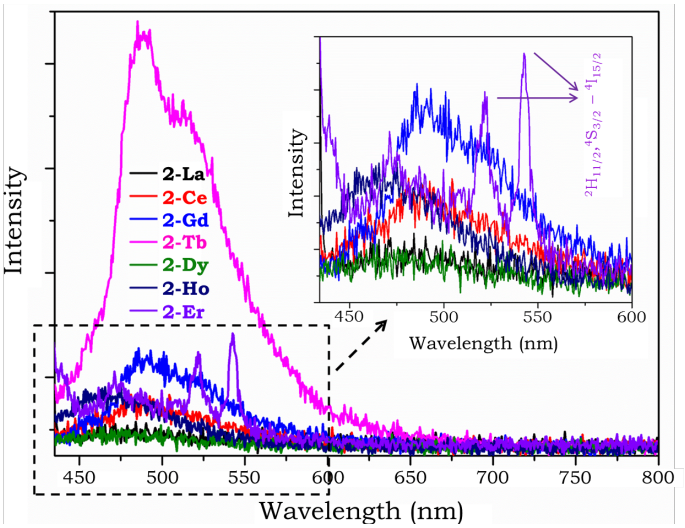

Figure 4.26. Emission spectra of **2-Ln** in the 10 ns – 60 ns time interval after the 430 nm laser excitation pulse. Inset is the magnification of the low intensity area. Intra-*f* transition peaks are observed for **2-Er** and indicated in the figure inset.[221]

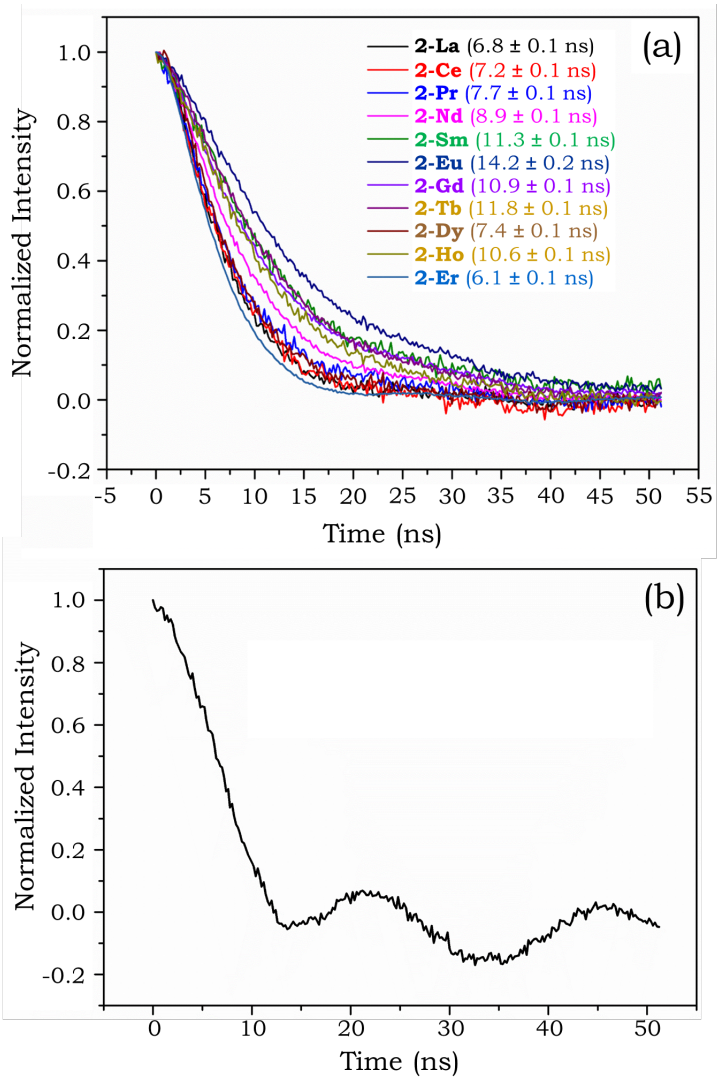

Figure 4.27. (a) Decaying profile of the emission signal at 525 nm for respective **2-Ln** clusters; calculated lifetimes using single exponential curve fitting are also shown; (b) decaying profile representing the response of the equipment employed.[221]

As a comparison, the photoluminescence excitation and emission spectra of solid-state **2-Eu** crystals were also recorded (Figure 4.28 and 4.29). Upon excitation at 400 nm, signature emission signals of Eu^{3+} ion can be clearly observed and unambiguously assigned to the $^5D_0 \rightarrow {}^7F_J$ (J = 0 – 5) transitions. Because the intensity of the Eu^{3+} $^5D_0 \rightarrow {}^7F_2$ emission (electrical dipole transition) varies strongly with the local symmetry, while that of the $^5D_0 \rightarrow {}^7F_1$ emission

(magnetic dipole transition) is independent on the local environment, the intensity ratio of these two signals can be employed to probe the local coordination environment of Eu^{3+}.[66] In this case, the ratio for **2-Eu** solid-state sample was determined to be around 14.8, satisfactorily matching with that from solution (*i.e.*, *ca.* 14.9). This result supports the hypothesis that there is no change of local symmetry around the Eu^{3+} ions upon dissolving **2-Eu** in *n*-pentane.

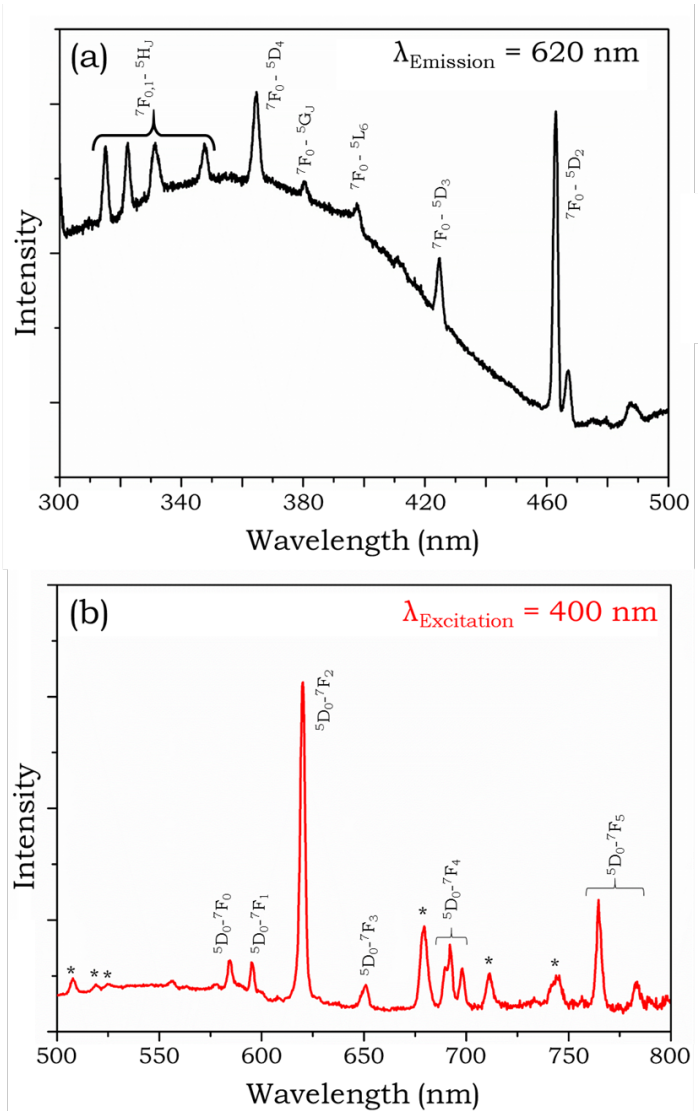

Figure 4.28. Photoluminescence excitation (a) and emission (b) spectra of **2-Eu** in the solid-state. The peaks marked with '*' are possibly from the scattering of the light source, as their positions change with the excitation wavelengths (see Figure 4.29).[221]

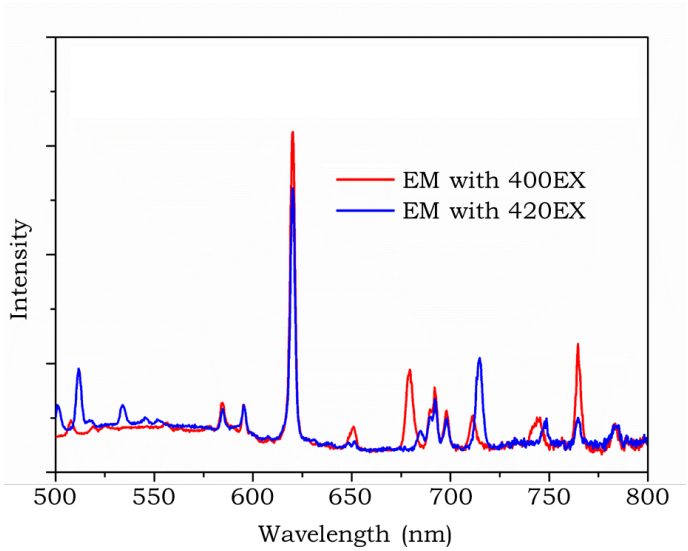

Figure 4.29. Emission spectra of a solid-state **2-Eu** sample with excitation at 400 nm (red trace) and 420 nm (blue trace).[221]

Furthermore, the NMR spectra of diamagnetic **2-La** (as an example of the **2-Ln** family) at low concentrations was also recorded, which shows similar peak positions and splitting patterns to the high concentration sample (Figure 4.30). These results indicate the cluster structure of **2-Ln** remains *intact* in dilute solutions, and the red-shifted excitation wavelengths, therefore, originate from the unique molecular structure of the clusters. The excitation spectrum of solid-state **2-Eu** upon monitoring the $^5D_0 \rightarrow {}^7F_2$ emission at 620 nm exhibits a number of intra-*f* transition peaks and a broad band centred at *ca.* 350 nm (Figure 4.28). This 350 nm excitation band differs from that of the **2-Eu** solution sample (*i.e.*, major excitation band at 400 nm and minor band at 300 nm), but it is in line with the intense absorption at similar wavelengths, corresponding to the salicylate HOMO level-to-Ti^{4+} charge-transfer state.

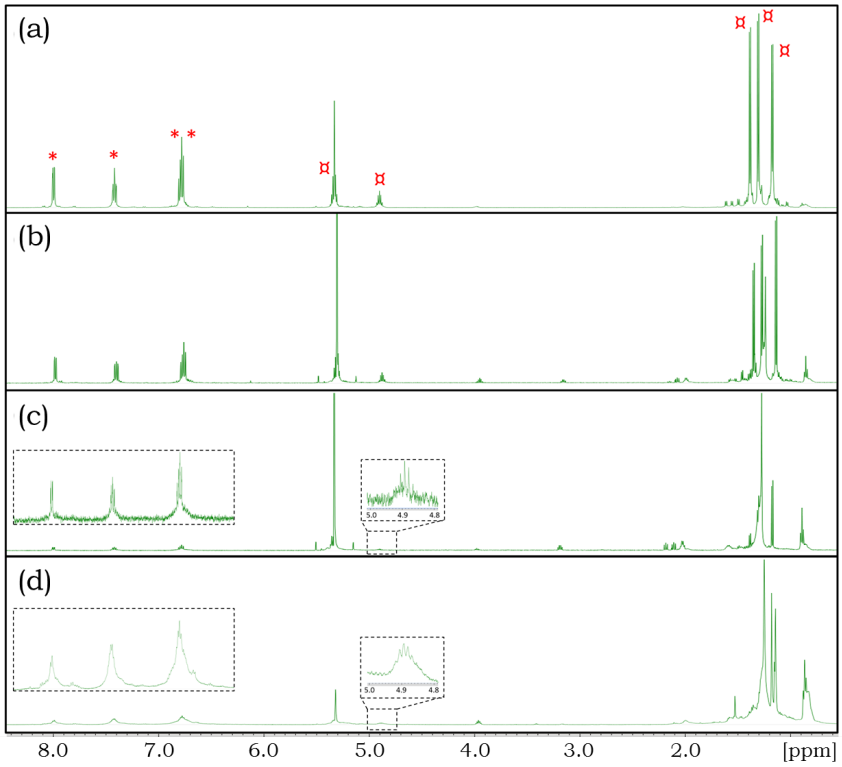

Figure 4.30. ^{1}H NMR spectra of **2-La** at room temperature with the sample prepared by: (a) dissolving 5.2 mg **2-La** in 0.7 mL anhydrous CD_2Cl_2; (b) dissolving one crystal block of **2-La** (around 0.5 mg) in 0.7 mL anhydrous CD_2Cl_2, with the resultant solution being of similar colour intensity to that used for photoluminescence study; (c) further diluted by 5 times from the sample in (b); (d) removing the *n*-pentane solvent *in vacuo* from the **2-La** sample used for the photoluminescence study, and re-dissolving the solid residue in 0.7 mL anhydrous CD_2Cl_2. The ^{1}H signals from the salicylate aromatic ring (denoted by '*') and that from the isopropoxide groups (denoted by '¤'; the signal at around 5.3 ppm overlaps with the residual signal from CD_2Cl_2) are all well resolved, indicating the majority of the **2-La** clusters retain their molecular structure in dilute solution.[221]

In view of all these experimental evidence, it is proposed that the largely red-shifted excitation is a result of the salicylate-to-Ti^{4+} charge-transfer (*i.e.*, ligand-to-metal charge-transfer, LMCT) process, which dramatically lowers the energy required for Ln^{3+} photoluminescence sensitisation. As shown in Figure 4.31 left panel, upon coordination of salicylate ligand with the Ti^{4+} ion, electron can be transferred through either the salicylate HOMO→LUMO→Ti^{4+} route or directly

from salicylate HOMO to Ti^{4+} *d* orbitals. The latter requires a much lower energy to trigger the charge-transfer process. This is also the reason why the **2-Ln** compounds are all bright yellow in colour, although both $Ti(O^iPr)_4$ and salicylic acid are colourless. Despite the fact that similar charge-transfer processes have been widely observed in many other ligand-modified TOCs and TiO_2 nanoparticles, the ability to sensitise Ln^{3+} photoluminescence in Ln-TOCs has not been revealed before.

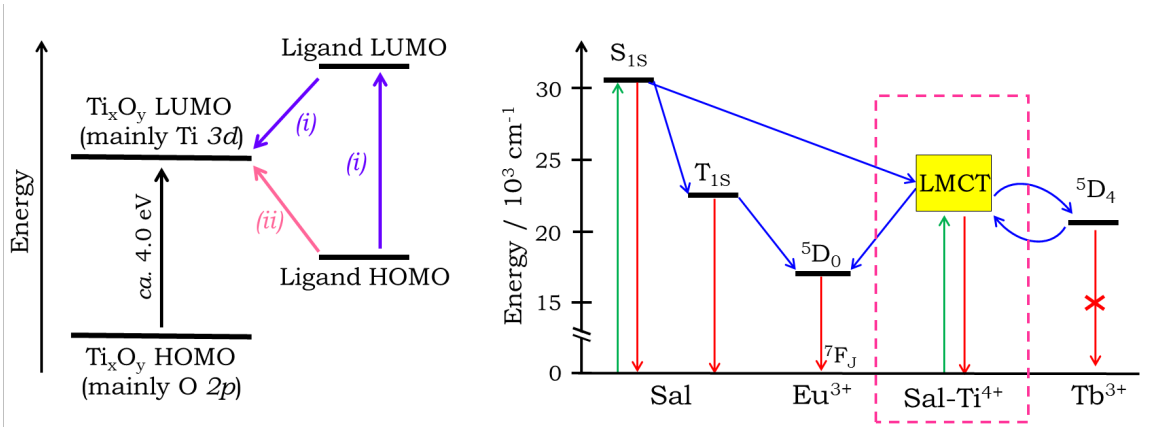

Figure 4.31. Left panel: charge-transfer pathways in ligand-modified TOCs: (i) ligand HOMO→LUMO→Ti^{4+} d orbital and (ii) ligand HOMO→Ti^{4+} *d* orbital. Right panel: proposed energy transfer mechanism for **2-Ln** clusters. **2-Eu** and **2-Tb** are shown as representatives.[221]

The reasons behind the mismatch between the excitation spectra in solution (two bands at *ca.* 300 nm and 400 nm) and in the solid-state (single band at *ca.* 350 nm) samples are unknown. One possibility is that the LMCT processes multiple excited states (n ≥ 1), similar to organic ligands. In the solution-phase absorption spectrum, all these excited states overlap into the broad band centred at *ca.* 350 nm. Only the lowest excited state S_1, corresponding to the excitation band at *ca.* 400 nm, contributes to the Ln^{3+} luminescence sensitisation, and others (S_n, n ≥ 2) are dissipated to the surrounding environment via molecular motion and vibration. However, in the solid-state sample, the cluster molecules are densely packed, and their molecular motion and vibration is much more restricted, so that all the excited states can now be used to sensitise Ln^{3+} luminescence.

Since the emission band at *ca.* 500 nm and the broad feature at 550 - 800 nm are both associated with the LMCT excitation band at *ca.* 400 nm, it is highly likely that they are from the singlet and triplet excited levels of the proposed charge-transfer state, denoted as S_{1ST} and T_{1ST}, respectively. In other words, both fluorescence and phosphorescence can be simultaneously observed at room temperature for **2-Ln** in solution, which is expected for coordination compounds containing heavy atoms (*i.e.*, lanthanides in the present case) because of the strong metal-induced spin-orbit coupling.[303,304] The assignment of the broad feature to phosphorescence is further supported by its higher intensity for **2-Gd** and **2-La** than the other **2-Ln** clusters (Figure 4.32). Since Gd^{3+} possesses an extremely high acceptor energy level at *ca.* 32000 cm^{-1} and La^{3+} does not have any *f* electrons ($4f^0$), energy transfer from the ligands to Gd^{3+} or La^{3+} ions is impossible, leaving a high likelihood that the excited energy is relaxed via the triplet phosphorescence process. Moreover, the relatively higher phosphorescence intensity for **2-Gd** over **2-La** can be explained by the fact that the degree of mixing of the singlet and triplet states in **2-Gd** is greater than that in **2-La**. This is due to the higher paramagnetism of Gd^{3+}, as Gd^{3+} has seven uncoupled electrons in the 4*f* sub-shell whereas La^{3+} has none (thus diamagnetic). Unfortunately, the broad feature at 550 – 800 nm could only be seen in the steady-state measurements but not in the time-resolved system. This could be due to the fact that in steady-state measurements there is continuous population of the excited states with a xenon lamp source and yet the emission intensity is still low; whereas in the time-resolved system, only a ns-pulsed laser with a frequency of 1 Hz was used, which should lead to an even lower population of the excited states.

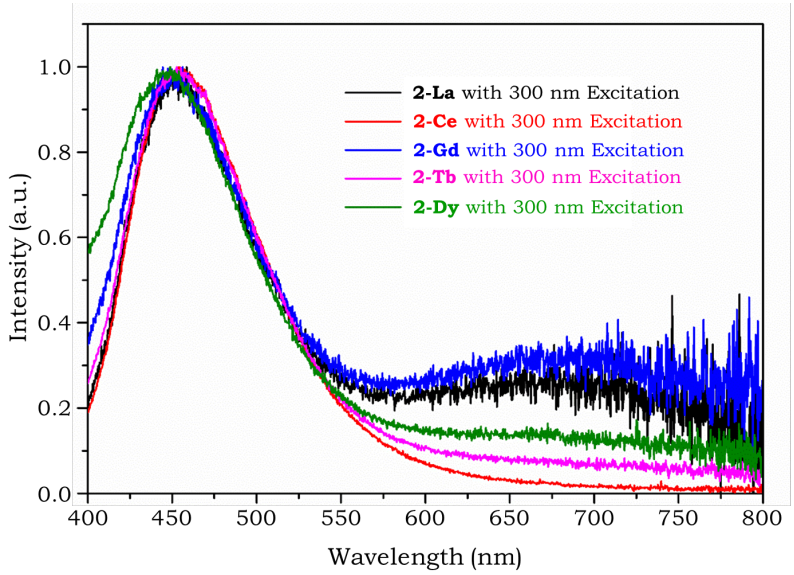

Figure 4.32. Comparison of the normalized steady-state emission spectra for **2-La**, **2-Ce**, **2-Gd**, **2-Tb** and **2-Dy**. The normalisation was based on the main emission band at *ca.* 450 nm.[221]

The proposed energy transfer mechanism involving the LMCT state in the **2-Ln** clusters is shown in the right panel of Figure 4.31, using **2-Eu** as an example in which sensitised Ln^{3+}-centred luminescence occurs (also for **2-Pr**, **2-Nd**, **2-Sm**, **2-Ho** and **2-Er**) and **2-Tb** as an example where this is not observed (for **2-Dy** as well; a detailed energy level diagram containing the proposed LMCT and emissive states of respective Ln^{3+} ions can be found in Figure 4.33). The energy level of the LMCT state relative to the ground level can be estimated to be 21050 cm^{-1} using the red edge of the absorption band (*i.e.*, 475 nm).[290] Upon excitation into the major excitation band at *ca.* 400 nm, the system is firstly excited to the proposed LMCT state before subsequent energy migration to the Eu^{3+} emissive state (*i.e.*, $^5D_0$ at 17500 cm^{-1}). However, this LMCT state is too low in energy to facilitate energy transfer to the Tb^{3+} $^5D_4$ emissive state (*i.e.*, *ca.* 20500 cm^{-1}), resulting in the absence of Tb^{3+}-centred emission signals.

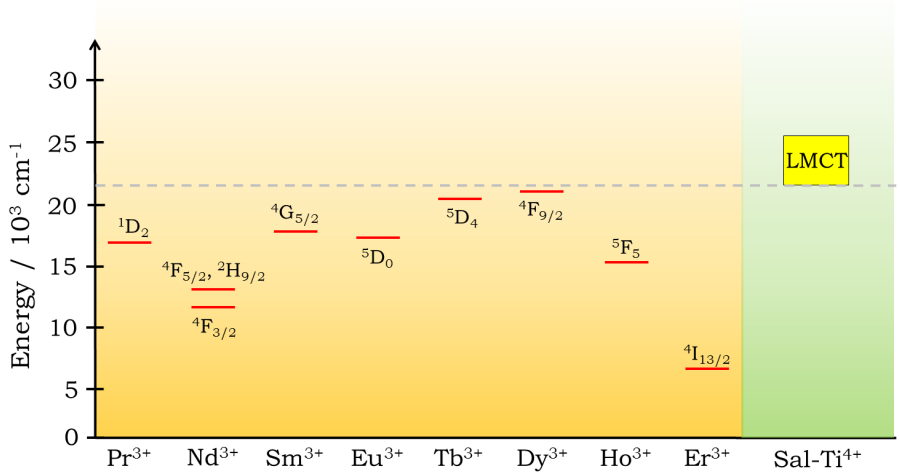

Figure 4.33. Energy diagram of the proposed LMCT state and the emissive state of respective Ln^{3+} ions.[221]

To double-check the proposed energy transfer mechanism, two new related TOCs with the salicylic acid replaced by 4-amino-salicylic acid (Figure 4.34) were synthesised, with the general formula being $[LnTi_6O_3(O^iPr)_9(4\text{-amino-salicylate})_6]$ (**2-Ln-NH$_2$**, Ln = Sm and Eu). The core structure of the **2-Ln-NH$_2$** cluster is similar with that of **2-Ln** (Figure 4.35), with the interstitial Ln^{3+} ion being encapsulated by six hexa-coordinate Ti^{4+} ions. Because the yields were low and the bulk products were impure, only a few brown colour crystalline blocks of **2-Ln-NH$_2$** were manually picked from the reaction mixture, which were then washed with isopropanol and dried *in vacuo*. Syntheses using other $LnCl_3$ salts were also attempted, but no crystalline products could be isolated.

Elemental analysis was performed on these two compounds, with the experimentally found C, H and N content (*i.e.*, 43.0 % C, 5.0 % H and 4.2 % N for **2-Sm-NH$_2$**; 43.1 % C, 5.0 % H, 4.2 % N for **2-Eu-NH$_2$**) satisfactorily matching with the calculated values (43.1 % C, 4.9 % H and 4.4 % N for **2-Sm-NH$_2$**; 43.0 % C, 4.9 % H, 4.4 % N for **2-Eu-NH$_2$**) using the molecular formulae determined by single-crystal X-ray diffraction. These results imply the chemical purity of the isolated crystalline blocks.

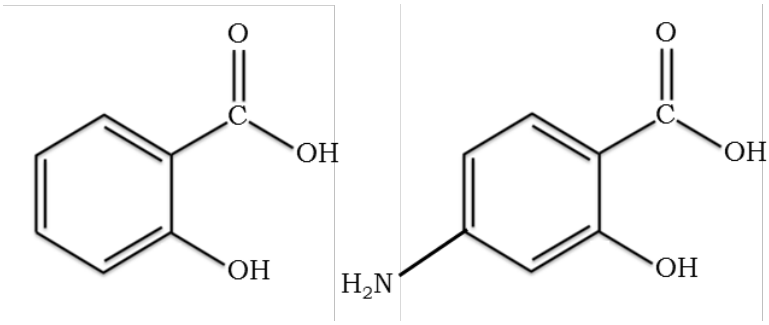

Figure 4.34. Molecular structure of salicylic acid and 4-amino-salicylic acid

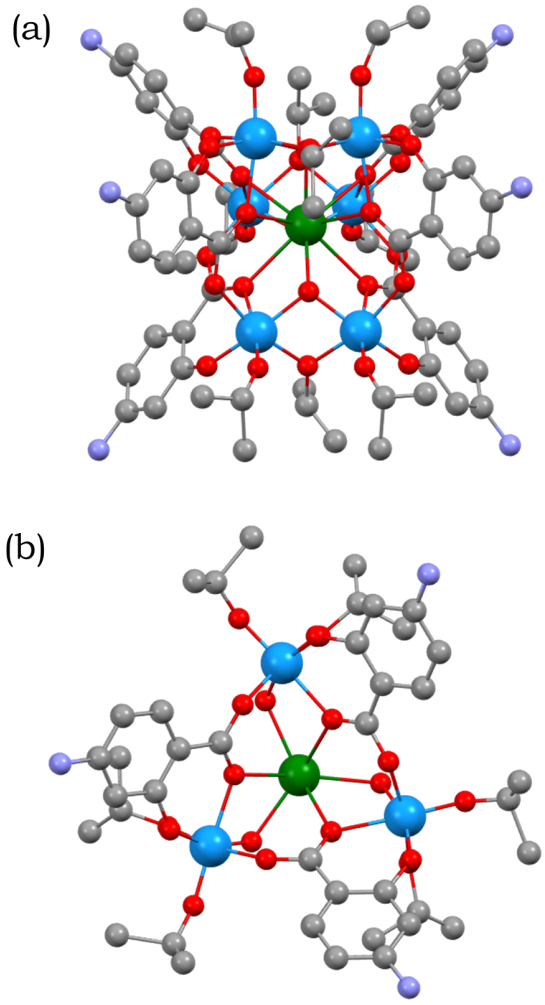

Figure 4.35. Ball-stick representation of the molecular structure of **2-Ln-NH$_2$**, viewed in the direction (a) perpendicular to and (b) along the C_3 axis. Colour code for atoms: Ti = cyan, Ln = green, C = grey, O = red, N = light blue. Hydrogen atoms are omitted for clarity.

As shown in Figure 4.36, the FTIR-ATR fingerprint regions of **2-Ln** and **2-Ln-NH$_2$** (Ln = Sm and Eu) are similar to each other, owning to the identical ligand connectivity in their cluster cores. In the higher-wavenumber functional group region, apart from the peaks in the 3100 – 3000 cm^{-1} and 3000 – 2850 cm^{-1} ranges that can be assigned to the C-H bond in the aromatic and ^{i}Pr moieties, some new peaks in the 3600 – 3100 cm^{-1} range were observed in the **2-Ln-NH$_2$** spectra (Figure 4.36). These new peaks can be readily assigned to the NH$_2$ groups on the aromatic ring, agreeing well with the literature.

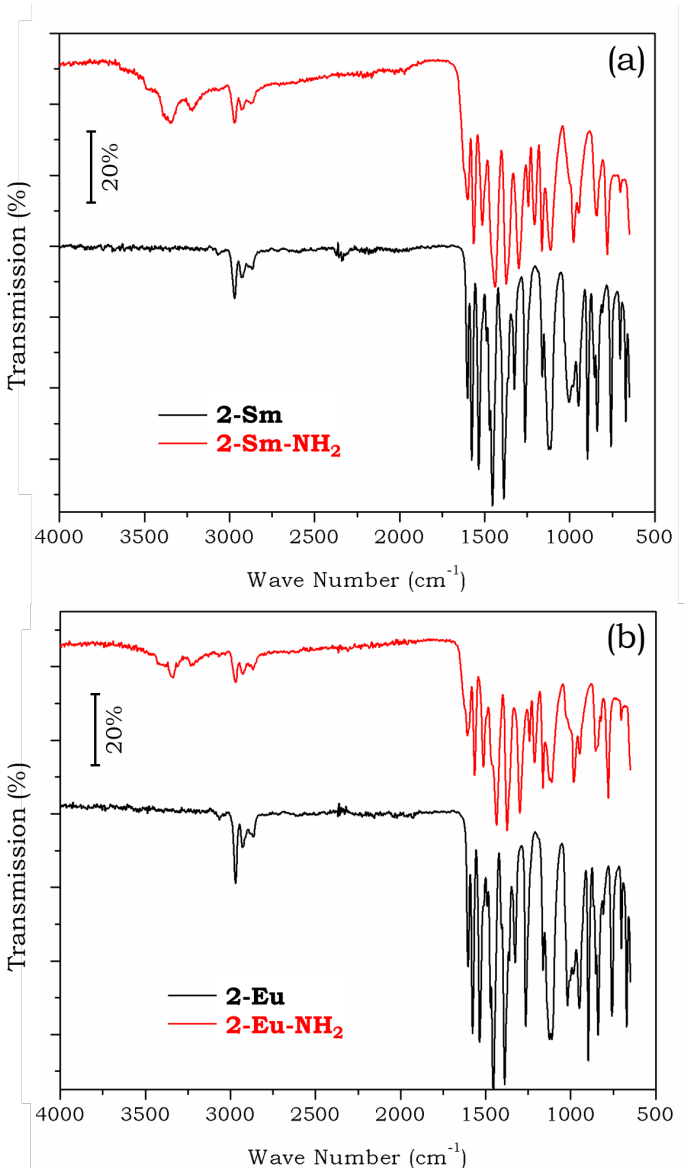

Figure 4.36. FTIR-ATR spectra of (a) **2-Sm** and **2-Sm-NH$_2$**; (b) **2-Eu** and **2-Eu-NH$_2$**

The optical properties of these **2-Ln-NH$_2$** clusters were investigated using the diffuse reflectance spectroscopy (Figure 4.37). High-purity crystalline blocks of **2-Ln-NH$_2$** were ground in a N_2-filled glove box and sealed between quartz windows before transferring to the spectrometer. Using the direct extrapolation method, a band gap of *ca.* 2.60 eV was estimated for both **2-Sm-NH$_2$** and **2-Eu-NH$_2$**, which is 0.10 eV narrower than that of their **2-Ln** counterparts. This is potentially because of the electron donating nature of the NH_2 groups, which should increase the valence band maximum and therefore lead to a narrower optical band gap.

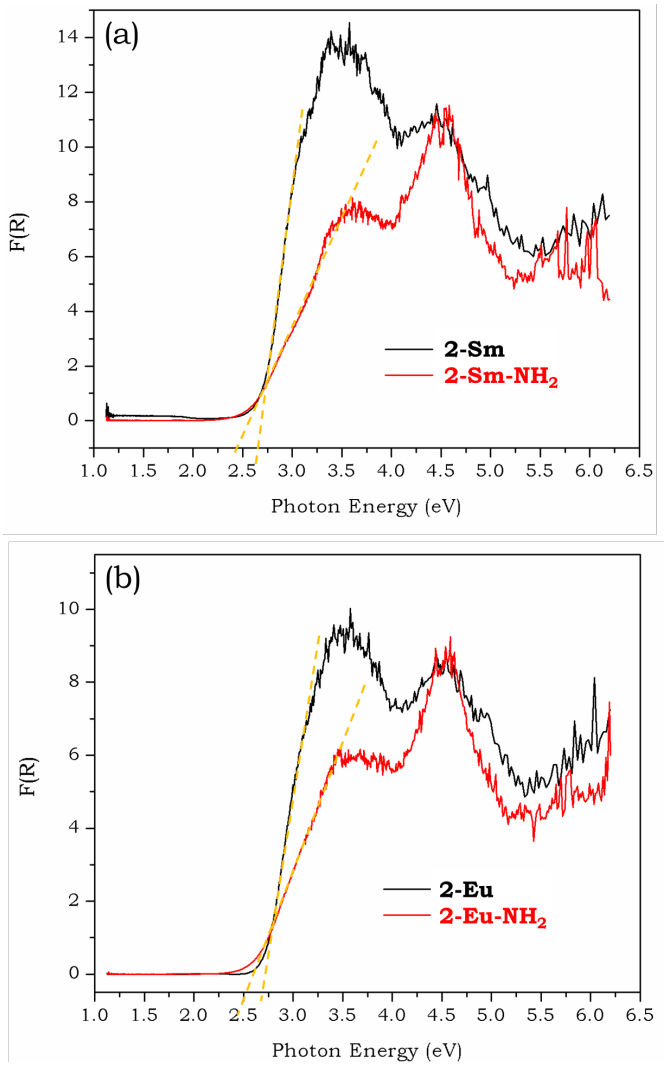

Figure 4.37. The diffuse reflectance spectra of (a) **2-Sm** and **2-Sm-NH$_2$**; (b) **2-Eu** and **2-Eu-NH$_2$**, showing F(R) *vs.* the incident photon energy.

However, no Ln^{3+}-centred photoluminescence signals can be observed for either of the **2-Ln-NH$_2$** clusters (Figure 4.38). This is potentially because of the fact that, with decreased band gap, the resultant LMCT state also becomes lower in energy, which makes it insufficient at facilitating the energy transfer to the Ln^{3+} emissive states. This observation provides tentative support for the proposed energy transfer mechanism from the LMCT excited levels to the Ln^{3+} emissive excited states in the **2-Ln** cluster series.

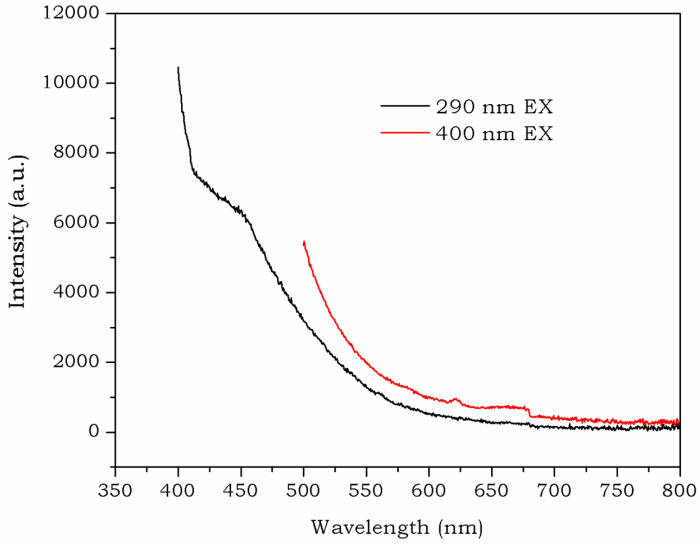

Figure 4.38. Emission spectra of **2-Eu-NH$_2$** with excitation at 290 nm (black trace) and 400 nm (red trace). The Sm-containing cluster exhibits similar behaviour.

4.4.3. Summary and Future Perspectives

This section describes the energy transfer mechanism and photoluminescence properties of the salicylate-coordinated Ln-TOCs of general formula [$LnTi_6O_3(O^iPr)_9$(salicylate)$_6$]. Both visible (for **2-Pr**, **2-Nd**, **2-Sm**, **2-Eu**, **2-Ho** and **2-Er**) and near infrared (for **2-Nd** and **2-Er**) photoluminescence can be sensitised via an excitation band in the visible range up to 475 nm. With the assistance of steady-state and time-resolved photoluminescence spectroscopy, an energy transfer mechanism involving salicylate HOMO to Ti^{4+} *d* orbital charge-transfer state is proposed to account for the red-shifted excitation wavelengths of these

Ln-TOCs. Through the proposed excitation channel, the photoluminescence quantum yield of Nd^{3+} reaches 0.30 ± 0.01% for the **2-Nd** solution, representing one of the highest reported values in the literatures for a Nd^{3+}-complex. This study is a significant step forward in the understanding of the photophysics of lanthanide-containing titanium-oxo clusters coordinated with organic ligands, and should stimulate further interest in related research fields.

In contrast to the unsubstituted salicylate ligands, substitution with the electron-donating NH_2 group in **2-Ln-NH_2** results in no Ln^{3+}-centred photoluminescence. This may suggest that electron-withdrawing groups might be able to improve the efficiency of this process, by means of increasing the LMCT energy state. However, preliminary experiments failed to produce crystalline products using nitro-substituted salicylic acid as the precursor. It should also be noted that, the electron-withdrawing moieties could possibly induce a blue-shift in the excitation wavelengths, as higher excitation energy would be needed. In this context, further synthetic efforts using ligands involving electron-withdrawing or -donating moieties would be of interest in the future as this could offer the possibility of fine-tuning the energy transfer efficiency and also the excitation wavelengths.

On a separate note, LMCT processes are also known to occur in TOCs containing other aromatic ligands (*e.g.*, catechol, 2,3-dihydroxynaphthalene, BINOL, etc.). Further exploration of the synthesis of new clusters containing a range of other aromatic ligands is also worthy of investigation, with the possibility of ultimately providing more control over the energy transfer mechanism in L-Ln-TOCs. This could lead to greater understanding of the molecular photophysics involved and the improvement of design principles for the construction of Ln^{3+}-based photoluminescence devices for technological applications.

4.5. Experimental Section

4.5.1. Synthesis of 2-Ln

All chemicals were purchased from commercial sources and used as received unless otherwise stated. Strict inert-atmospheric conditions (moisture- and O_2-free) were employed throughout all the synthesis and handling procedures by using Schleck and vacuum-line techniques, as well as a N_2-filled glove box (Saffron type α).

Titanium isopropoxide [$Ti(O^iPr)_4$, 5.0 mL, 16.8 mmol], $LnCl_3{\cdot}xH_2O$ (0.5 mmol, including $LaCl_3$, $CeCl_3$, $NdCl_3$, $SmCl_3$, $TbCl_3$, $ErCl_3$, $PrCl_3{\cdot}xH_2O$, $EuCl_3{\cdot}6H_2O$, $GdCl_3{\cdot}6H_2O$, $DyCl_3{\cdot}6H_2O$, $HoCl_3{\cdot}6H_2O$) and salicylic acid (345 mg, 2.5 mmol) were loaded into a Teflon-lined autoclave in a N_2 environment and heated to 150 °C for 72 hours. Gradually cooling to 40 °C and retaining this temperature for another 48 hours before further cooling to room temperature produced crystalline blocks of **2-Ln** (Ln ≠ Er) directly from the reaction mixtures. For **2-Er**, single-crystals were grown by adding 3.0 mL of dry THF to the formed oily yellow solution and storing at -30 °C for a week. The crystalline blocks were filtered off at room temperature, washed with anhydrous isopropanol and dried *in vacuo*. These cluster compounds are stable in air, with no physical appearance changes or loss of crystallinity observed after 1 hour of air exposure. A similar procedure was also used for the synthesis of **2-Ln-NH_2**, with the salicylic acid precursor being replaced by 4-amimo salicylic acid. The reaction solution became dark brown in colour, and the solid-state bulk products were impure. In this case, only a few brown colour crystalline blocks of **2-Ln-NH_2** were manually picked from the reaction mixture, washed with isopropanol and dried *in vacuo*.

4.5.2. Single-Crystal X-Ray Diffraction

Single-crystal X-ray diffraction was carried out using a Bruker D8 Quest (Cu-Kα, λ = 1.54184 Å). Data reduction was executed using the Bruker SAINT Software package. Structure solutions were obtained using the SHELXT-14 software[305] and structure refinement was completed using the SHELXL-14 program.[306] Details of the crystallographic data refinements are provided in Table A2 - A13 in the

Appendix. Although the quality of the X-ray data is relatively poor for all the compounds (apart from **2-Eu**), the structures and connectivity of all of the clusters are determined unambiguously (and supported by the extensive analytical and spectroscopic data). The disorder in ^{i}Pr groups can be resolved satisfactorily by treating the C-C and C-O bond lengths with DFIX and modelling isotropically.

4.5.3. Spectroscopic Analysis

Infrared (IR) spectroscopic measurements were performed on powder samples using a PerkinElmer Spectrum One FTIR-ATR setup fitted with a diamond attenuated total reflectance system. The UV-Vis diffuse reflectance and absorbance spectra were recorded using a VARIAN Cary 50 Bio UV-Vis Spectrophotometer.

4.5.4. Thermal and NMR Analysis

Thermal decomposition behaviour was characterised in air using TGA Q500, TA Instruments. All the NMR spectra were recorded on a Bruker Advance 500 MHz or 400 MHz Cryo-spectrometer at 298 K, and analysed using the Topspin and/or MestReNova software.

4.5.5. Photoluminescence Analysis

The **2-Ln** samples for photoluminescence studies were prepared in anhydrous *n*-pentane, since *n*-pentane was found to give the best excitation spectra and it is a non-coordinating solvent. The solubility of **2-Ln** in anhydrous *n*-pentane is poor and also dependent on the choice of Ln^{3+} ion, making it difficult to precisely control the solution concentration. Therefore, the solution samples for photoluminescence studies were prepared by adding a few high-purity **2-Ln** crystalline blocks (*ca.* 5 mg) into 3.0 mL anhydrous *n*-pentane and incubating for three minutes at room temperature, before decanting the clear solutions from the remaining undissolved solids to a quartz cuvette with a 10 mm path-length. It can be estimated that the solution concentration for photoluminescence measurements is approximately in the range of 50 – 400 μM, depending on the

choice of Ln^{3+} ions. It was further found that the excitation and emission spectra are insensitive to the amount of **2-Ln** used (within the range of a few milligrams) and the incubation time (with the range of a few minutes). All the manipulations were carried out in a N_2-filled glovebox in order to ensure that there was no possibility of aerial hydrolysis of the **2-Ln** compounds, which would give aggregated clusters in solution and/or lanthanide-doped bulk titanium oxide species.

The steady-state photoluminescence data in the visible range was obtained using an Edinburgh Instruments FS5 spectrofluorometer with a monochromated xenon lamp as the light source. All the excitation spectra were corrected for the varied xenon lamp intensity. The steady-state photoluminescence measurements in the NIR region were performed using a Coherent OBIS 405 nm laser for excitation. The luminescence emission was focused into an Andor SOLIS spectrometer, using an InGaAs CCD detector. The photoluminescence quantum yields were measured using the integrating sphere method. Time-resolved photoluminescence studies were carried out using an Edinburgh Instrument flash-photolysis spectrometer LP920 equipped with an Edinburgh Instrument LP-920-K PMT detector and a time-gated Andor DH720 CCD camera. All the measurements were carried out at room temperature under N_2 atmospheric condition unless otherwise stated, and done with the assistance from Mr. James Xiao (Cambridge) and Ms. Gomathy Sandhya Subramanian (Singapore).

CHAPTER 5.

Overall Conclusions

Titanium-oxo clusters (TOCs) of the type $[Ti_xO_y(OR)_z]$ (OR = alkoxide) have attracted considerable research interest in recent years. This interest mainly stems from their use as atomically well-defined molecular models for solid-state TiO_2. Research has also been extended to various applications that are closely related to those of the parent TiO_2 materials. In this context, the thesis has presented research in the design, synthesis and characterisation of chemically modified TOCs with both metal doping and functional ligand decoration (L-M-TOCs), together with their extended novel applications as molecular materials for multifunctional coating and host scaffold uses.

$[Ti_{18}Mn_4O_{30}(OEt)_{20}Phen_3]$ (**1**, Phen = 1,10-phenanthroline) was synthesized by the solvothermal reaction of titanium(IV) ethoxide, manganese(III) acetate dihydrate and 1,10-phenanthroline in anhydrous ethanol at 150 °C. It has been extensively characterised using single-crystal and powder X-ray diffraction, elemental analysis, diffuse reflectance spectroscopy, X-ray photoelectron spectroscopy, electrode-based and solution-phase electrochemical analysis, infrared spectroscopy, mass spectrometry, magnetic analysis and thermogravimetric analysis. Cluster **1** self-assembles into hollow microparticles upon solvent evaporation on both solid surface and flexible textile substrate. This has been developed into a novel coating technology for cellulosic cotton substrates, which readily imparts the coated surface with robust hydrophobicity, antibacterial activity and enhanced UV-blocking capabilities. Nevertheless, it is worth mentioning that the bio-safety of TOCs has to be considered in the context of real-life applications.

The isostructural L-M-TOCs $[LnTi_6O_3(O^iPr)_9(salicylate)_6]$ (**2-Ln**, Ln = La – Er, except for Pm) have also been synthesised, by a solvent-free reaction of titanium(IV) isopropoxide, lanthanide(III) chloride and salicylic acid at 150 °C, and characterised by single-crystal and powder X-ray diffraction, elemental analysis, UV-Vis diffuse reflectance and absorbance spectroscopy, infrared spectroscopy, and thermogravimetric analysis. These isostructural L-M-TOCs provide an excellent basis for investigating the influence of paramagnetic Ln^{3+} ions on the NMR behaviour of the peripheral ligands. Related theoretical

principles on lanthanide-induced NMR shifts have been under development over four decades but have been challenged recently. New experimentally-determined datasets of isostructural compounds can be used to validate and improve the theory in this area. In **2-Ln** the peripheral ligands are separated from the Ln^{3+} centres by diamagnetic Ti^{4+}-oxo linkages and hence only experience a moderate influence from the paramagnetic lanthanide ions. As a result, almost all of the ^{1}H and ^{13}C signals are observed and can be unambiguously assigned, which should be of great value for the corroboration and improvement of existing theoretical principles of lanthanide-induced NMR chemical shifts.

Departing from paramagnetic NMR, these **2-Ln** clusters can also act as a favourable host scaffolds for the study of the photophysical interplay between Ln^{3+} dopants, Ti^{4+} ions and the coordinated ligands. Both visible and near infrared photoluminescence can be sensitised via an excitation band in the visible range up to 475 nm. With the assistance of steady-state and time-resolved photoluminescence spectroscopy, an energy transfer mechanism involving salicylate HOMO to a Ti^{4+} *d* orbital charge-transfer state is proposed to account for the largely red-shifted excitation wavelengths observed. In particular, through the proposed excitation mechanism, the photoluminescence quantum yield of Nd^{3+} reaches 0.30 ± 0.01% for the **2-Nd** solution, and represents one of the highest reported values in the literatures for a Nd^{3+}-complex.

Future works within the scope of this thesis will be: (i) to design other chemically modified TOCs that could be used towards multifunctional coating applications on textile and similar substrates, (ii) to investigate the potential of **2-Ln** clusters as single molecular magnets, (iii) to synthesise Ln-TOCs using aromatic ligands involving electron-withdrawing or -donating moieties that could offer the possibility of fine-tuning the energy transfer efficiency and the excitation wavelengths. With the versatile but synthetically controllable structural features, TOCs represent a unique family of molecular materials that can be customised by introducing favourable metal/non-metal dopants and functional ligands. To this end, a collection of rationally designed TOCs (potentially also the related

polyoxometalate clusters) would provide a useful toolkit for a wide range of technologically important applications.

References

[1] BP, BP Statistical Review of World Energy June 2015, 2015, www.bp.com/statisticalreview.

[2] G. Pfaff and P. Reynders, *Chem. Rev.*, **1999**, *99*, 1963.

[3] J. H. Braun, A. Baidins and R. E. Marganski, *Prog. Org. Coat.*, **1992**, *20*, 105.

[4] A. Salvador, M. C. Pascual-Marti, J. R. Adell, A. Requeni and J. G. March, *J. Pharm. Biomed. Anal.*, **2000**, *22*, 301.

[5] R. Zallen and M. P. Moret, *Solid State Commun.*, **2006**, *137*, 154.

[6] S. A. Yuan, W. H. Chen and S. S. Hu, *Mater. Sci. Eng. C*, **2005**, *25*, 479.

[7] A. Fujishima and K. Honda, *Nature*, **1972**, *238*, 37.

[8] M. Grätzel, *Nature*, **2001**, *414*, 338.

[9] A. Hagfeldt and M. Grätzel, *Chem. Rev.*, **1995**, *95*, 49.

[10] A. L. Linsebigler, G. Lu and J. T. Yates, *Chem. Rev.*, **1995**, *95*, 735.

[11] M. Ni, M. K. H. Leung, D. Y. C. Leung and K. Sumathy, *Renew. Sustain. Energy Rev.*, **2007**, *11*, 401.

[12] X. Chen and S. S. Mao, *Chem. Rev.*, **2007**, *107*, 2891.

[13] D. T. Cromer and K. Herrington, *J. Am. Chem. Soc.*, **1955**, *77*, 4708.

[14] S.-D. Mo and W. Y. Ching, *Physical Review B*, **1995**, *51*, 13023.

[15] W. H. Baur, *Acta Crystallogr.*, **1961**, *14*, 214.

[16] M. Landmann, E. Rauls and W. G. Schmidt, *J. Phys.: Condens. Matter*, **2012**, *24*, 195503.

[17] This was a lecture given by Physicist Richard Feynman at an American Physical Society meeting at California Institute of Technology on December 29, 1959.

[18] J. P. Corden, W. Errington, P. Moore, M. G. Partridge and M. G. H. Wallbridge, *Dalton Trans.*, **2004**, 1846.

[19] N. Steunou, G. Kickelbick, K. Boubekeur and C. Sanchez, *J. Chem. Soc., Dalton Trans.*, **1999**, 3653.

[20] L. G. Hubert-Pfalzgraf, V. Abada and J. Vaissermann, *Polyhedron*, **1999**, *18*, 3497.

[21] P. Coppens, Y. Chen and E. Trzop, *Chem. Rev.*, **2014**, *114*, 9645.

[22] P. D. Matthews, T. C. King and D. S. Wright, *Chem. Commun.*, **2014**, *50*, 12815.

[23] N. Li, P. D. Matthews, H.-K. Luo and D. S. Wright, *Chem. Commun.*, **2016**, *52*, 11180.

[24] L. Rozes and C. Sanchez, *Chem. Soc. Rev.*, **2011**, *40*, 1006.

[25] Z. Liu, J. Lei, M. Frasconi, X. Li, D. Cao, Z. Zhu, S. T. Schneebeli, G. C. Schatz and J. F. Stoddart, *Angew. Chem. Int. Ed.*, **2014**, *53*, 9193.

[26] W.-H. Fang, L. Zhang and J. Zhang, *Chem. Soc. Rev.*, **2018**, *47*, 404.

[27] J. B. Benedict and P. Coppens, *J. Am. Chem. Soc.*, **2010**, *132*, 2938.

[28] N. Narayanam, W.-H. Fang, K. Chintakrinda, L. Zhang and J. Zhang, *Chem. Commun.*, **2017**, *53*, 8078.

[29] G. Zhang, J. Hou, C.-H. Tung and Y. Wang, *Inorg. Chem.*, **2016**, *55*, 3212.

[30] G. Zhang, J. Hou, M. Li, C.-H. Tung and Y. Wang, *Inorg. Chem.*, **2016**, *55*, 4704.

[31] G. Zhang, C. Liu, D.-L. Long, L. Cronin, C.-H. Tung and Y. Wang, *J. Am. Chem. Soc.*, **2016**, *138*, 11097.

[32] G. A. Khitrov, G. F. Strouse and J.-J. Gaumet, *J. Am. Soc. Mass Spectrom.*, **2004**, *15*, 260.

[33] C. Maurer, E. Pittenauer, V. A. Du, G. Allmaier and U. Schubert, *Dalton Trans.*, **2012**, *41*, 2346.

[34] S. Eslava, A. C. Papageorgiou, S. K. Beaumont, G. Kyriakou, D. S. Wright and R. M. Lambert, *Chem. Mater.*, **2010**, *22*, 5174.

[35] R. Schmid, A. Mosset and J. Galy, *J. Chem. Soc., Dalton Trans.*, **1991**, 1999.

[36] U. Schubert, E. Arpac, W. Glaubitt, A. Helmerich and C. Chau, *Chem. Mater.*, **1992**, *4*, 291.

[37] U. Schubert, *J. Mater. Chem.*, **2005**, *15*, 3701.

[38] S. O. Baumann, M. Bendova, H. Fric, M. Puchberger, C. Visinescu and U. Schubert, *Eur. J. Inorg. Chem.*, **2009**, 3333.

[39] J. B. Benedict, R. Freindorf, E. Trzop, J. Cogswell and P. Coppens, *J. Am. Chem. Soc.*, **2010**, *132*, 13669.

[40] M.-Y. Gao, F. Wang, Z.-G. Gu, D.-X. Zhang, L. Zhang and J. Zhang, *J. Am. Chem. Soc.*, **2016**, *138*, 2556.

[41] W.-H. Fang, L. Zhang and J. Zhang, *J. Am. Chem. Soc.*, **2016**, *138*, 7480.

[42] B. Botar, P. Kögerler and C. L. Hill, *Chem. Commun.*, **2005**, 3138.

[43] Y. Chen, E. Trzop, A. Makal, J. D. Sokolow and P. Coppens, *Inorg. Chem.*, **2013**, *52*, 4750.

[44] J. Hu, L. Zhan, G. Zhang, Q. Zhang, L. Du, C.-H. Tung and Y. Wang, *Inorg. Chem.*, **2016**, *55*, 8493.

[45] Y. Chen, E. Trzop, A. Makal, Y.-S. Chen and P. Coppens, *Dalton Trans.*, **2014**, *43*, 3839.

[46] Y. Lv, J. Cheng, P. D. Matthews, J. P. Holgado, J. Willkomm, M. Leskes, A. Steiner, D. Fenske, T. C. King, P. T. Wood, L. Gan, R. M. Lambert and D. S. Wright, *Dalton Trans.*, **2014**, *43*, 8679.

[47] S. Eslava, M. McPartlin, R. I. Thomson, J. M. Rawson and D. S. Wright, *Inorg. Chem.*, **2010**, *49*, 11532.

[48] Y. Chen, J. Sokolow, E. Trzop, Y.-S. Chen and P. Coppens, *J. Chin. Chem. Soc.*, **2013**, *60*, 887.

[49] S. Yang, H.-C. Su, J.-L. Hou, W. Luo, D.-H. Zou, Q.-Y. Zhu and J. Dai, *Dalton Trans.*, **2017**, *46*, 9639.

[50] S. Eslava, F. Hengesbach, M. McPartlin and D. S. Wright, *Chem. Commun.*, **2010**, *46*, 4701.

[51] Y. Lv, J. Willkomm, A. Steiner, L. Gan, E. Reisner and D. S. Wright, *Chem. Sci.*, **2012**, *3*, 2470.

[52] Y.-Y. Wu, P. Wang, Y.-H. Wang, J.-B. Jiang, G.-Q. Bian, Q.-Y. Zhu and J. Dai, *J. Mater Chem. A*, **2013**, *1*, 9862.

[53] Y. Lv, J. Cheng, A. Steiner, L. Gan and D. S. Wright, *Angew. Chem. Int. Ed.*, **2014**, *53*, 1934.

[54] K. N. Jarzembska, Y. Chen, J. N. Nasca, E. Trzop, D. F. Watson and P. Coppens, *Phys. Chem. Chem. Phys.*, **2014**, *16*, 15792.

[55] S. Eslava, B. P. R. Goodwill, M. McPartlin and D. S. Wright, *Inorg. Chem.*, **2011**, *50*, 5655.

[56] J. Zhang, W. Hu, J. Zhang, S. Liu, J. Tong, X. Hou, W. Liu, J. Yang and B. Liu, *J. Phys. Chem. C*, **2017**, *121*, 18326.

[57] S. Liu, W. Hu, J. K. Nath, J. Tong, X. Hou, W. Liu, J. Yang and B. Liu, *Dalton Trans.*, **2017**, *46*, 678.

[58] J.-X. Liu, X.-C. Zeng, L. Zhang and J. Zhang, *Dalton Trans.*, **2016**, *45*, 4501.

[59] C. Artner, S. Kronister, M. Czakler and U. Schubert, *Eur. J. Inorg. Chem.*, **2014**, *2014*, 5596.

[60] Y. Lv, J. Willkomm, M. Leskes, A. Steiner, T. C. King, L. Gan, E. Reisner, P. T. Wood, and D. S. Wright, *Chem. Eur. J.*, **2012**, *18*, 11867.

[61] Y. Lv, M. Yao, J. P. Holgado, T. Roth, A. Steiner, L. Gan, R. M. Lambert and D. S. Wright, *RSC Adv.*, **2013**, *3*, 13659.

[62] S. Wang, H.-C. Su, L. Yu, X.-W. Zhao, L.-W. Qian, Q.-Y. Zhu and J. Dai, *Dalton Trans.*, **2015**, *44*, 1882.

[63] D.-F. Lu, X.-J. Kong, T.-B. Lu, L.-S. Long and L.-S. Zheng, *Inorg. Chem.*, **2017**, *56*, 1057.

[64] G.-L. Zhang, S. Wang, J.-L. Hou, C.-J. Mo, C.-J. Que, Q.-Y. Zhu and J. Dai, *Dalton Trans.*, **2016**, *45*, 17681.

[65] Y. Lv, Z. Cai, D. Yan, C. Su, W. Li, W. Chen, Z. Ren, Y. Wei, O. Mi, C. Zhang and D. S. Wright, *RSC Adv.*, **2016**, *6*, 57.

[66] D.-F. Lu, Z.-F. Hong, J. Xie, X.-J. Kong, L.-S. Long and L.-S. Zheng, *Inorg. Chem.*, **2017**, *56*, 12186.

[67] Y. Lv, W. Du, Y. Ren, Z. Cai, K. Yu, C. Zhang, Z. Chen and D. S. Wright, *Inorg. Chem. Front.*, **2016**, *3*, 1119.

[68] G. Westin, R. Norrestam, M. Nygren and M. Wijk, *J. Solid State Chem.*, **1998**, *135*, 149.

[69] F. D. M. Haldane and P. W. Anderson, *Phys. Rev. B*, **1976**, *13*, 2553.

[70] X. Li, Z. Li and J. Yang, *Phys. Rev. Lett.*, **2014**, *112*, 018301.

[71] P. Gorai, A. G. Hollister and E. G. Seebauer, *Appl. Phys. Lett.*, **2013**, *103*, 141601.

[72] S. Hanf, P. D. Matthews, N. Li, H.-K. Luo and D. S. Wright, *Dalton Trans.*, **2017**, *46*, 578.

[73] R. Asahi, T. Morikawa, T. Ohwaki, K. Aoki and Y. Taga, *Science*, **2001**, *293*, 269.

[74] S. In, A. Orlov, R. Berg, F. Garc, S. Pedrosa-Jimenez, M. S. S. Tikhov, D. S. Wright and R. M. Lambert, *J. Am. Chem. Soc.*, **2007**, *129*, 13790.

[75] S. In, A. Orlov, F. Garcia, M. Tikhov, D. S. Wright and R. M. Lambert, *Chem. Commun.*, **2006**, 4236.

[76] Q.-R. Ding, J.-X. Liu, N. Narayanam, L. Zhang and J. Zhang, *Dalton Trans.*, **2017**, *46*, 16000.

[77] X. Fan, N. Narayanam, M. Gao, L. Zhang and J. Zhang, *Dalton Trans.*, **2018**, *47*, 663.

[78] J. Bao, L. Gundlach, Z. Yu, J. B. Benedict, R. C. Snoeberger III, V. S. Batista, P. Coppens and P. Piotrowiak, *J. Phys. Chem. C*, **2016**, *120*, 20006.

[79] R. C. Snoeberger III, K. J. Young, J. Tang, L. J. Allen, R. H. Crabtree, G. W. Brudvig, P. Coppens, V. S. Batista and J. B. Benedict, *J. Am. Chem. Soc.*, **2012**, *134*, 8911.

[80] C. F. A. Negre, K. J. Young, M. B. Oviedo, L. J. Allen, C. G. Sánchez, K. N. Jarzembska, J. B. Benedict, R. H. Crabtree, P. Coppens, G. W. Brudvig, V. S. Batista, *J. Am. Chem. Soc.*, **2014**, *136*, 16420.

[81] M Janek, T. M. Muziol and P. Piszczek, *Polyhedron*, **2018**, *141*, 110.

[82] M.-Y. Gao, S. Chen, L.-X. Hu, L. Zhang and J. Zhang, *Dalton Trans.*, **2017**, *46*, 10630.

[83] Y.-Y. Wu, W. Luo, Y.-H. Wang, Y.-Y. Pu, X. Zhang, L.-S. You, Q.-Y. Zhu and J. Dai, *Inorg. Chem.*, **2012**, *51*, 8982.

[84] J. D. Sokolow, E. Trzop, Y. Chen, J. Tang, L. J. Allen, R. H. Crabtree, J. B. Benedict and P. Coppens, *J. Am. Chem. Soc.*, **2012**, *134*, 11695.

[85] K. Sharma, R. Antony, A. C. Kalita, S. K. Gupta, P. Davis and R. Murugavel, *Inorg. Chem.*, **2017**, *56*, 12848.

[86] T. Frot, S. Cochet, G. Laurent, C. Sassoye, M. Popall, C. Sanchez and L. Rozes, *Eur. J. Inorg. Chem.*, **2010**, *2010*, 5650.

[87] J.-L. Hou, W. Luo, Y. Guo, P. Zhang, S. Yang, Q.-Y. Zhu and J. Dai, *Inorg. Chem.*, **2017**, *56*, 6451.

[88] Y. Fan, H.-M. Li, R.-H. Duan, H.-T. Lu, J.-T. Cao, G.-D. Zou and Q.-S. Jing, *Inorg. Chem.*, **2017**, *56*, 12775.

[89] Y. Fan, Y. Cui, G.-D. Zou, R.-H. Duan, X. Zhang, Y.-X. Dong, H.-T. Lv, J.-T. Cao and Q.-S. Jing, *Dalton Trans.*, **2017**, *46*, 8057.

[90] Y.-Y. Wu, X.-W. Lu, M. Qi, H.-C. Su, X.-W. Zhao, Q.-Y. Zhu and J. Dai, *Inorg. Chem.*, **2014**, *53*, 7233.

[91] R. Mahrwald and B. Schetter, *Org. Lett.*, **2006**, *8*, 281.

[92] J. Hou, J. Hu, Q. Sun, G. Zhang, C.-H. Tung and Y. Wang, *Inorg. Chem.*, **2016**, *55*, 7075.

[93] G. Fornasieri, L. Rozes, S. L. Calvé, B. Alonso, D. Massiot, M. N. Rager, M. Evain, K. Boubekeur and C. Sanchez, *J. Am. Chem. Soc.*, **2005**, *127*, 4869.

[94] W.-H. Fang, L. Zhang and J. Zhang, *Dalton Trans.*, **2017**, *46*, 803.

[95] R. Hayami, T. Sagawa, S. Tsukada, K. Yamamoto and T. Gunji, *Polyhedron*, **2018**, *147*, 1.

[96] R.-H. Wu, M. Guo, M.-X. Yu and L.-G. Zhu, *Dalton Trans.*, **2017**, *46*, 14348.

[97] N. Narayanam, K. Chintakrinda, W.-H. Fang, Y, Kang, L. Zhang and J. Zhang, *Inorg. Chem.*, **2016**, *55*, 10294.

[98] C. Chaumont, A. Chaumont, N. Kyritsakas, P. Mobian and M. Henry, *Dalton Trans.*, **2016**, *45*, 8760.

[99] K. Gigant, A. Rammal and M. Henry, *J. Am. Chem. Soc.*, **2001**, *123*, 11632.

[100] B.-C. Zhu, L. Zhang and J. Zhang, *Inorg. Chem. Commun.*, **2017**, *86*, 14.

[101] A. Rammal, F. Brisach and M. Henry, *J. Am. Chem. Soc.*, **2001**, *123*, 5612.

[102] J.-F. Wang, W.-H. Fang, D.-S. Li, L. Zhang and J. Zhang, *Inorg. Chem.*, **2017**, *56*, 2367.

[103] J.-X. Liu M.-Y. Gao, W.-H. Fang, L. Zhang and J. Zhang, *Angew. Chem. Int. Ed.*, **2016**, *55*, 5160.

[104] J. Bao, L. Gundlach, Z. Yu, J. B. Benedict, R. C. Snoeberger III, V. S. Batista, P. Coppens and P. Piotrowiak, *J. Phys. Chem. C*, **2016**, *120*, 20006.

[105] H.-T. Lv, Y. Cui, Y.-M. Zhang, H.-M. Li, G.-D. Zou, R.-H. Duan, J.-T. Cao, Q.-S. Jing and Y. Fan, *Dalton Trans.*, **2017**, *46*, 12313.

[106] M. Lomoschitz, H. Peterlik, K. Zorn, S. O. Baumann and U. Schubert, *J. Mater. Chem.*, **2010**, *20*, 5527.

[107] L. Wu, J. C. Yu, L. Zhang, X. Wang and W. Ho, *J. Solid State Chem.*, **2004**, *177*, 2584.

[108] S. Eslava, A. Reynal, V. G. Rocha, S. Barg and E. Saiz, *J. Mater. Chem. A*, **2016**, *4*, 7200.

[109] M. Martos, B. Julián-López, J. V. Folgado, E. Cordoncillo and P. Escribano, *Eur. J. Inorg. Chem.*, **2008**, 3163.

[110] A. Rammal, F. Brisach and M. Henry, *C. R. Chimie*, **2002**, *5*, 59.

[111] T. J. Boyle, L. J. Tribby, T. M. Alam, S. D. Bunge and G. P. Holland, *Polyhedron*, **2005**, *24*, 1143.

[112] T. J. Boyle, R. P. Tyner, T. M. Alam, B. L. Scott, J. W. Ziller and B. G. Potter Jr., *J. Am. Chem. Soc.*, **1999**, *121*, 12104.

[113] I. Karatchevtseva, D. J. Cassidy, Z. Zhang, G. Triani, K. S. Finnie, S. L. Cram and C. J. Barbé, *J. Am. Ceram. Soc.*, **2008**, *91*, 2015.

[114] A. Mehner, T. Rüffer, H. Lang, A. Pohlers, W. Hoyer and S. Spange, *Adv. Mater.*, **2008**, *20*, 4113.

[115] Z. Xu, H. Fu, T. Wen, L. Zhang and J. Zhang, *Int. J. Hydrogen Energy*, **2017**, *42*, 24737.

[116] G. Férey, *Chem. Soc. Rev.*, **2008**, *37*, 191.

[117] U. Schubert, *Chem. Soc. Rev.*, **2011**, *40*, 575.

[118] N. Miele-Pajot, L. G. Hubert-Pfalzgraf, R. Papiernik, J. Vaissermann and R. Collier, *J. Mater. Chem.*, **1999**, *9*, 3027.

[119] N. Steunou, S. Förster, P. Florian, C. Sanchez and M. Antonietti, *J. Mater. Chem.*, **2002**, *12*, 3426.

[120] M. Dan-Hardi, C. Serre, T. Frot, L. Rozes, G. Maurin, C. Sanchez and G. Férey, *J. Am. Chem. Soc.*, **2009**, *131*, 10857.

[121] H. Assi, G. Mouchaham, N. Steunou, T. Devic and C. Serre, *Chem. Soc. Rev.*, **2017**, *46*, 3431.

[122] Y. Chen, J. D. Sokolow, E. Trzop and P. Coppens, *Dalton Trans.*, **2013**, *42*, 15285.

[123] P. Heinz, M. Puchberger, M. Bendova, S. O. Baumann and U. Schubert, *Dalton Trans.*, **2010**, *39*, 7640.

[124] Y. Horiuchi, T. Toyao, M. Saito, K. Mochizuki, M. Iwata, H. Higashimura, M. Anpo and M. Matsuoka, *J. Phys. Chem. C*, **2012**, *116*, 20848.

[125] Y. Fu, D. Sun, Y. Chen, R. Huang, Z. Ding, X. Fu and Z. Li, *Angew. Chem. Int. Ed.*, **2012**, *51*, 3364.

[126] M. A. Nasalevich, M. G. Goesten, T. J. Savenije, F. Kapteijn and J. Gascon, *Chem. Commun.*, **2013**, *49*, 10575.

[127] J. García-Glez, Z. Amghouz, I. da Silva, C. O. Ania, J. B. Parra, C. Trobajo and S. García-Granda, *Chem. Commun.*, **2017**, *53*, 2249.

[128] L. Zou, D. Feng, T.-F. Liu, Y.-P. Chen, S. Yuan, K. Wang, X. Wang, S. Fordham and H.-C. Zhou, *Chem. Sci.*, **2016**, *7*, 1063.

[129] S. Yuan, T.-F. Liu, D. Feng, J. Tian, K. Wang, J. Qin, Q. Zhang, Y.-P. Chen, M. Bosch, L. Zou, S. J. Teat, S. J. Dalgarno and H.-C. Zhou, *Chem. Sci.*, **2015**, *6*, 3926.

[130] C. Wang, C. Liu, X. He and Z.-M. Sun, *Chem. Commun.*, **2017**, *53*, 11670.

[131] C. Wang, C. Liu, H.-R. Tian, L.-J. Li and Z.-M. Sun, *Chem. Eur. J.*, **2018**, *24*, 2952.

[132] W.-H. Fang, J.-F. Wang, L. Zhang and J. Zhang, *Chem. Mater.*, **2017**, *29*, 2681.

[133] Y.-H. Lai, C.-Y. Lin, Y. Lv, T. C. King, A. Steiner, N. M. Muresan, L. Gan, D. S. Wright and E. Reisner, *Chem. Commun.*, **2013**, *49*, 4331.

[134] J.-X. Yin, P. Huo, S. Wang, J. Wu, Q.-Y. Zhu and J. Dai, *J. Mater. Chem. C*, **2015**, *3*, 409.

[135] Y.-H. Lai, T. C. King, D. S. Wright and E. Reisner, *Chem. Eur. J.*, **2013**, *19*, 12943.

[136] C. Chaumont, P. Mobian and M. Henry, *Dalton Trans.*, **2014**, *43*, 3416.

[137] J.-L. Hou, W. Lou, Y.-Y. Wu, H.-C. Su, G.-L. Zhang, Q.-Y. Zhu and J. Dai, *Dalton Trans.*, **2015**, *44*, 19829.

[138] L. Ni, D. Liang, Y. Cai, G. Diao and Z. Zhou, *Dalton Trans.*, **2016**, *45*, 7581.

[139] W. Luo and G. Ge, *J. Cluster Sci.*, **2016**, *27*, 635.

[140] M.-Y. Gao, W.-H. Fang, T. Wen, L. Zhang and J. Zhang, *Cryst. Growth Des.*, **2017**, *17*, 3592.

[141] Y. Lin, Y.-F. Zhu, Z.-H. Chen, F.-H. Liu, L. Zhao and Z.-M. Su, *Inorg. Chem. Commun.*, **2014**, *40*, 22.

[142] Z. Jiang, J. Liu, M. Gao, X. Fan, L. Zhang and J. Zhang, *Adv. Mater.*, **2017**, *29*, 1603369.

[143] D.-F. Lu, Z.-F. Hong, J. Xie, X.-J. Kong, L.-S. Long and L.-S. Zheng, *Inorg. Chem.*, **2017**, *56*, 12186.

[144] F. Bella, C. Gerbaldi, C. Barolo and M. Grätzel, *Chem. Soc. Rev.*, **2015**, *44*, 3431.

[145] Z. Ning, Y. Fu and H. Tian, *Energy Environ. Sci.*, **2010**, *3*, 1170.

[146] H.-C. Su, Y.-Y. Wu, J.-L. Hou, G.-L. Zhang, Q.-Y. Zhu and J. Dai, *Chem. Commun.*, **2016**, *52*, 4072.

[147] Y. Guo, J.-L. Hou, W. Luo, Z.-Q. Li, D.-H. Zou, Q.-Y. Zhu and J. Dai, *J. Mater. Chem. A*, **2017**, *5*, 18270.

[148] K. Mikami, Y. Matsumoto and L. Xu, *Inorg. Chim. Acta*, **2006**, *359*, 4159.

[149] R. Ishimoto, K. Kamata, K. Suzuki, K. Yamaguchi and N. Mizuno, *Dalton Trans.*, **2015**, *44*, 10947.

[150] S. Pandiaraju, G. Chen, A. Lough and A. K. Yudin, *J. Am. Chem. Soc.*, **2001**, *123*, 3850.

[151] J. Balsells, T. J. Davis, P. Carroll and P. J. Walsh, *J. Am. Chem. Soc.*, **2002**, *124*, 10336.

[152] B. Schetter, B. Ziemer, G. Schnakenburg and R. Mahrwald, *J. Org. Chem.*, **2008**, *73*, 813.

[153] R. Yu, Y. Yamashita and S. Kobayashi, *Adv. Synth. Catal.*, **2009**, *351*, 147.

[154] M. Terada, Y. Matsumoto, Y. Nakamura and K. Mikami, *Inorg. Chim. Acta*, **1999**, *296*, 267.

[155] K. Mikami, M. Ueki, Y. Matsumoto and M. Terada, *Chirality*, **2001**, *13*, 541.

[156] K. Hong, W. Bak and H. Chun, *Inorg. Chem.*, **2014**, *53*, 7288.

[157] K. Hong and H. Chun, *Inorg. Chem.*, **2013**, *52*, 9705.

[158] N. B. McKeown, *J. Mater. Chem.*, **2010**, *20*, 10588.

[159] C. Zhao, Y.-Z. Han, S. Dai, X. Chen, J. Yan, W. Zhang, H. Su, S. Lin, Z. Tang, B. K. Teo and N. Zheng, *Angew. Chem. Int. Ed.*, **2017**, *56*, 16252.

[160] Y.-Y. Huang, *J. Phys. Chem.*, **1973**, *77*, 103.

[161] E. Beyreuther, S. Grafström, L. M. Eng, C. Thiele and K. Dörr, *Phys. Rev. B*, **2006**, *73*, 155425.

[162] V. R. Galakhov, M. Demeter, S. Bartkowski, M. Neumann, N. A. Ovechkina, E. Z. Kurmaev, N. I. Lobachevskaya, Y. M. Mukovskii, J. Mitchell and D. L. Ederer, *Phys. Rev. B*, **2002**, *65*, 113102.

[163] L. Z. Zhao and V. Young, *J. Electron. Spectrosc. Relat. Phenom.*, **1984**, *34*, 45.

[164] Y. Gorlin and T. F. Jaramillo, *J. Am. Chem. Soc.*, **2010**, *132*, 13612.

[165] C. Bosch-Navarro, E. Coronado, C. Martí-Gastaldo, B. Rodríguez-González and L. M. Liz-Marzán, *Adv. Funct. Mater.*, **2012**, *22*, 979.

[166] N. Li, P. D. Matthews, J. J. Leung, T. C. King, P. T. Wood, H.-K. Luo and D. S. Wright, *Dalton Trans.*, 2015, 44, 19090.

[167] L. Lu, X. Xia, J. K. Luo and G. Shao, *J. Phys. D: Appl. Phys.*, **2012**, *45*, 485102.

[168] Q. Javed, F. P. Wang, M. Y. Rafique, A. M. Toufiq, Q. S. Li, H. Mahmood and W. Khan, *Nanotechnology*, **2012**, *23*, 415603.

[169] X. Gu, J. Yue, L. Li, H. Xue, J. Yang and X. Zhao, *Electrochimica Acta*, **2015**, *184*, 250.

[170] Q. Javed, F. P. Wang, M. Y. Rafique, A. M. Toufiq, Q. S. Li, H. Mahmood and W. Khan, *Nanotechnology*, **2012**, *23*, 415603.

[171] Q. Javed, F. P. Wang, M. Y. Rafique, A. M. Roufiq and M. Z. Iqbal, *Chin. Phys. B*, **2012**, *21*, 117311.

[172] R. Schmid, A. Mosset and J. Galy, *J. Chem. Soc., Dalton Trans.*, **1991**, 1999.

[173] L. Cao, D. Chen, W.-Q. Wu, J. Z. Y. Tan and R. A. Caruso, *J. Mater. Chem. A*, **2017**, *5*, 3645.

[174] X. Hu, G. Zeng, J. Chen, C. Lu and Z. Wen, *J. Mater. Chem. A*, **2017**, *5*, 4535.

[175] M. Regue, K. Armstrong, D. Walsh, E. Richards, A. L. Johnson and S. Eslava, *Sustainable Energy Fuels*, **2018**, *2*, 2674.

[176] M. Kitano, M. Matsuoka, M. Ueshima and M. Anpo, *Appl. Catal., A*, **2007**, *325*, 1.

[177] M. Pelaez, N. T. Nolan, S. C. Pillai, M. K. Seery, P. Falaras, A. G. Kontos, P. S. M. Dunlop, J. W. J. Hamilton, J. A. Byrne, K. O'Shea, M. H. Entezari and D. D. Dionysiou, *Appl. Catal., B*, **2012**, *125*, 331.

[178] A. C. Balazs, T. Emrick and T. P. Russell, *Science*, **2006**, *314*, 1107.

[179] A. F. Abouraddy, M. Bayindir, G. Benoit, S. D. Hart, K. Kuriki, N. Orf, O. Shapira, F. Sorin, B. Temelkuran, and Y. Fink, *Nature Mater.*, **2007**, *6*, 336.

[180] F. Natalio, R. Fuchs, S. R. Cohen, G. Leitus, G. Fritz-Popovski, O. Paris, M. Kappl and H.-J. Butt, *Science*, **2017**, *357*, 1118.

[181] Z. Li, Z. Xu, Y. Liu, R. Wang and C. Gao, *Nature Commun.*, **2016**, *7*, 13684.

[182] Y. Qin, X. Wang and Z. L. Wang, *Nature*, **2008**, *451*, 809.

[183] J. A. Rogers, T. Someya and Y. Huang, *Science*, **2010**, *327*, 1603.

[184] T. Someya, Z. Bao and G. G. Malliaras, *Nature*, **2016**, *540*, 379.

[185] W. Gao, S. Emaminejad, H. Y. Y. Nyein, S. Challa, K. Chen, A. Peck, H. M. Fahad, H. Ota, H. Shiraki, D. Kiriya, D.-H. Lien, G. A. Brooks, R. W. Davis and A. Javey, *Nature*, **2016**, *529*, 509.

[186] A. Chortos, J. Liu and Z. Bao, *Nature Mater.*, **2016**, *15*, 937.

[187] K. C. Krogman, J. L. Lowery, N. S. Zacharia, G. C. Rutledge and P. T. Hammond, *Nature Mater.*, **2009**, *8*, 512.

[188] Y. Bai, I. Mora-Seró, F. D. Angelis, J. Bisquert and P. Wang, *Chem. Rev.*, **2014**, *114*, 10095.

[189] X. Chen, L. Liu, P. Y. Yu and S. S. Mao, *Science*, **2011**, *331*, 746.

[190] M. Zimbone, M. A. Buccheri, G. Cacciato, R. Sanz, G. Rappazzo, S. Boninelli, R. Reitano, L. Romano, V. Privitera and M. G. Grimaldi, *Applied Catalysis B: Environmental*, **2015**, *165*, 487.

[191] S. Benerjee, D. D. Dionysiou and S. C. Pillai, *Applied Catalysis B: Environmental*, **2015**, *176-177*, 396.

[192] J. Y. Huang, S. H. Li, M. Z. Ge, L. N. Wang, T. L. Xing, G. Q. Chen, X. F. Liu, S. S. Al-Deyab, K. Q. Zhang, T. Chen and Y. K. Lai, *J. Mater. Chem. A*, **2015**, *3*, 2825.

[193] M. A. Torres Arango, A. S. Valença de Andrade, D. T. Cipollone, L. O. Grant, D. Korakakis and K. A. Sierros, *ACS Appl. Mater. Interfaces*, **2016**, *8*, 24659.

[194] F. D. Giacomo, V. Zardetto, A. D'Epifanio, S. Pescetelli, F. Matteocci, S. Razza, A. D. Carlo, S. Licoccia, W. M. M. Kessels, M. Greatore and T. M. Brown, *Adv. Energy Mater.*, **2015**, *5*, 1401808.

[195] X. Lu, M. Yu, G. Wang, T. Zhai, S. Xie, Y. Ling, Y. Tong and Y. Li, *Adv. Mater.*, **2013**, *25*, 267.

[196] G. Doganli, B. Yuzer, I. Aydin, T. Gultekin, A. H. Con, H. Selcuk and S. Palamutcu, *J. Coat. Technol. Res.*, **2016**, *13*, 257.

[197] M. Bonet, E. Bou-Belda, P. Monllor, J. Gisbert, P. Díaz and I. Montava, *Cellulose*, **2015**, *22*, 1347.

[198] D. Wu and M. Long, *ACS Appl. Mater. Interfaces*, **2011**, *3*, 4770.

[199] B. M. Kale, J. Wiener, J. Militky, S. Rwawiire, R. Mishra, K. I. Jacob and Y. Wang, *Carbohydrate Polym.*, **2016**, *150*, 107.

[200] M. Yu, Z. Wang, H. Liu, S. Xie, J. Wu, H. Jiang, J. Zhang, L. Li and J. Li, *ACS Appl. Mater. Interfaces*, **2013**, *5*, 3697.

[201] M. K. Smith and K. A. Mirica, *J. Am. Chem. Soc.*, **2017**, *139*, 16759.

[202] P. Ragesh, V. A. Ganesh, S. V. Nair and A. S. Nair, *J. Mater. Chem. A*, **2014**, *2*, 14773.

[203] N. Li, D. Pranantyo, E.-T. Kang, D. S. Wright and H.-K. Luo, *Adv. Funct. Mater.*, **2018**, *28*, 1800345.

[204] L. Wang, X. Zhang, B. Li, P. Sun, J. Yang, H. Xu and Y. Liu, *ACS Appl. Mater. Interfaces*, **2011**, *3*, 1277.

[205] S. Ayazi-Yazdi, L. Karimi, M. Mirjalili and M. Karimnejad, *J. Text. Inst.*, **2016**, *108*, 856.

[206] M. Shateri-Khalilabad and M. E. Yazdanshenas, *J. Text. Inst.*, **2013**, *104*, 861.

[207] X.-M. Li, D. Reinhoudt and M. Crego-Calama, *Chem. Soc. Rev.*, **2007**, *36*, 1350.

[208] M. E. Yazdanshenas and M. Shateri-Khalilabad, *Ind. Eng. Chem. Res.*, **2013**, *52*, 12846.

[209] H. Zhou, H. Wang, H. Niu, A. Gestos and T. Lin, *Adv. Funct. Mater.*, **2013**, *23*, 1664.

[210] H. Zhou, H. Wang, H. Niu, J. Fang, Y. Zhao and T. Lin, *Adv. Mater. Interfaces*, **2015**, *2*, 1400559.

[211] H. Zhou, H. Wang, H. Niu, Y. Zhao, Z. Xu and T. Lin, *Adv. Funct. Mater.*, **2017**, *27*, 1604261.

[212] Pictures adapted from the website of http://www.ecorr.org/news/tec_ac/2015-12-17/3827.html and www.kangzhiyuan120.com

[213] E. Hernandez, B. Nowack and D. M. Mitrano, *Environ. Sci. Technol.*, **2017**, *51*, 7036.

[214] Z. Xu, Y. Zhao, H. Wang, X. Wang and T. Lin, *Angew. Chem. Int. Ed.*, **2015**, *54*, 4527.

[215] S. M. Dizaj, F. Lotfipour, M. Barzegar-Jalali, M. H. Zarrintan and K. Adibkia, *Mater. Sci. Eng. C*, **2014**, *44*, 278.

[216] F. G. Svensson, G. A. Seisenbaeva and V. G. Kessler, *Eur. J. Inorg. Chem.*, **2017**, *2017*, 4117.

[217] G. M. Sheldrick, *Acta Crystallogr.*, **2008**, *64*, 112.

[218] G. A. Bain and J. F. Berry, *J. Chem. Edu.*, **2008**, *85*, 532.

[219] G. Zhang, W. Li, C. Liu, J. Jia, C.-H. Tung and Y. Wang, *J. Am. Chem. Soc.*, **2018**, *140*, 66.

[220] Y.-P. He, L.-B. Yuan, G.-H. Chen, Q.-P. Lin, F. Wang, L. Zhang and J. Zhang, *J. Am. Chem. Soc.*, **2017**, *139*, 16845.

[221] N. Li, G. S. Subramanian, P. D. Matthews, J. Xiao, V. Chellappan, T. E. Rosser, E. Reisner, H.-K. Luo and D. S. Wright, *Dalton Trans.*, **2018**, *47*, 5679.

[222] M. S. M. Abdelbaky, Z. Amghouz, S. García-Granda, J. R. García, *Polymers*, **2016**, *8(3)*, 86.

[223] H. Heise, F. H. Köhler, M. Herker and W. Hiller, *J. Am. Chem. Soc.*, **2002**, *124*, 10823.

[224] F. H. Köhler and R. Lescouëzec, *Angew. Chem. Int. Ed.*, **2004**, *43*, 2571.

[225] C. P. Grey and N. Dupré, *Chem. Rev.*, **2004**, *104*, 4493.

[226] N. P. Wickramasinghe, M. Shaibat and Y. Ishii, *J. Am. Chem. Soc.*, **2005**, *127*, 5796.

[227] G. Kervern, G. Pintacuda, Y. Zhang, E. Oldfield, C. Roukoss, E. Kuntz, E. Herdtweck, J. Basset, S. Cadars, A. Lesage, C. Copéret and L. Emsley, *J. Am. Chem. Soc.*, **2006**, *128*, 13545.

[228] A. Flambard, F. H. Köhler and R. Lescouëzec, *Angew. Chem. Int. Ed.*, **2009**, *48*, 1673.

[229] I. Bertini, L. Emsley, M. Lelli, C. Luchinat, J. Mao and G. Pintacuda, *J. Am. Chem. Soc.*, **2010**, *132*, 5558.

[230] J. Estephane, E. Groppo, J. G. Vitillo, A. Damin, D. Gianolio, C. Lamberti, S. Bordiga, E. A. Quadrelli, J. M. Basset, G. Kervern, L. Emsley, G. Pintacuda and A. Zecchina, *J. Phys. Chem. C*, **2010**, *114*, 4451.

[231] M. J. Knight, A. J. Pell, I. Bertini, I. C. Felli, L. Gonnelli, R. Pierattelli, T. Herrmann, L. Emsley and G. Pintacuda, *Proc. Natl. Acad. Sci. USA*, **2012**, *109*, 11095.

[232] C. Luchinat, G. Parigi, E. Ravera and M. Rinaldelli, *J. Am. Chem. Soc.*, **2012**, *134*, 5006.

[233] L. Emsley, I. Bertini, *Acc. Chem. Res.*, **2013**, *46*, 1912, and related papers in that issue.

[234] L. Martel, N. Magnani, J. Vigier, J. Boshoven, C. Selfslag, I Farnan, J.-C. Griveau, J. Somers and T. Fanghänel, *Inorg. Chem.*, **2014**, *53*, 6928.

[235] S. Parthasarathy, Y. Nishiyama and Y. Ishii, *Acc. Chem. Res.*, **2013**, *46*, 2127.

[236] L. Russo, M. Maestre-Martinez, S. Wolff, S. Becker and C. Griesinger, *J. Am. Chem. Soc.*, **2013**, *135*, 17111.

[237] J. Novotný, M. Sojka, S. Komorovsky, M. Nečas and R. Marek, *J. Am. Chem. Soc.*, **2016**, *138*, 8432.

[238] I. Bertini and C. Luchinat. Chapter 1: Introduction. *Coord. Chem. Rev.*, **1996**, *150*, 1.

[239] I. Bertini, C. Luchinat, and G. Parigi. Solution NMR of paramagnetic molecules; application to metallobiomolecules and models. Elsevier, London, **2001**.

[240] I. Bertini, C. Luchinat, and G. Parigi, *Prog. Nucl. Magn. Reson. Spectrosc.*, **2002**, *40*, 249.

[241] J. Koehler and J. Meiler, *Prog. Nucl. Magn. Reson. Spectrosc.*, **2011**, *59*, 360.

[242] A. J. Pell, G. Pintacuda, C. P Grey, *Prog. Nucl. Magn. Reson. Spectrosc.*, **2018**, in press

[243] W. Levason, Chemistry and Applications of the Lanthanides, *Coord. Chem. Rev.*, **2017**, *340*, 1-298. [Themed issue]

[244] P. V. Demarco, T. K. Elzey, R. B. Lewis and E. Wenkert, *J. Am. Chem. Soc.*, **1970**, *52*, 9734.

[245] H. C. Aspinall, *Chem. Rev.*, **2002**, *102*, 1807.

[246] M. S. Genčić and N. S. Radulović, *RSC Adv.*, **2015**, *5*, 72670.

[247] W.-M. Liu, M. Overhand and M. Ubbink, *Coord. Chem. Rev.*, **2014**, *273-274*, 2.

[248] T. Yamaguchi, Y. Sakae, Y. Zhang, S. Yamamoto, Y. Okamoto and K. Kato, *Angew. Chem., Int. Ed.*, **2014**, *52*, 10941.

[249] X.-C. Su, H. Liang, K. V. Loscha and G. Otting, *J. Am. Chem. Soc.*, **2009**, *131*, 10352.

[250] M. John, G. Pintacuda, A. Y. Park, N. E. Dixon and G. Otting, *J. Am. Chem. Soc.*, **2006**, *128*, 12910.

[251] J. H. Forsberg, R. M. Delaney, Q. Zhao, G. Harakas and R. Chandran, *Inorg. Chem.*, **1995**, *34*, 3705.

[252] G. Guarino, F. Rastrelli, P. Scrimin and F. Mancin, *J. Am. Chem. Soc.*, **2012**, *134*, 7200.

[253] D. D. Castelli, M. C. Caligara, M. Botta, E. Terreno and S. Aime, *Inorg. Chem.*, **2013**, *52*, 7130.

[254] S. P. Babailov, *Inorg. Chem.*, **2012**, *51*, 1427.

[255] M. Bottrill, L. Kwok, N. J. Long, *Chem. Soc. Rev.*, **2006,** *35*, 557.

[256] M. C. Heffern, L. M. Matosziuk, T. J. Meade, *Chem. Rev.*, **2014**, *114*, 4496.

[257] B. Bleaney, *J. Magn. Reson.*, **1972**, *8*, 91.

[258] A. M. Funk, K.-L. N. A. Finney, P. Harvey, A. M. Kenwright, E. R. Neil, N. J. Rogers, P. K. Senanayake and D. Parker, *Chem. Sci.*, **2015**, *6*, 1655.

[259] M. Hiller, M. Maier, H. Wadepohl and M. Enders, *Organometallics*, **2016**, *35*, 1916.

[260] V. S. Mironov, Y. G. Galyametdinov, A. Ceulemans, C. Görller-Walrand and K. Binnemans, *J. Chem. Phys.*, **2002**, *4673*.

[261] G. T. P. Charnock and I. Kuprov, *Phys. Chem. Chem. Phys.*, **2014**, *16*, 20184.

[262] E. A. Suturina, K. Mason, C. F. G. C. Geraldes, I. Kuprov and D. Parker, *Angew. Chem. Int. Ed.*, **2017**, *56*, 12215.

[263] I. Bertini, C. Luchinat, G. Parigi, E. Ravera, NMR of Paramagnetic Molecules, Applications to Metallobiomolecules and Models, 2nd Edition, Elsevier.

[264] O. A. Blackburn, R. M. Edkins, S. Faulkner, A. M. Kenwright, D. Parker, N. J. Rogers and S. Shuvaev, *Dalton Trans.*, **2016**, *45*, 6782.

[265] R. M. Golding and M. P. Halton, *Aust. J. Chem.*, **1972**, *25*, 2577.

[266] N. Li, R. García-Rodríguez, P. D. Matthews, H.-K. Luo and D. S. Wright, *Dalton Trans.*, **2017**, *46*, 4287.

[267] O. A. Blackburn, A. M. Kenwright, P. D. Beer and S. Faulkner, *Dalton Trans.*, **2015**, *44*, 19509.

[268] J. Reuben, *J. Magn. Reson.*, **1982**, *50*, 233.

[269] C. N. Reilley and B. W. Good, *Anal. Chem.*, **1975**, *47*, 2110.

[270] I. Bertini, C. Luchinat and G. Parigi, *Prog. Nucl. Magn. Reson. Spectrosc.*, **2002**, *40*, 249.

[271] A. A. Pinkerton, *J. Magn. Reson.*, **1985**, *64*, 420

[272] C. N. Reilley, B. W. Good and R. D. Allendoerfer, *Anal. Chem.*, **1976**, *48*, 1446.

[273] G. A. Elgavish, *J. Magn. Reson.*, **1981**, *42*, 242.

[274] C. C. Bryden, C. N. Reilley and J. F. Desreux, *Anal. Chem.*, **1981**, *53*, 1418.

[275] R. M. Golding and P. Pyykkö, *Mol. Phys.*, **1973**, *26*, 1389.

[276] B. Bleaney, C. M. Dobson, B. A. Levine, R. B. Martin, R. J. P. Williams and A. V. Xavier, *J. Chem. Soc., Chem. Commun.*, **1972**, 791b.

[277] M. A. Khaled and D. W. Urry, *J. Chem. Soc., Chem. Commun.*, **1981**, 230.

[278] M. Moustiakimov, M. Kritikos and G. Westin, *Acta Cryst.*, **1998,** *C54*, 29.

[279] E. Berger and G. Westin, *J. Sol-Gel Sci.Technol.*, **2010**, *53*, 681.

[280] J. C. G. Bünzli and C. Piguet, *Chem. Soc. Rev.*, **2005**, *34*, 1048.

[281] S. I. Klink, H. Keizer and F. C. J. M. van Veggel, *Angew. Chem. Int. Ed.*, **2000**, *39*, 4319.

[282] R. D. Archer and H. Chen, *Inorg. Chem.*, **1998**, *37*, 2089.

[283] M.-C. Yin, L.-J. Yuan, C.-C. Ai, C.-W. Wang, E.-T. Yuan and J.-T. Sun, *Polyhedron*, **2004**, *23*, 529.

[284] G. Sharma and A. K. Narula, *J. Fluoresc.*, **2015**, *25*, 355.

[285] G. Kaur and S. B. Rai, *J. Phys. D: Appl. Phys.*, **2011**, *44*, 425306.

[286] S. Biju, Y. K. Eom, J.-C. G. Bünzli and H. K. Kim, *J. Mater. Chem. C*, **2013**, *1*, 3454.

[287] G.-L. Law, T. A. Pham, J. Xu and K. N. Raymond, *Angew. Chem. Int. Ed.*, **2012**, *51*, 2371.

[288] N. Wartenberg, O. Raccurt, E. Bourgeat-Lami, D. Imbert and M. Mazzanti, *Chem. Eur. J.*, **2013**, *19*, 3477.

[289] S. Quici, M. Cavazzini, G. Marzanni, G. Accorsi, N. Armaroli, B. Ventura and F. Barigelletti, *Inorg. Chem.*, **2005**, *44*, 529.

[290] C. Y. Chow, S. V. Eliseeva, E. R. Trivedi, T. N. Nguyen, J. W. Kampf, S. Petoud and V. L. Pecoraro, *J. Am. Chem. Soc.*, **2016**, *138*, 5100.

[291] S. Quici, M. Cavazzini, G. Marzanni, G. Accorsi, N. Armaroli, B. Ventura and F. Barigelletti, *Inorg. Chem.*, **2005**, *44*, 529.

[292] K. T. Rim, K. H. Koo and J. S. Park, *Health Work*, **2013**, *4*, 12.

[293] S. Hirano and K. T. Suzuki, *Environmental Health Perspectives*, **1996**, *104*, 85.

[294] P.-J. Tseng, C.-Y. Wang, T.-Y. Huang, Y.-Y. Chuang, S.-F. Fu and Y.- W. Lin, *Anal. Methods*, **2014**, *6*, 1759.

[295] H.-B. Guo, F. He, B. Gu, L. Liang and J. C. Smith, *J. Phys. Chem. A*, **2012**, *116*, 11870.

[296] P. B. Bisht, H. B. Tripathi, D. D. Pant, *J. Photochem. Photobiol. A: Chem.*, **1995**, *90*, 103.

[297] Ž. Antić, R. M. Krsmanović, M. G. Nikolić, M. Marinović-Cincović, M. Mitrić, S. Polizzi and M. D. Dramićanin, *Mater. Chem. Phys.*, **2012**, *135*, 1064.

[298] F. J. Steemers, W. Verboom, D. N. Reinhoudt, E. B. van der Tol and J. W. Verhoeven, *J. Am. Chem. Soc.*, **1995**, *117*, 9408.

[299] K. Binnemans, *Chem. Rev.*, **2009**, *109*, 4283.

[300] W. Luo, J. Liao, R. Li and X. Chen, *Phys. Chem. Chem. Phys.*, **2010**, *12*, 3276.

[301] J. C. de Mello, H. F. Wittmann and R. H. Friend, *Adv. Mater.*, **1997**, *9*, 230.

[302] E. R. Trivedi, S. V. Eliseeva, J. Jankolovits, M. M. Olmstead, S. Petoud and V. L. Pecoraro, *J. Am. Chem. Soc.*, **2014**, *136*, 1526.

[303] Q. Zhao, F. Li and C. Huang, *Chem. Soc. Rev.*, **2010**, *39*, 3007.

[304] H. Zhao, L. Zang and C. Guo, *Phys. Chem. Chem. Phys.*, **2017**, *19*, 7728.

[305] G. M. Sheldrick, *Acta Crystallogr., Sect. A: Fundam. Crystallogr.*, **2015**, *71*, 3.

[306] G. M. Sheldrick, *Acta Crystallogr., Sect. C: Cryst. Struct. Commun.*, **2015**, *71*, 3.

Publication List

The following publications were produced during the period from October 2014 to August 2018, and are closely related to this thesis.

1. Ning Li, Peter D. Matthews, Jane J. Leung, Timothy C. King, Paul T. Wood, He-Kuan Luo and Dominic S. Wright, Synthesis, structure and properties of the manganese-doped polyoxotitanate cage $[Ti_{18}MnO_{30}(OEt)_{20}(MnPhen)_3]$ (Phen = 1,10-phenanthroline), *Dalton Trans.*, **2015**, *44*, 19090-19096.
2. Ning Li, Peter D. Matthews, He-Kuan Luo and Dominic S. Wright, Novel properties and potential applications of functional ligand-modified polyoxotitanate cages, *Chem. Commun.*, **2016**, *52*, 11180-11190.
3. Ning Li, Raúl García-Rodríguez, Peter D. Matthews, He-Kuan Luo and Dominic S. Wright, Synthesis, structure and paramagnetic NMR analysis of a series of lanthanide-containing $[LnTi_6O_3(O^iPr)_9(salicylate)_6]$ cages, *Dalton Trans.*, **2017**, *46*, 4287-4295.
4. Ning Li, Dicky Pranantyo, En-Tang Kang, Dominic S. Wright and He-Kuan Luo, *In Situ* Self-Assembled Polyoxotitanate Cages on Flexible Cellulosic Substrates: Multifunctional Coating for Hydrophobic, Antibacterial and UV-Blocking Applications, *Adv. Funct. Mater.*, **2018**, *28*, 1800345.
5. Ning Li, Gomathy Sandhya Subramanian, Peter D. Matthews, James Xiao, Vijila Chellappan, Timothy E. Rosser, Erwin Reisner, He-Kuan Luo and Dominic S. Wright, Energy transfer and photoluminescence properties of lanthanide-containing polyoxotitanate cages coordinated by salicylate ligands, *Dalton Trans.*, **2018**, *47*, 5679-5686.
6. Schirin Hanf, Peter D. Matthews, Ning Li, He-Kuan Luo and Dominic S. Wright, The influence of halides in polyoxotitanate cages; dipole moment, splitting and expansion of d-orbitals and electron–electron repulsion, *Dalton Trans.*, **2017**, *46*, 578-585.
7. Peter D. Matthews, Ning Li, He-Kuan Luo, and Dominic S. Wright, How Does Substitutional Doping Affect Visible Light Absorption in a Series of Homodisperse Ti_{11} Polyoxotitanate Nanoparticles—A Comment on the Band

Gap Determination of the Fe^{II} Cages (Chem. Eur. J. 2015, 21, 11538), *Chem. Eur. J.*, **2016**, *22*, 4632-4633.

Appendix

Table A1. Crystal data and structure refinement for compound **1**

Empirical formula	$C_{76}H_{124}Mn_4N_6O_{50}Ti_{18}$	
Formula Weight	3003.76	
Temperature	180(2) K	
Wavelength	0.71073 Å	
Crystal system	Monoclinic	
Space group	$P2_1/c$	
Unit cell dimension	a = 15.723(3) Å	α = 90°
	b = 23.832(5) Å	β = 96.44(3)°
	c = 31.971(6) Å	γ = 90°
Volume	11905(4) $Å^3$	
Z	4	
Density (calculated)	1.676 Mg m^{-3}	
Absorption coefficient	1.621 mm^{-1}	
F(000)	6072	
Crystal size	0.46 × 0.46 × 0.46 mm^3	
Theta range for data collection	3.516 to 25.054°	
Index ranges	$-18 \le h \le 18$, $-27 \le k \le 28$, $-35 \le l \le 38$	
Reflections collected	61565	
Independent reflections	19760 [R(int) = 0.052]	
Completeness of theta = 22.211°	93.8%	
Absorption correction	Semi-empirical from equivalents	
Max. and min. tranmission	0.492 and 0.420	
Refinement method	Full-matrix least-squares on F^2	
Data/restraints/parameters	19760/582/1317	
Goodness-of-fit on F_2	1.025	
Final R indices [I > 2σ(I)]	R_1 = 0.099, wR_2 = 0.271	
R indices (all data)	R_1 = 0.152, wR_2 = 0.314	
Largest diff. peak and hole	1.414 and -0.824 e $Å^{-3}$	
CCDC number	1423275	
Notes	Nil	

Table A2. Crystal data and structure refinement for compound **2-La**

Empirical formula	$C_{69}H_{87}LaO_{30}Ti_6$	
Formula Weight	1822.69	
Temperature	180(2) K	
Wavelength	1.54178 Å	
Crystal system	Hexagonal	
Space group	P-6	
Unit cell dimension	a = 15.0084(4) Å	α = 90°
	b = 15.0084(4) Å	β = 90°
	c = 23.5238(7) Å	γ = 120°
Volume	4588.9(3) $Å^3$	
Z	2	
Density (calculated)	1.319 Mg m^{-3}	
Absorption coefficient	8.328 mm^{-1}	
F(000)	1860	
Crystal size	0.29 × 0.25 × 0.24 mm^3	
Theta range for data collection	3.400 to 66.713°	
Index ranges	$-17 \le h \le 17$, $-17 \le k \le 17$, $-28 \le l \le 27$	
Reflections collected	61633	
Independent reflections	5571 [R(int) = 0.0504]	
Completeness to theta = 66.713°	99.9%	
Absorption correction	Semi-empirical from equivalents	
Max. and min. transmission	0.240 and 0.196	
Refinement method	Full-matrix least-square on F^2	
Data/retraints/parameters	5571/142/331	
Goodness-of-fit on F_2	1.154	
Final R indices [I > 2σ(I)]	R_1 = 0.0667, wR_2 = 0.1886	
R indices (all data)	R_1 = 0.0678, wR_2 = 0.1900	
Largest diff. peak and hole	6.820 and -0.717 e $Å^{-3}$	
CCDC number	1504171	
Notes	Nil	

Table A3. Crystal data and structure refinement for compound **2-Ce**

Empirical formula	$C_{69}H_{87}CeO_{30}Ti_6$	
Formula Weight	1823.90	
Temperature	180(2) K	
Wavelength	1.54178 Å	
Crystal system	Hexagonal	
Space group	P-6	
Unit cell dimension	a = 15.0280(4) Å	$\alpha = 90°$
	b = 15.0280(4) Å	$\beta = 90°$
	c = 23.6224(9) Å	$\gamma = 120°$
Volume	4620.2 (3) $Å^3$	
Z	2	
Density (calculated)	1.311 Mg m^{-3}	
Absorption coefficient	8.505 mm^{-1}	
F(000)	1862	
Crystal size	0.19 × 0.19 × 0.15 mm^3	
Theta range for data collection	7.773 to 61.315°	
Index ranges	$-17 \le h \le 17$, $-17 \le k \le 17$, $-26 \le l \le 26$	
Reflections collected	102902	
Independent reflections	4874 [R(int) = 0.0653]	
Completeness to theta = 61.315°	99.3%	
Absorption correction	Semi-empirical from equivalents	
Max. and min. transmission	0.362 and 0.295	
Refinement method	Full-matrix least-squares on F^2	
Data/restraints/parameters	4874/136/331	
Goodness-of-fit on F_2	1.062	
Final R indices [$I > 2\sigma(I)$]	R_1 = 0.0688, wR_2 = 0.1884	
R indices (all data)	R_1 = 0.0711, wR_2 = 0.1910	
Largest diff. peak and hole	2.950 and -0.441 e $Å^{-3}$	
CCDC number	1504173	
Notes	Treated with SQUEEZE	

Table A4. Crystal data and structure refinement for compound **2-Pr**

Empirical formula	$C_{69}H_{87}PrO_{30}Ti_6$	
Formula Weight	1824.69	
Temperature	180(2) K	
Wavelength	1.54184 Å	
Crystal system	Hexagonal	
Space group	P-6	
Unit cell dimension	a = 14.9478(6) Å	$\alpha = 90°$
	b = 14.9478(6) Å	$\beta = 90°$
	c = 23.5581(11) Å	$\gamma = 120°$
Volume	4558.5 (4) $Å^3$	
Z	2	
Density (calculated)	1.329 Mg m^{-3}	
Absorption coefficient	8.862 mm^{-1}	
F(000)	1864	
Crystal size	0.20 × 0.16 × 0.14 mm^3	
Theta range for data collection	3.414 to 65.308°	
Index ranges	$-17 \le h \le 17$, $-17 \le k \le 17$, $-27 \le l \le 27$	
Reflections collected	39041	
Independent reflections	5331 [R(int) = 0.1004]	
Completeness to theta = 65.308°	99.8%	
Absorption correction	Semi-empirical from equivalents	
Max. and min. transmission	0.370 and 0.270	
Refinement method	Full-matrix least-square on F^2	
Data/restraints/parameters	5331/208/331	
Goodness-of-fit on F_2	1.132	
Final R indices [$I > 2\sigma(I)$]	R_1 = 0.0792, wR_2 = 0.2114	
R indices (all data)	R_1 = 0.0879, wR_2 = 0.2215	
Largest diff. peak and hole	8.674 and -1.144 e $Å^{-3}$	
CCDC number	1504170	
Notes		

Table A5. Crystal data and structure refinement for compound **2-Nd**

Empirical formula	$C_{69}H_{87}NdO_{30}Ti_6$	
Formula Weight	1828.02	
Temperature	180(2) K	
Wavelength	1.54178 Å	
Crystal system	Hexagonal	
Space group	P-6	
Unit cell dimension	a = 14.9289(4) Å	α = 90°
	b = 14.9289(4) Å	β = 90°
	c = 23.5597(7) Å	γ = 120°
Volume	4547.3 (3) $Å^3$	
Z	2	
Density (calculated)	1.335 Mg m^{-3}	
Absorption coefficient	9.130 mm^{-1}	
F(000)	1886	
Crystal size	0.15 × 0.14 × 0.12 mm^3	
Theta range for data collection	3.418 to 61.253°	
Index ranges	$-16 \le h \le 16$, $-16 \le k \le 16$, $-26 \le l \le 26$	
Reflections collected	26755	
Independent reflections	4755 [R(int) = 0.0745]	
Completeness to theta = 61.253°	99.8%	
Absorption correction	Semi-empirical from equivalents	
Max. and min. transmission	0.407 and 0.341	
Refine method	Full-matrix least-squares on F^2	
Data/restraints/parameters	4755/212/331	
Goodness-of-fit on F_2	1.118	
Final R indices [I > 2σ(I)]	R_1 = 0.0603, wR_2 = 0.1638	
R indices (all data)	R_1 = 0.0708, wR_2 = 0.1729	
Largest diff. peak and hole	4.636 and -0.549 e $Å^{-3}$	
CCDC number	1504167	
Notes	Nil	

Table A6. Crystal data and structure refinement for compound **2-Sm**

Empirical formula	$C_{69}H_{87}SmO_{30}Ti_6$	
Formula Weight	1834.13	
Temperature	180(2) K	
Wavelength	1.54178 Å	
Crystal system	Hexagonal	
Space group	P-6	
Unit cell dimension	a = 14.9683(4) Å	$\alpha = 90°$
	b = 14.9683(4) Å	$\beta = 90°$
	c = 23.6974(9) Å	$\gamma = 120°$
Volume	4598.1 (3) $Å^3$	
Z	2	
Density (calculated)	1.325 Mg m^{-3}	
Absorption coefficient	9.516 mm^{-1}	
F(000)	1870	
Crystal size	0.21 × 0.19 × 0.14 mm	
Theta range for data collection	3.409 to 66.858°	
Index ranges	$-17 \le h \le 16$, $-17 \le k \le 17$, $-28 \le l \le 28$	
Reflections collected	104538	
Independent reflections	5582 [R(int) = 0.0692]	
Completeness to theta = 66.858°	99.9%	
Absorption correction	Semi-empirical from equivalents	
Max. and min. transmission	0.349 and 0.240	
Refinement method	Full-matrix least-squares on F^2	
Data/restraints/parameters	5582/212/331	
Goodness-of-fit on F_2	1.126	
Final R indices [I > 2σ(I)]	R_1 = 0.0377, wR_2 = 0.1000	
R indices (all data)	R_1 = 0.0398, wR_2 = 0.1018	
Largest diff. peak and hole	3.028 and -0.447 e $Å^{-3}$	
CCDC number	1504172	
Notes	Treated with SQUEEZE	

Table A7. Crystal data and structure refinement for compound **2-Eu**

Empirical formula	$C_{69}H_{87}EuO_{30}Ti_6$	
Formula Weight	1835.74	
Temperature	180(2) K	
Wavelength	1.54178 Å	
Crystal system	Orthorhombic	
Space group	Pnma	
Unit cell dimension	a = 14.9147(4) Å	α = 90°
	b = 22.5136(6) Å	β = 90°
	c = 25.0990(7) Å	γ = 90°
Volume	8427.8(4) $Å^3$	
Z	4	
Density (calculated)	1.447 Mg m^3	
Absorption coefficient	10.479 mm^{-1}	
F(000)	3744	
Crystal size	0.24 × 0.19 × 0.17 mm^3	
Theta range for data collection	2.636 to 72.297°	
Index ranges	$-18 \le h \le 16$, $-26 \le k \le 27$, $-30 \le l \le 30$	
Reflections collected	57628	
Independent reflections	8537 [R(int) = 0.0593]	
Completeness to theta = 67.679°	100.0%	
Absorption correction	Semi-empirical from equivalents	
Max. and min. transmission	0.269 and 0.188	
Refinement method	Full-matrix least-squares on F^2	
Data/restraints/parameters	8537/273/559	
Goodness-of-fit on F_2	1.032	
Final R indices [$I > 2\sigma(I)$]	R_1 = 0.0385, wR_2 = 0.0909	
R indices (all data)	R_1 = 0.0490, wR_2 = 0.0971	
Largest diff. peak and hole	0.741 and -0.777 e $Å^{-3}$	
CCDC number	1504165	
Notes		

Table A8. Crystal data and structure refinement for compound **2-Eu** (the other polymorph)

Empirical formula	$C_{69}H_{87}EuO_{30}Ti_6$	
Formula Weight	1835.74	
Temperature	180(2) K	
Wavelength	1.54178 Å	
Crystal system	Hexagonal	
Space group	P-6	
Unit cell dimension	a = 14.9021(3) Å	α = 90°
	b = 14.9021(3) Å	β = 90°
	c = 23.5900(6) Å	γ = 120°
Volume	4536.8 (2) $Å^3$	
Z	2	
Density (calculated)	1.344 Mg m^{-3}	
Absorption coefficient	9.733 mm^{-1}	
F(000)	1872	
Crystal size	0.30 × 0.24 × 0.22 mm^3	
Theta range for data collection	3.424 to 66.626°	
Index ranges	$-17 \le h \le 16$, $-17 \le k \le 17$, $-28 \le l \le 28$	
Reflections collected	40425	
Independent reflections	5463 [R(int) = 0.0567]	
Completeness to theta = 66.626°	99.9%	
Absorption correction	Semi-empirical from equivalents	
Max. and min. transmission	0.223 and 0.158	
Refinement method	Full-matrix least-squares on F^2	
Data/restraints/parameters	5463/208/331	
Goodness-of-fit on F_2	1.140	
Final R indices [$I > 2\sigma(I)$]	R_1 = 0.0500, wR_2 = 0.1546	
R indices (all data)	R_1 = 0.0514, wR_2 = 0.1555	
Largest diff. peak and hole	2.399 and -0.541 e $Å^{-3}$	
CCDC number	1531652	
Notes	Nil	

Table A9. Crystal data and structure refinement for compound **2-Gd**

Empirical formula	$C_{69}H_{87}GdO_{30}Ti_6$	
Formula Weight	1841.03	
Temperature	180(2) K	
Wavelength	1.54178 Å	
Crystal system	Hexagonal	
Space group	P-6	
Unit cell dimension	a = 14.9227(4) Å	α = 90°
	b = 14.9227(4) Å	β = 90°
	c = 23.5803(8) Å	γ = 120°
Volume	4547.5 (3) $Å^3$	
Z	2	
Density (calculated)	1.345 Mg m^{-3}	
Absorption coefficient	9.490 mm^{-1}	
F(000)	1874	
Crystal size	0.31 × 0.22 × 0.20 mm^3	
Theta range for data collection	3.420 to 66.722°	
Index ranges	$-17 \le h \le 17$, $-16 \le k \le 12$, $-28 \le l \le 28$	
Reflections collected	29382	
Independent reflections	5479 [R(int) = 0.0659]	
Completeness to theta = 66.722°	99.9%	
Absorption correction	Semi-empirical from equivalents	
Max. and min. transmission	0.253 and 0.157	
Refinement method	Full-matrix least-squares on F^2	
Data/restraints/parameters	5479/210/331	
Goodness-of-fit on F_2	1.126	
Final R indices [I > 2σ(I)]	R_1 = 0.0698, wR_2 = 0.1918	
R indices (all data)	R_1 = 0.0728, wR_2 = 0.1961	
Largest diff. peak and hole	5.413 and -1.326 e $Å^{-3}$	
CCDC number	1504168	
Notes	Nil	

Table A10. Crystal data and structure refinement for compound **2-Tb**

Empirical formula	$C_{69}H_{87}TbO_{30}Ti_6$	
Formula Weight	1842.70	
Temperature	180(2) K	
Wavelength	1.54184 Å	
Crystal system	Hexagonal	
Space group	P-6	
Unit cell dimension	a = 14.9365(3) Å	α = 90°
	b = 14.9365(3) Å	β = 90°
	c = 23.6008(6) Å	γ = 120°
Volume	4559.9 (2) $Å^3$	
Z	2	
Density (calculated)	1.342 Mg m^{-3}	
Absorption coefficient	8.574 mm^{-1}	
F(000)	1876	
Crystal size	0.29 × 0.20 × 0.19 mm^3	
Theta range for data collection	3.417 to 66.641°	
Index ranges	$-17 \le h \le 17$, $-17 \le k \le 16$, $-28 \le l \le 28$	
Reflections collected	39344	
Independent reflections	5531 [R(int) = 0.0553]	
Completeness to theta = 66.641°	99.9%	
Absorption correction	Semi-empirical from equivalents	
Max. and min. transmission	0.293 and 0.190	
Refinement method	Full-matrix least-squares on F^2	
Data/restraints/parameters	5531/212/331	
Goodness-of-fit on F_2	1.101	
Final R indices [I > 2σ(I)]	R_1 = 0.0684, wR_2 = 0.1920	
R indices (all data)	R_1 = 0.0707, wR_2 = 0.1949	
Largest diff. peak and hole	6.042 and -0.572 e $Å^{-3}$	
CCDC number	1504169	
Notes	Nil	

Table A11. Crystal data and structure refinement for compound **2-Dy**

Empirical formula	$C_{69}H_{87}DyO_{30}Ti_6$	
Formula Weight	1846.28	
Temperature	180(2) K	
Wavelength	1.54178 Å	
Crystal system	Hexagonal	
Space group	P-6	
Unit cell dimension	a = 14.9065(3) Å	α = 90°
	b = 14.9065(3) Å	β = 90°
	c = 23.6229(6) Å	γ = 120°
Volume	4545.8 (2) $Å^3$	
Z	2	
Density (calculated)	1.349 Mg m^{-3}	
Absorption coefficient	9.172 mm^{-1}	
F(000)	1878	
Crystal size	0.20 × 0.19 × 0.18 mm^3	
Theta range for data collection	3.423 to 65.170°	
Index ranges	$-17 \le h \le 17$, $-16 \le k \le 17$, $-27 \le l \le 27$	
Reflections collected	26874	
Independent reflections	5239 [R(int) = 0.0479]	
Completeness to theta = 65.170°	99.9%	
Absorption correction	Semi-empirical from equivalents	
Max. and min. transmission	0.289 and 0.261	
Refinement method	Full-matrix least-squares on F^2	
Data/restraints/parameters	5239/208/331	
Goodness-of-fit on F_2	1.113	
Final R indices [I > 2σ(I)]	R_1 = 0.0550, wR_2 = 0.1594	
R indices (all data)	R_1 = 0.0589, wR_2 = 0.1647	
Largest diff. peak and hole	3.585 and -0.642 e $Å^{-3}$	
CCDC number	1504163	
Notes	Nil	

Table A12. Crystal data and structure refinement for compound **2-Ho**

Empirical formula	$C_{69}H_{87}HoO_{30}Ti_6$	
Formula Weight	1848.71	
Temperature	180(2) K	
Wavelength	1.54178 Å	
Crystal system	Hexagonal	
Space group	P-6	
Unit cell dimension	a = 14.8834(4) Å	$\alpha = 90°$
	b = 14.8834(4) Å	$\beta = 90°$
	c = 23.5900(11) Å	$\gamma = 120°$
Volume	4525.5 (3) $Å^3$	
Z	2	
Density (calculated)	1.357 Mg m^{-3}	
Absorption coefficient	6.429 mm^{-1}	
F(000)	1880	
Crystal size	0.34 × 0.30 × 0.27 mm^3	
Theta range for data collection	3.429 to 66.780°	
Index ranges	$-17 \le h \le 16$, $-17 \le k \le 17$, $-28 \le l \le 28$	
Reflections collected	41759	
Independent reflections	5479 [R(int) = 0.0625]	
Completeness to theta = 66.780°	99.9%	
Absorption correction	Semi-empirical from equivalents	
Max. and min. transmission	0.276 and 0.218	
Refinement method	Full-matrix least-squares on F^2	
Data/restraints/parameters	5479/202/326	
Goodness-of-fit on F_2	1.104	
Final R indices [$I > 2\sigma(I)$]	R_1 = 0.0655, wR_2 = 0.1850	
R indices (all data)	R_1 = 0.0692, wR_2 = 0.1914	
Largest diff. peak and hole	3.177 and -0.844 e $Å^{-3}$	
CCDC number	1504166	
Notes	Nil	

Table A13. Crystal data and structure refinement for compound **2-Er**

Empirical formula	$C_{69}H_{87}ErO_{30}Ti_6$	
Formula Weight	1851.04	
Temperature	180(2) K	
Wavelength	1.54178 Å	
Crystal system	Hexagonal	
Space group	P-6	
Unit cell dimension	a = 15.0340(3) Å	$\alpha = 90°$
	b = 15.0340(3) Å	$\beta = 90°$
	c = 23.8089(6) Å	$\gamma = 120°$
Volume	4660.4 (2) $Å^3$	
Z	2	
Density (calculated)	1.319 Mg m^{-3}	
Absorption coefficient	6.329 mm^{-1}	
F(000)	1882	
Crystal size	0.17 × 0.13 × 0.11 mm^3	
Theta range for data collection	3.394 to 66.495°	
Index ranges	$-17 \le h \le 17$, $-17 \le k \le 17$, $-28 \le l \le 28$	
Reflections collected	40624	
Independent reflections	5643 [R(int) = 0.0485]	
Completeness to theta = 66.495°	99.9%	
Absorption correction	Semi-empirical from equivalents	
Max. and min. transmission	0.543 and 0.413	
Refinement method	Full-matrix least-squares on F^2	
Data/restraints/parameters	5463/208/331	
Goodness-of-fit on F_2	1.113	
Final R indices [$I > 2\sigma(I)$]	R_1 = 0.0520, wR_2 = 0.1540	
R indices (all data)	R_1 = 0.0556, wR_2 = 0.1576	
Largest diff. peak and hole	1.776 and -0.470 e $Å^{-3}$	
CCDC number	1504164	
Notes		

Table A14. Crystal data and structure refinement for compound **2-Sm-NH_2**

Empirical formula	$C_{69}H_{93}N_6SmO_{30}Ti_6$	
Formula Weight	1924.24	
Temperature	180(2) K	
Wavelength	1.54178 Å	
Crystal system	Hexagonal	
Space group	$P6_3/m$	
Unit cell dimension	a = 14.5945(2) Å	$\alpha = 90°$
	b = 14.5945(2) Å	$\beta = 90°$
	c = 22.9484(5) Å	$\gamma = 120°$
Volume	4233.13 (15) $Å^3$	
Z	2	
Density (calculated)	1.510 Mg m^{-3}	
Absorption coefficient	10.386 mm^{-1}	
F(000)	1966	
Crystal size	0.13 × 0.13 × 0.12 mm^3	
Theta range for data collection	3.497 to 65.186°	
Index ranges	$-17 \le h \le 16$, $-13 \le k \le 17$, $-26 \le l \le 27$	
Reflections collected	24249	
Independent reflections	2480 [R(int) = 0.0555]	
Completeness to theta = 65.186°	99.9%	
Absorption correction	Semi-empirical from equivalents	
Max. and min. transmission	0.369 and 0.345	
Refinement method	Full-matrix least-squares on F^2	
Data/restraints/parameters	2480/0/180	
Goodness-of-fit on F_2	1.073	
Final R indices [$I > 2\sigma(I)$]	R_1 = 0.0400, wR_2 = 0.1081	
R indices (all data)	R_1 = 0.0494, wR_2 = 0.1174	
Largest diff. peak and hole	0.864 and -0.462 e $Å^{-3}$	
CCDC number	Not deposited yet	
Notes	Nil	

Table A15. Crystal data and structure refinement for compound **2-Eu-NH_2**

Empirical formula	$C_{69}H_{93}N_6EuO_{30}Ti_6$	
Formula Weight	1925.85	
Temperature	180(2) K	
Wavelength	1.54178 Å	
Crystal system	Hexagonal	
Space group	$P6_3/m$	
Unit cell dimension	a = 14.5951(5) Å	α = 90°
	b = 14.5951(5) Å	β = 90°
	c = 22.9159(8) Å	γ = 120°
Volume	4227.5 (3) $Å^3$	
Z	2	
Density (calculated)	1.508 Mg m^{-3}	
Absorption coefficient	10.471 mm^{-1}	
F(000)	1968	
Crystal size	0.26 × 0.25 × 0.08 mm^3	
Theta range for data collection	3.497 to 65.090°	
Index ranges	$-16 \le h \le 17$, $-17 \le k \le 16$, $-26 \le l \le 26$	
Reflections collected	30152	
Independent reflections	2478 [R(int) = 0.0728]	
Completeness to theta = 65.186°	100.0%	
Absorption correction	Semi-empirical from equivalents	
Max. and min. transmission	0.488 and 0.172	
Refinement method	Full-matrix least-squares on F^2	
Data/restraints/parameters	2478/0/180	
Goodness-of-fit on F_2	1.113	
Final R indices [$I > 2\sigma(I)$]	R_1 = 0.0466, wR_2 = 0.1152	
R indices (all data)	R_1 = 0.0555, wR_2 = 0.1228	
Largest diff. peak and hole	1.417 and -0.655 e $Å^{-3}$	
CCDC number	Not deposited yet	
Notes	Nil	

Three-Nuclei-Plot Method

A parameter $Y_{Ce}^{Ln,i}$ is defined as shown in [Eqn. A1], where $\sigma_{para}^{Ln,i}$ is the paramagnetic NMR shift of the nucleus i in the **2-Ln** cage and $\langle S_z \rangle_{Ln}$ is only dependent on the choice of Ln^{3+} ion.

$$Y_{Ce}^{Ln,i} = \sigma_{para}^{Ln,i} \cdot \frac{\langle S_z \rangle^{Ce}}{\langle S_z \rangle^{Ln}} - \sigma_{para}^{Ce,i} \qquad \text{[Eqn. A1]}$$

For a certain nucleus, varying the choice of Ln^{3+} (*i.e.*, Ce^{3+}, Pr^{3+}, Nd^{3+}, Sm^{3+} and Eu^{3+}) gives a series of Cartesian coordinates ($x = Y_{Ce}^{Ln,H^d}$ and $y = Y_{Ce}^{Ln,i}$) that can be fitted into a straight line. The slope and intercept of the straight line can then be calculated using the linear fitting function in common data processing software (*e.g.*, Microsoft Excel, Origin, etc.).

With known chemical shift of H^d, the value Y_{Ce}^{Ln,H^d} (Ln = Tb, Dy, Ho and Er) can be calculated. Substituting the values back in the obtained linear equation gives the value of $Y_{Ce}^{Ln,i}$ (Ln = Tb, Dy, Ho and Er, i could be any ^1H nucleus except for H^d), from which the paramagnetic shift $\sigma_{para}^{Ln,i}$ can be calculated.

For example, the linear fitting of the plot Y_{Ce}^{Ln,H^e} *vs.* Y_{Ce}^{Ln,H^d} (Ln = Ce, Pr, Nd, Sm and Eu) is shown in Figure A1, with the slope and intercept being 0.9188 and -0.019, respectively. Y_{Ce}^{Tb,H^d} is then calculated to be -7.47 since the chemical shift of H^d for **2-Tb** is 86.73 ppm. Using the linearly-fitted equation, $Y_{Ce}^{Tb,H^e} = -6.88$ can be easily obtained. Further substituting Y_{Ce}^{Tb,H^e} back in the [Eqn. A1] results in the calculated chemical shift of H^e for **2-Tb** being at 76.20 ppm, which is very close to the experimentally observed chemical shift of σ 76.05 ppm. Applying such a method to all the other ^1H environments can give the corresponding calculated chemical shifts for the **2-Ln** cages with heavier lanthanide ions (*i.e.*, Tb^{3+}, Dy^{3+}, Ho^{3+} and Er^{3+}).

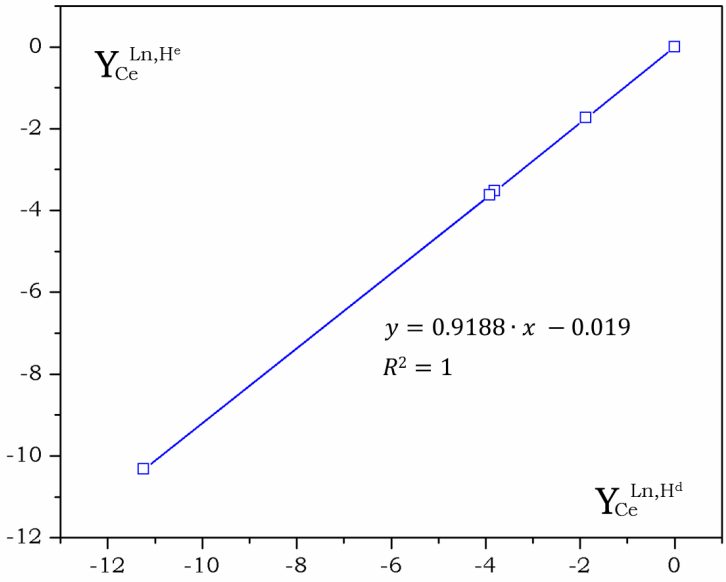

Figure A1. Illustration of the Three-Nuclei-Plot Method

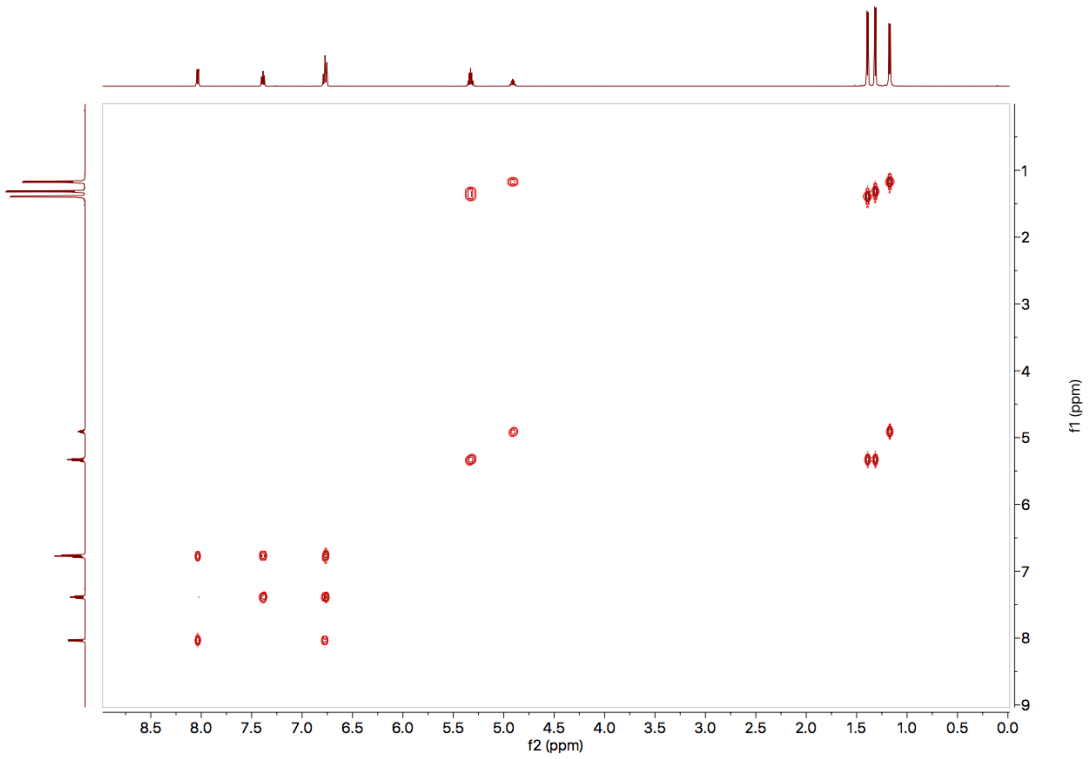

Figure A2. ^{1}H-^{1}H COSY NMR correlation spectrum of **2-La**

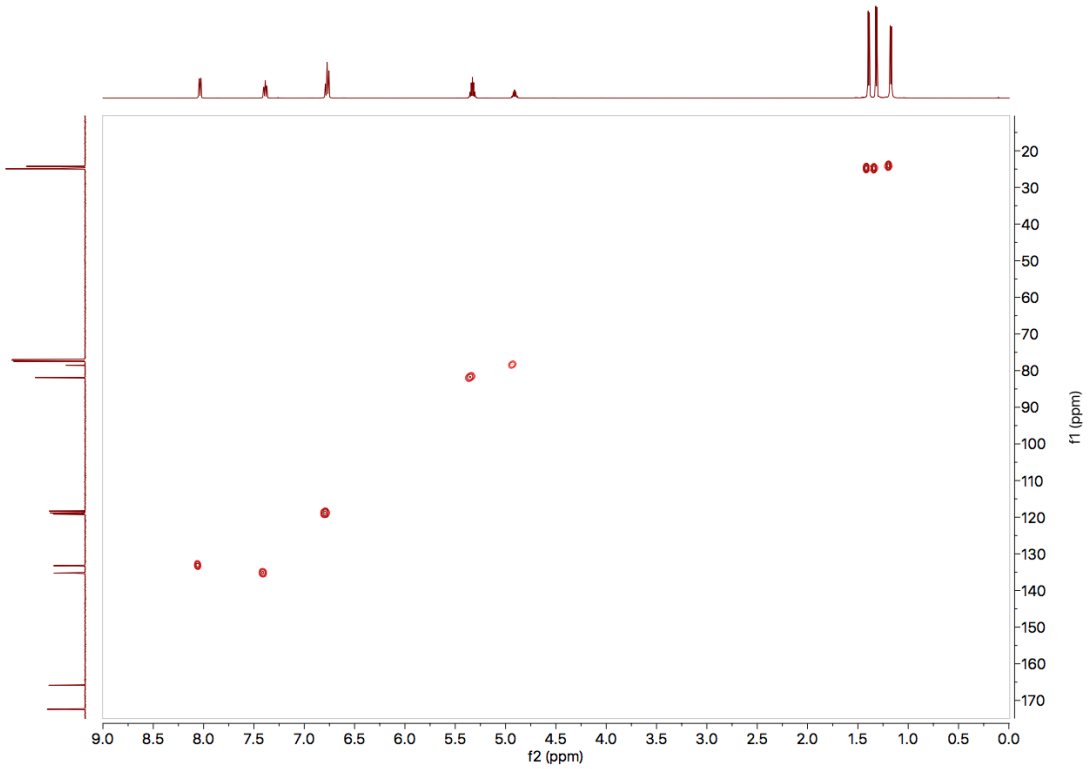

Figure A3. ^{1}H-^{13}C HMQC NMR correlation spectrum of **2-La**

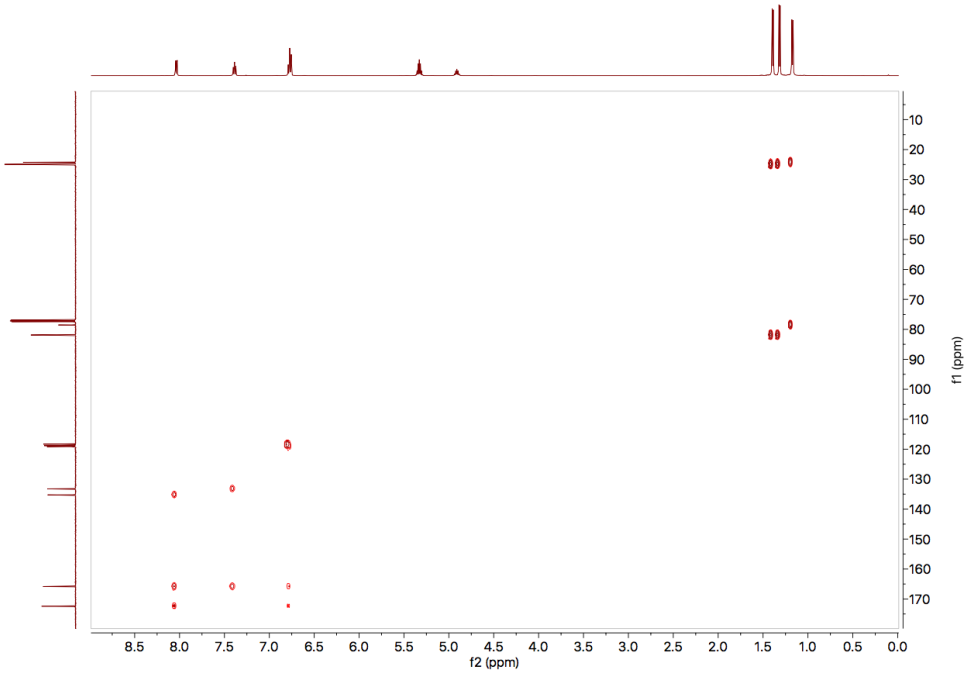

Figure A4. ^{1}H-^{13}C HMBC NMR correlation spectrum of **2-La**

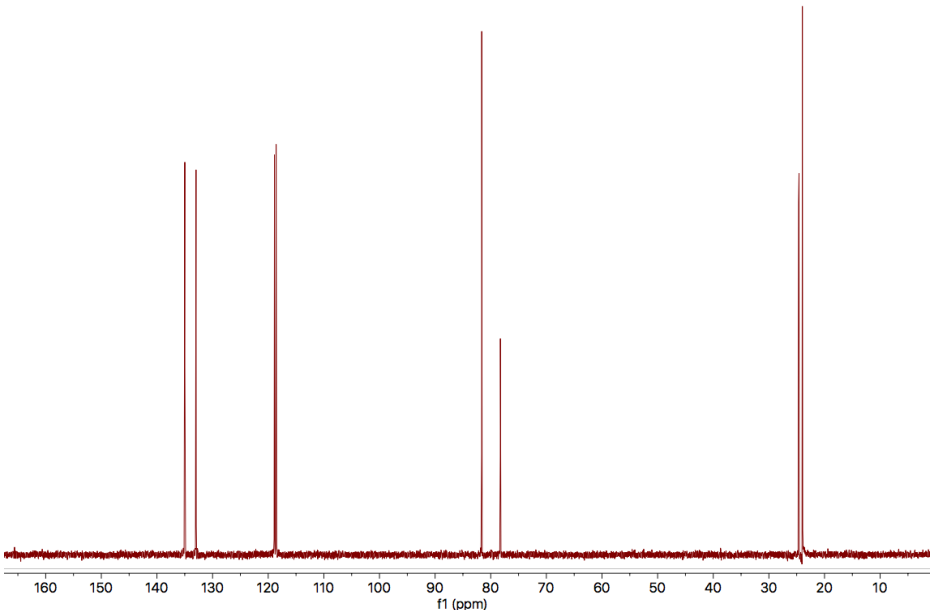

Figure A5. DEPT-135 ^{13}C NMR spectrum of **2-La**

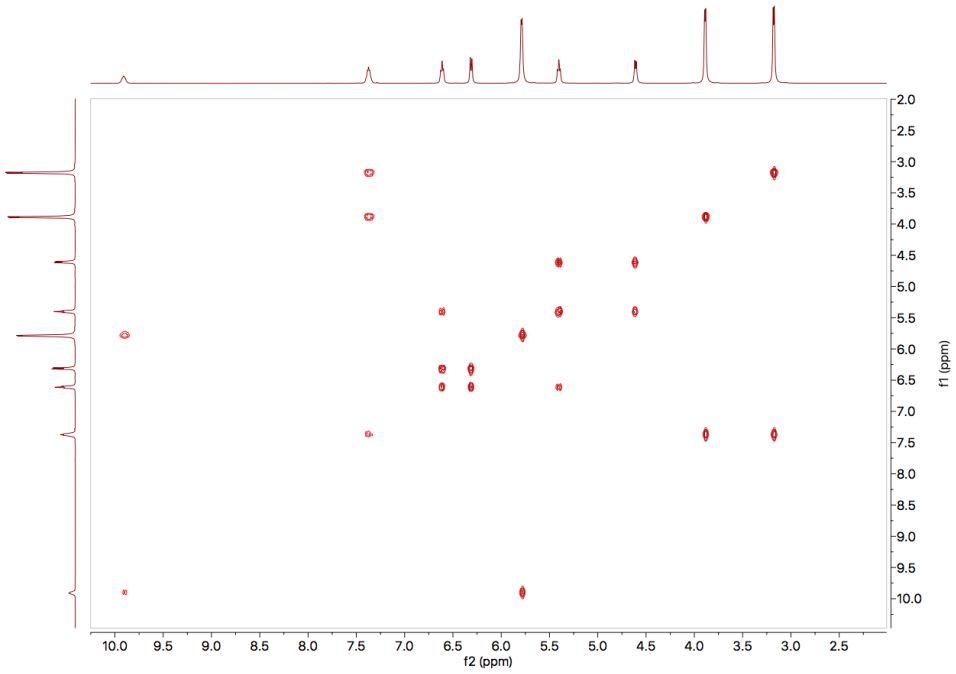

Figure A6. ^{1}H-^{1}H COSY NMR correlation spectrum of **2-Ce**

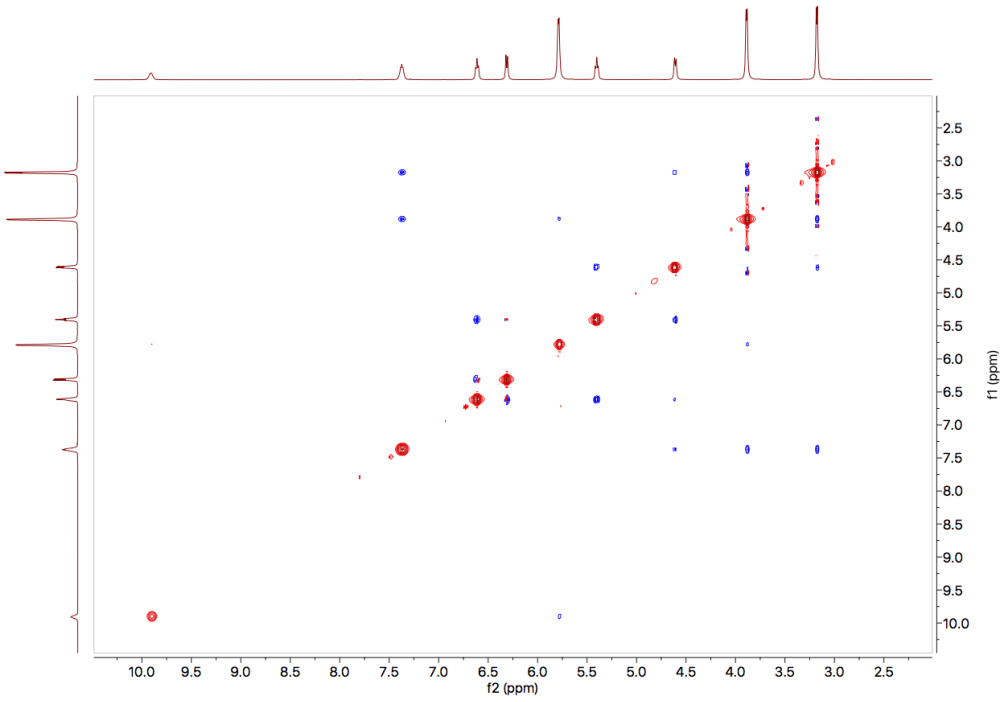

Figure A7. ^{1}H-^{1}H NOESY NMR correlation spectrum of **2-Ce**

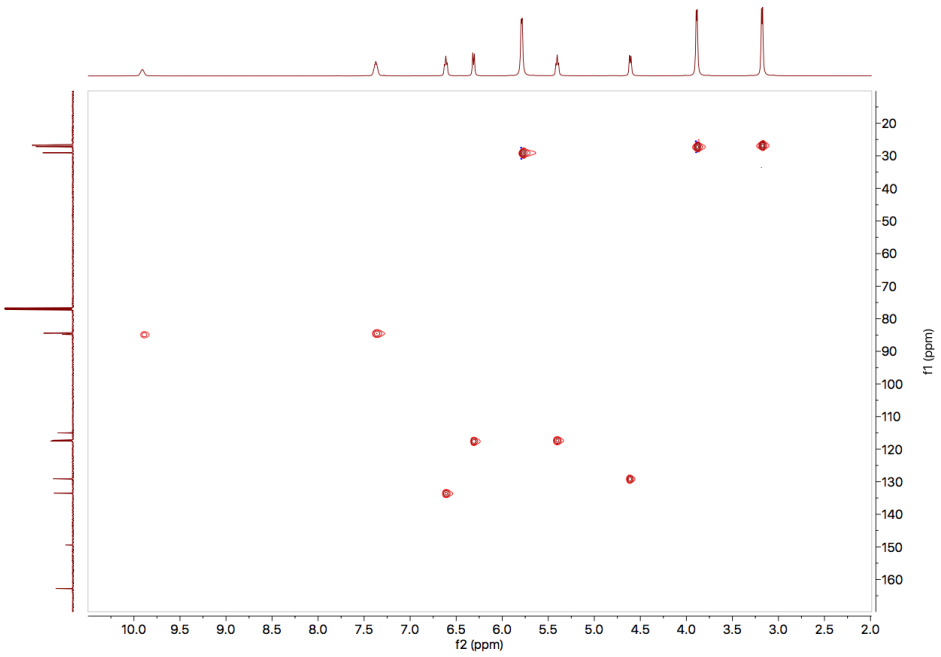

Figure A8. ^{1}H-^{13}C HMQC NMR correlation spectrum of **2-Ce**

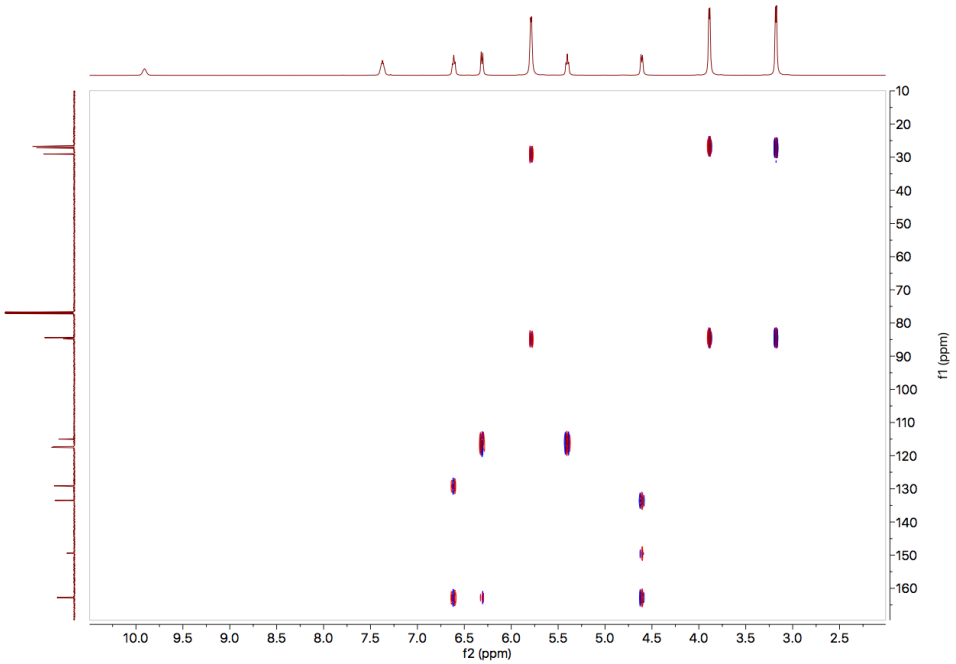

Figure A9. ^{1}H-^{13}C HMBC NMR correlation spectrum of **2-Ce**

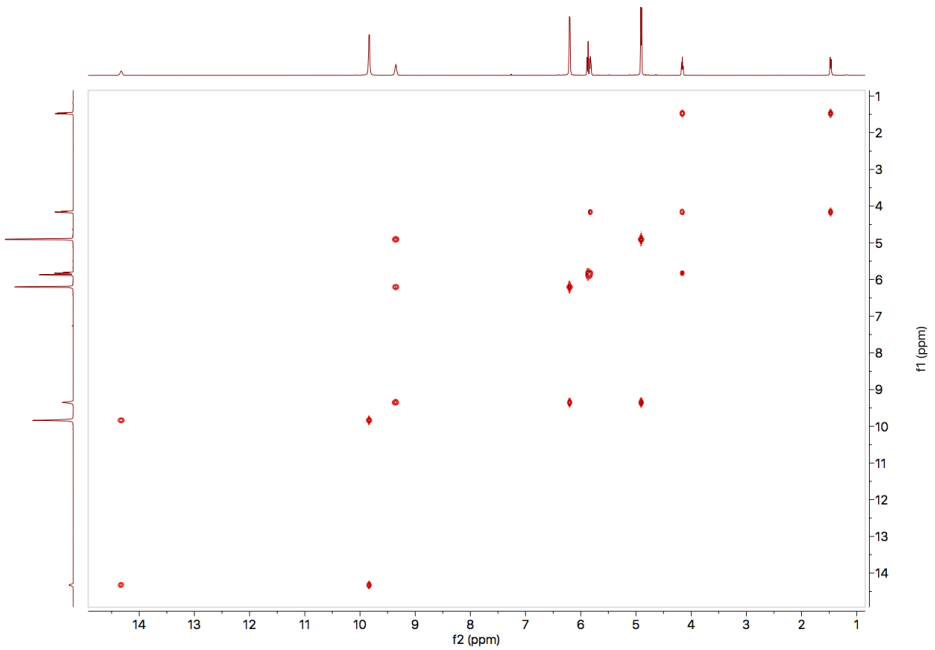

Figure A10. ^{1}H-^{1}H COSY NMR correlation spectrum of **2-Pr**

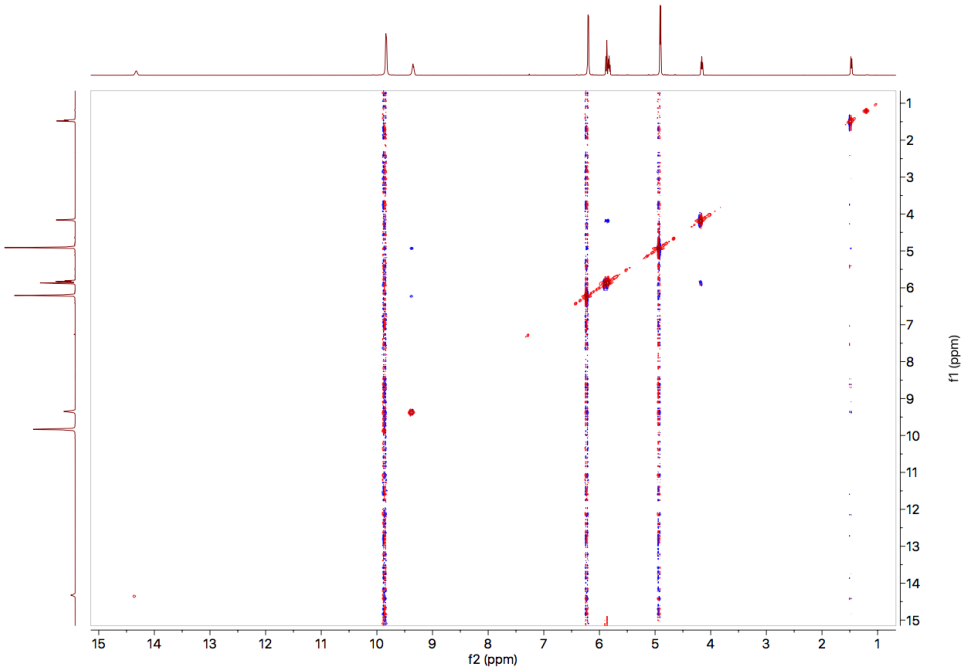

Figure A11. ^{1}H-^{1}H NOESY NMR correlation spectrum of **2-Pr**

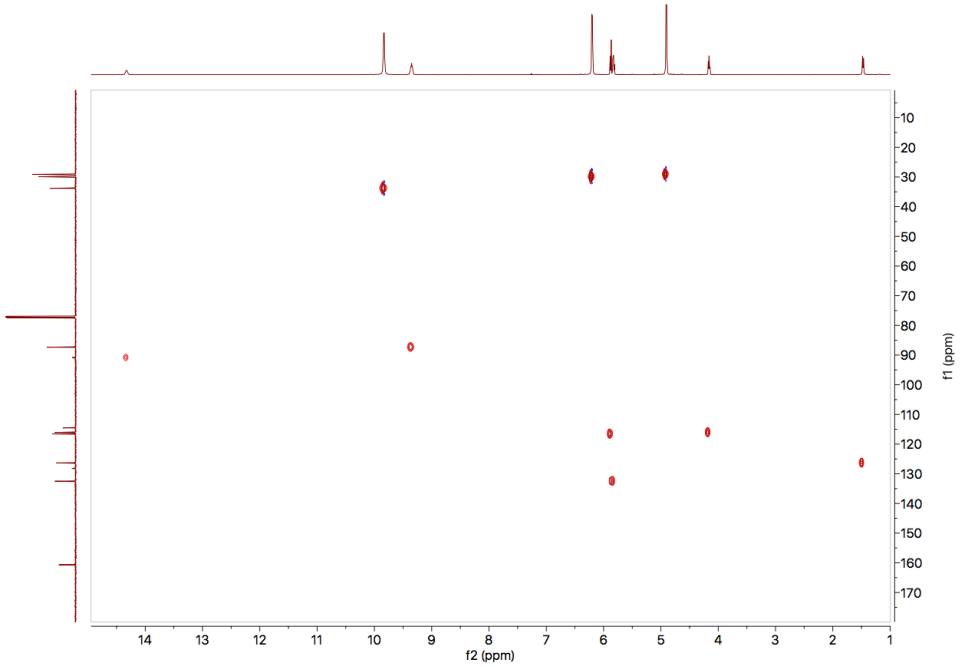

Figure A12. ^{1}H-^{13}C HMQC NMR correlation spectrum of **2-Pr**

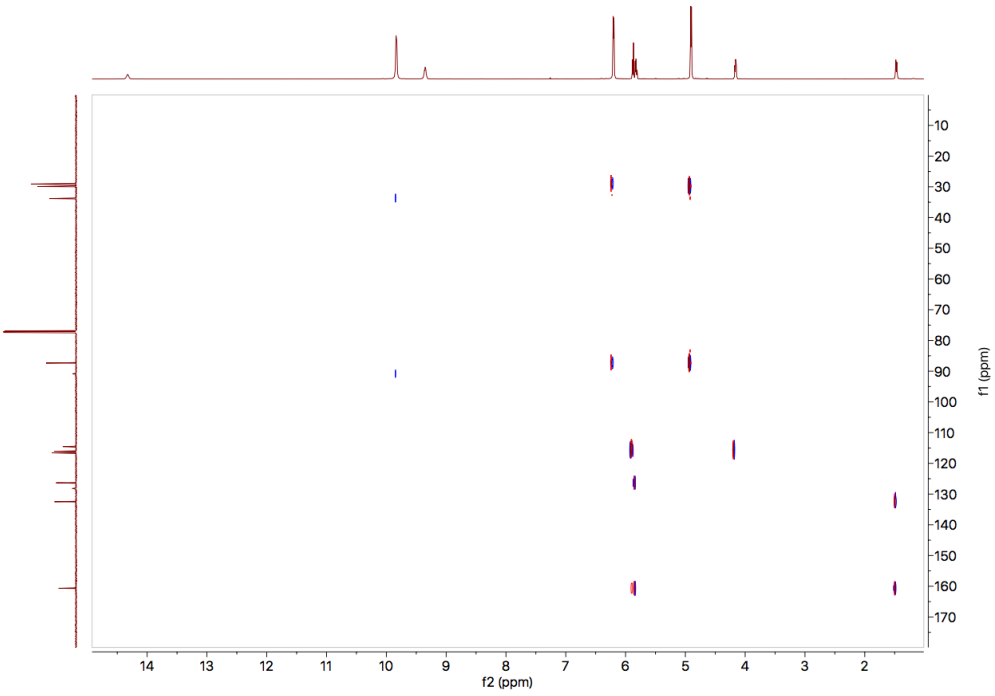

Figure A13. ^{1}H-^{13}C HMBC NMR correlation spectrum of **2-Pr**

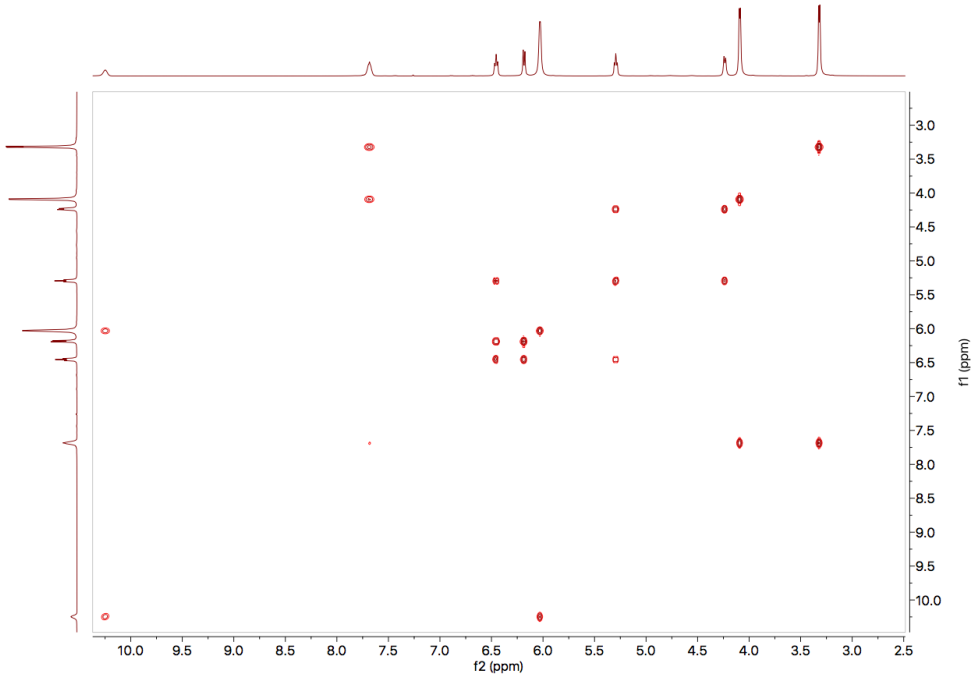

Figure A14. ^{1}H-^{1}H COSY NMR correlation spectrum of **2-Nd**

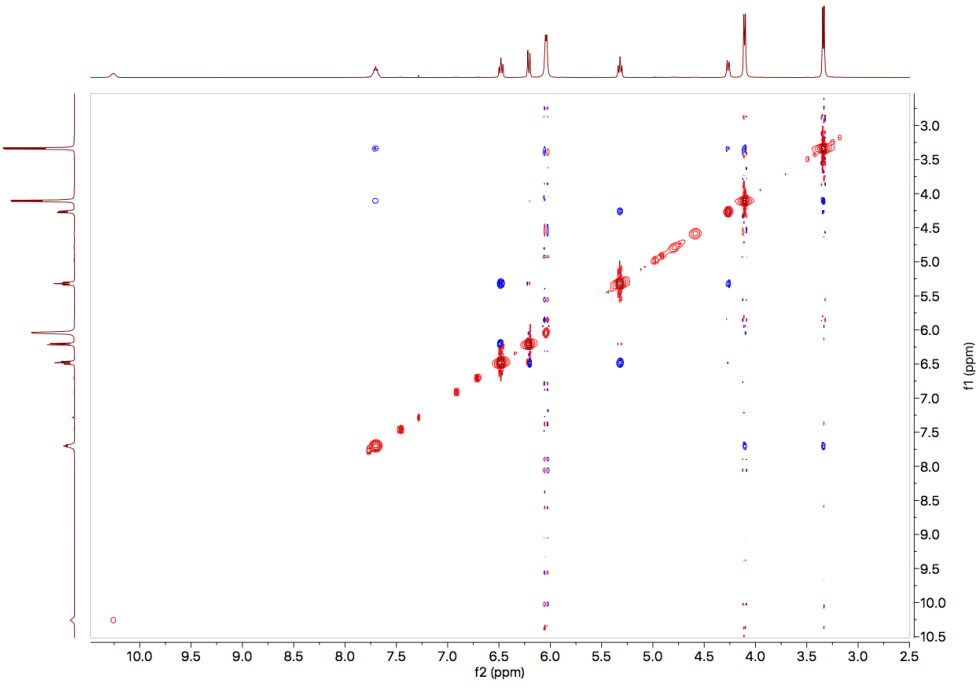

Figure A15. ^{1}H-^{1}H NOESY NMR correlation spectrum of **2-Nd**

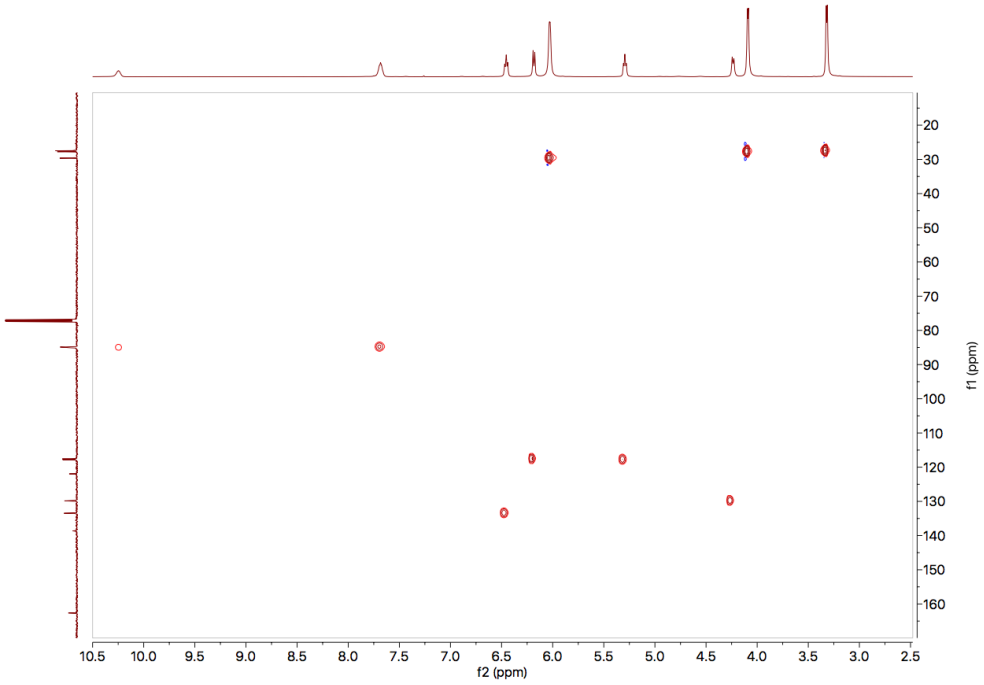

Figure A16. ^{1}H-^{13}C HMQC NMR correlation spectrum of **2-Nd**

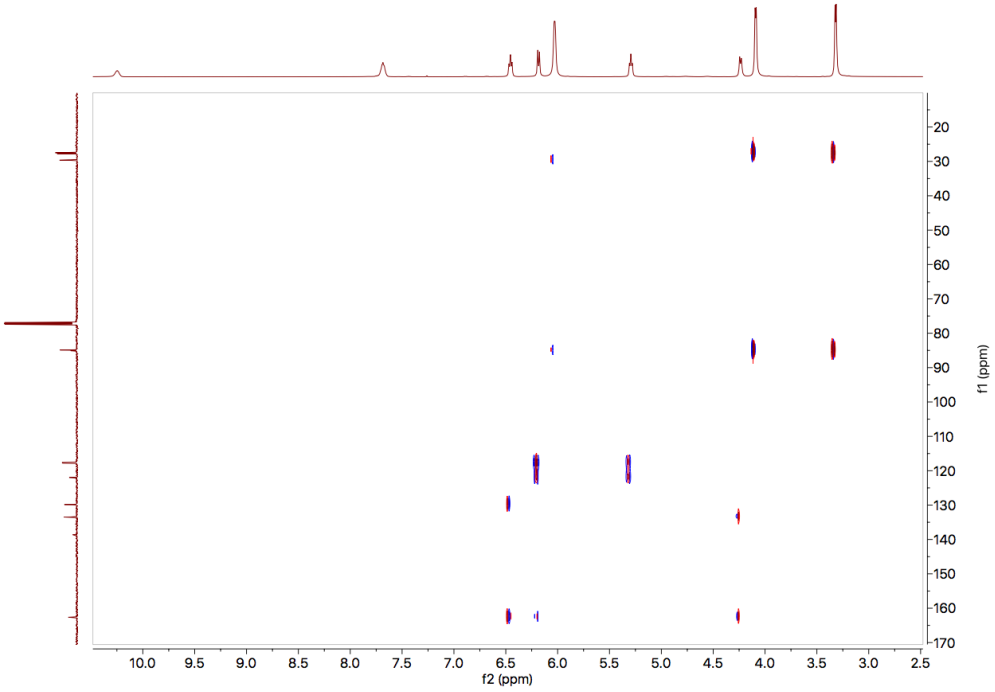

Figure A17. ^{1}H-^{13}C HMBC NMR correlation spectrum of **2-Nd**

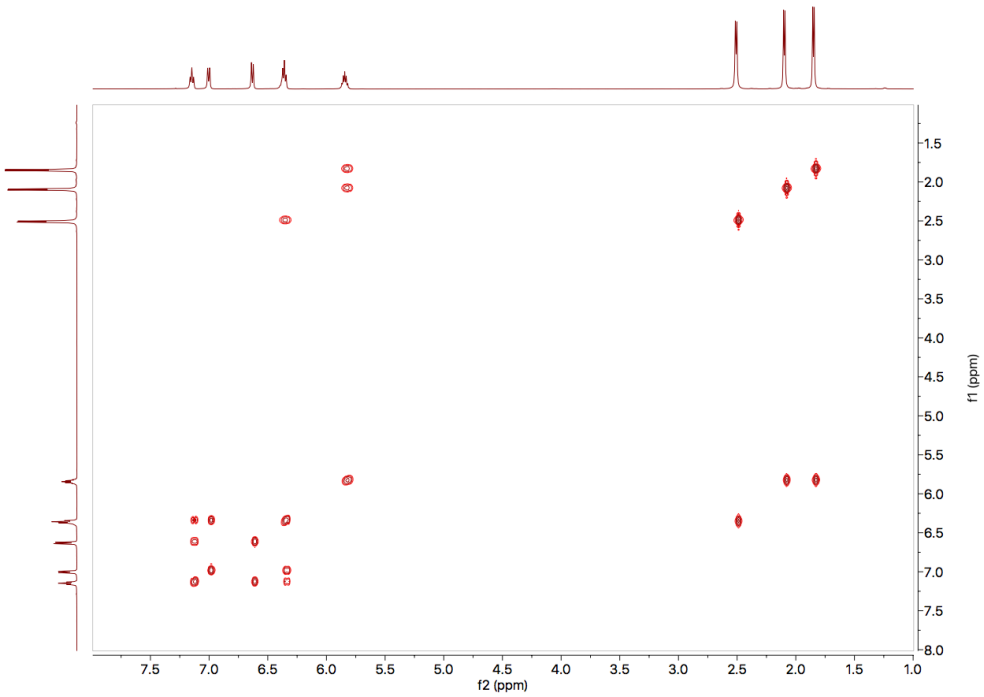

Figure A18. ^{1}H-^{1}H COSY NMR correlation spectrum of **2-Sm**

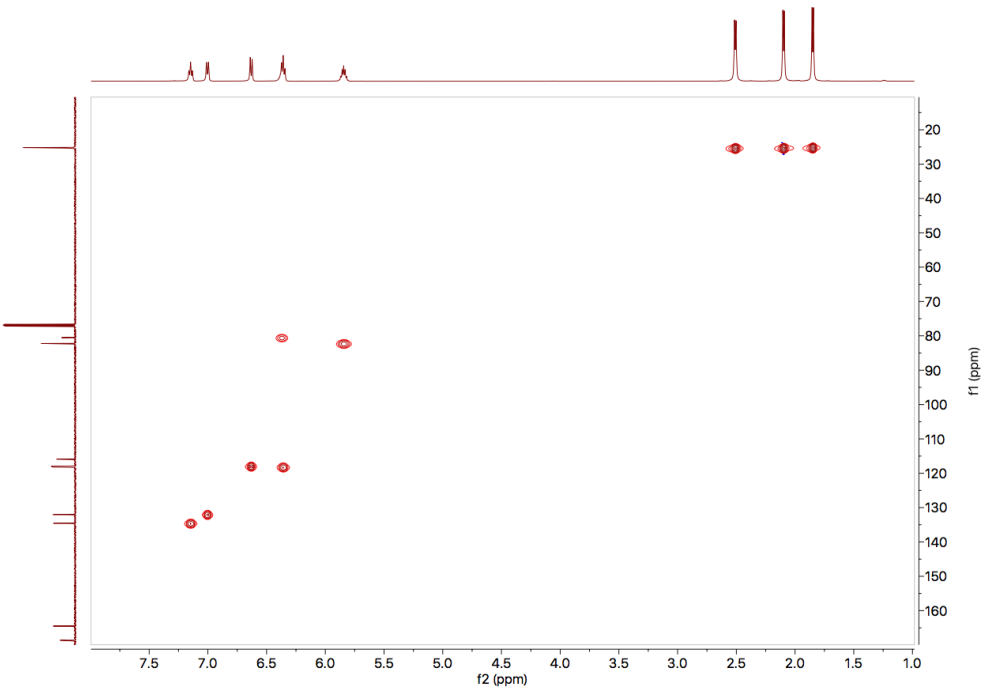

Figure A19. ^{1}H-^{13}C HMQC NMR correlation spectrum of **2-Sm**

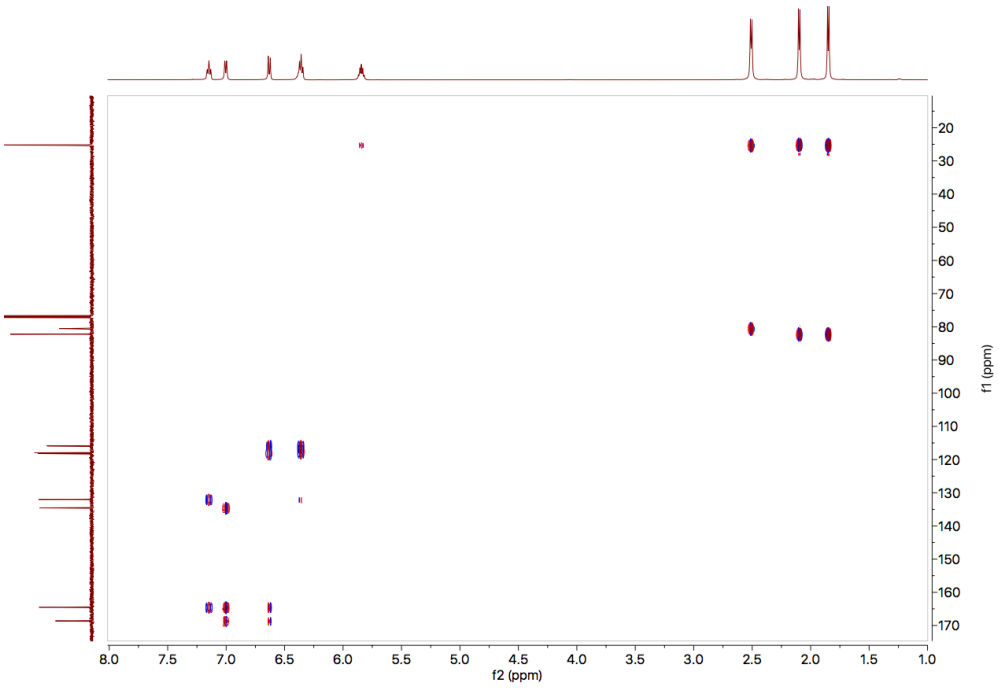

Figure A20. ^{1}H-^{13}C HMBC NMR correlation spectrum of **2-Sm**

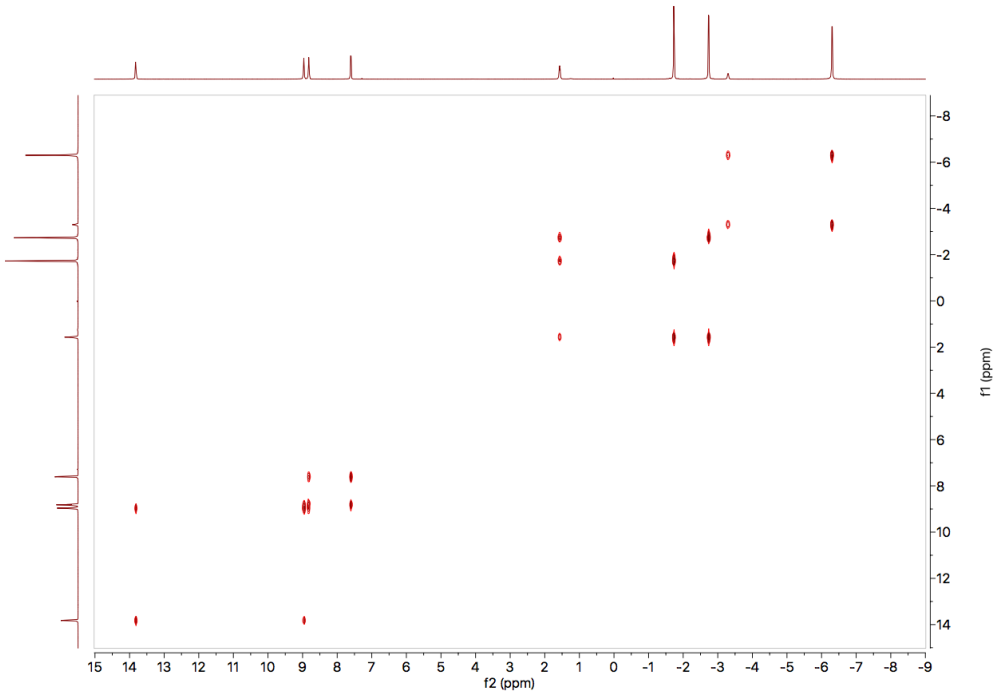

Figure A21. ^{1}H-^{1}H COSY NMR correlation spectrum of **2-Eu**

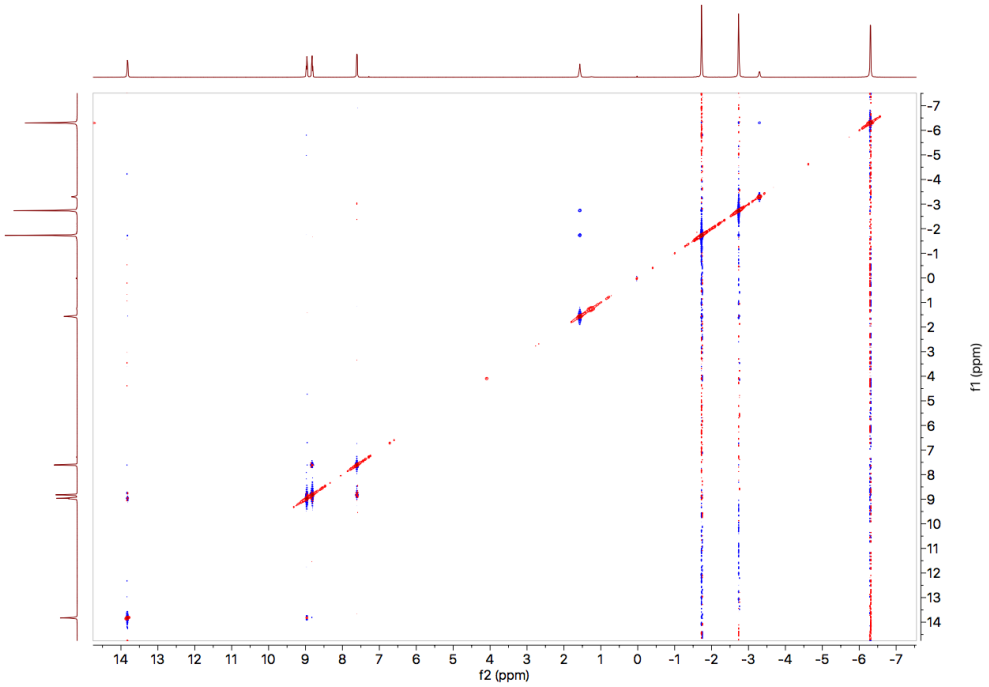

Figure A22. ^{1}H-^{1}H NOESY NMR correlation spectrum of **2-Eu**

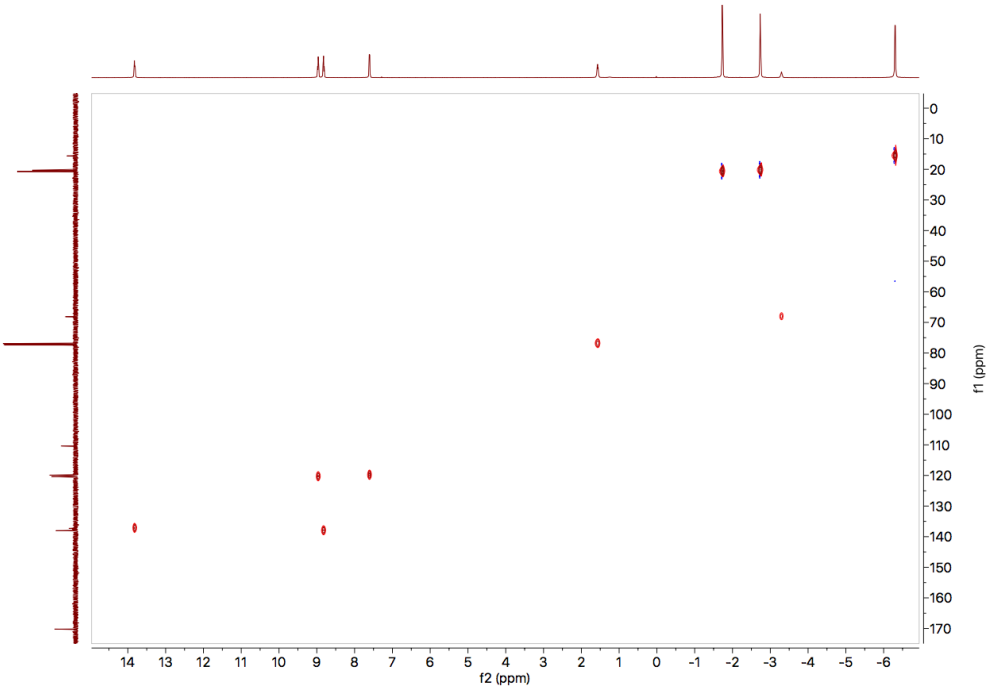

Figure A23. ^{1}H-^{13}C HMQC NMR correlation spectrum of **2-Eu**

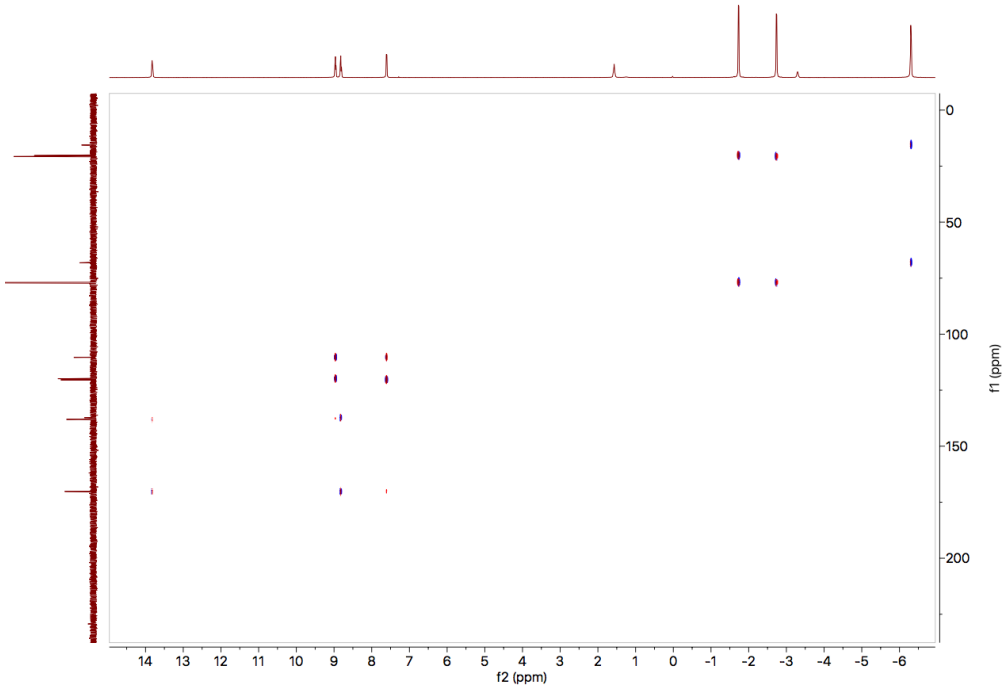

Figure A24. ^{1}H-^{13}C HMBC NMR correlation spectrum of **2-Eu**

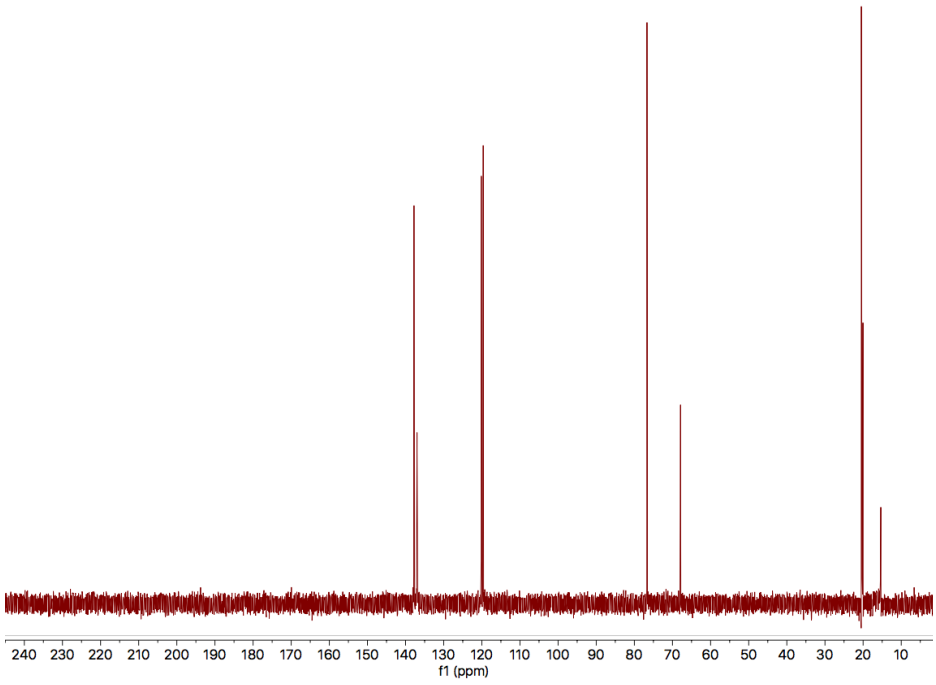

Figure A25. DEPT-135 ^{13}C NMR spectrum of **2-Eu**

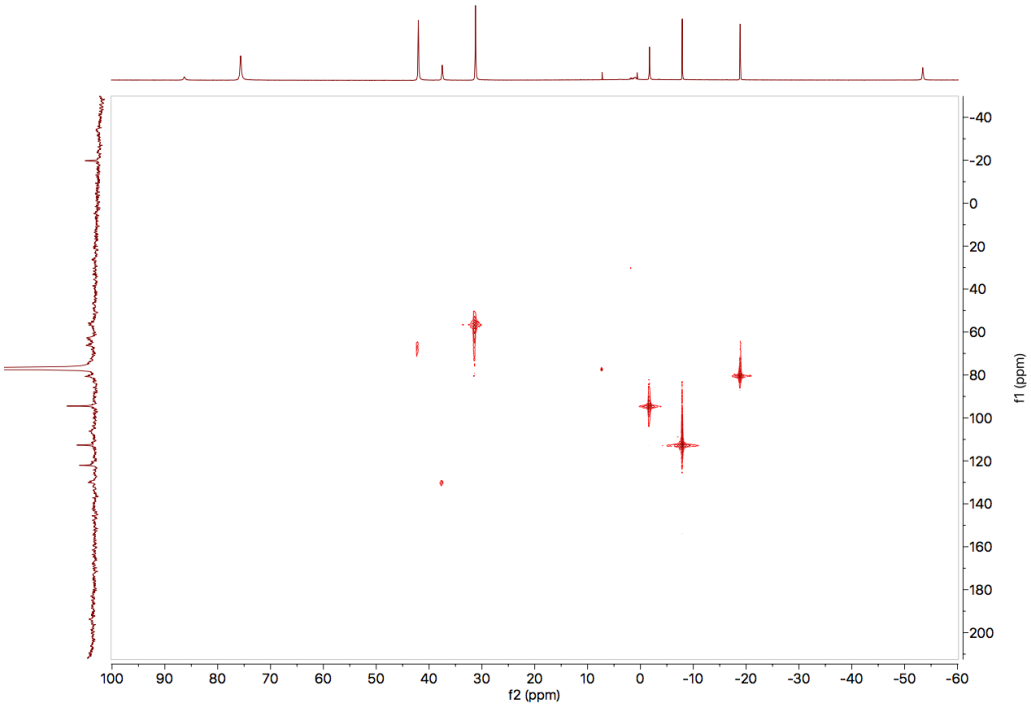

Figure A26. ^{1}H-^{13}C HMQC NMR correlation spectrum of **2-Tb**

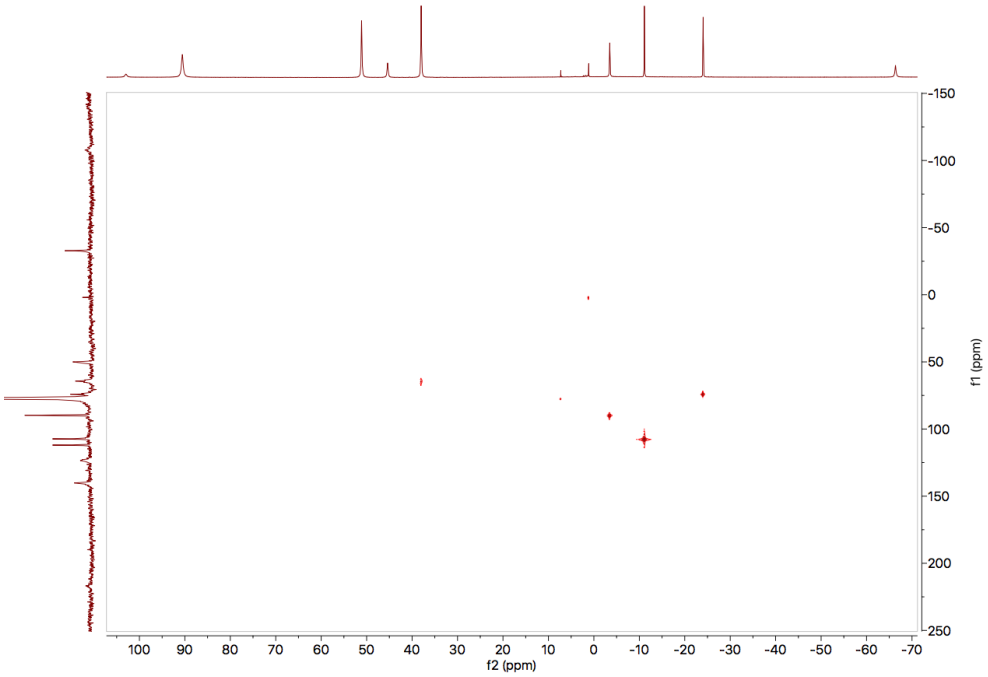

Figure A27. ^{1}H-^{13}C HMQC NMR correlation spectrum of **2-Dy**

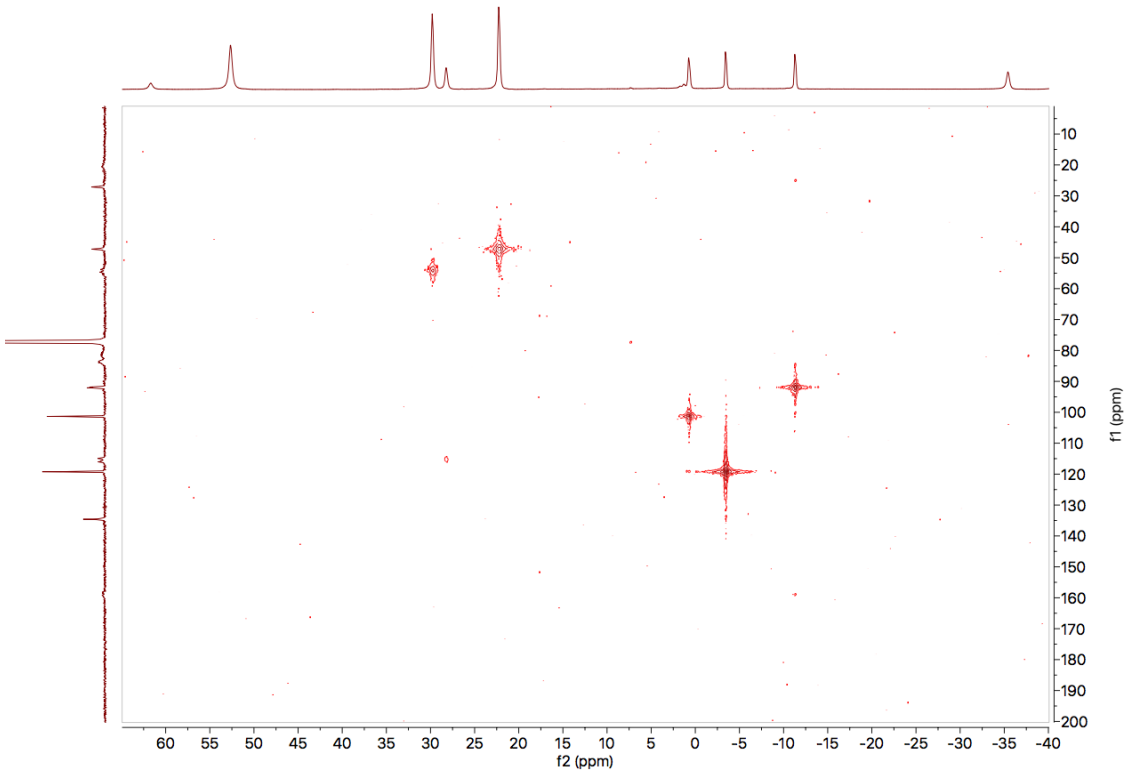

Figure A28. ^{1}H-^{13}C HMQC NMR correlation spectrum of **2-Ho**

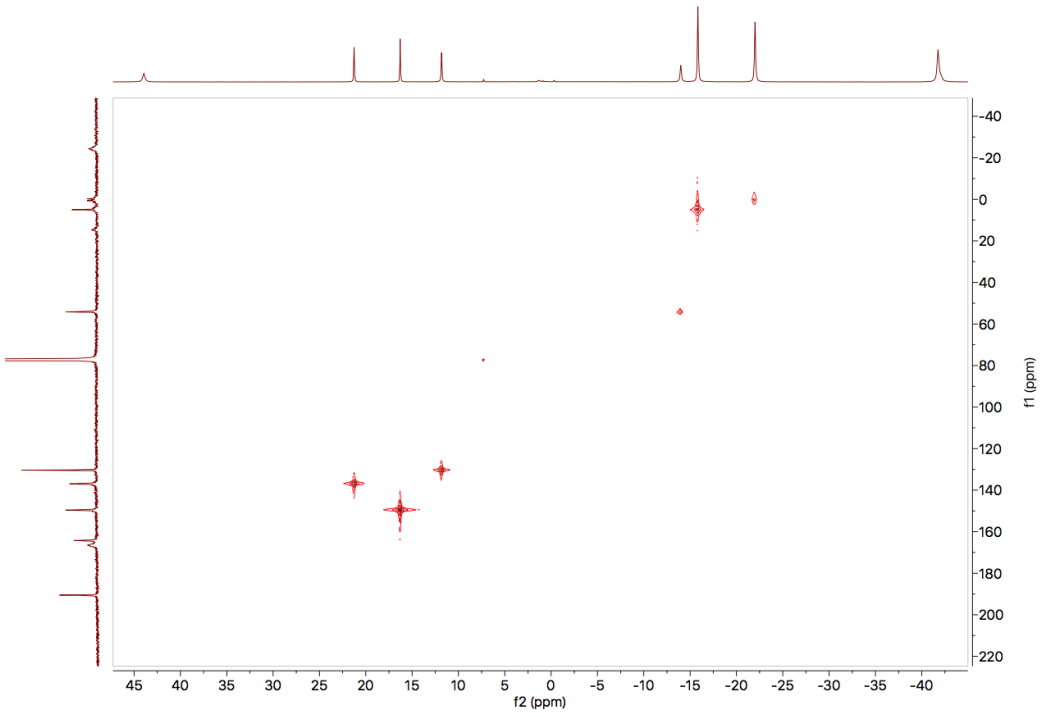

Figure A29. ^{1}H-^{13}C HMQC NMR correlation spectrum of **2-Er**